Real-Time Angle-of-Arrival Estimation through phase interferometry: theory, techniques, applications, and hardware implementation

Politecnico di Bari

Department of Electrical and Information Engineering

ELECTRICAL AND INFORMATION ENGINEERING
Ph.D. Program

SSD: ING-INF/01 – ELECTRONICS

Final Dissertation

REAL-TIME ANGLE-OF-ARRIVAL ESTIMATION THROUGH PHASE INTERFEROMETRY: THEORY, TECHNIQUES, APPLICATIONS, AND HARDWARE IMPLEMENTATION

---

by

Antonello Florio

Referees:

Prof. Walid Dabbous

Prof. Zoran Stamenkovic

Supervisors:

Prof. Ing. Gianfranco Avitabile

Prof. Ing. Giuseppe Coviello

Coordinator of Ph.D. Program:

Prof. Ing. Mario Carpentieri

Course n°35, 03/08/2020-02/08/2023

To my beloved family.

Abstract

THIS thesis focuses on the study and deployment of real-time Angle-of-Arrival (AoA) estimation methods. AoA estimation is a localization approach that exploits the propagation properties of radio signals. The classical techniques for localization are analyzed, with a comparison of their advantages and disadvantages. The methods for performing AoA estimation and their potential hardware implementation in specialized hardware architectures are presented. Phase interferometry is introduced as a lightweight way to estimate AoAs. A method for estimating AoA using an approach inspired by I/Q coherent demodulation is detailed, including in the presence of multiple sources. Phase integrity issues are also addressed, with the proposal of a method for unbiasing the final estimation results in the presence of mutual coupling and realization artifacts. The core of this work is the proposal of a novel digital architecture for real-time AoA estimation based on phase interferometry performed entirely in hardware. The prototype of this architecture was synthesized on a FPGA and used as the foundation for a coarse positioning system based on the AoA estimation of signals of opportunity from Low-Earth Orbit satellites.

Summary and Thesis organization

LOCALIZATION in the telecommunications field enables a set of services that were unimaginable even a decade ago. Thanks to localization, the end-user can improve their quality of experience while accessing a given service. For example, it is possible to deploy environmental and health monitoring systems or organize smart cities with intelligent buildings, thanks to IoT devices connected to form a Wireless Sensor Network. In general, the presence of an increasing number of connected devices requires the capacity of communication channels to be empowered. This goal can be achieved through space diversity techniques, for which real-time localization is a key enabling technology. The industry itself benefits from localization in various scenarios covered by Industry 4.0, smart grids for electricity distribution planning and optimization, and smart precision agriculture. Over the years, the scientific community has developed several techniques to determine the location of a target. This thesis focuses on localization through the electromagnetic propagation properties of radio waves. By using geometric relationships, it is possible to associate the general quantities characterizing a signal with the direction from which it is emitted, known as the Angle of Arrival (AoA).

This thesis is the non-exhaustive synthesis of three years of research in the field of low-complexity real-time localization systems based on AoA estimation. The structure of the chapters reflects the main phases of this research: analysis of the state-of-the-art, first attempts to assess the viability of the technique, analysis and correction of possible artifacts, deployment of a first prototype, and application to a real scenario. The chapters are organized as follows.

- Chapter 1 introduces the basic definitions and approaches defining the localization process, discussing the challenges and issues that each technique or operating scenario may introduce, along with examples of communication technologies based on localization. Particular attention is put to geometric localization techniques.
- Chapter 2 is focused on the AoA definition, and on the main estimation techniques and challenges when implementing systems operating in real-time. Also, phase interferometry some examples of systems based on this technique are presented.

- Chapter 3 describes a novel technique for AoA estimation through phase interferometry in the presence of multiple sources. The technique relies on multi-channel phase difference estimation and angle computation.
- Chapter 4 describes a linear technique aiming to minimize the AoA estimation error due to analog front-ends realization artifacts and mutual coupling between the receiving antenna array elements.
- Chapter 5 introduces a novel technique for AoA estimation based on phase interferometry. The architecture was implemented on FPGA and it was validated through a large set of experiments involving both custom-designed analog hardware boards and Hardware-in-the-Loop testing tools.
- Chapter 6 introduces a novel coarse positioning technique based on AoA estimation through phase interferometry from multiple receiver nodes. The technique works with Signals of Opportunity from Low Earth Orbit spacecraft.
- The Appendices describe the (analog) "hardware tools" (boards and components) designed to perform the experiments in the other chapters and a small mathematical introduction to phase extraction from I/Q samples.

Contents

Acronyms

ADC Analog-to-Digital Converter

AI Artficial Intelligence

AoA Angle of Arrival

AoD Angle of Departure

BLE Bluetooth® Low-Energy

CC Clock Cycle

CRLB Cramer-Rao Lower Bound

CW Continuous Wave

DAC Digital-to-Analog Converter

DSP Digital Signal Processor

DVB Digital Video Broadcasting

e.m. electromagnetic

FM Frequency Modulation

FPGA Field-Programmable Gate Array

GNSS Global Navigation Satellite System

GPS Global Positioning System

GT Ground Truth

HPBW Half Power Beam Width

IF Intermediate Frequency

IMU Intertial Measurement Unit

IoT Internet of Things

LBS Location Based Service

LEO Low-Earth Orbit

LO Local Oscillator

LoS Line-of-Sight

LPWAN Low-Power Wide Area Network

LUT Look-Up Table

MEO Medium-Earth Orbit

MIMO Multiple-Input-Multiple-Output

ML Machine Learning

mmWave millimeter wave

MN Mobile Node

NB-IoT Narrow-Band IoT

nLoS near-LoS

NLoS Non-LoS

OFDM Orthogonal Frequency Division Multiplexing

OSR Over Sampling Ratio

PDoA Phase Difference of Arrival

PNT Position Navigation and Timing

PoA Phase of Arrival

RF Radio Frequency

RFID Radio Frequency IDentification

RMSE Root Mean-Square Error

RN Reference Node

RSS Received Signal Strength

RSSI Received Signal Strength Indicator

RTLS Real-Time Localization System

SDR Software Defined Radio

SoOp Signals of Opportunity

TDoA Time Difference of Arrival

ToA Time of Arrival

ULA Uniform Linear Array

UWB Ultra-Wide Band

WBAN Wireless Body Area Network

Wi-Fi Wireless Fidelity

WLAN Wireless LAN

WSN Wireless Sensor Network

CHAPTER 1

Localization: Definitions, Techniques and Applications.

This chapter is partially based on the book chapter: A. Florio, G. Avitabile, and G. Coviello, "Geometric Indoor Radiolocation: History, Trends and Open Issues", in Machine Learning for Indoor Localization and Navigation, S. Tiku and S. Pasricha, Eds. Cham: Springer International Publishing, 2023, pp. 49–69.

In many situations, knowing the location of a person or object is crucial. For this reason, spatial localization represents an important topic, widely examined by the scientific community. As for many other technologies, localization origins are strongly bonded to military applications and warfare [1]. The first examples of RADARs (RAdio Detection And Ranging systems) were developed to identify a given target with respect to a known geographic reference point where the station was located. The original plants were mainly devoted to detect the presence of incoming hostile flying vehicles from a fixed direction without furnishing any precise ranging information. However, like most of military technology, once it was introduced, RADAR found many civil fields of applications, improving everyday life.

Many recently born paradigms strive for the development of new devices with capabilities that even a decade ago would be unimaginable, in many cases deploying Location Based Service (LBS). LBS are meant to improve end-user quality of experience while accessing a given service thanks to the identification of their location. One of the most important use cases is the Internet of Things (IoT) [2]. For example, it is possible to deploy environmental and health monitoring systems or organize smart cities with intelligent buildings thanks to IoT devices connected to form a Wireless Sensor Network (WSN). The industry itself benefits from this technology, for instance, in the manifold scenarios covered by Industry 4.0, or in the smart grids for electricity distribution planning and optimization and smart precision agriculture [2].

Over the years the scientific community developed several techniques to determine the location of a target. As proposed by *Subedi et al.* in [3], the technologies can be divided into Radio Frequency (RF), lightwave, acoustic and mechanical. In the RF technologies, the localization process is performed thanks to the radio waves. In the lightwave techniques, visible light and infrared can be exploited to carry out the localization process [3]. Also, the positioning can be performed by means of videos and images from which they can be extracted some features to be compared: this is the case of vision-based localization [4]. In mechanical or Dead Reckoning (DR) techniques, different Intertial Measurement Unit (IMU), atmospheric pressure sensors or magnetic field sensors are employed to determine the actual position of a target starting from a known initial point and performing some computations based on sensed data [3, 4]. Especially in indoor localization, acoustic wave-based techniques can be employed, taking into account the ambient sound or ultrasound techniques [3].

This thesis is focused on localization by means of radio waves. One interesting definition of this way of performing localization is given by the International Telecommunications Union (ITU) in the last edition of the Radio Regulations (RR). In fact, Article 1.9 defines the radiodetermination as the *"determination of the position, velocity, and/or other characteristics of an object, or obtaining of information relating to those parameters, by means of the propagation properties of the radio waves"* [5]. The radionavigation is then defined at Article 1.10 as *"the radiodetermination used for the purposes of navigation, including obstruction warning"* [5]. Article 1.11 generically indicates the radiolocation as the *"radiodetermination used for purposes other than those of the radionavigation"*. Throughout this thesis, the terms "radiodetermination", "radiolocation" and, generally, "localization" will be used as synonyms.

The presence of an increasing number of connected devices requires to empower the capacity of the communication channels. This goal may be achieved thanks to space diversity techniques like Multiple-Input-Multiple-Output (MIMO) that allow for enhancing each user experience by particular optimization algorithms and coding techniques [6, 7]. One of the enabling technologies for MIMO is adaptive beamforming, i.e. the dynamic array pattern synthesis. From this simple example, we understand how localizing the user to be served becomes critical [8, 9]. The same consideration holds for smart industries, self-driving robots, or asset tracking in which localization plays a key role [10]. Even in telemedicine, localization is an important ingredient when striving to create smart hospitals, in which the patients needing medical assistance have to be localized to furnish them with sanitary services timely.

The aim of this chapter is to introduce the basic definitions and approaches defining the localization process, discussing the challenges and issues that each technique or operating scenario may introduce, along with examples of communication technologies based on localization. Particular attention is put into geometric localization techniques.

1.1 Definitions and taxonomy

A definition of localization was already given through the words of the ITU RR. A more practical definition considers localization as the process of establishing the position of a given target in the space with respect to some predefined reference points.

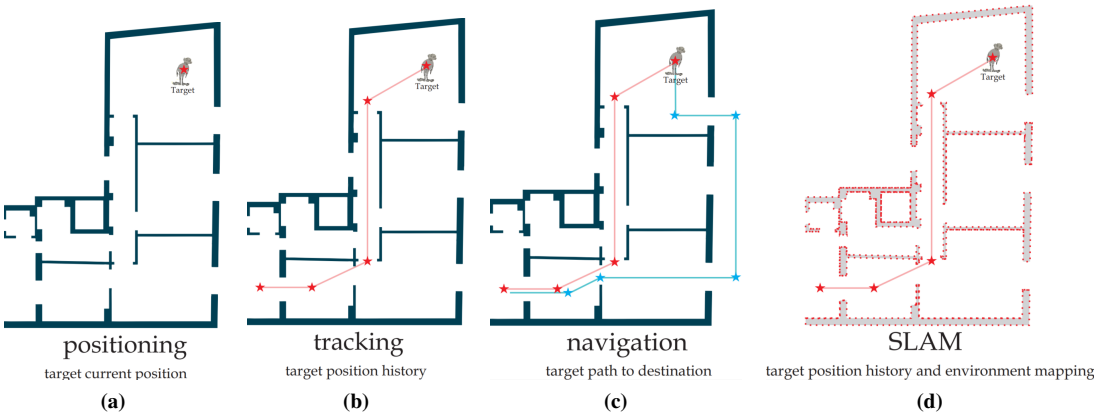

Figure 1.1: Sketch of the (a) positioning, (b) tracking, (c) navigation and (d) SLAM localization definitions presented in this section.

This is done by using any suitable procedure, algorithm, or technology, based on the parameters characterizing the emitted electromagnetic signal by the object whose position has to be determined. As described by *Montroni et al.* in [10], there are mainly four different ways of deploying localization. A sketch is presented in Figure 1.1.
The first one is positioning, in which the target is static with respect to the reference points. If the target is moving, we talk about tracking, in which the aim is to estimate a trajectory, defined as the sequence of positions assumed by the target time by time. In navigation, the trajectory is predefined, and the aim is to exploit the localization to follow this trajectory, usually through the shortest path. Finally, Simultaneous Localization And Tracking (SLAM), as suggested by the name, consists in concurrently establishing the trajectory while acquiring a map of the environment.

1.2 Actors of the localization process

The actors participating localization process are clearly described in the work [2] by *Farahsari et al.*. A Reference Node (RN) (also called anchor node) is placed to establish a reference point for the system. RNs positions are precisely known *a priori*. Along with the RNs, the targets (or Mobile Node (MN)) are the objects to be localized. If the target participates in the localization process actively, it is said to be cooperative. Otherwise, if the estimation is done without any hint from the target, this latter is said to be non-cooperative. In some cases, targets implement some strategies to jam the localization process, as in warfare applications.

Another paradigm is the collaborative localization [1], in which the process is performed between the anchor and mobile nodes and nodes proactively collaborate in the final result refinement, or to lighten the localization process. An example of collaborative localization is offered by Received Signal Strength (RSS) crowdsourcing that will be analyzed in Section 1.5.4.

1.3 Localization architectures

In the literature there are different topologies to perform localization. In their work [11], *Laoudias et al.* on this topic.

The first is the MN-based, in which the MN is responsible for the localization. This is useful when the target itself takes advantage of the result of the location estimation, and no information about the localization outcome is sent back to the network controller. However, the node must have some computational capability to determine its position from the measurement taken from the reference nodes (i.e. the location estimation algorithm has to be implemented on each MN, and this is a non-trivial requirement to be met on IoT devices since they are usually units with limited computational power). MN-based architecture is usually employed in navigation [12].

In MN-assisted architectures, the role of the MN is to only perform measurements, which are then sent back to the network controller. This latter is in charge of sending back the localization estimation to each MN. The advantage is that the device can have limited computational resources since the algorithms are implemented on the network core. Also, the localization process can rely on information coming from multiple nodes to refine the results. The drawback is that the localization information is not immediately available to the MNs. Moreover, the network controller becomes a critical node like in every centralized architecture (i.e. a single point of failure for the localization infrastructure).

The Network-based architecture is the most passive way to realize localization, from the MN point of view. In this architecture, the network is responsible both for the measurements and the location estimation, and the MNs have no active part in the process. Hence, this architecture is non-cooperative. From the point of view of the MNs' computational resources burden, this is an advantage, as the MNs are totally free from any involvement in the localization process. The network is in charge of providing support to detect the presence of a target and estimate its location without any hint (usually this is done through network sniffing). Both MN-assisted and network-based architectures are specifically employed in tracking [12].

1.4 Localization techniques

Assuming that the measurements are available, there are five different techniques to establish the target position [1, 2, 11]. Each technique is based on a different physical quantity to estimate (i.e. distance and/or angle) or by the way those quantities are obtained.

Angulation This technique relies on the position estimation from estimated angles. One example of angulation is the Angle of Arrival (AoA) estimation. Knowing the target angular position with respect to each anchor node allows estimating the target position through the intersection of lines relying on the direction of the MN with respect to the RN. With this technique, it is necessary to rely on at least two anchors for 2D positioning and three anchors for 3D positioning. Figure 1.2a sketches angulation-based localization in 2D.

Figure 1.2: Sketch of the (a) angulation and (b) lateration position identification techniques in bidimensional space. The anchor nodes are set in the known positions $(x_i, y_i) \in \mathbb{R}^2$, $i = \{1, 2, 3\}$ while the target in the unknown position $(x, y) \in \mathbb{R}^2$. The position is then determined to the angles-of-arrival $\{\alpha, \beta\}$ and the distances d_i, respectively for the two techniques.

Lateration Lateration relies on the computation of the distances between RNs and MNs. These distances are employed for tracing curves (circumferences or hyperbolas) whose intersection determines the estimated position of the target. In trilateration, a set of three anchors is necessary for 2D positioning, while four are required for 3D positioning. The insertion of more anchors allows for an increase in the accuracy of the localization system [2]. A sketch of the lateration approach is shown in Figure 1.2b.

Fingerprinting Fingerprinting is the technique on which RSS positioning systems are based. In this technique, some off-line measurements of a given quantity (e.g. the signal power) in many reference points are used to create a map of the propagation environment. Each reference point is known, hence it is possible to start from a comparison between previous stored measurements, and current measured values. This technique is less resilient to propagation environment variations: as soon as there are changes (people moving, furniture displacements, and so on) it is necessary to reconstruct the entire database to obtain meaningful results.

Proximity Proximity can be thought of as a recombination of the fingerprinting and lateration but in a less accurate way. In fact, the anchor nodes detect only the presence of the target in their region, without estimating the exact position, which is considered unnecessary.

Trajectory In trajectory localization, the initial position of the target and the movements with respect to the anchor nodes are the basic information. If movements are not available, the trajectory estimation is done through probabilistic characterization. In this way, the position is reconstructed through trajectory tracking.

1.4.1 Metrics

The localization process has satisfy some basic requirements to be considered accurate and/or precise, as in any measurement system.

We call accuracy the measure of how much the measured value (in this case, the target coordinates) is close to the real one, the so-called Ground Truth (GT). The propagation scenario and the electronic components are affected by phenomena disturbing the accuracy of the system. Those phenomena are modeled through random processes. In this context, we can introduce the concept of precision as the repeatability of the accuracy: we consider a measurement to be precise if by repeating it multiple times, we obtain the same accuracy.

Having introduced the random nature of the localization artifacts, we could discuss the two main mathematical tools for evaluating the performance of a localization system: the probability of error and the Cramer-Rao Lower Bound (CRLB) [1]. The probability of error describes the possibility of the positioning error falling in a given range of values. We talk about linear, circular, and spherical error probability respectively for 1, 2, or 3 dimensions positioning systems.
The CRLB offers a (theoretical) lower bound to the error variance of the repeated estimations of a localization system.

The error is usually evaluated using the Root Mean-Square Error (RMSE), which is defined as the square root of the MSE of a given estimator [13]. In our case, the estimation of the error is derived from the comparison of the GT and the measured value, so

$$RMSE(\hat{\mathbf{x}}) = \sqrt{\frac{1}{N}\sum_{i=0}^{N-1}[\hat{x}_i - x]^2} \tag{1.1}$$

where $\hat{\mathbf{x}} = \{\hat{x}_i \mid i = 0, \cdots, N-1\}$ is the set of measured samples for the GT value x and N is the set cardinality (i.e. the available estimations).

Accuracy and precision are usually considered the most important characteristics. However, as also mentioned by *Subedi et al.* in [3], other metrics like the ease of implementation, the feasibility of the system cost, robustness, scalability, and the low computational complexity play a key role, especially in power constrained domains or high devices density contexts.

1.5 Geometric localization approaches

The geometric radiolocation aims to derive some geometric quantities, i.e. angles, and distances, associated with the signal path through a given radio medium. The approaches we are going to describe allow us to estimate those quantities and employ them to implement the positioning techniques described in Section 1.4. It is clear that no single technique can be eligible as the best for each environment. The choice has to be made taking into account the best achievable trade-off between precision, availability, and the overall cost of the system.

Technology also plays a role. As an example, when discussing the Phase of Arrival (PoA), the first assumption is the initial phase of the transmitted signal is known. This is always possible in Radio Frequency IDentification (RFID) systems, but it is not a trivial requirement to be satisfied in other applications. Another example is given

by Wireless LAN (WLAN) and RSS. Because the IEEE 802.11 standard directly furnishes the Received Signal Strength Indicator (RSSI), and because of the widespread of WLAN Access Points, it is simple to think of these latter as anchor nodes and employ the RSS, leading to lower implementation costs.

1.5.1 Angle-of-Arrival

The AoA is also called Direction-of-Arrival (DoA) since it indicates the direction connecting the transmitter and the receiver. Multiple receivers or a single receiver with more than one antenna are necessary to estimate the AoA. This technique can provide high localization accuracy [12]. Moreover, it is sufficient to have two receivers for estimating a position in the 2D space (Figure 1.3) and three receivers for a 3D space [1], since it is based on angulation. The AoA estimation is discussed in detail in Chapter 2.

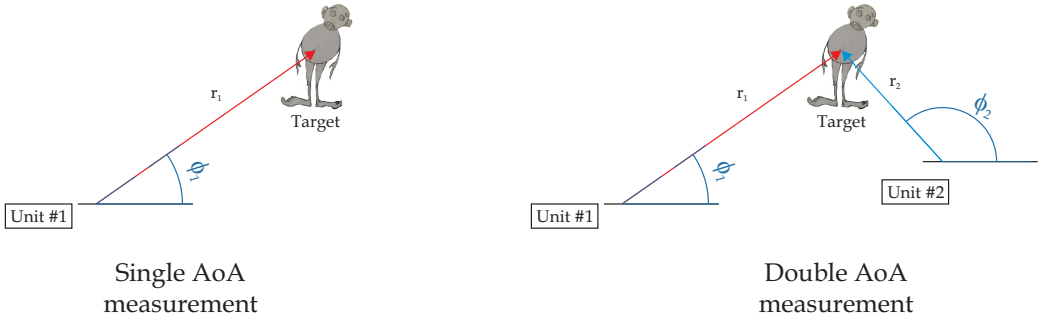

Figure 1.3: Localization by AoA estimation.

1.5.2 Phase of Arrival and Phase Difference of Arrival

PoA and Phase Difference of Arrival (PDoA) localization are based on the estimation of the received signal phase. Thanks to the space/time periodicity of electromagnetic (e.m.) signals, the phase information can be linked to fractions of the signal wavelength (see Figure 1.4a). To apply this technique, the signal received by the localization system must be transmitted with zero or known phase offset [12]. If this condition is satisfied, the measured distance $d(\Delta\varphi)$ can be obtained from the measured phase $\Delta\varphi$ is

$$d(\Delta\varphi) = \frac{\Delta\varphi}{2\pi}\,\lambda \tag{1.2}$$

with λ the wavelength associated with the carrier of the signal and $\Delta\varphi$ the PoA. This approach intrinsically hypothesizes a monochromatic or very narrowband received signal (note the dependency on λ). Note that, due to the nature of the phase periodicity, it is necessary to correctly unwrap the phase value in order to estimate distance values over the λ limit [10].
If more than one antenna or, in general, more than one receiver is available, it is possible to exploit the difference between the PoAs at each sensor. This is the definition of PDoA [14], that is sketched in Figure 1.4b. Being associated with the phase information, PoA/PDoA estimations require a strong component for the Line-of-Sight (LoS) as considered for the AoA, to avoid phase corruption. The main applications

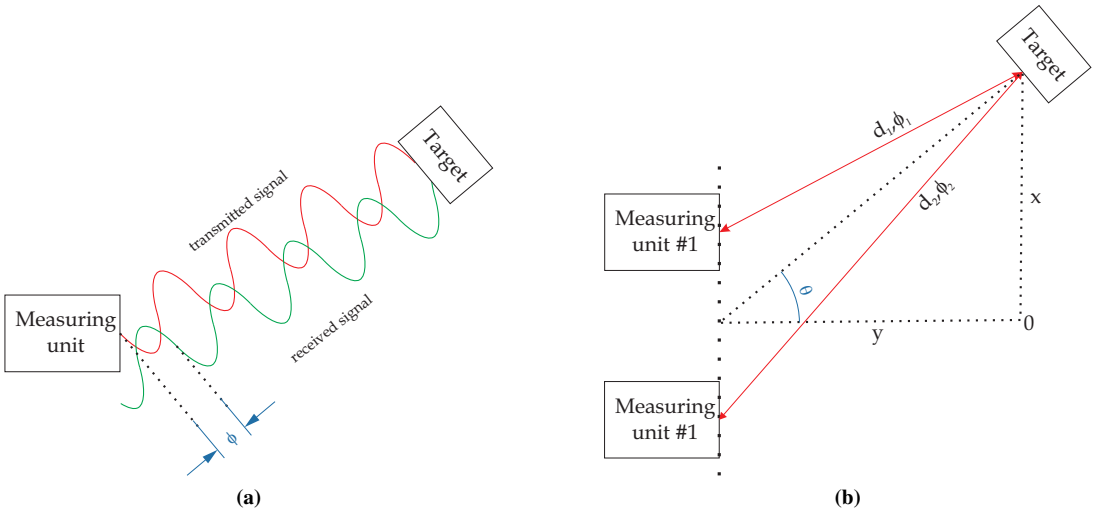

Figure 1.4: (a) PoA vs (b) PDoA approaches geometrical sketch.

are associated with RFID tag tracking [15]. Each tag responds to the reader with a backscattered signal whose phase uncertainty determines a localization error of a wavelength at its maximum, and thus allows the reader to exploit the PoA as a way of identifying the distance, using very simple and reduced cost units. Usually, this technique is employed concurrently with RSS measurements.

1.5.3 Time of Arrival and Time Difference of Arrival

With Time of Arrival (ToA), it is possible to determine the position of the target thanks to the reception time of a signal. In fact, a wave traveling in the air for a time interval τ covers a distance d such that:

$$d(\tau) = c \cdot \tau \tag{1.3}$$

where $c = 2,99792458 \cdot 10^8$ m/s is the speed of light in vacuum. The key problem with ToA estimation is that a strong synchronization between transmitters and receivers is needed. In fact, it is necessary for the transmitter and receivers to be synchronized to agree on a common time stamp for the beginning and the end of the signal sequence. Furthermore, lowering the sampling time of the receivers leads to a degradation of the ToA estimation [12]. For an n-dimensional scenario, it is required to have at least $n + 1$ receivers, $n = 2, 3$ (Figure 1.5a). This is true since one of those receivers acts as the reference of the system (the so-called *dummy receiver*).
The Time Difference of Arrival (TDoA) is introduced to relax the synchronization constraints. This latter exploits the time difference of reception to different receivers. This means the computed distances are employed for estimating through hyperboloid intersection (Figure 1.5b) the position of the target [16]. For a target in the position $(x_T, y_T, z_T) \in \mathbb{R}^3$, having the measured distances d_{ij} and d_i the distances between the

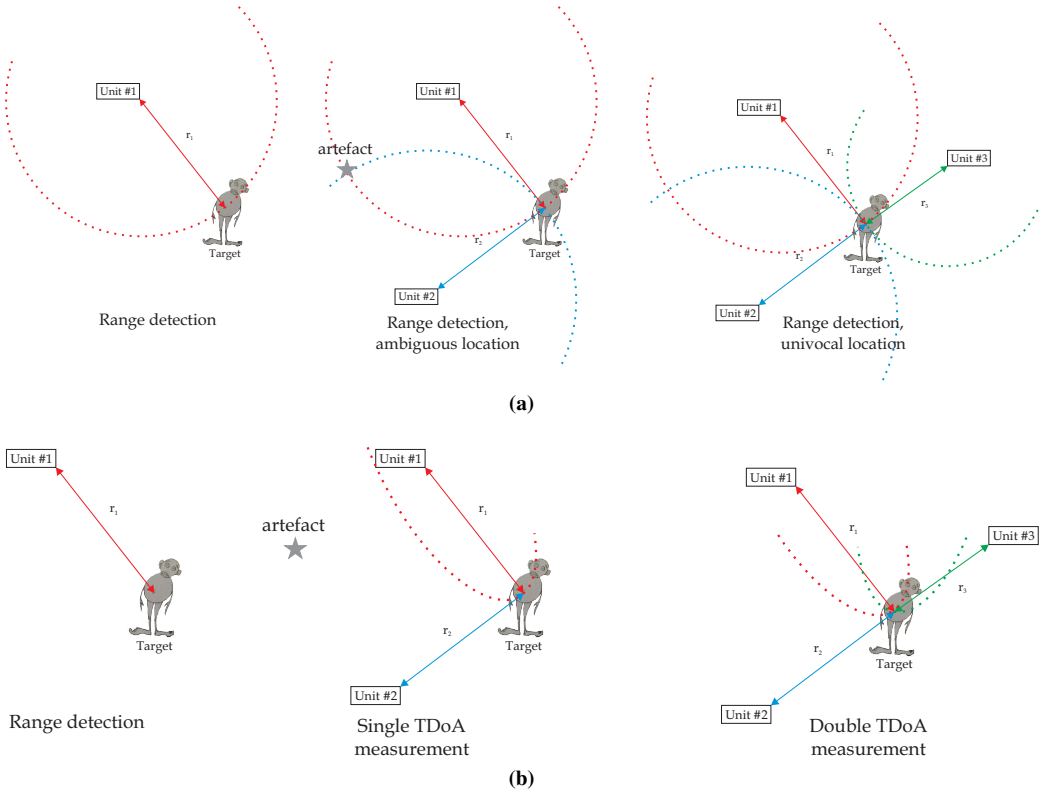

Figure 1.5: Sketch describing the difference between (a) ToA and (b) TDoA position estimation. The figure highlights the need of more than one receiver in order to unambiguously determine the target location.

receivers and the transmitter, the system equation is [17]:

$$\begin{cases} (x_t - x_0)^2 + (y_t - y_0)^2 + (z_t - z_0)^2 = (d + d_0)^2 \\ (x_t - x_1)^2 + (y_t - y_1)^2 + (z_t - z_1)^2 = (d + d_1)^2 \\ (x_t - x_2)^2 + (y_t - y_2)^2 + (z_t - z_2)^2 = (d + d_2)^2 \\ (x_t - x_3)^2 + (y_t - y_3)^2 + (z_t - z_3)^2 = (d + d_3)^2 \\ d_1 - d_0 = d_{10} \\ d_2 - d_0 = d_{20} \\ d_3 - d_0 = d_{30} \end{cases} \tag{1.4}$$

where $(x_i, y_i, z_i) \in \mathbb{R}^3,\ i = 0, \cdots, 3$ are the coordinates of the i^{th} receiver. Receiver 0 is the dummy receiver. Thanks to the differential approach, the synchronization is necessary only among the receivers, and not between transmitter and receivers, which is a more feasible requirement [18]. Also for ToA and TDoA, multipath represents an issue: in the absence of LoS, ToA, and TDoA perform worse, since the traveled path by the wave may be longer than the real one [1].

1.5.4 Received Signal Strength

One of the most employed localization techniques is based on the RSS. Its popularity is because almost every receiver is equipped with a signal strength evaluation circuit.

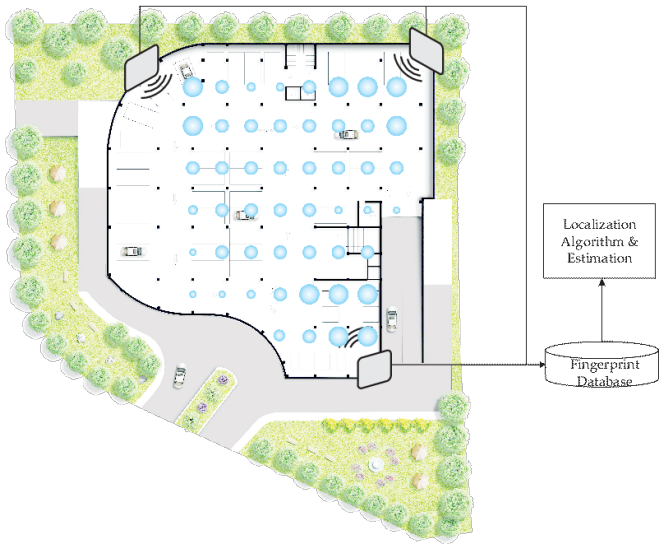

Figure 1.6: RSS fingerprinting applied to the real scenario a car parking garage. The blue dots are representing the measured signal strength. Varying diameters are corresponding to the different measured magnitudes.

One of the reasons for the RSS spreading is the diffusion of Wireless Fidelity (Wi-Fi) systems and standards (i.e. the IEEE 802.11).

RSS can be employed for localization since every signal propagating in a given environment experiences a loss that reduces its strength, which is referred to as path loss. For a signal at a given frequency, f (expressed in GHz) that travels a distance d (expressed in meters) in free space, the path loss $\mathrm{FSPL}(d)$ expressed in dB can be evaluated by [19]:

$$\mathrm{FSPL}(d) = 32.4 + 20\log_{10}(f) + 10\,n\log_{10}(d) + X_\sigma \quad [dB] \tag{1.5}$$

where n is the so-called pathloss exponent (in free space $n = 2$) and X_σ the shadow fading with variance σ. Once the transmitted power is known, it is possible to reconstruct the path length traveled by the e.m. signal by evaluating the amount of lost power.

For RSS, the reference technique is fingerprinting (also referred to as scene analysis or pattern matching). RSS fingerprinting involves an off-line and an on-line phase. The off-line phase leads to the construction of a radiomap (Figure 1.6), indexed by a database of signal power values in some points. The on-line phase can be performed in two ways [11]. In deterministic RSS analysis, each measured RSS value is directly compared with the offline site measurements in order to establish the best approximation of the MN position. In the probabilistic RSS analysis, each measured value is compared with the probability distribution function of the RSS characterizing a given area. Note that a purely deterministic approach can lead to fast radiomap outdating since even small changes in the room can lead to dramatic RSS distribution variations. Hence, in deterministic methods, it is necessary to repeat the off-line phase with new measurements, while in probabilistic methods it is only necessary to correct the probability distribution function.

The off-line phase is very heavy in deterministic approaches. As an example, if we think about a huge building or a room subject to continuous changes in people or

objects moving, it is unfeasible to reconstruct the entire radiomap every time. That is why nowadays researchers are focusing on the probabilistic approach or a hybrid among the two. As discussed by [20], there are three approaches to handle this problem. The first one is the SLAM: thanks to the definition of a proper probability model for the moving object, and with the set of past positions and landmarks being available, it is possible to extract the position of the MN and concurrently build the radiomap. Another technique involves the interpolation or the extrapolation of RSS data measured by different anchors to the MN and to the other anchors. This allows for determining the position by drawing some mappings starting from the aforementioned data. The last way is to employ crowdsourcing for building it in a collaborative way [21], having many devices contributing with their measurements to the mapping process. Please note that different units can have different sensitivity in measuring the same RSS, due to hardware fabrication mismatches. Hence, it is necessary to pay attention to the data merging process, to correctly fuse data. All the mentioned techniques aim to avoid or reduce the effort put into the off-line radiomap building. The price to pay is associated with the computational complexity of the algorithms.
The main challenge associated with RSS-based localization is the reliability of the path loss model. If a wrong pathloss model is chosen, this may lead to dramatic estimation errors. That is why new research trends involve not only RSS optimization but also proposing new ways of correctly choosing the propagation model subject to the propagation environment [22].

1.5.5 Comparison of the approaches

To make a fair comparison of the aforementioned approaches to geometric localization, it is necessary to set some common points. From an availability and deployment cost point of view, the winning solution is represented by RSS [23]. In fact, WLAN standards like the IEEE 802.11 propose the RSSI as a measure of the quality of the link. This information is directly related to the RSS and allows the design of positioning systems based on lateration through distance measurements. TDoA or AoA estimation systems are less common because they need additional hardware and complex algorithms to make the positioning system properly work. When considering indoor vehicle localization inside industries [10], PoA and PDoA are the most feasible solution, because of their compliance with the RFID standard that is largely employed in this field. However, if long distances are necessary to be covered, the number of anchor nodes and also the level of complexity of the algorithms, to take into account phase unwrapping, may be high. Also, AoA may be a promising solution in this field. From the accuracy point of view, each technique strongly determines some differences in the way it is implemented. It is clear that an RSS radiomapping with few points leads to poor accuracy as long as in ToA/TDoA systems the sampling time determines the granularity of the localization system itself. By comparing the number of required receivers, AoA has the lowest impact, when compared to ToA/TDoA or RSS, as on distances larger than the wavelength, PoA and PDoA-based systems may need more receivers than the AoA-based ones in order to perform phase unwrapping [10].
In general, all the described techniques are affected by the multipath propagation problem, which leads to the degradation of the estimation due to the coherent copies reception if not correctly taken into account.

1.6 Indoor and outdoor localization

Localization can happen indoor or outdoor. Different effects happen in the two environments. In this section, the aim is first to highlight the basic propagation mechanisms and how they affect indoor and outdoor propagation. Then, the comparison between already-deployed indoor and outdoor localization techniques is proposed, along with the emerging role of machine learning in supporting channel state estimation.

1.6.1 Basic propagation mechanisms

Since radiolocation mechanisms rely on the e.m. properties of the received signal, it is interesting to study the phenomena affecting the channel characteristics, which concur to deteriorate the estimation. In a radio system design, engineers are concerned with two main issues: the link budget and the time dispersion [24]. The link budget is related to the effective amount of power received from a transmitter. In Section 1.5.4 the path loss concept was already introduced, along with equation (1.5) for free-space path loss. The time dispersion is related to the study of the different time delays with which different copies of the signal reach the receiver from the transmitter. In a real communications system, if present, the LoS component (or direct component) is not the only version of the signal reaching the receiver. When objects and obstacles are present, multipath propagation arises. These obstructions partly reflect the signal determining the generation of multiple (unwanted) copies. The received signal is the sum of all these components. In some cases, the LoS may exhibit a strength that is comparable with or lower than the unwanted copies of the signal. In this case, we talk about near-LoS (nLoS) and Non-LoS (NLoS), respectively. The copies are characterized by different amplitudes and phases from those of the LoS component, as they travel along different paths to reach the receiver. Also, the constitutive materials of the obstacles may impact the propagation environment, since some of them expose some absorption windows in the frequency spectrum that determine unwanted power losses. Reflection, diffraction, and scattering (sketched in Figure 1.7) are the three basic propagation mechanisms which have an impact on a radio communication system [25]:

- Reflection: this phenomenon occurs when the dimensions of the objects are greater than the wavelength of the impinging e.m. wave. In this case, the wave may be reflected with a strength that depends on the reflection coefficient and the angle of incidence.
- Scattering: when the object is much smaller than the wavelength, the e.m. wave may "brake and surround" the obstacle, determining the growth of multiple copies of the signal traveling in different directions. Scattering also arises when the imperfections of the surfaces are comparable to or even smaller than the wavelength.
- Diffraction: when the wave impinges a surface with sharp edges, this phenomenon determines the generation of waves in all directions, bending around the obstacle.

The study of both path loss and time dispersion through e.m. simulations is unfeasible. The computational burden required to solve the general Maxwell's equations in wide

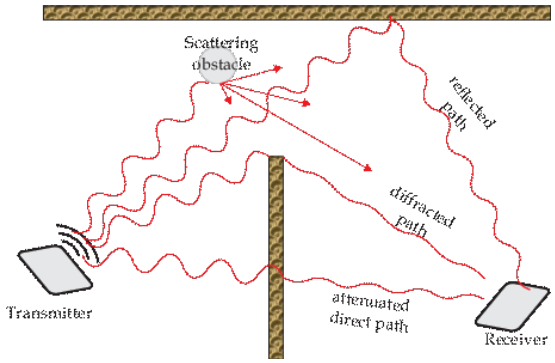

Figure 1.7: A sketch of the basic propagation mechanisms which may generate artifacts on the positioning systems.

scenarios is too high to cope with, even using optimized algorithms. That is why most of the time probabilistic or empirical models are used. Probabilistic models describe the probability of a given phenomenon to arise. In empirical models, researchers simply do measurements and try to develop closed-form characterizations of a given environment. However, those models should be correctly applied to the scenario, being careful on checking that the chosen model is correctly fitting the considered situation.
Since the presence and strength of the artifacts vary as a function of the considered frequency range, the scientists strive to correctly characterize the radio channel at the various frequencies.

The generation of coherent copies of the same signal may lead to different problems in the geometric radiolocation techniques. In AoA and PoA, the received copies constructively compose and this determines the degradation of the phase estimation quality, which leads to the loss of accuracy of the estimation. Still, multipath propagation determines artifacts on RSS and ToA/TDoA. In fact, if the traveled path is different from the LoS one, this determines different pathloss values/time of arrivals at the receivers, and so the estimated distance is not the real one. Focusing on RSS the other problem concerns the choice of the proper propagation model in order to take into account and approximate as many effects as possible [26]. However, using concurrently more than one technique may lead to a performance improvement, that can be further enhanced by the use of multipath mitigation techniques [27–29]. We will see in Section 1.6.5 that also Machine Learning plays a role in correct channel behavior estimation.

1.6.2 Propagation in outdoor environment

Historically, communications in outdoor environments have always been organized in cells of different sizes to allow frequency reuse. The in-cell propagation modeling distinctions are due to the cell extensions. Macrocells extension is in the order of kilometers. The base stations are put at high points allowing a better coverage of the area. Most of the empirical models for path loss take into account as a "gain factor" the relative height of transmitter and receiver antennas, since it is less likely for high points to be intercepted by obstacles [25]. As regards the multipath, the most relevant contribution in this scenario is due to the ground reflection which occurs differently

since the traveled path may not be homogeneous (i.e. presence of lakes, forests, seaside, etc.). The distribution model for the outdoor multipath fading is the Rayleigh distribution. The average path loss has a log-normal distribution since several (uncorrelated) phenomena compose together and their resulting distribution is a normal one in the dB domain [24].
Microcells and picocells are more challenging to be analyzed. The reference scenarios are city streets. This scenario is also referred to as an urban canyon. Generally speaking, the transmission powers are lower than the macrocell case, the distances to be covered are under 1 kilometer and the presence of buildings strongly affects the overall propagation model accuracy, since it strongly depends on a correct characterization of building materials in terms of the electrical constants and the surface roughness [30]. In their survey [24], *Andersen et al.* propose a very interesting discussion on the pathloss in a microcell urban environment with streets (the reference is Manhattan). The reference sketch is in Figure 1.8.

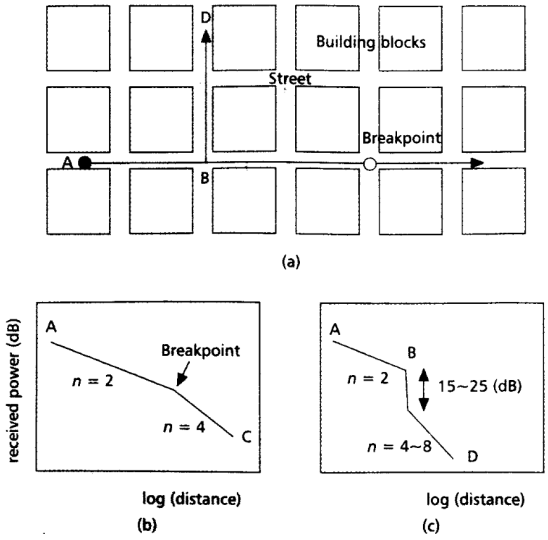

Figure 1.8: Ideal urban street layout sketched by *Anderset et al.* in [24]: path loss scebario (a) and curves along an LoS street. In (c) the pathloss curve when turning the corner (NLOS). © 1995, IEEE.

The path loss exponent is approximately two as in free space propagation. It is possible to define a *breakpoint* in the distance d_b determined as [24]:

$$d_b = \frac{2\pi}{\lambda} h_{tx} h_{rx} \tag{1.6}$$

being h_{tx} and h_{rx} the transmitter and receiver antenna heights. After this breakpoint, the path loss exponent approaches four. This is valid in LoS. However, by "turning the corner" from one street to the other, the predominant propagation is the NLoS one, and the receiver experiences a huge degradation in the received signal level.

Outdoor, it is not possible to forget about the presence of vegetation, which strongly impacts both path loss and time dispersion. Also, in this case, statistical models are employed [30].

1.6.3 Propagation in indoor environment

Indoor propagation is one of the most difficult to analyze. A first remark can be made based on the distances that we consider: with respect to outdoor communications, indoor ones rely on smaller distances, and so, the loss of power is reduced when compared to long range communications. However, the multipath phenomena have greater influence than outdoor, because the number of scattering/diffraction/reflecting generators is substantially higher. The physical phenomena which are at the basis of indoor propagation are analyzed in works like those of *Sarkar et al.* [31] and, more recently, of *Diago-Mosquera et al.* [32].
Pathloss in indoor environments taking into account also the way (and the materials) buildings were internally constructed. It is common to consider the influence of the presence of floor and wall attenuation in classical pathloss models for the indoor scenario. Considering what is stated by [31], an example of this is offered by the introduction of Wall Attenuation Factors (WAF) and Floor Attenuation Factors (FAF). Those terms introduce a further attenuation that depends on the materials employed for the construction, the number of floors in the case of the FAF, or the thickness of the walls in the case of the WAF. Also, the incidence angles play a role to determine the amount of energy transferred over the obstacle.
The advent of 5th generation (5G) and beyond cellular systems and the rush to find new spectrum slices to allocate high-capacity links is pushing attention to the characterization of the centimeter-wave and millimeter-wave indoor phenomena. Surveys like [19] propose some preliminary results. Other works consider higher frequencies, either by analytical [33] or empirical measurements [34]. As anticipated, those works also take into account how the building itself is constituted (presence of stairs, number of floors, walls, etc.) [35].

1.6.4 Indoor and outdoor localization technologies

A visual comparison of the standardized radio location approaches for indoor and outdoor scenarios is in Figure 1.9.

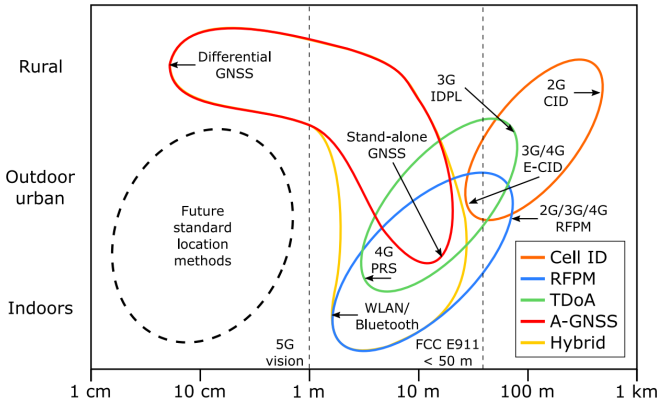

Figure 1.9: Expected accuracy of mobile standard radio localization methods for indoor and outdoor scenarios. Image by *del Peral-Rosado et. al*, [36]. © 2018, IEEE.

Outdoor In outdoor environment, well established communication technologies are available: the cellular system, the Global Navigation Satellite System (GNSS), the Low-Power Wide Area Network (LPWAN), the Low-Earth Orbit (LEO) Position Navigation and Timing (PNT) and the localization through terrestrial Signals of Opportunity (SoOp) like the Frequency Modulation (FM) radio and the Digital Video Broadcasting (DVB).

The survey by *del Peral-Rosado et. al* [36] offers insights into the challenges of localization through cellular networks. First, the transmit power, the number, and the location of the base stations directly impact the accuracy. In this scenario, the main issue is inter-cell interference, which is mitigated by means of mute transmission periods, at the cost of reduced throughput. Location can be determined through the Cell Identifier (CellID), in which the position of the device is assigned to the geographic position of the base station. The accuracy can be improved by the cell sector info and time-ranging measurements. The cost is practically null, but the accuracy is low. This localization feature is available since GSM. Later standards such as LTE enabled other ranging measurements to improve the CellID estimation. Fingerprinting is another viable solution. An alternative is represented by the uplink ToA and TDoA measurements, respectively implemented in GSM and UMTS.

GNSS represents the *de-facto* standard for large scale localization. Currently, four major constellations are in operation: Global Positioning System (GPS), GLONASS, Galileo, and BeiDou. GNSS satellites rely on the Medium-Earth Orbit (MEO). Hence, the received signals have very low power (noise level) and so they cannot reach the so-called GNSS-denied areas (indoor or dense urban environments. In this latter, multipath errors degrade the accuracy). The accuracy is in the order of tenths of meters. The localization infrastructure is well established and always available [37]. The cost of the architecture deployment is high. Also, the computational complexity required by pseudorange computation and the compensation of space to Earth propagation effects is not negligible.

LPWAN is an emerging solution for localization, especially suitable for IoT devices. LPWANs are designed to support long-range communications and low-power. Examples are LoRa and Narrow-Band IoT (NB-IoT). *Janssen et al.* in [37] compare the localization through GNSS and LPWAN. Basically, LPWAN employs RSS, TDoA, and AoA as localization techniques. In the NB-IoT standard, the 3GPP has defined the Observed Time Difference of Arrival (OTDoA) which represents the most accurate localization estimation technique for those technologies. In terms of accuracy, LPWAN performs worse than GNSS, reaching hundreds of meters as the lowest estimation error.

Another emerging solution is LEO-PNT, which represents the state of the art of innovations in localizations and positioning systems. LEO-PNT is more appealing than GNSS and it is expected to deliver a better positioning estimation because of the lower altitude of the constellations (resulting in a reduced pathloss). Several PNT solutions are already available [38]. Also, given the higher power levels, LEO-PNT is the best candidate for penetrating building walls, thus providing also indoor localization (and communications) solutions [37, 38]. More details on the LEO-based localization are in Chapter 6, where an application for coarse positioning employing real-time AoA estimation through phase interferometry is presented.

The last option is represented by terrestrial SoOp. In the survey by *Asaad et al.* [4] a localization solution based on the RSS measurements of FM radio signals is presented. Since FM radio uses long-wavelength technology (i.e. frequency from 87.5 to 108 MHz), it can travel long distances without interacting with indoor items and forniture. Another possible SoOp is the DVB signal, employed by *Chen et al.* in [39] for performing ToA-based localization.

Indoor For indoor localization, it is not possible to rely on the same systems deployed for outdoor. For instance, indoor localization by means of cellular networks does not provide accurate results since cellular networks were not designed for [36]. Hence it is necessary to rely upon network infrastructures already available inside the buildings. The classical technique is the RSSI fingerprinting and localization through WLAN networks. However, in the Wi-Fi infrastructure, also ToA, TDoA, and AoA techniques are employed [4]. The advantage of Wi-Fi is that being one of the most spread wireless communications technologies, several attempts in literature had been made to realize localization systems based on it [12].

Another attempt is to operate with a Wireless Body Area Network (WBAN), for instance, based on Bluetooth technology [12]. Bluetooth and its latest version, Bluetooth® Low-Energy (BLE) originally did not provide any support for localization. Hence, devices employed techniques based on RSS measurements to perform it. Since version 5.1 of the BLE standard, the technology comes with native AoA and Angle of Departure (AoD) support for localization. More details are in Chapter 2.

Another technology to support indoor localization is RFID [1]. RFID is especially employed in industrial environments for asset tracking. Each RFID tag has a unique ID to identify the target device [4]. High localization accuracy is not guaranteed due to hardware limitations. In fact, RFID tags may be divided into active and passive RFID tags [12]. Active RFID tags are equipped with a power generator (i.e. a battery) and can operate hundreds of meters far from the RFID reader. Instead, passive RFID tags are limited to units of meters, with the advantage of very low deployment costs. The RFID technology relies on the backscattering of a signal, hence the most employed localization approaches are PoA, PDoA and RSS [3].

1.6.5 The role of Machine learning

Machine Learning (ML) and Artficial Intelligence (AI) represent new tools supporting the mitigation of propagation artifacts. ML algorithms aim to directly acquire information and find possible data recurring patterns once a training phase has taken place. In this context, one issue associated to ML is the high dimensionality of radio channel features [40]. This is overcome by using classification algorithms aiming to reduce the number of features. ML can also help when the objective is to fuse positioning data coming from different and heterogeneous sensors or techniques.

In the previous section, we discussed the indoor environment as the most tricky propagation setting for localization techniques. ML can be applied in two ways to support indoor positioning. The first consists in exploiting ML to estimate the channel response, either by mitigating or pre-compensating artifacts. Another way is represented by ML-aided fingerprinting for RSS, where ML algorithms are employed to improve the power-pattern recognition in the online phase of the RSS retrieval.

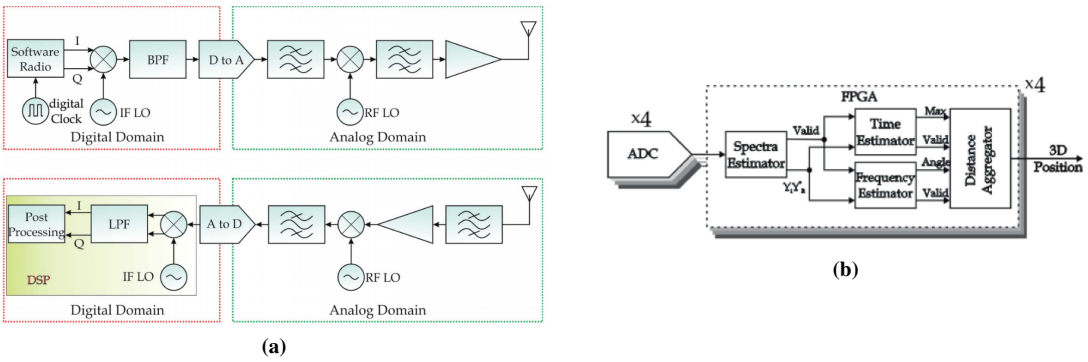

Figure 1.10: Block diagrams for the RTLS presented by *Piccinni et al.* in [18]: (a) analog functional blocks and (b) digital functional blocks. © 2020, IEEE.

Depending on the specific task to perform, different learning procedures can be employed. Transfer learning is useful when a particular model for the propagation artifacts estimation is trained on empirical data in a specific setting. Thanks to transfer learning, the model will quickly adapt to the new situation, bringing the knowledge acquired from the initial context [40]. On the other hand, deep learning and convolutional neural networks or feed-forward neural networks may be employed as classificators to refine the channel response estimation after empirical data acquisition [41].

1.7 Real-Time Localization Systems

This thesis is focused on Real-Time Localization System (RTLS). An RTLS is a system capable of determining the location of a given target with reduced latency employing one of the approaches described in Section 1.5. As it is deeply explained in forthcoming chapters, the deployment of an RTLS is related to its hardware implementation. Dedicated hardware structures allow us to get rid of all the random latencies related to the interfaces of general purpose architectures. For instance, thinking about the ISO/OSI networking model, reaching the APP layer requires crossing all the layers below it, their interfaces, and the associated queues. In this section three hardware structures are described as possible examples of RTLS.

The first example is the architecture developed by *Piccinni et al.* that is presented in their work [18]. The block diagrams for the analog and digital sections are in Figure 1.10. The authors propose a distance measurement system for performing positioning through trilateration. The distances are estimated through a TDoA approach. The transmitted signal is built through Orthogonal Frequency Division Multiplexing (OFDM) of the Frank-Zadoff-Chu sequence. By correlating this sequence with the same sequence stored on receiver side, it is possible to retrieve the trip time. The localization process is split into a coarse and a refinement phase. The core of the system is implemented through an Intel Stratix IV EP4SGX70HF35C3 Field-Programmable Gate Array (FPGA).

Bottigliero et al. in [42] propose a 2D RTLS for low-power cooperative tags based on the TDoA computation of Ultra-Wide Band (UWB) signals. The logical architecture for localization is in Figure 1.11. The time synchronization among receivers is achieved through the presence of a reference tag.

This allows to eliminate the presence of a wired clock synchronization network infrastructure. Each of the sensors (i.e. the devices devoted to perform TDoA measurements) is based on a custom-designed hardware structure comprising an UWB RF chain and a processing board deploying an Analog-to-Digital Converter (ADC), a clock generator, and the Xilinx Zynq 7000 SoC platform (with an FPGA and an ARM processor on it). The tags are very simple devices transmitting a known sequence. The TDoA measurement involves a coarse estimation phase demanded by the FPGA and a refinement phase managed by the ARM processor. Thanks to a super-resolution technique implemented on the ARM processor, the system can reach 10 cm positioning accuracy with an update time of 50 ms.

Zhang et al. in [43] propose an RTLS of RFID tags by means of RSS measurement, using a peculiar network infrastructure based on Zigbee. The RTLS is particularly devoted to asset tracking on large organizations. The localization scheme is sketched in Figure 1.12. In the first phase, reference tags with known coordinates are spread in the environment, and they serve as anchors for the localization process. Each object to be tracked is equipped with an RFID tag. A group of reference and unknown tags spatially close are managed by a coordinator, which is a simplified RFID reader capable of RSS measurements. The coordinators are interfaced through a Zigbee network to expand the system area of operability. As with every RSS-based localization system, a preliminary fingerprinting stage precedes the actual localization stage, which is done through RSS matching. The authors claim to reach 30 cm accuracy but no information is provided regarding the time needed for the estimation.

1.8 Localization applications: the adaptive beamforming

A possible LBS is the adaptive beamforming. Adaptive beamforming is one of the key enabling technologies for millimeter wave (mmWave) communications. First, a brief introduction to the operating context is given, discussing the advantages and the challenges for mmWave communications. Hence, main beamforming architectures and techniques are presented. For analog beamforming, a brief discussion regarding phase shifters and phase distribution networks is presented. Although differently mentioned, the reference is beamforming on the transmission side: thanks to the reciprocity theorem [44], the discussion can be extended to the receiver side.

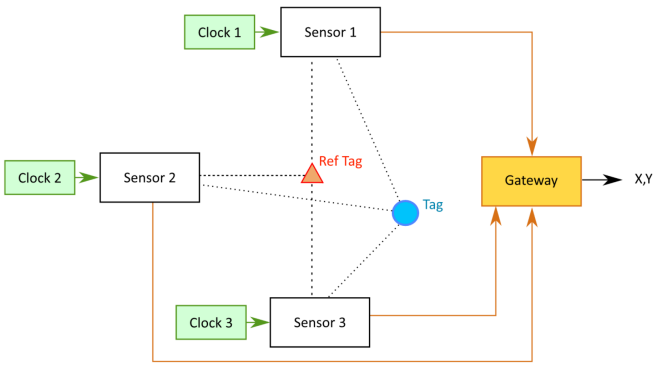

Figure 1.11: Block diagram of the TDoA measurement system proposed by *Bottigliero et al.* in [42] with the use of a reference tag in the center position. © 2021, IEEE.

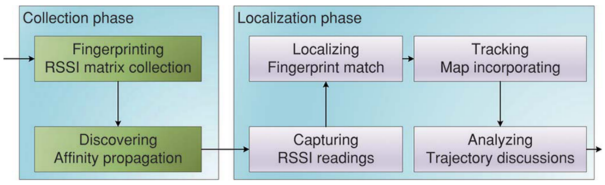

Figure 1.12: Architecture of the localization system proposed by *Zhang et al.* in [43]. © 2016, IEEE.

1.8.1 Context: Millimeter-wave communications

Novel telecommunications standards have to deal with a new operative scenario. New technology such as smartphones, tablets, and IoT devices require and evoke new operation paradigms. The main requirements ask for augmented capacity and higher Quality of Experience (QoE) for the end-users, which can be humans or machines. These new wireless standards are employed mostly for Internet content access, for example very high-quality live videos, and, nowadays, immersive virtual reality streaming applications. For these reasons, there are many target requirements to address, such as [45]:

- Low latency: next-generation cellular standards should provide low latency, in the order of milliseconds and sub-milliseconds for great responsiveness.
- High capacity and high throughput: considering 5G networks as a reference, they are demanded to address the 10 Gbps data rate. Beyond 5G networks are supposed to break the 10 TBps threshold.
- Reliability and availability: networks can be overloaded with a high amount of connected devices. New architectures for network radio access should provide the availability of the first connection for each device and the possibility of having access to network resources
- Low interference with existing telecommunications standards

Since the spectrum in the sub-6 GHz band has become more and more crowded, available spectrum slices in the upper bands gathered the attention of communications engineers. mmWaves correspond to frequencies in the range from 30 GHz up to 300 GHz and they are called millimeters because of the associated wavelength in free space (Figure 1.13). They were mainly employed for space communications [45]. However, higher frequencies are linked with higher losses, since the path loss increases with the square of the frequency, as previously described by the (1.5). One way to reduce the path loss is to increase the antenna gain, both in transmission and in receiving sections. To do so, it is necessary to focus the antenna beam, and usually, this is possible by employing antenna systems instead of single antenna elements.

1.8.2 Radiation from multiple antenna elements

Every antenna is characterized by a given radiation pattern. For example, if we consider a dipole antenna, the radiation pattern is omnidirectional and centered in the dipole itself. If we consider an array of N antennas, the global radiated far-field is the linear superposition of the single contributes, which may compose constructively

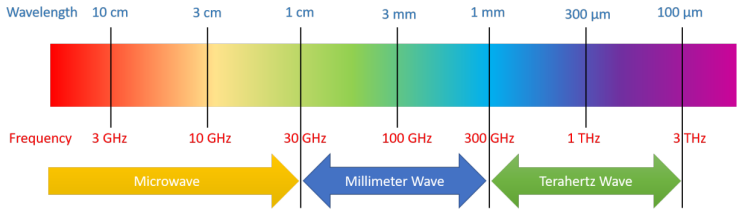

Figure 1.13: mmWaves and sub-mmWaves spectrum and relationship between frequency and wavelength. Image by *Chataut et al.* [45]. *Image licensed under CC BY 4.0.*

in some points and destructively in some other points because of their interference. The idea is to steer the global radiation pattern towards a direction, so that the power density is maximum in that direction, and it approaches zero in the other points of the space. This technique is called beam steering.

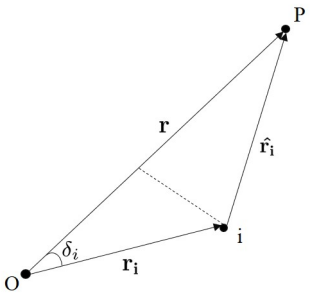

Figure 1.14: Geometrical sketch used to derive global radiation field expressions.

Let us consider an array of N antennas and a common origin O as showed in Figure 1.14. We call $\hat{\mathbf{r}}_\mathbf{i}$ the distance between the i-th element of the array and the point in which we want to evaluate the e.m. field. It is possible to show that the global radiated field $\mathbf{E_T}$ is [44]:

$$\mathbf{E_T} = \sum_{i=1}^{N} \dot{I}_i \mathbf{N_i} \frac{e^{-j\beta\hat{r}_i}}{4\pi\hat{r}_i} \tag{1.7}$$

with $\mathbf{N_i}$ representing the radiation vector of the i-th antenna, β the propagation constant in the considered medium and $\dot{I}_i \in \mathbb{C}$ the excitation current phasor. Since we deal with N nominally identical antennas, $\mathbf{N_i} = \mathbf{N}, \forall i$. Making some simple geometrical assumptions, it is possible to find that

$$\hat{\mathbf{r}}_\mathbf{i} = \mathbf{r} - \mathbf{r_i} \cdot \mathbf{u_r} \tag{1.8}$$

with $\mathbf{r}$ the distance between the origin and the point of evaluation, $\mathbf{u_r}$ such that $\mathbf{r} = r \cdot \mathbf{u_r}$ and $\mathbf{r_i}$ the distance between the common origin and the i-th antenna element. Hence, it is possible to prove that

$$\mathbf{E_T} = \sum_{i=1}^{N} \dot{I}_i \mathbf{N_i} \frac{e^{-j\beta\hat{r}_i}}{4\pi\hat{r}_i} \approx \mathbf{N} \sum_{i=1}^{N} \dot{I}_i \frac{e^{-j\beta r_i \cdot \cos(\delta_i)}}{4\pi r} \tag{1.9}$$

We define the array factor F as

$$F = \sum_{i=1}^{N} \dot{w}_i e^{-j\beta r_i \cos(\delta_i)} \tag{1.10}$$

with $\dot{w}_i \in \mathbb{C}$ a generalization of the excitation current. The variation of the quantity $\dot{w}_i$ allows to obtain different directions and shapes for the radiation pattern.

1.8.3 Beamforming: taxonomy and discussion

A possible definition and taxonomy of beamforming systems is given by *Kutty et al.* in their survey [8]. Beamforming is a spatial filtering operation made by an array of antennas to capture or radiate e.m. energy in a given direction in the space, reaching an improvement in the transmit or receive gain. There are many possible ways of realizing a taxonomy of beamforming systems. A first distinction is made on the role of the beamformer, which can be either on transmit or receive side. The advantage on transmit side is to focus the power density to reach a farther point in the space with less amount of energy. For the beamforming on receiving side, it is possible to perform noise or interference rejection, improving the SNR or SINR respectively. An example block diagram of a receiver beamforming network is in Figure 1.15.
Beamforming can be described as the result of the superposition of the radiation pattern of the N array elements to which amplitude and phase shifts are applied to realize the constructive/destructive interference previously described. To apply those phase shifts, the mathematical model employs complex-valued weights. If those weights are fixed with time, we talk about fixed beamforming, since also the array pattern does not change in time. Instead, if those weights are time-varying, we deal with adaptive beamforming.

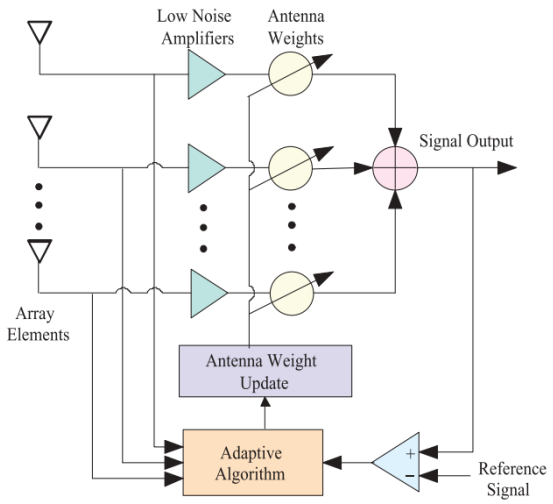

Figure 1.15: Example of receiver (analog) beamforming architecture described by *Kutty et al.* in [8]. © 2016, IEEE.

Another possible taxonomy involves signal bandwidth. For narrowband beamforming we consider signals which have small frequency deviations relative to the RF carrier, opposite to the wideband beamforming. Narrowband beamforming implementation is

simpler. For example, a phase shift φ at frequency ω can be realized by applying a time delay τ such that:

$$\tau = \frac{\varphi(\omega)}{\omega} \tag{1.11}$$

The previous equation still holds for narrowband signals, because the phase errors when considering frequencies around ω are negligible:

$$\varphi(\omega + \Delta\omega) = \varphi(\omega) + \tau\,\Delta\omega \approx \varphi(\omega) \iff \Delta\omega \approx 0 \tag{1.12}$$

For wideband signals ($\Delta\omega \gg 0$) this is not true. If this problem is not correctly handled, the beam squint problem can arise, in which different spectral components are steered toward different directions [46].
Also the signal domain can be taken into account when considering the possible categories of beamforming. We can consider the difference between frequency domain beamforming and space-time domain beamforming. In the first category, all the beamforming procedures are performed in the frequency domain and then inverse transformed. In the second one, all operations are performed in the time domain. Analog beamforming, digital beamforming and hybrid beamforming belong to this latter category.
To perform beam steering, it is necessary to compute the steering vectors. To do so, beamforming algorithms and techniques rely on the Channel-State Information (CSI) estimation or prediction. Once the reciprocity of the channel is assumed, it is necessary to understand how the channel responds to the e.m. wave.

1.8.4 Beamforming and Massive MIMO

MIMO systems for telecommunications are the state of the art for channel capacity maximization. Before MIMO systems, single-input/output systems (SISO) had lower throughput and did not support a lot of users. Thanks to MIMO, it is possible to serve multiple users at the same time. Massive MIMO (mMIMO) is an improvement of MIMO in which a higher number of antenna array elements is required, introducing increased throughput and reduced bit error rate [45].
MIMO and beamforming systems boundaries are somehow confused, especially in current literature. It should be clear that MIMO, and in particular mMIMO takes advantage of beamforming for steering different informative streams toward different end users. Nevertheless, beamforming can be also employed in SISO for just steering the antenna beam towards a given direction. In this latter case, it is more correct to speak about beamsteering instead of beamforming. Hence, beamforming is an enabling technology for MIMO and mMIMO. A visual representation of beamforming in mMIMO is in Figure 1.16.

1.8.5 Analog beamforming

Analog beamforming is realized through the phase and amplitude control of the transmitted signals. This is done by employing phase shifters and variable gain amplifiers for each antenna element or a particular phase distribution network for more complex architectures.
Usually, in analog beamforming antenna there is a single transmitted data stream [47].

Figure 1.16: Beamforming in mMIMO. Image by *Chataut et al.* [45]. *Image licensed under CC BY 4.0.*

In this case, depicted in Figure 1.17, the beamforming weights are fixed in amplitude and with varying phases, which can be a limitation. Analog beamforming offers lower implementation complexity than hybrid or digital beamforming. However, as stated in [47], most of the techniques provide insufficient performances in terms of array gain.

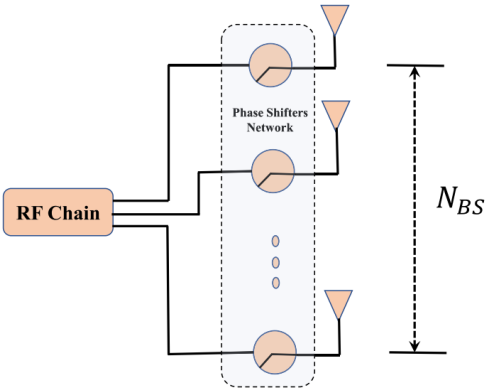

Figure 1.17: Example of an analog beamforming network for N_{BS} antennas by *Rihan et al.* in [47]. *Image licensed under CC BY 4.0.*

Since they are crucial for the analog beamforming implementation, we introduce a brief discussion on the phase shifting architectures and phase distribution networks.

Phase shifter technologies There are many possible techniques to realize phase shifting in the analog domain. As already said, the phase control architecture must be suitably designed for the signal bandwidth. otherwise, the beam squint problem can occur. In phase-only beamforming control, only phases are adjusted. Amplitudes are known *a priori* or fixed. This type of beam pattern synthesis is much easier for most architectures. Phase-only control has the advantage of short response in time and high-efficiency [48]. For RF phase shifters there are many requirements [49]. Among them, the most meaningful is the frequency of operation, the tolerated bandwidth, the effective phase variation it can introduce (in the case of non-continuous phase shifters, also the number of steps), the insertion and return losses, the speed and, for power-constrained domains, also the power consumption. The phase shift can be introduced in three points: the RF section, the Local Oscillator (LO) section, or the Intermediate Frequency (IF) section [50] (Figure 1.18). For example, the hybrid beamforming

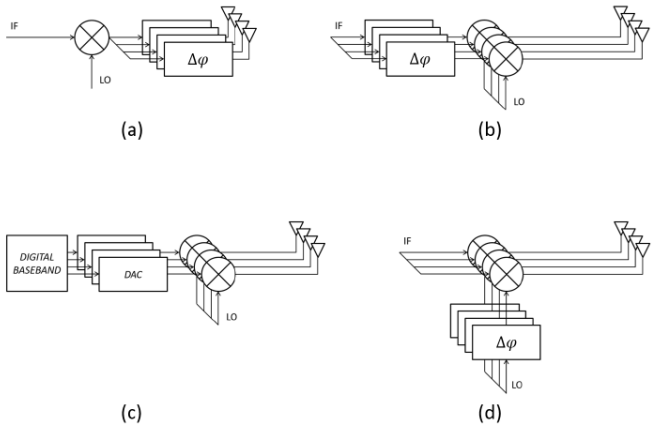

Figure 1.18: (a) RF (b) LO (c) Digital Baseband (d) IF beamforming architecture schemes. Image by *D'Amato et al.* [50]. *Image licensed under CC BY 4.0.*

architectures rely on the IF phase shifting. The most reliable way to introduce phase shift is in the RF section, because the mixing stage can introduce harmonic spurs that can generate artifacts on the phase shift, distorting the final result. However, realizing RF phase shift is more costly than the others [50].

Let us focus on RF phase shifters. Mainly there are three general types of phase shifters [49]:

- Switched-Line phase shifters (Figure 1.19a): they are the simplest in their design and they rely on true time delay introduced by the path between two transmission lines. As long as the signal travels along a longer path than the reference one, it is phase-shifted of a quantity that varies with the length. The path is enabled with the use of digitally controlled switches.
- Loaded-Line phase shifters (Figure 1.19b): a loaded line produces a phase variation $\phi = \beta l$ where β is the propagation constant of the line with length l. In this way, by matching different lines, it is possible to obtain the wanted phase shift. However, in practical design, insertion and return losses are inherently present in the design.
- Reflection-type phase shifters (Figure 1.19c): the reflection on a load with adjustable value is exploited. These phase shifters are continuously controlled by a bias so the resolution is very high. They are commonly designed as an electrically-adjustable reactive element that provides a phase shift.

Chen et al. in [51] propose a discussion on the devices needed for the deployment of a phase shifting architecture. One of the traditional ways is to employ P-type, Intrinsic, and N-type diodes or FETs switched transmission lines or reflective shifters with $\pi/2$-hybrids tuned with varactor diodes. However, they strongly suffer from temperature variations [51] and they have little phase resolution. Only varactor-tuned phase shifters present continuous phase shifting, but still, they have a strong dependency on the insertion loss from the phase change itself, and this may require a challenging calibration action for the whole system [51]. Variable attenuators are introduced in the chain, to equalize the insertion loss behavior.

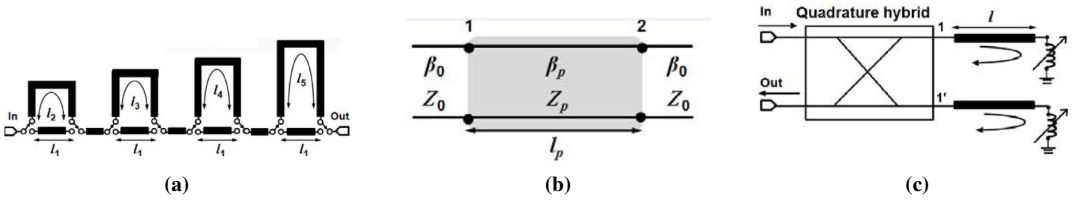

(a) (b) (c)

Figure 1.19: (a) 4-bit switched-line phase shifter example allowing the choice of 2^4 possible path lengths (b) Loaded line phase shifter with the insertion of a line with length l_p, phase constant β_p and characteristic impedance Z_p. (c) Concept of reflection-type phase shifter inserting a $\pi/2$-hybrid coupler. The images are from the work of *Chen et al.* [49]. © 2013, IEEE.

Another technology is based on ferrites, but they lack integrability, especially in planar circuits [49].
As regards the materials, phase shifters for analog chains are realized with semiconductor technologies (in particular CMOS or BiCMOS), with MEMS or ferrites. From the years 2000, a new emerging technology is the liquid crystal mixture [52], which can achieve great performances. However, attention should be put on the biasing schemes. In very high frequencies such as hundreds or thousands of GHz applications, graphene-based technology is a very interesting way to develop phase shifters [49].
Other emerging techniques for realizing phase shifters are the Filter-Type Phase Shifters (FTPS). In this technique, LC networks are combined with switches building unit phase shifters. By cascading those units, the wanted resolution is achievable [53]. This approach can be also employed in very high-frequency applications.
RF MEMS are another technology enabling the realization of low-insertion loss phase shifters with low-power consumption and high linearity. Usually, RF MEMS are employed for realizing switched-line phase shifters. RF MEMS are very integrable also on planar technologies [54]. This technology has almost zero DC power consumption and they offer high-quality factors.

Phase distribution networks A phase distribution network is usually made up of phase shifters, power dividers, amplifiers, switches, hybrids, and attenuators. By combining these elements it is possible to achieve multiple beams pointing from a single array of antennas [55]. Examples of phase distribution networks are the Blass matrix, the Nolen matrix, and the Butler matrix [56]. All of them offer different advantages in terms of resolution, bandwidth, and losses, and also some disadvantages mainly from the implementation complexity point of view. As a reference, let us focus on the Butler matrix.

Butler matrix allows controlling N beams by a matrix of hybrid couplers and phase shifters with fixed values. This device has N inputs and N output ports. Even if simple in its concept, Butler matrix implementation is not free of circuitry complexity. The main disadvantage involves the insertion loss [55]. An example of Butler matrix for a Uniform Linear Array (ULA) of 4 elements is in Figure 1.20.

1.8.6 Digital and Hybrid Beamforming

In digital beamforming, the phase shifting operations are performed by a Digital Signal Processor (DSP) in the baseband using a digital codebook [8].

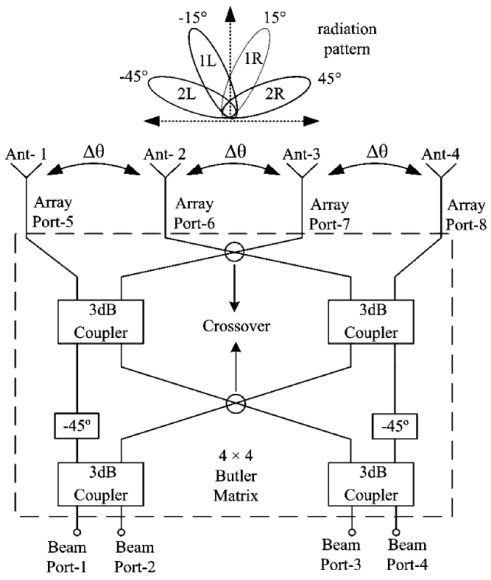

Figure 1.20: Butler matrix for a 4-elements ULA. Image by *Chang et al.* in [57]. © 2008, IEEE.

In digital beamforming, it is possible to manage also multiple data streams. The architecture is more flexible and it allows to implement whatever beamforming algorithm. Digital beamforming is the only procedure that can approach Shannon's capacity limit. An example of a digital beamforming architecture is depicted in Figure 1.21a.

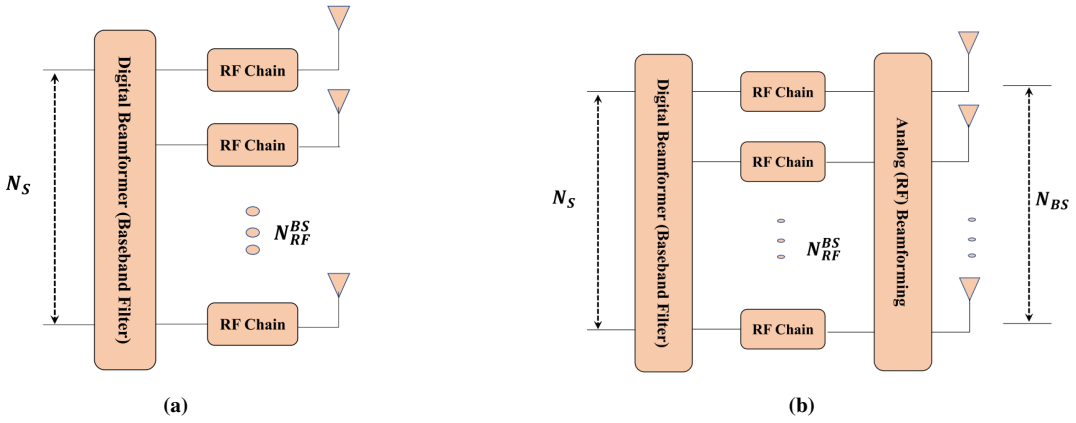

Figure 1.21: Block diagrams of (a) a digital beamforming network and (b) a hybrid beamforming network by *Rihan et al.* [47]. *Image licensed under CC BY 4.0.*

However, having a full RF chain for each antenna element in a Massive MIMO environment would be too costly. In this case, analog beamforming is more cost-effective compared to the digital counterpart even offering lower accuracy [47]. This is because, in a typical RF system, most of the power is associated with the mixed signal blocks like the ADC and the Digital-to-Analog Converter (DAC) [8]. Lowering the number of RF chains thus could allow to decrease the power consumption.

A good trade-off is represented by Hybrid Beamforming (HB), which is currently the most employed and appreciated solution [47]. In fact, in HB, the problem of digital beamforming is reduced by not associating each antenna element to a single RF chain.

In this way, the architectural complexity is reduced. The solution to the beamforming problem is then divided into a digital baseband beamforming section and an analog beamforming section [8]. An example of a hybrid beamforming architecture is in Figure 1.21b.
A first taxonomy of HB architectures can be done in terms of the number of RF chains for each antenna element. First, a possible implementation is represented by the sub-array configuration, in which each user data is first digitally precoded and then fed to the analog beamforming via a single RF chain for each stream [8]. Each analog beamforming network controls a subset of the array elements which is chosen thanks to a digital baseband algorithm. A block diagram is reported in Figure 1.22a. In the fully-connected architecture [8], the signal is first precoded in the digital baseband domain, then it is processed by each RF chain and transmitted using all the antenna elements in the array through the analog beamforming unit. A block diagram is in Figure 1.22b. This architecture is slightly more complex, but the gain is higher of a factor N_{RF} than the sub-array architecture [8], having the same number of antenna elements and being N_{RF} the number of the RF chains.

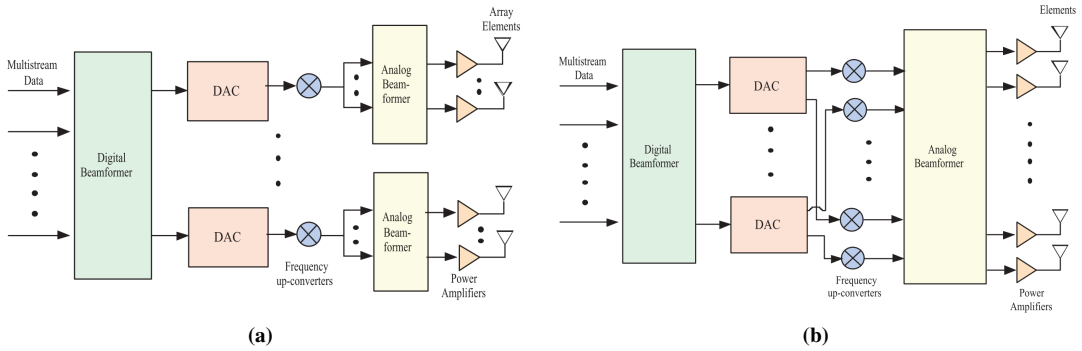

Figure 1.22: (a) Sub-array HB and (b) Full-connected HB reference block diagrams [8]. © 2016, IEEE.

A good compromise is represented by the dynamic partially-connected architecture [47], shown in Figure 1.23a. This is a dynamic sub-array architecture, in which the subarrays dynamically change with time to optimize channel statistics according to some Figures of Merit (FoMs), driven by a low complexity algorithm for antenna selection. The gain is in the middle between full and sub-array configurations, but losses are higher, since it employs switches that cause insertion losses [47].
Another architecture that can achieve performance near the fully-connected one is the virtual sectorization architecture (Figure 1.23b) [47]. It is a particular type of fully-connected architecture in which there is a separate digital beamformer is connected to every virtual sector.

1.8.7 Beamforming and Green Networking

The beamforming concept is commonly related to capacity maximization. In reality, nowadays it becomes imperative to carefully design energy-efficient systems aiming to minimize their environmental impact.

Energy-efficiency-spectral-efficiency (EE-SE) co-design [58] has become of great interest in the definition of the so-called green networks. Beamforming allows to

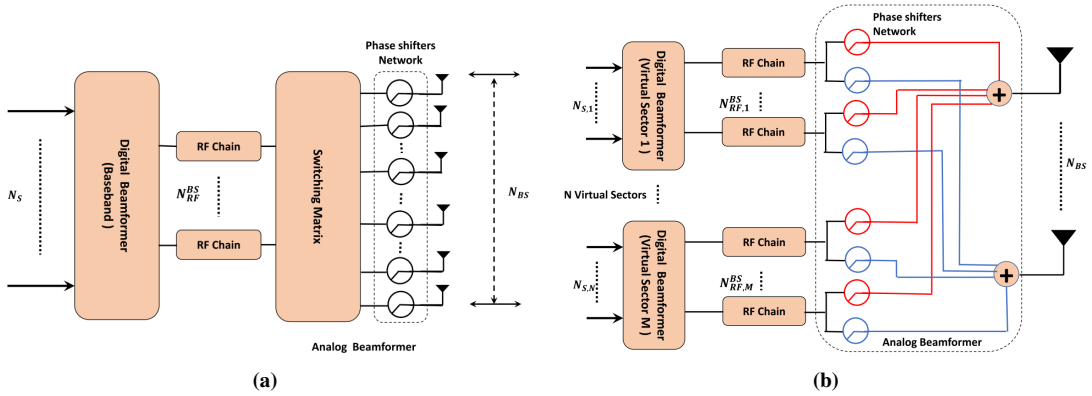

Figure 1.23: (a) Partially-connected and (b) Virtual-sectorization HB block diagrams [47]. *Image licensed under CC BY 4.0.*

increase the power efficiency and in order to maximize its impact, it is also necessary to take care the beamforming architecture does not lower the so-called "green point" [58] on the EE-SE curve (Figure 1.24), and this is achieved by suitably design hybrid beamforming architectures with a limited number of RF chains with respect to the number of array elements [8]. The basic idea is so to maximize the energy efficiency of the global architecture when a fixed spectral efficiency is given. However, this is an open and interesting topic in literature.

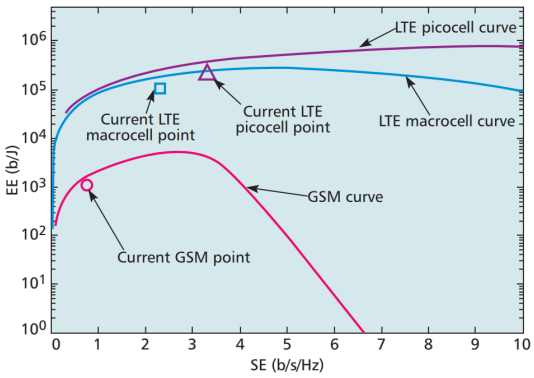

Figure 1.24: Example of the EE-SE curve for various telecommunications standards employed for the cellular communications, such as LTE and GSM. The SE is measured in bps/Hz while the EE is measured in bit/J. Image by *Chih-Lin et al.* [58]. © 2014, IEEE.

1.8.8 Beamforming and energy harvesting

This section is inspired by the paper of *Alsaba et al.* [59] that presents the state-of-the-art on beamforming technologies applied to energy harvesting networks.

Energy harvesting allows employing alternative power supplies in order to power the devices. It is possible to extract electrical energy from mechanical movements, vibrations, and also electromagnetic waves. Then it is possible to store it or directly employ the generated energy. Nowadays there is a lot of electromagnetic pollution, and so with energy harvesting, it is possible to exploit these actually useless waves

traveling around for producing energy, mostly for IoT devices, designed to be less power-hungry than other technologies.

In energy harvesting networks there are two ways of transferring energy. The first one is wireless power transfer in which the power transmitter just transfers power. Instead, in wireless-powered communications, the information is carried along with the power. This scheme is more interesting and it is possible to implement it with simultaneous power transfer to the information transfer or by time division duplexing.

To harvest energy from the electromagnetic waves, the energy harvesting circuit (usually a rectenna, that is an antenna system with a rectifier circuit) needs the received power to be over the sensitivity (in the order of -10 to -30 dBm). However, those power values are not always achievable, especially at mmWaves, because of the described phenomena like path loss, reflection, scattering, and fading (especially affecting systems with omnidirectional antennas). By exploiting multi-antenna techniques like beamforming it is possible, again, to increase the gain towards a given direction and increase both wireless power and information transfer efficiency. However, also, in this case, the Channel-State Indicator (CSI) plays a crucial role in correctly estimating the direction toward which the radiation pattern is steered.

Since there are many possible deployments for wireless-powered communication, also beamforming design objectives change accordingly. Beamforming algorithms constraints can be optimized according to the total transmitted power minimization (power wave and information wave), to the overall energy efficiency maximization, or to maximize only the throughput in the information-carrying. The energy harvester device design objective changes if we consider power-splitting receivers, time-switching receivers, or antenna selection receivers. In the first case, part of the energy is carried to the rectifier circuitry and the other part to the information decoding. In the second scheme, the energy is totally carried to one or the other branch but in different time slots. Finally, as regards the latter case, part of the array is employed for energy harvesting and the remaining antennas are employed for information decoding.

References

[1] S. R. Zekavat, R. M. Buehrer, G. D. Durgin, L. Lovisolo, Z. Wang, S. T. Goh, and A. Ghasemi, "An Overview on Position Location: Past, Present, Future," *International Journal of Wireless Information Networks*, vol. 28, no. 1, pp. 45–76, Mar 2021.

[2] P. S. Farahsari, A. Farahzadi, J. Rezazadeh, and A. Bagheri, "A Survey on Indoor Positioning Systems for IoT-based Applications," *IEEE Internet of Things Journal*, pp. 1–1, 2022.

[3] S. Subedi and J.-Y. Pyun, "A Survey of Smartphone-Based Indoor Positioning System Using RF-Based Wireless Technologies," *Sensors*, vol. 20, no. 24, 2020.

[4] S. M. Asaad and H. S. Maghdid, "A Comprehensive Review of Indoor/Outdoor Localization Solutions in IoT era: Research Challenges and Future Perspectives," *Computer Networks*, vol. 212, p. 109041, 2022.

[5] I. T. Union, "Radio Regulations - Articles - Volume I," p. 7, 2020, [Online] http://handle.itu.int/11.1002/pub/814b0c44-en (visited on 2023-01-31).

[6] E. G. Larsson, O. Edfors, F. Tufvesson, and T. L. Marzetta, "Massive MIMO for next generation wireless systems," *IEEE Communications Magazine*, vol. 52, no. 2, pp. 186–195, 2014.

[7] E. Björnson, L. Sanguinetti, H. Wymeersch, J. Hoydis, and T. L. Marzetta, "Massive MIMO is a reality—What is next?: Five promising research directions for antenna arrays," *Digital Signal Processing*, vol. 94, pp. 3–20, 2019, special Issue on Source Localization in Massive MIMO.

[8] S. Kutty and D. Sen, "Beamforming for Millimeter Wave Communications: An Inclusive Survey," *IEEE Communications Surveys Tutorials*, vol. 18, no. 2, pp. 949–973, 2016.

[9] G. Avitabile, A. Florio, and G. Coviello, "Angle of Arrival Estimation Through a Full-Hardware Approach for Adaptive Beamforming," *IEEE Transactions on Circuits and Systems II: Express Briefs*, vol. 67, no. 12, pp. 3033–3037, 2020.

[10] A. Motroni, A. Buffi, and P. Nepa, "A Survey on Indoor Vehicle Localization Through RFID Technology," *IEEE Access*, vol. 9, pp. 17 921–17 942, 2021.

[11] C. Laoudias, A. Moreira, S. Kim, S. Lee, L. Wirola, and C. Fischione, "A Survey of Enabling Technologies for Network Localization, Tracking, and Navigation," *IEEE Communications Surveys Tutorials*, vol. 20, no. 4, pp. 3607–3644, 2018.

[12] F. Zafari, A. Gkelias, and K. K. Leung, "A Survey of Indoor Localization Systems and Technologies," *IEEE Communications Surveys Tutorials*, vol. 21, no. 3, pp. 2568–2599, 2019.

[13] G. Bohm and G. Zech, *Introduction to Statistics and Data Analysis for Physicists; 3rd revised*. Hamburg: Verlag Deutsches Elektronen-Synchrotron, 2017.

[14] Y. Zhang and L. Duan, "Toward Elderly Care: A Phase-Difference-of-Arrival Assisted Ultra-Wideband Positioning Method in Smart Home," *IEEE Access*, vol. 8, pp. 139 387–139 395, 2020.

[15] M. Scherhäufl, M. Pichler, E. Schimbäck, D. J. Müller, A. Ziroff, and A. Stelzer, "Indoor Localization of Passive UHF RFID Tags Based on Phase-of-Arrival Evaluation," *IEEE Transactions on Microwave Theory and Techniques*, vol. 61, no. 12, pp. 4724–4729, 2013.

[16] Y. Qi, C. B. Soh, E. Gunawan, K.-S. Low, and A. Maskooki, "An Accurate 3D UWB Hyperbolic Localization in Indoor Multipath Environment Using Iterative Taylor-Series Estimation," in *2013 IEEE 77th Vehicular Technology Conference (VTC Spring)*, 2013, pp. 1–5.

[17] G. Han, D. Choi, and W. Lim, "A Novel Reference Node Selection Algorithm Based on Trilateration for Indoor Sensor Networks," in *7th IEEE International Conference on Computer and Information Technology (CIT 2007)*, 2007, pp. 1003–1008.

[18] G. Piccinni, G. Avitabile, G. Coviello, and C. Talarico, "Real-Time Distance Evaluation System for Wireless Localization," *IEEE Transactions on Circuits and Systems I: Regular Papers*, vol. 67, no. 10, pp. 3320–3330, 2020.

[19] F. D. Diba, M. A. Samad, and D.-Y. Choi, "Centimeter and Millimeter-Wave Propagation Characteristics for Indoor Corridors: Results From Measurements and Models," *IEEE Access*, vol. 9, pp. 158 726–158 737, 2021.

[20] B. Jang and H. Kim, "Indoor Positioning Technologies Without Offline Fingerprinting Map: A Survey," *IEEE Communications Surveys Tutorials*, vol. 21, no. 1, pp. 508–525, 2019.

[21] Y. Li, S. Williams, B. Moran, and A. Kealy, "A Probabilistic Indoor Localization System for Heterogeneous Devices," *IEEE Sensors Journal*, vol. 19, no. 16, pp. 6822–6832, 2019.

[22] B.-h. Lee, D. Ham, J. Choi, S.-C. Kim, and Y.-H. Kim, "Genetic Algorithm for Path Loss Model Selection in Signal Strength-Based Indoor Localization," *IEEE Sensors Journal*, vol. 21, no. 21, pp. 24 285–24 296, 2021.

[23] Y. Duan, K.-Y. Lam, V. C. S. Lee, W. Nie, K. Liu, H. Li, and C. J. Xue, "Data Rate Fingerprinting: A WLAN-Based Indoor Positioning Technique for Passive Localization," *IEEE Sensors Journal*, vol. 19, no. 15, pp. 6517–6529, 2019.

[24] J. Andersen, T. Rappaport, and S. Yoshida, "Propagation measurements and models for wireless communications channels," *IEEE Communications Magazine*, vol. 33, no. 1, pp. 42–49, Jan. 1995.

[25] T. Sarkar, Z. Ji, K. Kim, A. Medouri, and M. Salazar-Palma, "A survey of various propagation models for mobile communication," *IEEE Antennas and Propagation Magazine*, vol. 45, no. 3, pp. 51–82, Jun. 2003.

[26] K. N. R. S. V. Prasad and V. K. Bhargava, "RSS Localization Under Gaussian Distributed Path Loss Exponent Model," *IEEE Wireless Communications Letters*, vol. 10, no. 1, pp. 111–115, 2021.

[27] H. Dun, C. C. J. M. Tiberius, and G. J. M. Janssen, "Positioning in a Multipath Channel Using OFDM Signals With Carrier Phase Tracking," *IEEE Access*, vol. 8, pp. 13 011–13 028, 2020.

[28] A. A. Abdallah and Z. M. Kassas, "Multipath Mitigation via Synthetic Aperture Beamforming for Indoor and Deep Urban Navigation," *IEEE Transactions on Vehicular Technology*, vol. 70, no. 9, pp. 8838–8853, 2021.

[29] S. M. Amjadi, M. Hoque, and K. Sarabandi, "An Iterative Array Signal Segregation Algorithm: A method for interference cancelation and multipath mitigation in complex environments." *IEEE Antennas and Propagation Magazine*, vol. 59, no. 3, pp. 16–32, 2017.

[30] K. Haneda, R. Rudd, E. Vitucci, D. He, P. Kyösti, F. Tufvesson, S. Salous, Y. Miao, W. Joseph, and E. Tanghe, "Chapter 2 - Radio propagation modeling methods and tools," in *Inclusive Radio Communications for 5G and Beyond*, C. Oestges and F. Quitin, Eds. Academic Press, Jan. 2021, pp. 7–48.

[31] T. Sarkar, Z. Ji, K. Kim, A. Medouri, and M. Salazar-Palma, "A survey of various propagation models for mobile communication," *IEEE Antennas and Propagation Magazine*, vol. 45, no. 3, pp. 51–82, 2003.

[32] M. E. Diago-Mosquera, A. Aragón-Zavala, and G. Castañón, "Bringing It Indoors: A Review of Narrowband Radio Propagation Modeling for Enclosed Spaces," *IEEE Access*, vol. 8, pp. 103 875–103 899, 2020.

[33] G. Zhang, K. Saito, W. Fan, X. Cai, P. Hanpinitsak, J.-I. Takada, and G. F. Pedersen, "Experimental Characterization of Millimeter-Wave Indoor Propagation Channels at 28 GHz," *IEEE Access*, vol. 6, pp. 76 516–76 526, 2018.

[34] G. R. Maccartney, T. S. Rappaport, S. Sun, and S. Deng, "Indoor Office Wideband Millimeter-Wave Propagation Measurements and Channel Models at 28 and 73 GHz for Ultra-Dense 5G Wireless Networks," *IEEE Access*, vol. 3, pp. 2388–2424, 2015.

[35] S. Y. Lim, Z. Yun, and M. F. Iskander, "Propagation Measurement and Modeling for Indoor Stairwells at 2.4 and 5.8 GHz," *IEEE Transactions on Antennas and Propagation*, vol. 62, no. 9, pp. 4754–4761, 2014.

[36] J. A. del Peral-Rosado, R. Raulefs, J. A. López-Salcedo, and G. Seco-Granados, "Survey of Cellular Mobile Radio Localization Methods: From 1G to 5G," *IEEE Communications Surveys & Tutorials*, vol. 20, no. 2, pp. 1124–1148, 2018.

[37] T. Janssen, A. Koppert, R. Berkvens, and M. Weyn, "A Survey on IoT Positioning leveraging LPWAN, GNSS and LEO-PNT," *IEEE Internet of Things Journal*, vol. PP, no. 99, p. 1, Feb. 2023, number: 99 Publisher: Institute of Electrical and Electronics Engineers (IEEE). [Online]. Available: https://sciprofiles.com/publication/view/1b373c1cb536edd1575a7525f1566f53

[38] F. S. Prol, R. M. Ferre, Z. Saleem, P. Välisuo, C. Pinell, E. S. Lohan, M. Elsanhoury, M. Elmusrati, S. Islam, K. Çelikbilek, K. Selvan, J. Yliaho, K. Rutledge, A. Ojala, L. Ferranti, J. Praks, M. Z. H. Bhuiyan, S. Kaasalainen, and H. Kuusniemi, "Position, Navigation, and Timing (PNT) Through Low Earth Orbit (LEO) Satellites: A Survey on Current Status, Challenges, and Opportunities," *IEEE Access*, vol. 10, pp. 83 971–84 002, 2022.

[39] L. Chen, O. Julien, P. Thevenon, D. Serant, A. G. Pena, and H. Kuusniemi, "TOA Estimation for Positioning With DVB-T Signals in Outdoor Static Tests," *IEEE Transactions on Broadcasting*, vol. 61, no. 4, pp. 625–638, Dec. 2015.

[40] A. Nessa, B. Adhikari, F. Hussain, and X. N. Fernando, "A Survey of Machine Learning for Indoor Positioning," *IEEE Access*, vol. 8, pp. 214 945–214 965, 2020.

[41] E. Schmidt, D. Inupakutika, R. Mundlamuri, and D. Akopian, "SDR-Fi: Deep-Learning-Based Indoor Positioning via Software-Defined Radio," *IEEE Access*, vol. 7, pp. 145 784–145 797, 2019.

[42] S. Bottigliero, D. Milanesio, M. Saccani, and R. Maggiora, "A Low-Cost Indoor Real-Time Locating System Based on TDOA Estimation of UWB Pulse Sequences," *IEEE Transactions on Instrumentation and Measurement*, vol. 70, pp. 1–11, 2021.

[43] D. Zhang, L. T. Yang, M. Chen, S. Zhao, M. Guo, and Y. Zhang, "Real-Time Locating Systems Using Active RFID for Internet of Things," *IEEE Systems Journal*, vol. 10, no. 3, pp. 1226–1235, 2016.

[44] C. A. Balanis, *Antenna Theory: Analysis and Design*. New York, NY, USA: Wiley-Interscience, 2005.

[45] R. Chataut and R. Akl, "Massive MIMO Systems for 5G and beyond Networks—Overview, Recent Trends, Challenges, and Future Research Direction," *Sensors*, vol. 20, no. 10, 2020.

[46] R. Bonjour, M. Singleton, S. A. Gebrewold, Y. Salamin, F. C. Abrecht, B. Baeuerle, A. Josten, P. Leuchtmann, C. Hafner, and J. Leuthold, "Ultra-Fast Millimeter Wave Beam Steering," *IEEE Journal of Quantum Electronics*, vol. 52, no. 1, pp. 1–8, 2016.

[47] M. Rihan, T. Abed Soliman, C. Xu, L. Huang, and M. I. Dessouky, "Taxonomy and Performance Evaluation of Hybrid Beamforming for 5G and Beyond Systems," *IEEE Access*, vol. 8, pp. 74 605–74 626, 2020.

[48] Y. Zhuang, X. Zhang, and Z. He, "Beampattern Synthesis for Phased Array With Dual-Phase-Shifter Structure," *IEEE Transactions on Antennas and Propagation*, vol. 69, no. 10, pp. 7053–7058, 2021.

[49] P.-Y. Chen, C. Argyropoulos, and A. Alù, "Terahertz Antenna Phase Shifters Using Integrally-Gated Graphene Transmission-Lines," *IEEE Transactions on Antennas and Propagation*, vol. 61, no. 4, pp. 1528–1537, 2013.

[50] G. D'Amato, G. Avitabile, G. Coviello, and C. Talarico, "DDS-PLL Phase Shifter Architectures for Phased Arrays: Theory and Techniques," *IEEE Access*, vol. 7, pp. 19 461–19 470, 2019.

[51] P. Chen, W. Hong, H. Zhang, J. Chen, H. Tang, and Z. Chen, "Virtual Phase Shifter Array and Its Application on Ku Band Mobile Satellite Reception," *IEEE Transactions on Antennas and Propagation*, vol. 63, no. 4, pp. 1408–1416, 2015.

[52] R. Jakoby, A. Gaebler, and C. Weickhmann, "Microwave Liquid Crystal Enabling Technology for Electronically Steerable Antennas in SATCOM and 5G Millimeter-Wave Systems," *Crystals*, vol. 10, no. 6, 2020.

[53] I. S. Song, G. Yoon, and C. S. Park, "A Highly Integrated 1-Bit Phase Shifter Based on High-Pass/Low-Pass Structure," *IEEE Microwave and Wireless Components Letters*, vol. 25, no. 8, pp. 523–525, 2015.

[54] K. Topalli, O. A. Civi, S. Demir, S. Koc, and T. Akin, "A Monolithic Phased Array Using 3-bit Distributed RF MEMS Phase Shifters," *IEEE Transactions on Microwave Theory and Techniques*, vol. 56, no. 2, pp. 270–277, 2008.

[55] H. N. Chu, T. H. Hoang, K.-J. Ji, and T.-G. Ma, "A Phase Distribution Network Using 2 x 4 Butler Matrix for Linear/Planar Beam-Scanning Arrays," *IEEE Access*, vol. 9, pp. 133 438–133 448, 2021.

[56] J. Butler, "Beam-forming matrix simplifies design of electronically scanned antennas," *Electronic Design*, vol. 9, pp. 170–173, 1961.

[57] C.-C. Chang, T.-Y. Chin, J.-C. Wu, and S.-F. Chang, "Novel Design of a 2.5-GHz Fully Integrated CMOS Butler Matrix for Smart-Antenna Systems," *IEEE Transactions on Microwave Theory and Techniques*, vol. 56, no. 8, pp. 1757–1763, 2008.

[58] C.-L. I, C. Rowell, S. Han, Z. Xu, G. Li, and Z. Pan, "Toward green and soft: a 5G perspective," *IEEE Communications Magazine*, vol. 52, no. 2, pp. 66–73, 2014.

[59] Y. Alsaba, S. K. A. Rahim, and C. Y. Leow, "Beamforming in Wireless Energy Harvesting Communications Systems: A Survey," *IEEE Communications Surveys Tutorials*, vol. 20, no. 2, pp. 1329–1360, 2018.

CHAPTER 2

The Angle-of Arrival Estimation

After having revised the main localization techniques and operative scenarios, the focus of this chapter is the Angle-of-Arrival (AoA) estimation. First, it is presented the definition of AoA for linear and planar arrays. Hence, the main techniques from classical array signal processing literature are discussed, along with the challenges to overcome when striving for their use in real-time AoA estimation systems. Thereafter, phase interferometry is introduced and detailed, and some examples of systems based on this technique are presented.

2.1 Definition and basic relationships

When an incoming wave impinges an array of N antennas from a given direction ϑ, each of the array elements receives a copy of the signal with different amplitudes and at a different time instant. Picking an element as a reference, the received signal at array element i is

$$s_i(t) = \alpha_i s_0(t - \Delta\tau_{0i}),\ i \in \{0, \dots, N-1\} \subset \mathbb{N},\ t, \alpha_i, \Delta\tau_{0i} \in \mathbb{R} \qquad (2.1)$$

where $i = 0$ is the reference element, α_i is the amplitude scale factor, and $\Delta\tau_{0i}$ is the time difference between the reception of the signal by the reference element and the i-th element. By convention, $\alpha_0 = 1$ and $\Delta\tau_{00} = 0$. Supposing to operate in the far field, for small size arrays, the amplitude difference is negligible, i.e. $\alpha_i \approx 1\ \forall i$. The time delay $\Delta\tau_{0i}$ depends on the direction from which the signals come and on the array geometry. As a first example, we consider a Uniform Linear Array (ULA), i.e. the elements are positioned along a line, with uniform spacing d, and symmetrically. Consider as reference the geometry in Figure 2.1. If we operate in free space, the time delay between element i and element j of the ULA, $i, j \in \{0, \cdots, N-1\}$, $i \neq j$ is

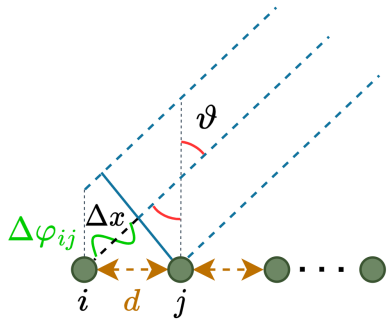

Figure 2.1: Reference geometry for the derivation of the relationship between time delay, phase shift, and AoA in a ULA.

related to the traveled path difference Δx as

$$\Delta\tau_{ij} = \frac{\Delta x}{c} \tag{2.2}$$

where c is the speed of light in vacuum. From a trivial trigonometric relationship, Δx can be linked to the AoA ϑ as

$$\Delta x = d(i-j)\sin\vartheta \tag{2.3}$$

Hence,

$$\Delta\tau_{ij} = \frac{d(i-j)}{c}\sin\vartheta \tag{2.4}$$

For a narrowband signal with center frequency f, the time delay and the phase difference $\Delta\varphi_{ij}$ are related as

$$\Delta\varphi_{ij} = 2\pi f\Delta\tau_{ij} \overset{(2.4)}{=\!=} 2\pi\frac{d(i-j)}{c}f\sin\vartheta \tag{2.5}$$

By substituting the definition of wavelength in free space, $\lambda = c/f$,

$$\Delta\varphi_{ij}(\vartheta) = \frac{2\pi}{\lambda}d(i-j)\sin\vartheta \tag{2.6}$$

In the context of linear arrays, the AoA ϑ is called broadside AoA, and it spans in 2D. In the same way, it is possible to derive an expression to link the AoA to the time delay and phase shift for other array geometries. For instance, it is possible to derive a similar expression for planar arrays. Planar arrays are attractive since the AoAs can be spanned in the 3D space. Each AoA can be decomposed in an azimuth angle α and an elevation angle ε. The simplest planar structure is the Uniform Rectangular Array (URA), shown in Figure 2.2. The URA can be seen as a "ULA of ULAs". Because the array has a bidimensional structure, each element is identified by a pair $(m,n) \in \mathbb{N}$:

$$(m,n) \in \{0,\cdots,M-1\}\times\{0,\cdots,N-1\} \subset \mathbb{N}^2 \tag{2.7}$$

where M is the number of elements along the x axis and N the elements along the y axis. By considering the element $(0,0)$ as the reference [1]:

$$\Delta\tau_{mn}(\alpha,\varepsilon) = \frac{1}{c}\left(md_x\sin\varepsilon\cos\alpha + nd_y\sin\varepsilon\sin\alpha\right) \tag{2.8}$$

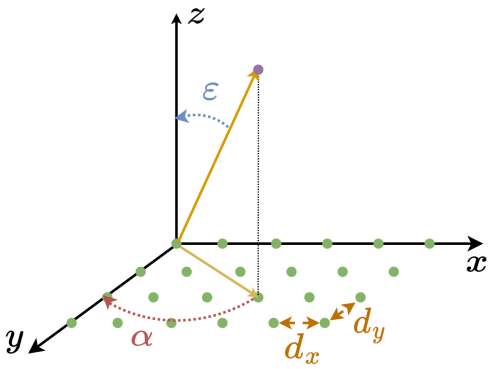

Figure 2.2: Reference geometry for the URA, with the azimuth angle α and the elevation angle ε.

where $\Delta\tau_{mn}$ is the time delay between the reference element and the (m, n) element. In a URA, $d_x = d_y = d$. Hence,

$$\Delta\tau_{mn}(\alpha, \varepsilon) = \frac{d}{c}\left(m \sin\varepsilon \cos\alpha + n \sin\varepsilon \sin\alpha\right) \tag{2.9}$$

Therefore, for a narrowband signal, the phase shift can be computed as

$$\Delta\varphi_{mn}(\alpha, \varepsilon) = \frac{2\pi}{\lambda} d\left(m \sin\varepsilon \cos\alpha + n \sin\varepsilon \sin\alpha\right) \tag{2.10}$$

2.2 Specialized Hardware Architectures for AoA estimation

A real-time AoA estimation system is capable of estimating the AoA of the received signal with the lowest latency. In this context, "lowest" is completely dependent on the specific application. Running the AoA estimator on the application layer of a device means naturally considering some sources of delays not completely controllable, due to the presence of buffers and queues. The aim of this section is to discuss the principal algorithms and techniques employed for the AoA estimation and evaluate their implementation in specialized hardware architectures. Usually, those architectures are synthesized on FPGA. Also, other hardware-friendly approaches not based on the reference algorithms are introduced.

2.2.1 Classical AoA estimation algorithms

The algorithms from array signal processing literature can be classified into two categories: the spectral-based approaches and the parametric approaches [2]. In spectral-based approaches, the aim is to compute a spectrum-like function of the single parameter of interest, in our case the AoA. The peak locations in the spectrum functions correspond to the AoA estimation. On the other hand, parametric techniques require a simultaneous search of all the signal parameters. Therefore, a multidimensional search is needed to find the estimates. This comes at the cost of higher computational complexity and latency before the first estimation, but it results in sensibly higher accuracy than the spectral-based approaches. The most known and appreciated parametric approach is the Maximum Likelihood Estimation (MLE) and its flavors.

As for the content of this thesis work, the attention is focused on spectral-based approaches. These latter can be classified into beamforming techniques and subspace-separation methods. Beamforming techniques result in pure blind search: the array pattern is steered in every possible direction in the space to measure the power associated with the parameter in a specific direction. Examples are Barlett's (or conventional) beamformer and Capon's beamformer. The subspace-separation methods compute the covariance matrix of the received signals from each array element. The covariance matrix describes the degree of correlation of the signals impinging different array elements. Historically, many approaches were implicitly based on the spectral decomposition of the covariance matrix [2]. However, the most important contributions arrived when the eigenstructure of the covariance matrix was directly involved. A subspace-separation technique basically assumes the columns space (i.e. the set of all vectors which can be expressed as a linear combination of the columns of the matrix) of the covariance matrix may be decomposed in two orthogonal subspaces: the signal subspace and the noise subspace.

MUSIC algorithm A huge step forward in subspace-separation techniques arrived with the advent of the Multiple Signal Classification (MUSIC) algorithm by R. Schmidt [3]. Originally, this algorithm was developed for AoA identification, but later it has been applied to other spectral analysis and system identification problems [2]. MUSIC still represents the basis for comparing the efficiency and the accuracy of an AoA estimation technique. Hence, it is taken as one of the reference algorithms throughout this thesis work. MUSIC assumes the signals impinging on each array element are not correlated or poorly correlated. The same hypothesis is made for the noise. The objective is to find and reorder the eigenvalues of the covariance matrix of the array. The following mathematical description follows what is in the book by *Rappaport et al.* [4] and it is developed in 2D space (i.e. it is considered a null elevation).
Suppose L uncorrelated signals to impinge a receiving array of M antennas from the far-field. It is worth representing the received signal in matrix form, in order to introduce a more compact notation:

$$\mathbf{X} = \mathbf{A}(\boldsymbol{\vartheta})\,\mathbf{S} + \boldsymbol{\eta} \tag{2.11}$$

where $\mathbf{S}$ is the signal matrix containing the sampled and quantized composition of the L signals, and $\boldsymbol{\eta}$ is the additive noise component. $\mathbf{A}(\boldsymbol{\vartheta})$ is the direction matrix defined as

$$\mathbf{A}(\boldsymbol{\vartheta}) = \begin{bmatrix} 1 & 1 & \cdots & 1 \\ e^{-j\Delta\varphi_1(\vartheta_0)} & e^{-j\Delta\varphi_1(\vartheta_1)} & \dots & e^{-j\Delta\varphi_1(\vartheta_{L-1})} \\ e^{-j\Delta\varphi_2(\vartheta_0)} & e^{-j\Delta\varphi_1(\vartheta_1)} & \dots & e^{-j\Delta\varphi_2(\vartheta_{L-1})} \\ \cdots & \cdots & \cdots & \cdots \\ e^{-j\Delta\varphi_{M-1}(\vartheta_0)} & e^{-j\Delta\varphi_{M-1}(\vartheta_1)} & \dots & e^{-j\Delta\varphi_{M-1}(\vartheta_{L-1})} \end{bmatrix} \tag{2.12}$$

where $\Delta\varphi_i(\vartheta_j)$ is the phase shift of array element i with respect to the reference element 0 due to AoA ϑ_j of the j-th source.
The covariance matrix can be computed as follows. First, the received signal matrix $\mathbf{X}$ is computed. $\mathbf{X}$ is a $M \times N$ matrix, with M being the number of antenna array elements and N the number of snapshots acquired (i.e. the available sampled signal

values):

$$\mathbf{X} = \begin{bmatrix} s_0[0] & s_0[1] & \cdots & s_0[N-1] \\ s_1[0] & s_1[1] & \cdots & s_1[N-1] \\ \cdots & \cdots & \cdots & \cdots \\ s_{M-1}[0] & s_{M-1}[1] & \cdots & s_{M-1}[N-1] \end{bmatrix} \tag{2.13}$$

where $s_p[k]$ is the k-th sample of the received signal at array element p, having $k \in \{0, \cdots, N-1\}$, $p \in \{0, \cdots, M-1\}$. The covariance matrix for finite sample size $\mathbf{R_{XX}}$ can approximated as [5]:

$$\mathbf{R_{XX}} \approx \left(\frac{1}{N}\right)\mathbf{X}^H\mathbf{X} \tag{2.14}$$

with $(\cdot)^H$ denoting the hermitian operator, i.e. the conjugate transpose operator. Hence, the characteristic polynomial of the (2.14) is

$$|\mathbf{R_{XX}} - \xi\mathbf{I}| = 0 \tag{2.15}$$

By solving the (2.15) for ξ it is possible to find the eigenvalues of the covariance matrix. It can be shown that a set of those eigenvalues have small and almost equal values. Hence, it is possible to expand the (2.15) as

$$|\mathbf{R_{XX}} - \xi\mathbf{I}| = (\xi - \rho_1)(\xi - \rho_2)\cdots(\xi - \rho_L)(\xi - \sigma_n^2)^{M-L} \tag{2.16}$$

denoting with σ_n^2 the noise variance, and being $(\xi - \sigma_n^2)$ a multiple root for the characteristic polynomial. $\mathbf{I}$ is the identity matrix, while ρ_i denotes the L highest-value eigenvalues. The eigenvectors associated with the multiple roots with the lowest eigenvalues define the noise subspace, while the others define the signal subspace. By denoting with $\mathbf{U}_N$ the former and with $\mathbf{U}_S$ the latter, the following property holds:

$$\mathbf{R_{XX}} = \mathbf{U}_S\mathbf{\Lambda}_S\mathbf{U}_S^H + \mathbf{U}_N\mathbf{\Lambda}_N\mathbf{U}_N^H \tag{2.17}$$

where $\mathbf{\Lambda}_S, \mathbf{\Lambda}_N$ are diagonal matrices containing signal and noise eigenvectors, respectively. This decomposition of the covariance matrix is called Eigen-Value Decomposition (EVD). It is possible to observe that any eigenvector of $\mathbf{R_{XX}}$ with eigenvalue σ_n^2 (i.e., the noise subspace) is orthogonal to the direction vector $\mathbf{A}(\boldsymbol{\vartheta})$ [2]. This allows us to write

$$\mathbf{U}_N\mathbf{U}_N^H = \mathbf{I} - \mathbf{A}(\mathbf{A}^H\mathbf{A})^{-1}\mathbf{A}^H \tag{2.18}$$

omitting the dependency on $\boldsymbol{\vartheta}$ for sake of compactness. This expression can be employed in the so-called pseudospectrum function $\mathrm{P_{MU}}(\hat{\boldsymbol{\vartheta}})$ as

$$\mathrm{P_{MU}}(\hat{\boldsymbol{\vartheta}}) = \frac{1}{a^H(\hat{\boldsymbol{\vartheta}})\Pi^N a(\hat{\boldsymbol{\vartheta}})} \tag{2.19}$$

where $\Pi^N = \mathbf{U}_N\mathbf{U}_N^H$ and $a(\hat{\boldsymbol{\vartheta}})$ is the steering vector, i.e. the vector that spans all the possible AoAs one expects the signal to be received from. The steering vector is extremely important since the granularity of the spacing between adjacent $\hat{\vartheta} \in \hat{\boldsymbol{\vartheta}}$ contributes to the overall estimation accuracy.

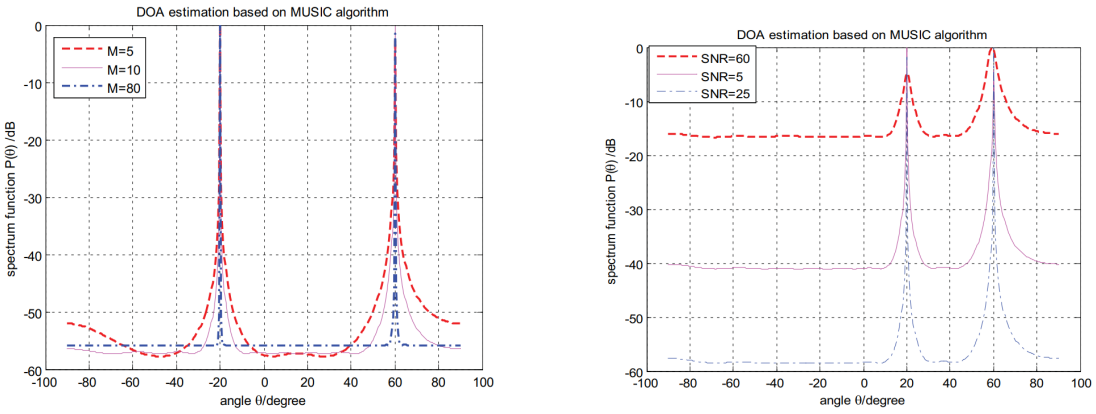

Figure 2.3: MUSIC pseudospectrum function computation and evaluation results from the work [6]. In detail (a) peak width degradation varying the number of array elements and (b) performance degradation depending on the SNR. © 2020, IEEE.

The pseudospectrum function is an "angular" dependent curve whose peaks determine the estimated AoAs for the L sources. Theoretically

$$\lim_{\hat{\boldsymbol{\vartheta}} \to \boldsymbol{\vartheta}} \mathrm{P}_{\mathrm{MU}}(\hat{\boldsymbol{\vartheta}}) = +\infty \tag{2.20}$$

i.e. the pseudospectrum function peaks correspond to those steering angles which approximate the actual AoAs for each of the sources. An example of pseudospectrum function of the steering angles is in Figure 2.3.

ESPRIT Estimation of Signal Parameters with Rotational Invariance Technique (ESPRIT) is a class of algorithms for estimating AoAs [7]. Temporal ESPRIT (T-ESPRIT) for estimating AoAs and Spatial ESPRIT (S-ESPRIT) which is a propagation delay estimation algorithm [4] belong to ESPRIT. Through the forthcoming sections and chapters the reference will be T-ESPRIT, simply denoted as ESPRIT. ESPRIT was originally developed for ULAs because of the particular structure of the direction matrix. For a ULA, the expression (2.12) can be simplified as:

$$\mathbf{A}_{VM}(\boldsymbol{\vartheta}) = \begin{bmatrix} 1 & 1 & \cdots & 1 \\ e^{-j\varphi(\vartheta_0)} & e^{-j\varphi(\vartheta_1)} & \cdots & e^{-j\varphi(\vartheta_{L-1})} \\ e^{-2j\varphi(\vartheta_0)} & e^{-2j\varphi(\vartheta_1)} & \cdots & e^{-2j\varphi(\vartheta_{L-1})} \\ \cdots & \cdots & \cdots & \cdots \\ e^{-(M-1)j\varphi(\vartheta_0)} & e^{-(M-1)j\varphi(\vartheta_1)} & \cdots & e^{-(M-1)j\varphi(\vartheta_{L-1})} \end{bmatrix} \tag{2.21}$$

with $\varphi(\theta_k) = \frac{2\pi d}{\lambda}\sin(\vartheta_k)$, $k \in \{0, \cdots, L-1\}$. The matrix structure (2.21) is called Vandermonde matrix. Each row of the (2.21) is an integer power of the first one, and the power is exactly equal to the row number.
ESPRIT basically breaks the array into smaller sub-arrays. Hence, the phase shift between the subarray is exploited to determine the AoA of the impinging signals. The sub-arrays must be identical except for the translational change in position but not in orientation [4]. ESPRIT can be computationally intensive since it requires more than

one EVD, but still, it is less greedy than MUSIC. The subarrays breaking is performed as follows [2,4]. The signal model (2.11) can be rewritten as

$$\mathbf{X} = \mathbf{A}_{VM}(\boldsymbol{\vartheta})\,\mathbf{S} + \boldsymbol{\eta} \tag{2.22}$$

Once two subarrays (i.e. two sub-blocks of the Vandermonde matrix) are chosen, the following holds:

$$\begin{cases} \mathbf{X_1} = \mathbf{A_1 S} + \sigma_n^2 \mathbf{I} \\ \mathbf{X_2} = \mathbf{A_2 \Psi S} + \sigma_n^2 \mathbf{I} \end{cases} \tag{2.23}$$

being $\mathbf{\Psi}$ a diagonal matrix accounting for the phase shift between subarrays. The diagonal elements can be employed for estimating the AoAs. In fact, by computing the covariance matrix and suitably partitioning the signal subspace $\mathbf{U}$ in $\mathbf{U_1}$ and $\mathbf{U_2}$ it is possible to find

$$\mathbf{U_2} = \mathbf{U_1 \Phi} \tag{2.24}$$

with $\mathbf{\Phi}$ being linked to $\mathbf{\Psi}$ through a similarity transformation, thus having the same eigenvalues. Hence, the AoA is computed starting from each eigenvalue as

$$\hat{\vartheta}_l = \arcsin\left(\frac{\lambda \arg(\rho_l)}{2\pi d}\right),\ l = \{0, \cdots, L-1\} \tag{2.25}$$

Root-MUSIC Root-MUSIC (RMUSIC) is the polynomial rooting version of the MUSIC technique, as the name suggests [8]. To describe it, it will be used as reference the work by *Krim et al.* [2]. We consider the polynomials

$$p_m(z) = \mathbf{u}_m^H\,\mathbf{p}(z),\ \ m = L, L+1, \cdots, M \tag{2.26}$$

being $\mathbf{u}_m$ the m-th eigenvector of the covariance matrix and being z the polynomial column vector

$$\mathbf{p}(z) = \left[1, z, \cdots, z^{M-1}\right]^T \tag{2.27}$$

Basically, $p_m(z)$ has L of its zeros at $e^{-mj\varphi(\vartheta_l)}$, $m = \{0, \cdots, M-1\}$ and $l \in \{0, \cdots, L-1\}$. To find these zeros, the RMUSIC polinomial is solved (recalling (2.18):

$$p(z) = z^{M-1}\mathbf{p}^T(z^{-1})\Pi^N\mathbf{p}(z) \tag{2.28}$$

The argument of the highest (in modulus) values of z can be inverted as described by (2.25) in the ESPRIT case.

2.2.2 Implementation of AoA estimation algorithms in hardware

The implementation of subspace separation techniques in digital specialized hardware architectures is challenging since the algorithm stages require a huge computational load [9].
As an example, by looking at the MUSIC algorithm, the source of such computational complexity relies on the fact it operates with complex-valued numbers and equations. Moreover, the autocorrelation matrix computation phase, the EVD phase, and the peak search phase require significant computational resources.

Some of the proposed improvements aim to implement variations to the standard MUSIC algorithm to make it hardware efficient. *Zou et al.* in [10] proposed a way

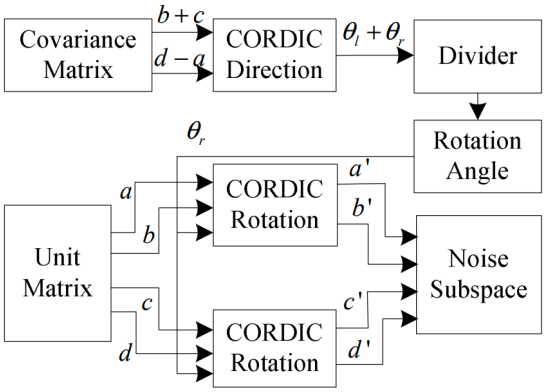

Figure 2.4: EVD structure based on CORDIC algorithm proposed by *Wang et al.* in [11]. © 2011, IEEE.

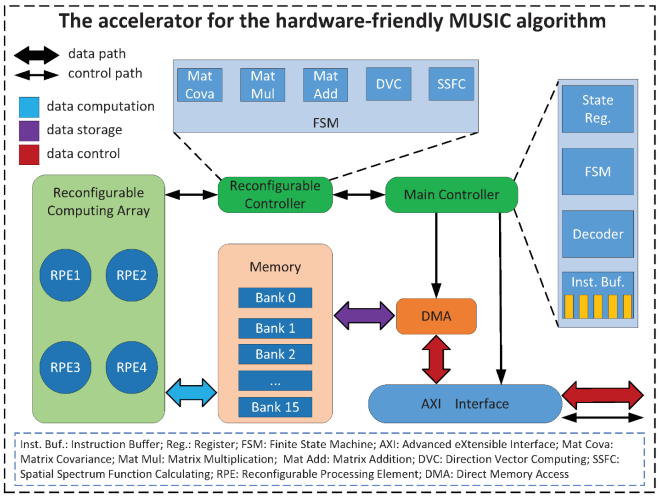

Figure 2.5: Accelerator for MUSIC algorithm proposed by *Chen et al.* in [12]. *Image licensed under CC BY 4.0.*

to skip the autocorrelation matrix decomposition, approximating it through an iterative method. They compared the performance in terms of time and accuracy obtained with a DSP running the non-modified MUSIC algorithm and an FPGA running the approach they were proposing. Results proved the novel approach to be 4 times faster than the original one. This performance increase comes at the cost of poorer accuracy only at low SNR values.

Wang et al. in [11] support the linear transformation with the decomposition of the EVD phase employing the CORDIC algorithm (Figure 2.4).

In [12] *Chen et al.* present a hardware-friendly implementation of the MUSIC algorithm in which they decrease the EVD computational cost by exploiting the conjugate symmetry property of the covariance matrix (Figure 2.5). The same property is employed for decreasing the memory access time. The algorithm was simulated to work up to 1 GHz clock frequency, on a Taiwan Semiconductor Manufacturing Company (TSMC) 40 nm CMOS technology.

Butt et al. in [9] implemented an optimized version of the MUSIC algorithm with reduced processing time and resource occupation on a Xilinx Zynq XC7Z020-CLG484 FPGA. The main steps of the modified algorithm are shown in Figure 2.6a. The im-

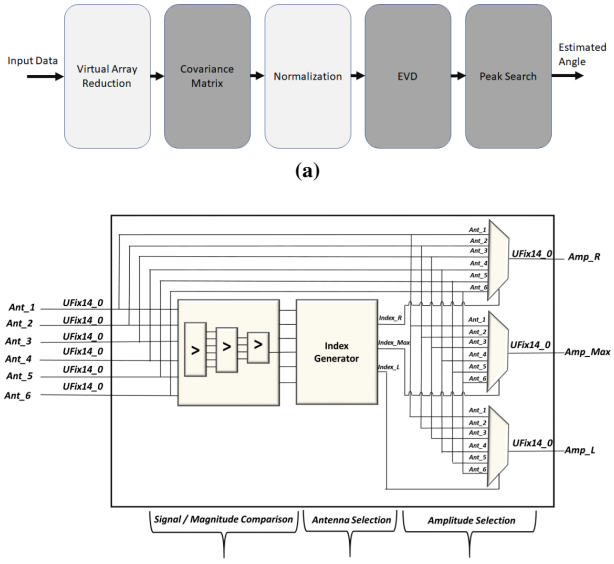

Figure 2.6: Optimized MUSIC algorithm proposed by *Butt et al.* in [9]: block diagrams representing (a) the main steps of the modified algorithm and (b) array size reduction unit block diagram. © 2021, IEEE.

provement is obtained by normalizing the covariance matrix and reducing its size by considering only three adjacent antennas and then choosing to evaluate the best-received signal level. The antenna receiving the maximum strength and the two adjacent ones are chosen, one on the left and one on the right (Figure 2.6b). The estimation takes a few µs. However, the peak search range is limited to 60 degrees.
Li et al. in [13] propose an EVD decomposition technique for Hermitian matrices with low resource occupancy and low latency. The proposed optimization has been demonstrated for sparse arrays (Figure 2.7a) and ULAs (Figure 2.7b), respectively.
Other implementations involve working with real values instead of complex numbers. This is the case of [14], where *Kim et al.* propose to use a linear transformation to perform the EVD with real numbers only (Figure 2.8). The approach was tested on the Altera EP20K600 FPGA producing the final result in tens of microseconds.

The efficient hardware implementation of RMUSIC and ESPRIT still represents an

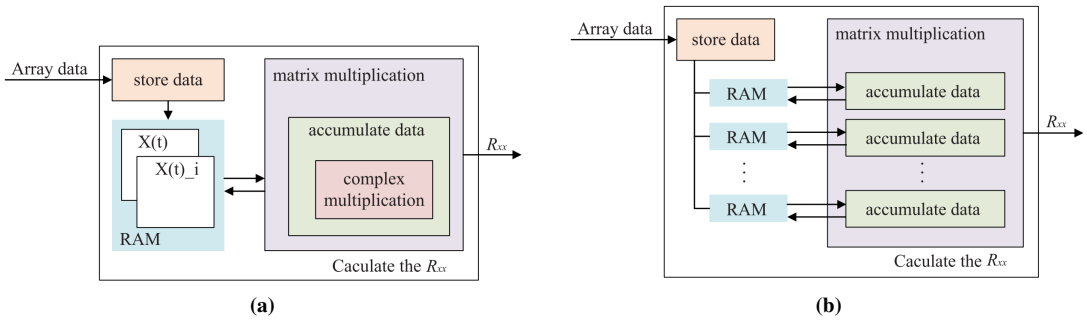

Figure 2.7: Computation of the autocorrelation matrix R_{xx} in the design proposed by *Li et al.* in [13]: (a) classical architecture suitable also for sparse arrays, and (b) high-parallelism architecture for uniform arrays with low-latency. © 2022, IEEE

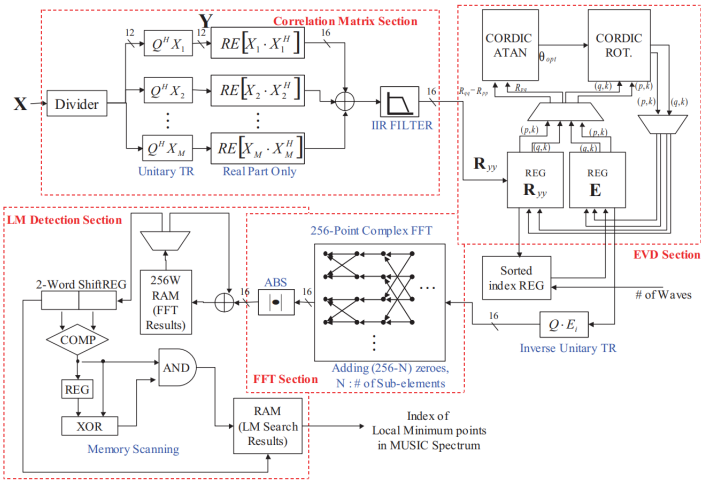

Figure 2.8: Block diagram of the MUSIC algorithm implementation proposed by *Kim et al.* in [14] © 2003, IEEE.

issue since both of them make use of EVD. Also, in this case, several implementations have been proposed aiming to lighten this step.
In [15], *Boonyanant et al.* propose the implementation of Recursive ESPRIT on a Xilinx Virtex-II FPGA. In this implementation, similarly to [14] they make use of a linear transformation to operate only on real numbers. This is one of the first efforts for implementing ESPRIT in digital hardware, and the implementation takes about half of the available resources. More recently, in [16] *Jung et al.* propose an ESPRIT-based scalable system that supports 2 to 8 array elements. The block diagram depicting the main stages is in Figure 2.9. The processor is based on a multiple invariances algorithm, with better performances than the existing ESPRIT processor, and the performances are increased thanks to the least-square and Jacobi methods for EVD. The system was tested on a Xilinx Virtex-5 FPGA.

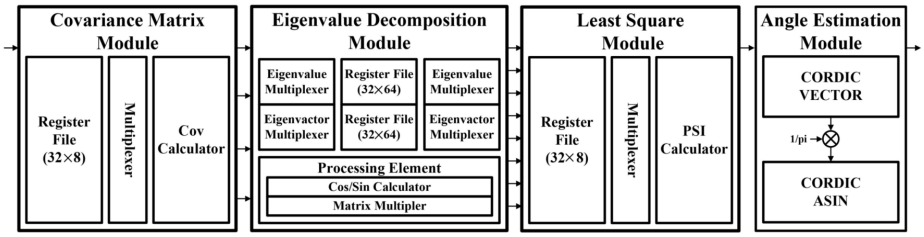

Figure 2.9: Hardware architecture for ESPRIT proposed by *Jung et al.* in [16]. *Image licensed under CC BY 4.0.*

2.2.3 Other hardware approaches and architectures

Badawy et al. in [17] propose a hardware-friendly and low-complexity AoA estimation scheme based on a Switched-Beam System (SBS) approach which main blocks are shown in Figure 2.10. In SBSs, the phased array can switch among a fixed number of possible beam directions to scan the space. The proposed system first acquires the received signal using only one antenna and then employs this signal as the reference for a cross-correlation operation on all the possible beams the system supports. Hence, the highest cross-correlation coefficient corresponds to the best estimation for

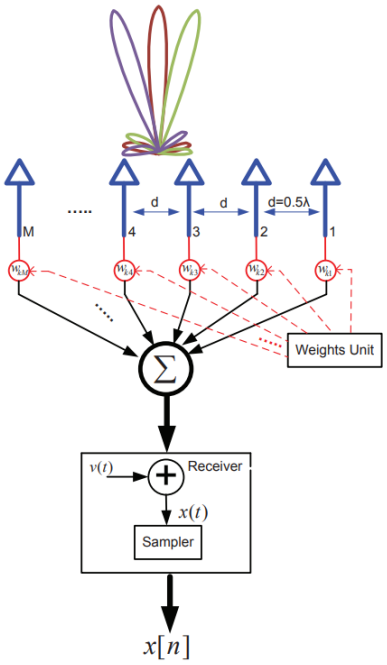

Figure 2.10: The cross-correlation based SBS proposed by *Badawy et al.* in [17] for hardware-friendly and low-complexity AoA estimation. © 2017, IEEE.

the AoA according to this technique. The performance proved to increase when employing orthogonal beams, i.e. the peak of the current beam is located at the minima of the two adjacent beams.

Another possibility consists in exploiting particular analog hardware architectures to support algorithms for the DoA estimation. This is the case of Rotman's lens, employed in [18] and [19]. Rotman's lens [20] is a physical structure that can be employed as a beamforming network. The lobe is focused in a given direction thanks to different time delays because of the propagation path from the so-called beam ports to the antenna ports. An example of a Rotman's lens is shown in Figure 2.11.

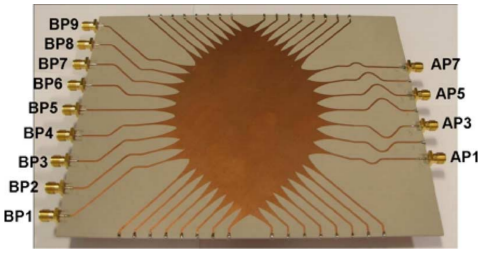

Figure 2.11: Example of a Rotman's lens designed in [21] with beam ports denoted with BP and antenna ports with AP. © 2010, IEEE.

In the mentioned works, the AoA estimation is performed by means of RSS-DoA matching, realizing something similar to an SBS. In [19] the RSS value corresponding to different beams is obtained through measurements or simulations, building a system response matrix. When receiving a signal from a given direction, the resulting received signals from different beam ports are compared to the system response

matrix. The direction which best fits the information corresponding to a value in the system response matrix determines the best approximation of the target angular position. Instead, in [18], in the first phase the direction corresponding to the beam port receiving the signal with the highest magnitude is assumed to be the coarse approximation of the incoming signal AoA. Hence, through a fitting function calculation on the beams in the neighborhood of the preliminary guess, it is possible to refine the estimation.

To seek hardware-efficient AoA estimation systems, sometimes subspace projections are employed. For instance, *Guo et al.* in [22] propose a beamspace AoA estimator which is hardware efficient and designed for unequal-sized subarrays. It is common to have arrays composed of analog subarrays at high frequencies (i.e. mmWaves). Hence, analog beamforming is performed upfront and it is possible to access only signals which already passed the beamforming procedure. We refer to space transformation when algorithms and techniques are not applied to the actual received signals but to their manipulation. In this case, we refer to the so-called beamspace. The proposed architecture is shown in Figure 2.12, and it is pipelined for reducing the latency. The approach is based on the Approximate Maximum Likelihood Estimation (AMLE) of the AoA, related to the phase of the cross-correlation function among the subarray outputs, which is computed by means of the CORDIC algorithm.

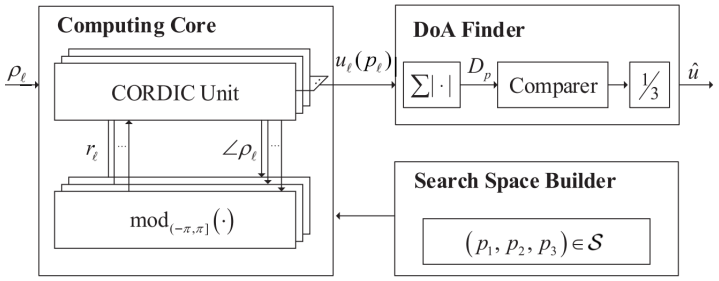

Figure 2.12: Block diagram of the hardware-efficient beamspace AoA estimator proposed by *Guo et al.* in [22] for unequal-sized subarrays. In this sketch, $\ell = 1, 2, 3$, being ℓ the label for each subarray. © 2022, IEEE.

Instead of actually computing the AoA, some techniques rely on identifying the angles by comparing the set of steering vectors stored in a codebook with the autocorrelation matrix. This is the basis of matching pursuit techniques on which the hardware DoA estimator and beamformer proposed by *Chen et al.* in [23] is based. Basically, the proposed architecture improves the classical matching pursuit approach by operating it on the signal sub-space. The computation of the autocorrelation matrix is lightened since only a subset of its coefficients is computed. The projection is realized by means of QR factorization i.e. the autocorrelation matrix is factorized into a unitary matrix Q and an upper triangular matrix R. The QR factorization is based on CORDIC units. The authors deployed their architecture on an Application-Specific Integrated Circuit (ASIC) through a TSMC 40 nm CMOS process, which can operate up to 333 MHz, thus performing an AoA estimation in 2.38 µs.

Another example of hardware AoA estimation is the work by *Zhang et al.* [24]. In the framework of coprime MIMO radar (i.e. transmitting and receiving arrays have inter-element spacings which are coprime), this solution makes use of the Discrete Fourier Transform (DFT) implementation. The AoA estimation accuracy is increased

by implementing a zero-padding scheme. Since no matrix operations or optimization problems are involved, the authors claim this solution to be keener on being implemented in hardware.

2.3 AoA estimation through Phase Interferometry

The simplest approach to estimate the AoA is phase interferometry [25]. This technique is also known as *naïve* approach to AoA estimation or PDoA approach to AoA estimation. Basically, the objective is to employ the measured phase shift as the basis for the AoA estimation.

2.3.1 The case of ULAs

Recall the (2.6) for a ULA composed by N elements (N-ULA):

$$\Delta\varphi_{ij}(\vartheta) = \frac{2\pi}{\lambda} d(i-j)\sin\vartheta,\ i,j \in \{0,\cdots,N-1\} \subset \mathbf{N} \tag{2.29}$$

The simple inversion of this formula with respect to $\sin\vartheta$ leads to

$$\sin\vartheta = \frac{\Delta\varphi_{ij}}{2\pi\delta(i-j)} \tag{2.30}$$

being $\delta = d/\lambda \in \mathbb{R}$. Hence, estimating ϑ depends on the estimation of $\Delta\varphi_{ij}$:

$$\hat{\vartheta}_{ij} = \arcsin\left(\frac{\Delta\varphi_{ij}}{2\pi} \cdot \frac{1}{\delta(i-j)}\right) \tag{2.31}$$

where $\hat{\vartheta}_{ij}$ denotes the estimation of ϑ through the phase shift φ_{ij}. The inverse sine (or arcsine) function $y = \arcsin(x)$ is such that

$$x \in [-1,1] \subset \mathbb{R}, y \in [-\pi/2, \pi/2] \subset \mathbb{R}. \tag{2.32}$$

Hence, studying the domain of the (2.31) [26]:

$$\left|\frac{\Delta\varphi_{ij}}{2\pi} \cdot \frac{1}{\delta(i-j)}\right| = \frac{|\Delta\varphi_{ij}|}{2\pi} \cdot \frac{1}{\delta(i-j)} \leq 1 \tag{2.33}$$

The phase difference under non-wrapping conditions is such that

$$\Delta\varphi_{ij} \in]-\pi,+\pi] \implies |\Delta\varphi_{ij}| \in [0,+\pi] \tag{2.34}$$

Therefore, the inequality (2.33) can be studied for the two interval limits cases, under the assumption of adjacent array elements (i.e. $i-j=1$). For $\max(\Delta\varphi_{ij}) = \pi$:

$$\frac{1}{2\delta} \leq 1 \implies \delta \geq \frac{1}{2} \iff d \geq \frac{\lambda}{2} \tag{2.35}$$

The case of $\min(\Delta\varphi_{ij}) = 0$ leads to a trivial solution. Hence, to estimate the AoA associated with the maximum phase shift, the spacing of the sensors should be at least $\lambda/2$. However, since the same antenna array can be employed by the system for focusing the array pattern, the phenomenon of grating lobes may arise with $d >$

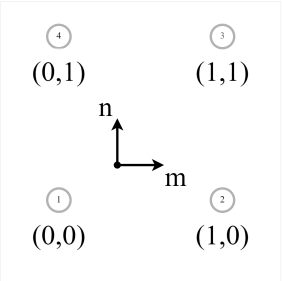

Figure 2.13: 2 x 2 URA with antenna elements numbering conventions used in this Section.

$\lambda/2$ [1]. Therefore, the optimum value for estimating the AoA associated with the maximum phase shift is

$$d_{opt} = \frac{\lambda}{2} \tag{2.36}$$

corresponding to $\hat{\vartheta}_{ij}^{max} = \pi/2$.

2.3.2 The case of URAs

For the sake of simplicity, let us consider a 2x2 URA as a reference. Also in this case it is possible to derive the equations that link the AoA information to the phase shift. Recalling the (2.10):

$$\Delta\varphi_{mn}(\alpha, \varepsilon) = \frac{2\pi}{\lambda} d \left(m \sin\varepsilon \cos\alpha + n \sin\varepsilon \sin\alpha \right) \tag{2.37}$$

For a 2x2 URA, $(m, n) \in \{0, 1\} \times \{0, 1\}$. By performing a counterclockwise numbering of the antenna elements $\mathbf{E} = \{\mathbf{1}, \mathbf{2}, \mathbf{3}, \mathbf{4}\}$ as in Figure 2.13 it is possible to write

$$\begin{cases} \Delta\varphi_{11}(\alpha, \varepsilon) = 0 \\ \Delta\varphi_{21}(\alpha, \varepsilon) = \pi \sin\varepsilon \cos\alpha \\ \Delta\varphi_{31}(\alpha, \varepsilon) = \pi(\sin\varepsilon \cos\alpha + \sin\varepsilon \sin\alpha) \\ \Delta\varphi_{41}(\alpha, \varepsilon) = \pi \sin\varepsilon \sin\alpha \end{cases} \tag{2.38}$$

by adopting the notation

$$\Delta\varphi_{ij} = \varphi_j - \varphi_i \tag{2.39}$$

To estimate the azimuth and elevation AoAs from the measured phase shifts, the procedure is less trivial than the (2.31). We observe that by doing the ratio between the fourth and the second equation of the linear system (2.38) it is possible to find,

$$\frac{\Delta\varphi_{41}}{\Delta\varphi_{21}} = \tan\alpha \tag{2.40}$$

and this leads to,

$$\hat{\alpha}_{421} = \arctan\left(\frac{\Delta\varphi_{41}}{\Delta\varphi_{21}}\right) \tag{2.41}$$

By substitution of this value in the fourth equation of (2.38) we find

$$\hat{\varepsilon}_{421} = \arcsin\left(\frac{\Delta\varphi_{41}}{\pi \sin\hat{\alpha}_{421}}\right) \tag{2.42}$$

where $\hat{\alpha}_{ijk}$ and $\hat{\varepsilon}_{ijk}$ are the estimations of the azimuth and the elevation angles respectively, employing array elements $i, j.k$. In this way, it is obtained one possible estimation, involving only three array elements. Those three array elements are arranged to form an "L" shape. In the case of a 2x2 URA, it is possible to find 4 possible arrangements of this type, as shown in Figure 2.14. These arrangements can be used to make the final estimation more robust. As an example, let us retrieve the azimuth

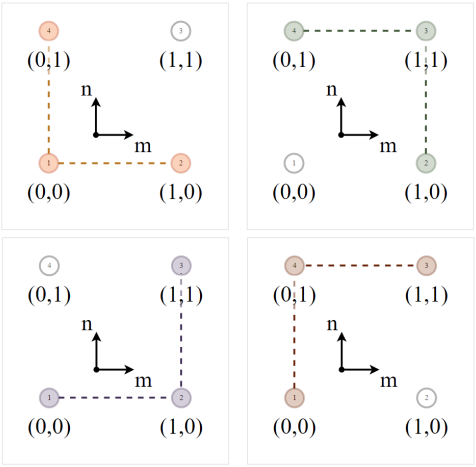

Figure 2.14: Possible "L"-shaped antenna elements configurations available in a 2 x 2 URA.

and elevation estimation due to the triple of array elements $\{4, 3, 2\}$.

First, it is clear the expressions in (2.38) are referred to the origin $(0, 0)$ (or, for the antenna numbering notation previously introduced, to the element 1). Following the notation (2.39) leads to

$$\Delta\varphi_{43} = \Delta\varphi_{41} - \Delta\varphi_{31} \tag{2.43}$$

By substituting the expressions of the (2.38) in the previous equation, we get

$$\Delta\varphi_{43} = -\pi \sin\varepsilon \cos\alpha \tag{2.44}$$

Similarly,

$$\Delta\varphi_{32} = \pi \sin\epsilon \sin\alpha \tag{2.45}$$

By doing the ratio between the (2.45) and the (2.44) it is possible to get

$$\frac{\Delta\varphi_{32}}{\Delta\varphi_{43}} = -\tan\alpha \tag{2.46}$$

Therefore,

$$\hat{\alpha}_{432} = -\arctan\left(\frac{\Delta\varphi_{32}}{\Delta\varphi_{43}}\right) \tag{2.47}$$

and similarly to what was done to obtain the (2.42),

$$\hat{\varepsilon}_{432} = \arcsin\left(\frac{\Delta\varphi_{32}}{\pi \sin\hat{\alpha}_{432}}\right) \tag{2.48}$$

In this way we have a set of estimations for the azimuth, $\mathcal{A}$, and a set of estimations for the elevations, $\mathcal{E}$, populated as

$$\begin{cases} \mathcal{A} = \{\hat{\alpha}_{421}, \hat{\alpha}_{432}, \hat{\alpha}_{321}, \hat{\alpha}_{431}\} \\ \mathcal{E} = \{\hat{\varepsilon}_{421}, \hat{\varepsilon}_{432}, \hat{\varepsilon}_{321}, \hat{\varepsilon}_{431}\} \end{cases} \tag{2.49}$$

Each of the L-shapes has elements that exhibit nominally the same phase differences relationship as the others (in modulus). This obviously leads to the same estimation for both azimuth and elevation angles. For larger arrays, this property can be still applied.

2.3.3 The problem of coherent signals reception

The biggest source of AoA identification error when applying the interferometric approach is constituted by coherent signal reception [27]. We define two signals $s_i(t)$ to be coherent when one of them (i.e., $s_2(t)$) if

$$s_2(t) = \alpha \cdot s_1(t - \tau) \quad \alpha, \tau \in \mathbb{R} \tag{2.50}$$

that is, one is the delayed and amplitude-scaled version of the other [2]. Note that, for narrowband signals, or, in our case, Continuous Wave (CW) signals, the time delay is equivalent to phase shift. In fact, considering a signal with frequency f, the phase shift $\Delta\varphi$ equivalent to a time delay τ is

$$\Delta\varphi = 2\pi f \tau \tag{2.51}$$

Coherent signal propagation occurs when considering an environment subject to multipath like the indoor environment. The presence of reflectors and scatters determines the birth of new copies of the signal that sum together at the receiver side. For more details, see Chapter 1.

In this simplified analysis we take into account only two paths: the direct one and the reflected path (Fig. 2.15a). To further isolate the phenomenon, besides reflection, the only considered artifact introduced by the communication channel is path loss.
Aiming to study what happens at the receiving side when composing two signals, a great contribution is furnished by the weights with which these contributes sum up together. Those weights are represented by the amplitudes of the direct ray and the coherent ray.

To study this scenario, it was conducted a simulation campaign considering a transmitted signal propagating in free space, with a frequency $f = 2.4$ GHz and phase $\varphi = 2$. The signal power was set to +5 dBm. The reflected ray path had a geometrical length arbitrarily set to obtain a phase value to the receiver $\varphi_r = 1$. As already stated, the second ray was supposed to be generated by a reflection. Also, sources of possible frequency drifts were neglected (e.g. Doppler Spread). In Fig. 2.15b it was depicted the estimated phase value varying with reflected signal power, starting from the worst case in which the two components had the same power, to the situation in which the reflected component power is very low when compared to the direct path. It is possible to appreciate that the more the coherent ray power loses its strength, the more the estimated phase difference (and so, the related AoA estimation) tends to the expected one.

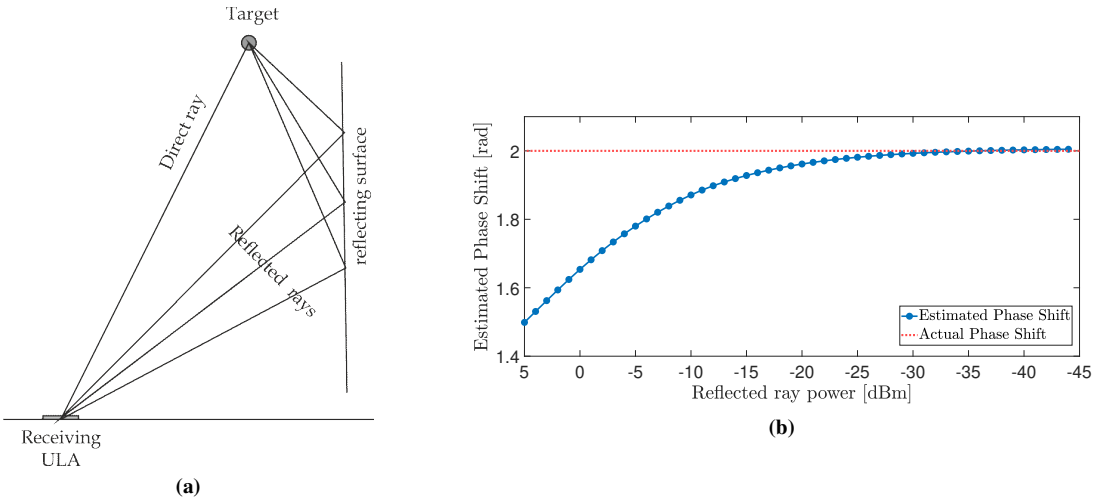

Figure 2.15: Impact of the reflected signal on the estimated phase shift at receiver side: (a) reference scenario and (b) results.

2.3.4 Examples of AoA estimation systems based on Phase Interferometry

In literature there are already some examples of systems and standards employing phase interferometry as a way of estimating the AoA.

From the systems deployment perspective, *Bnilam et al.* in [28] propose an AoA estimation system based on phase interferometry of LoRa signals. The phase shift is estimated through the AD8302 phase and envelope detector by Analog Devices [29]. Three isotropic antenna elements arranged in a triangular configuration are employed for the phase shift estimation, while a fourth antenna element acts as a trigger for the estimation process. Once the phase differences are estimated by the phase detectors, they are sent through LoRa packets to a LoRaWAN gateway connected to a processing system in the cloud that extrapolates the AoA information.

Another notable example is the BLE. From version 5.1 the direction finding (DF) is supported by this protocol and it is realized through AoA and AoD by means of phase interferometry [30]. These features are enabled only for uncoded PHY layers. Let us concentrate on AoA. The reference block diagram with the involved actors is in Figure 2.16. The transmitting peer which has to be localized allows the procedure by having in its Link Layer packet the Constant Tone Extension (CTE) Info field. This field defines the length of the CTE, which is a constant modulated series of 1s that

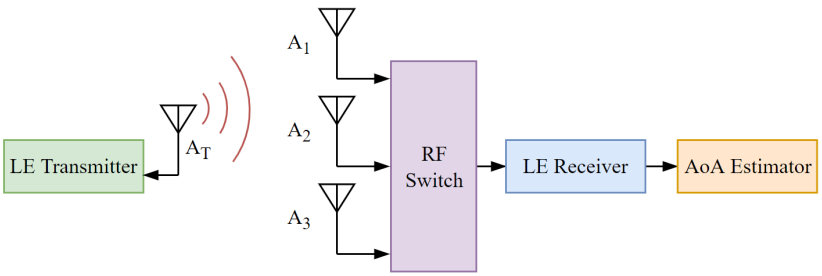

Figure 2.16: AoA estimation in Bluetooth® LE. The transmitter appends a CTE to the Link Layer packet that is estimated by the receiver through antenna switching.

should last at least 16 µs and no more than 160 µs. This results in the transmission of an unmodulated tone at the end of the packet. The receiver should expose at least 2 antennas (it is necessary to recall that AoA is inherently based on a differential measure), which are activated (i.e. switched) by means of an RF switch through a predefined pattern defined in the Bluetooth LE protocol. The CTE of a packet can be divided into three fields. The first one is the guard period and it lasts 4 µs. In this time segment, the first antenna in the pattern is switched and the Host dedicates resources to the DF. Right after the guard period, there is the reference period, in which the first antenna of the pattern is used to receive the IQ samples. Therefore, the subsequent time duration of the CTE is divided into switch slots and sample slots of equal size, that last 1 or 2 µs as specified by the Host. During the switch slot, the RF switch enables the successive antenna elements in the pattern, which are employed in the subsequent sample slot for acquiring the IQ samples. The phase shift is computed on the stored IQ streams from different antenna elements, and that phase shift is employed for the AoA estimation using the inversion formulas (2.31).

References

[1] C. A. Balanis, *Antenna Theory: Analysis and Design*. New York, NY, USA: Wiley-Interscience, 2005.

[2] H. Krim and M. Viberg, "Two decades of array signal processing research: the parametric approach," *IEEE Signal Processing Magazine*, vol. 13, no. 4, pp. 67–94, 1996.

[3] R. Schmidt, "Multiple emitter location and signal parameter estimation," *IEEE Transactions on Antennas and Propagation*, vol. 34, no. 3, pp. 276–280, March 1986.

[4] T. S. Rappaport, R. W. Heath, R. C. Daniels, and J. N. Murdock, *Millimeter wave wireless communications*, ser. Prentice Hall communications engineering and emerging technologies series. Prentice Hall, 2015.

[5] N. H. Bni Lam, "Angle of arrival estimation for low power and long range communication networks," Ph.D. dissertation, University of Antwerp, 2021.

[6] M. W. T. S. Chowdhury and M. Mastora, "Performance Analysis of MUSIC Algorithm for DOA Estimation with Varying ULA Parameters," in *2020 23rd International Conference on Computer and Information Technology (ICCIT)*, 2020, pp. 1–5.

[7] R. Roy and T. Kailath, "ESPRIT-estimation of signal parameters via rotational invariance techniques," *IEEE Transactions on Acoustics, Speech, and Signal Processing*, vol. 37, no. 7, pp. 984–995, 1989.

[8] A. Barabell, "Improving the resolution performance of eigenstructure-based direction-finding algorithms," in *ICASSP '83. IEEE International Conference on Acoustics, Speech, and Signal Processing*, vol. 8, 1983, pp. 336–339.

[9] U. M. Butt, S. A. Khan, A. Ullah, A. Khaliq, P. Reviriego, and A. Zahir, "Towards Low Latency and Resource-Efficient FPGA Implementations of the MUSIC Algorithm for Direction of Arrival Estimation," *IEEE Transactions on Circuits and Systems I: Regular Papers*, vol. 68, no. 8, pp. 3351–3362, 2021.

[10] Z. Zou, W. Hongyuan, and Y. Guowen, "An Improved MUSIC Algorithm Implemented with High-speed Parallel Optimization for FPGA," in *2006 7th International Symposium on Antennas, Propagation EM Theory*, Oct 2006, pp. 1–4.

[11] F. Wang, H.-t. Gao, L. Zhou, and Y.-x. Sun, "Hardware Implementation of MUSIC Algorithm for Airborne Digital Direction Finding System," in *2011 7th International Conference on Wireless Communications, Networking and Mobile Computing*, 2011, pp. 1–4.

[12] H. Chen, K. Chen, K. Cheng, Q. Chen, Y. Fu, and L. Li, "An Efficient Hardware Accelerator for the MUSIC Algorithm," *Electronics*, vol. 8, no. 5, 2019.

[13] Z. Li, W. Wang, R. Jiang, S. Ren, X. Wang, and C. Xue, "Hardware Acceleration of MUSIC Algorithm for Sparse Arrays and Uniform Linear Arrays," *IEEE Transactions on Circuits and Systems I: Regular Papers*, vol. 69, no. 7, pp. 2941–2954, 2022.

[14] Minseok Kim, K. Ichige, and H. Arai, "Implementation of FPGA based fast DOA estimator using unitary MUSIC algorithm," in *2003 IEEE 58th Vehicular Technology Conference. VTC 2003-Fall.*, vol. 1, Oct 2003, pp. 213–217 Vol.1.

[15] P. Boonyanant and S. Tan-a ram, "FPGA implementation of a subspace tracker based on a recursive unitary ESPRIT algorithm," in *2004 IEEE Region 10 Conference TENCON 2004.*, vol. A, 2004, pp. 547–550 Vol. 1.

[16] Y. Jung, H. Jeon, S. Lee, and Y. Jung, "Scalable ESPRIT Processor for Direction-of-Arrival Estimation of Frequency Modulated Continuous Wave Radar," *Electronics*, vol. 10, no. 6, 2021.

[17] A. Badawy, T. Khattab, D. Trinchero, T. ElFouly, and A. Mohamed, "A Simple Angle of Arrival Estimation System," in *2017 IEEE Wireless Communications and Networking Conference (WCNC)*, 2017, pp. 1–6.

[18] P.-C. Chiang, W.-J. Liao, Y.-T. Tu, and H.-C. Liu, "Implementation of direction-of-arrival estimation using Rotman lens array antenna," in *2013 International Symposium on Electromagnetic Theory*, 2013, pp. 855–858.

[19] N. BniLam, A. Aerts, D. Joosens, J. Steckel, and M. Weyn, "RSS-based AoA Estimation System for IoT Applications using Rotman Lens," in *2020 14th European Conference on Antennas and Propagation (EuCAP)*. IEEE, Mar. 2020, pp. 1–5.

[20] W. Rotman and R. Turner, "Wide-angle microwave lens for line source applications," *IEEE Transactions on Antennas and Propagation*, vol. 11, no. 6, pp. 623–632, 1963.

[21] A. Lambrecht, S. Beer, and T. Zwick, "True-time-delay beamforming with a rotman-lens for ultrawideband antenna systems," *IEEE Transactions on Antennas and Propagation*, vol. 58, no. 10, pp. 3189–3195, 2010.

[22] Z. Guo, W. Wang, X. Wang, and X. Zeng, "Hardware-Efficient Beamspace Direction-of-Arrival Estimator for Unequal-Sized Subarrays," *IEEE Transactions on Circuits and Systems II: Express Briefs*, vol. 69, no. 3, pp. 1044–1048, 2022.

[23] K.-T. Chen, W.-H. Ma, Y.-T. Hwang, and K.-Y. Chang, "A Low Complexity, High Throughput DoA Estimation Chip Design for Adaptive Beamforming," *Electronics*, vol. 9, no. 4, 2020.

[24] Z. Zhang, C. Zhou, Y. Gu, and Z. Shi, "FFT-Based DOA Estimation for Coprime MIMO Radar: A Hardware-Friendly Approach," in *2018 IEEE 23rd International Conference on Digital Signal Processing (DSP)*, 2018, pp. 1–5.

[25] I. T. Union, "Spectrum monitoring handbook," p. 674, 2011, [Online] http://handle.itu.int/11.1002/pub/80399e8b-en (visited on 2023-06-01).

[26] A. Florio and G. Avitabile, "The Correlation between Phase Interferometric Angle of Arrival Estimation Quality Degradation and Uniform Linear Array Spacing," in *2021 29th Mediterranean Conference on Control and Automation (MED)*, 2021, pp. 244–248.

[27] A. Florio, G. Avitabile, G. Coviello, J. Ma, and K. L. Man, "The Impact of Coherent Signal Reception on Interferometric Angle of Arrival Estimation," in *2020 International SoC Design Conference (ISOCC)*, 2020, pp. 167–168.

[28] N. BniLam, S. Nasser, and M. Weyn, "Angle of Arrival Estimation System for LoRa Technology based on Phase Detectors," in *2022 16th European Conference on Antennas and Propagation (EuCAP)*, 2022, pp. 1–5.

[29] *AD8302 - LF-2.7 GHz RF/IF Gain and Phase Detector*, Analog Devices Inc., 2018, rev. B.

[30] "Bluetooth SIG - Bluetooth® Core Specification 5.1," p. 2985, 2019, [Online] https://www.bluetooth.com/specifications/specs/core-specification-5-1/ (visited on 2023-06-21).

CHAPTER 3

Multiple Source I/Q Phase Interferometric AoA estimation

This chapter is based on the following publications:

- *G. Avitabile, A. Florio, and G. Coviello, "Angle of Arrival Estimation through a Full-Hardware Approach for Adaptive Beamforming," IEEE Transactions on Circuits and Systems II: Express Briefs, vol. 67, no. 12, pp. 3033–3037, 2020.*
- *A. Florio, G. Avitabile and G. Coviello, "Multiple Source Angle of Arrival Estimation Through Phase Interferometry," in IEEE Transactions on Circuits and Systems II: Express Briefs, vol. 69, no. 3, pp. 674-678, March 2022.*
- *A. Florio and G. Avitabile, "Characterization of a Multisource Angle of Arrival Estimation Technique based on Phase Interferometry," 2022 18th International Conference on Synthesis, Modeling, Analysis and Simulation Methods and Applications to Circuit Design (SMACD), Villasimius, Italy, 2022, pp. 1-4.*

This chapter describes a novel technique for AoA estimation through phase interferometry in the presence of multiple sources. The methodology is very simple and suitable for the implementation of digital hardware. The approach fully reflects the Software Defined Radio (SDR) paradigm of reconfigurability. The proposed AoA estimation technique relies on a multi-channel phase difference estimation followed by an averaging stage to refine the results. The core of the approach is a phase-difference estimation algorithm called I/Q Low-Pass Mixing (IQ LPM).

3.1 Algorithm description

In this section, first, the mathematical description of the algorithm is presented. Then, the simple case of two RF chains and one source is analyzed. Therefore, the case of q possible sources and M available channels is described.

3.1.1 Mathematical description

Consider two channels for the receiving side in the presence of a single transmitting source as a simplified scenario. Each of the channels is equipped with an RF chain in charge of amplifying, downconverting, filtering, sampling, and quantizing the received signal.

IQ LPM is inspired by the theory of I/Q incoherent demodulation. Let us consider two single-tone signals in the discrete time domain, denoted as $s_i[k],\ i = a, b$, being a, b the channel labeles. Both signals have same frequency $\omega = 2\pi f$ but different amplitudes K_a, K_b and phases, φ_a, φ_b respectively:

$$\begin{cases} s_a[k] = \mathrm{K}_a\ \cos\left(\omega k + \varphi_a\right) \\ s_b[k] = \mathrm{K}_b\ \cos\left(\omega k + \varphi_b\right) \end{cases},\ k \in \mathbb{Z} \tag{3.1}$$

By multiplying (i.e., *beating*) the two signals, we obtain:

$$s_a[k] \cdot s_b[k] = \frac{\mathrm{K}_a \cdot \mathrm{K}_b}{2}\left[\cos(2\omega k + \varphi_b + \varphi_a) + \cos(\varphi_b - \varphi_a)\right] \tag{3.2}$$

We observe that by applying a low-pass filtering stage, it is possible to obtain the phase difference $\Delta\varphi_{ab} = \varphi_b - \varphi_a$. To simplify the notation, the low-pass filtering operation is denoted as $\mathrm{LPF}\{\cdot\}$. Hence,

$$\mathrm{LPF}\{s_a[k] \cdot s_b[k]\} = \frac{\mathrm{K}_a \cdot \mathrm{K}_b}{2}\left[\cos(\Delta\varphi_{ab})\right] \tag{3.3}$$

After some trivial manipulations:

$$\Delta\varphi_{ab} = \arccos\left[\frac{2}{\mathrm{K}_a \cdot \mathrm{K}_b}\ \mathrm{LPF}\{s_a[k] \cdot s_b[k]\}\right] \tag{3.4}$$

It is known that the inverse cosine (or arccosine) function is constructed from the inverse of the restriction to $[0, \pi[$ of the cosine function. The restriction is an injective function, so, it is invertible. Hence, there is an intrinsic ambiguity in the $[0, 2\pi[$ interval:

$$\cos(x) = \cos(2\pi - x),\ \forall x \in [0, \pi[\tag{3.5}$$

that is, a single cosine value in $[0, \pi[$ corresponds ambiguously to two possible angles (i.e. two possible phase difference values). This result is visually presented in Figure 3.1. In order to unambiguously determine a point on the unit circle in a two-dimensional plane, a minimum of two distinct parameters must be specified. These parameters can be the sine and cosine values for that point. In fact, even the sign of the sine value is sufficient to determine the quadrant of the angle, along with its cosine value. If the samples are represented by signed binary strings of equal length, the Most Significant Bit (MSB) usually represents the sign of the string. Therefore, by modulating each signal with two carriers of the same frequency and a mutual phase difference of $\pi/2$ (namely, an I/Q pair), it is possible to obtain the two required pieces of information and unambiguously determine the desired phase difference value.

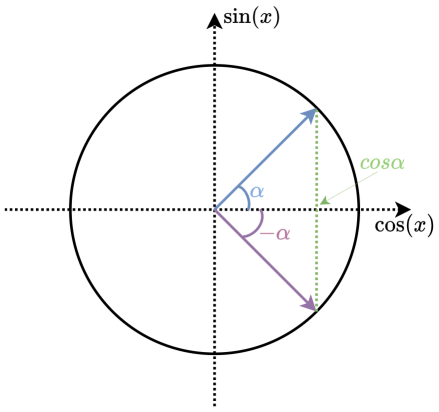

Figure 3.1: Graphical representation of the inverse cosine 2π ambiguity problem.

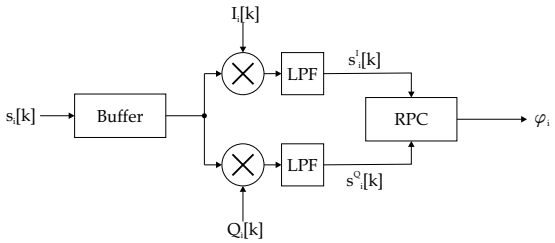

Figure 3.2: Block diagram sketching the operations performed by IQ LPM for channel i.

3.1.2 IQ LPM: the case of $q = 1$ source

The block diagram in Figure 3.2 represents the algorithm stages. The samples are first buffered and normalized. Then, each channel $s_i[k]$ is beaten with the respective I_i and Q_i samples stored in a Look-Up Table (LUT) populated previously. The output is successively fed to a digital LPF stage. The generated binary word, $s_i^I[k]$, is such that:

$$s_i^I[k] = \text{LPF}\{s_i[k] \cdot I_i[k]\} = \frac{1}{2}\cos(\hat{\varphi}_i[k]) \tag{3.6}$$

where $\hat{\varphi}_i$ is the i^{th} channel estimated phase, prior to quadrant disambiguation. Then,

$$\hat{\varphi}_i[k] = \arccos(2 \cdot s_i^I[k]) = \arccos(\xi_i[k]) \tag{3.7}$$

To solve the ambiguity (3.5), a simple quadrant decision can be implemented thanks to the Q branch MSB information, properly compensating the phase value. This compensation is performed according to the Real Phase Computer (RPC) algorithm described in Algorithm 1. Once the phase has been estimated for each channel i, it is possible to compute the phase difference $\Delta\varphi_{ij}$ as

$$\Delta\varphi_{ij} = \varphi_j - \varphi_i, \quad i \neq j \tag{3.8}$$

The approach can be extended to M possible channels. In fact, each pair of antennas can provide an estimation of the same AoA. The average value of the AoA estimations is one of the best estimators of the expected one [1]. Hence, it is possible to improve the estimation results by averaging the phase difference estimations obtained by properly-chosen pairs of RF chains.

Algorithm 1 Phase value adjustment algorithm, with $\varphi_i[k]$ the estimated phase value for channel i at discrete time instant $[k]$

Require: $\xi_i[k] = 2 \cdot s_i^I[k] \in \mathbb{R},\ \psi_i[k] = \mathrm{MSB}(s_i^Q[k])$
  if $\psi_i(k) = 0$ **then**
    $\varphi_i[k] \leftarrow \arccos(\xi_i[k])$
  end if
  if $\psi_i(k) = 1$ **then**
    $\varphi_i[k] \leftarrow 2\pi - \arccos(\xi_i[k])$
  end if
  return $\varphi_i[k]$

3.1.3 M-IQ LPM: the case of q sources

Assume that each of the q sources operates in a spectrum slice, $B(p),\ p = 1, \cdots, q$, and that each device operates on a different center-band carrier, $f_c(p)$, (namely it doesn't exist a time instant in which two devices employ the same carrier to communicate). To separate each spectrum slice, let us suppose to introduce guardbands, GB.

The proposed technique assumes the filtering of each spectrum slice, $B(p)$, estimating the AoA, $\vartheta(p)$, through IQ LPM, and proceeding to the next slice, realizing spectral polling. As soon as this operation is rapidly completed, the angular position of the q devices can be retrieved in less time than classical array processing techniques based on subspace separation methods. As previously described, each source is characterized by a spectral occupation $2 * \mathrm{GB} + \mathrm{B}(p),\ p = \{1, \cdots, q\}$. Hence the total bandwidth to allocate for the system is

$$\mathrm{TB} = \sum_{p=1}^{q} (2 * \mathrm{GB} + \mathrm{B(p)}) = 2q * \mathrm{GB} + \sum_{p=1}^{q} \mathrm{B(p)} \tag{3.9}$$

For sake of simplicity, let us suppose $B(p) = B\ \forall p$, hence

$$\mathrm{TB} = q * (2\,\mathrm{GB} + \mathrm{B}) \tag{3.10}$$

Suppose to define a bandpass digital filter whose passband (PB) frequencies $f_p(p)$ and stopband (SB) frequencies $f_s(i)$ are respectively

$$\begin{cases} f_p(p) & = \{f_c(p) - \mathrm{B}/2; f_c(p) + \mathrm{B}/2\} \\ f_s(p) & = \{f_c(p) - \mathrm{B}/2 - \mathrm{GB}; f_c(p) + \mathrm{B}/2 + \mathrm{GB}\} \end{cases} \tag{3.11}$$

Namely, changing the digital filter parameters consists of just updating the filter coefficients. Once those different coefficients have been stored in a LUT, it is simple to recall the ones necessary to filter the needed channel and make the spectral polling very fast. Hence, the filtering stage allows operating on a single source at a time, obtaining the phase difference, $\Delta\varphi_{ij}(p)$, from channels i, j and the source p and then, after changing the filter coefficients, repeat the same procedure for the successive source, until the overall bandwidth allocated to the system TB is analyzed. If the phase estimation stage is preceded by an envelope tracker, it is possible to skip the spectrum slice if the revealed power is below a given threshold, and so, speed up the spectral polling.

From a delay analysis point of view, each filtering stage impacts with a delay that is a function of the number of filter taps, N. Also, in IQ LPM and M-IQ LPM, the most time-consuming tasks are associated with the filtering stages, since the other operations are just multiplications, algebraic sums, and signal multiplexings. Therefore, minimizing the impact on the estimation delay calls for the optimization of the number of taps required for the filtering stages.

3.2 Simulation results

In this section, we evaluate the influence of some parameters characterizing the receiver front-end on the accuracy of IQ LPM and M-IQ LPM. The following set of simulations considers only one source to be present. In the last simulation, the impact of the number of sources is taken into account.

3.2.1 Impact of additive noise

The presence of noise can determine an accuracy loss. Suppose the noise is Additive White Gaussian Noise (AWGN). Given that the receiver is typically the most vulnerable component in a transmitter-receiver system, it is analyzed the case of noise source on the receiver side. Each of the channels is affected by noise that is uncorrelated to the others.
Let us consider two sampled CW signals, $s_a[k], s_b[k]$, with same frequency $f = 2$ GHz, and random phases, φ_a, φ_b, respectively, with

$$\varphi_i \sim \mathcal{U}(0, 2\pi), \; i = a, b \tag{3.12}$$

Each signal is sampled with $f_s = 40$ GS/s, and quantized with ideally infinite precision. These settings were chosen to unbias the results from the sampling time and quantization influence, later investigated. Then, thanks to the `awgn` function implemented on MATLAB, the levels of noise were increased by lowering the target SNR value. The SNR was considered to be ranging from +80 down to 0 dB. For each SNR, there were extracted $n_a = 20$ values for the random variable φ_a and $n_b = 20$ values for φ_b, independently one from the other, so 400 possible phase estimations were generated for each SNR value. Then, the phase average absolute error (AAE) was computed and its standard deviation was evaluated. As an example, 5 possible realizations of the random process associated with the AAE are depicted in Figure 3.3. By applying the curve fitting to each AAE realization, a negative exponential function of the increasing SNR is obtained. Indeed, by calling ϵ_{SNR} the AAE committed with an SNR, a possible synthetic empirical law to model the artifacts introduced is

$$\epsilon_{\mathrm{SNR}} = \alpha \, \exp\left(-\beta \cdot \mathrm{SNR}\right) \tag{3.13}$$

where α, β are the model parameters. In this case, it was found

$$\begin{cases} \alpha \in [0.53, 0.69] \\ \beta \in [0.06, 0.08] \end{cases} \tag{3.14}$$

The model found for the estimated phase difference error can be associated with the AoA estimation error. Recalling the (2.6), the absolute AoA estimation error $\epsilon_{\vartheta,\mathrm{SNR}}$

is:

$$\epsilon_{\vartheta,\mathrm{SNR}} = \left|\sin^{-1}\left(\Delta\varphi\lambda_d\right) - \sin^{-1}\left(\left[\Delta\varphi \pm \epsilon_{\mathrm{SNR}}\right]\lambda_d\right)\right| \tag{3.15}$$

with $\lambda_d = \lambda/2\pi d$. The behavior is still a decreasing exponential function of the increasing SNR. Therefore, the estimation accuracy strongly depends on the SNR on the receiver side.

3.2.2 Impact of Over Sampling Ratio

Another parameter that may influence M-IQ LPM performance is the Over Sampling Ratio (OSR). For a CW signal with frequency f, the OSR with respect to the Nyquist sampling frequency f_s is defined as

$$\mathrm{OSR} = \frac{f_s}{2f} \tag{3.16}$$

The OSR is directly proportional to the number of samples stored per period, and consequently, to the number of samples that must be processed. As such, it is essential to maintain the OSR at the minimum value that balances the desired error level with a manageable quantity of samples. To evaluate the OSR impact, a simulation similar to those described in Section 3.2.1 was performed. The OSR was spanned in the range $[1, 30]$ with 0.5 steps, thus changing f_s and leaving all other parameters as in the previously described simulation setup. Successively, for each estimation it was computed the AAE, obtaining what is depicted in Figure 3.4a. The case of OSR = 1 led to larger errors when compared to the other cases. Hence the interval $[1, 1.5]$ was studied with a finer step, set to 0.01. Results are in Figure 3.4b. We deduce the OSR does not have a significant impact on the phase (and thus, AoA) estimation made through M-IQ LPM, as soon as the sampling frequency is chosen to be strictly greater than Nyquist's.

3.2.3 Impact of quantization bits

Since the M-IQ LPM accuracy is directly related to the amplitude value of the DC component generated after low-pass filtering of a mixer, it is interesting to evaluate how the ADC stage impacts the overall estimation. Suppose the ADC stage takes place after the downconversion from the RF to the IF that keeps unchanged the phase

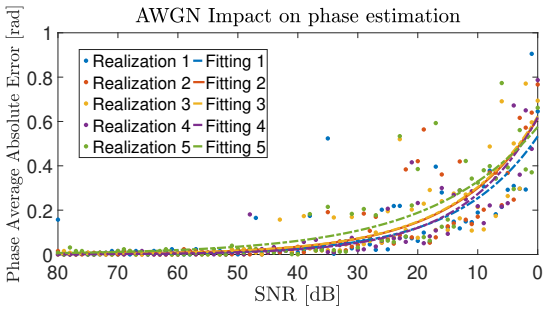

Figure 3.3: Simulation realizations and exponential fitting of the AWGN impact analysis on phase estimation accuracy.

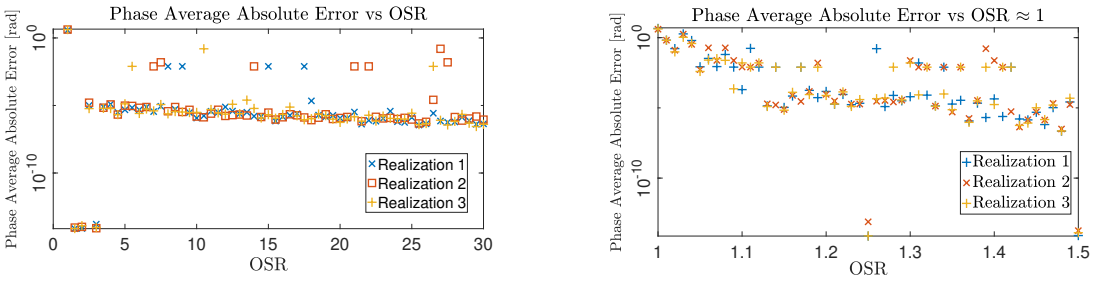

Figure 3.4: (a) Dependancy of the AAE on phase estimation from the OSR (b) Detail of the AAE phase estimation error around OSR=1. Both graphs are in log-scale to highlight the behaviors.

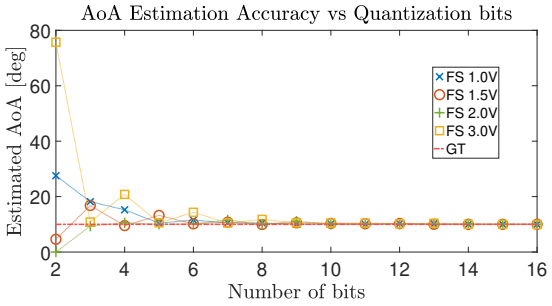

Figure 3.5: Dependency of the estimation accuracy (GT AoA $\vartheta = 10$ deg) from the quantization bits for each signal sample and from the representation scale employed.

value. This artifact was analyzed and characterized by setting up a MATLAB simulation in which two signals are quantized with a different number of bits, modeling the two down-converted signals at Intermediate Frequency (IF) $f_{IF} = 1$ MHz, respectively from two antenna elements of a ULA. The two signals' phase difference corresponds to an AoA of 10 degrees. Assume that each signal has an amplitude of 1 V and a full scale (FS) representation value in the $\{1, 1.5, 2, 3\}$ V range. Under these settings, it is obtained what is in Figure 3.5. The estimation accuracy strongly depends on the quantization scale of the downconverted signals, so the higher the acquisition accuracy, the better the error obtained on the AoA estimation. However, considering a number of bits greater than 8, for every considered FS, the AoA estimation converges to the GT value.

3.2.4 Impact of the number of sources

To compare the accuracy depending on the number of sources for M-IQ LPM, the results were compared to the ones obtained with ESPRIT and RMUSIC algorithms (see Chapter 2). Like all subspace-separation methods, the number of sources ESPRIT and RMUSIC can identify depends on the number of antenna array elements. For a ULA of M antennas, ESPRIT can estimate up to $M - 2$ uncorrelated sources while RMUSIC can estimate up to $M - 1$ uncorrelated sources [2]. Conversely, the M-IQ LPM has theoretically no upper boundary on the number of possible source positions to estimate.

In the simulation, it was considered a ULA with $M = 4$ array elements. For sim-

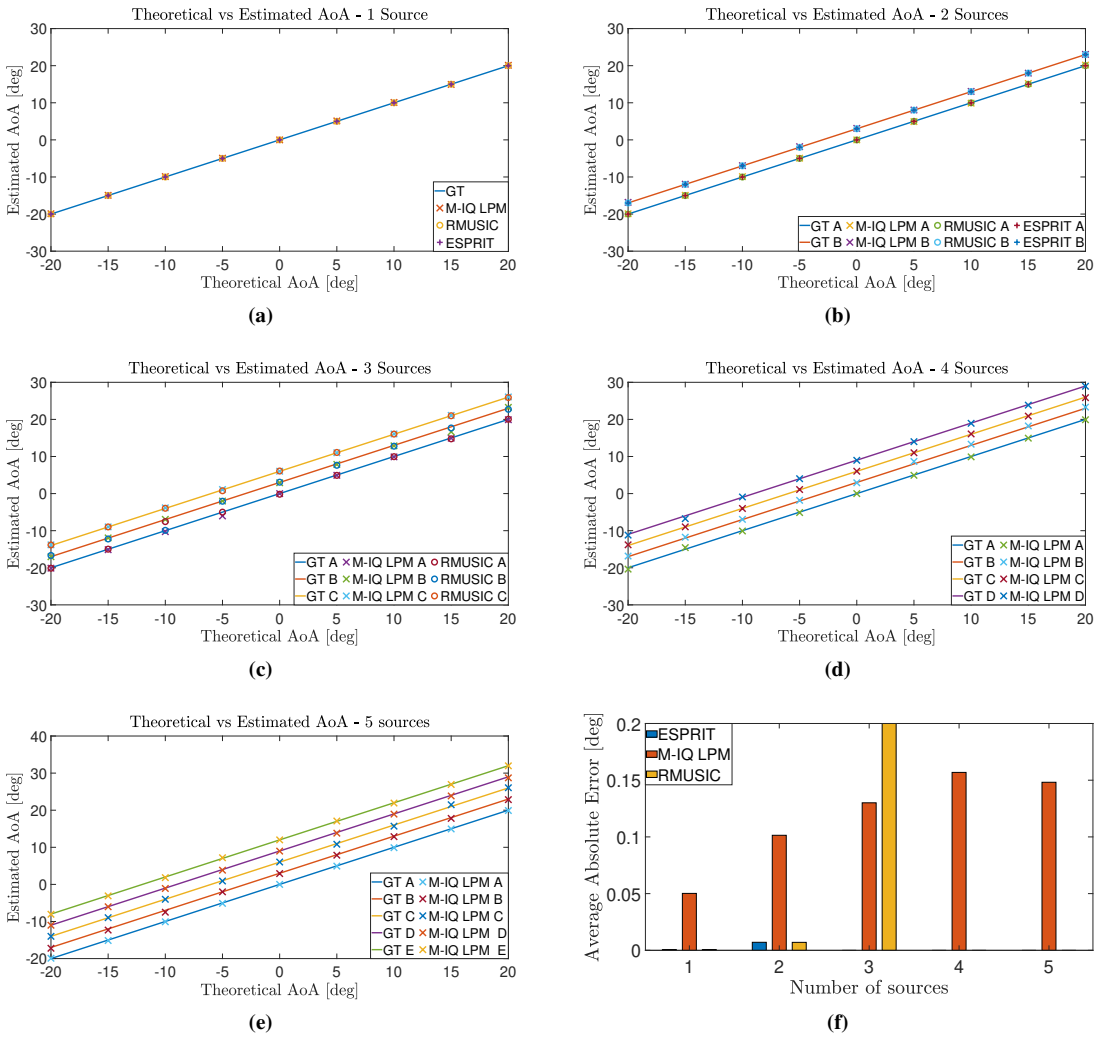

Figure 3.6: Results of the AoA estimation made through M-IQ LPM, ESPRIT and RMUSIC algorithms, compared to the GT AoAs in the case of (a) one source, (b) two (c) three (d) four (e) five sources. In (f) the AAEs for the three algorithms.

ulation labeled with j there were constructed j sources transmitting from j different AoAs. This latter determined the phase shift to impose on the signals for each antenna array element. The radio medium acts as a signal adder, so on each array element, we see the sum of j different uncorrelated sources. It was considered an IF $f_{\text{IF}} = 5$ MHz, a B of 100 kHz for each source, and a GB/B ratio of 0.6. The OSR was set to 10. Also, the SNR was considered to be high enough to neglect noise. The stop-band attenuation for the M-IQ LPM was -60 dB. The results are shown in Figure 3.6. For the simulation, the MATLAB implementations of ESPRIT and RMUSIC were employed, `espritdoa` and `rootmusicdoa` respectively. Note that in Figures 3.6c-3.6d-3.6e ESPRIT values are missing since $N_{\text{sources}} > M - 2$ while in Figure 3.6d-3.6e RMUSIC estimation is missing because $N_{\text{sources}} > M - 1$.
Figure 3.6f reports some statistical indexes of the AAEs. The AAE is computed on the AAEs for each device, while the standard deviation is the standard deviation of

the AAEs themselves. M-IQ LPM exhibits a higher variance and absolute error than the other algorithms, even on a few number sources. However, the AAE experiences a log-like growth with the number of sources, while the other algorithms experience a stop derived from the maximum number of possible sources that it is possible to reveal.

	M-IQ LPM [deg]		**RMUSIC [deg]**		**ESPRIT [deg]**	
	avg	std	avg	std	avg	std
1 Device	0.05	0.00	0.001	0.00	0.001	0.00
2 Devices	0.10	0.01	0.02	0.01	0.01	0.01
3 Devices	0.13	0.05	0.23	0.01	N.A.	
4 Devices	0.16	0.07	N.A.		N.A.	
5 Devices	0.15	0.07	N.A.		N.A.	

Table 3.1: AAEs and std deviation results from the simulation campaign.

3.3 Real-scenario experimental results

After the simulation campaign, the approach was validated through experiments performed at different distances. In the first experiment, a single source was considered. Hence, the presence of multiple sources was analyzed. The objective was to prove both the estimation accuracy and the computation time.

3.3.1 Experiments setup

The experimental setup is composed of a receiving and a transmitting section sharing LoS to consider the multipath effect to be less influential. The campaign was first performed for the single source case and then expanded to evaluate the multisource scenario.

The basic transmission stage was composed by an ADF4355 Evaluation Board by Analog Devices [3] connected to a custom-designed patch antenna element (see Appendix A.1). The ADF4355 generated a CW tone with a $P_{RF} = +5$ dBm. In the single-source scenario, only one transmission chain was employed. In the multisource experiment, there were employed N separate transmission chains, with N being the number of sources to localize in the experiment, composed as described for the single source case. The transmission frequency for the single source was set to $f_{RF} = 3.35$ GHz while for the multisource experiment, $f_{RF}(q) = [3.30 + 0.01\,(q-1)]$ GHz, $q = \{1, 2, \cdots, N\}$.

The receiver side was composed of a custom-designed 4-element microstrip ULA each of its antenna elements connected to the custom-designed RF front end. The ULA and the RF front-end are described in Appendix A.1 and A.2, respectively. The signal was downconverted to the intermediate frequency $f_{IF} = 200$ MHz for the first experiment and $f_{IF}(q) = [150 + 10\,(q-1)]$ MHz for the second experiment. The sampling frequency was $f_s = 5$ GS/s in the single source case and $f_s = 10$ GS/s rate for the multiple source case.

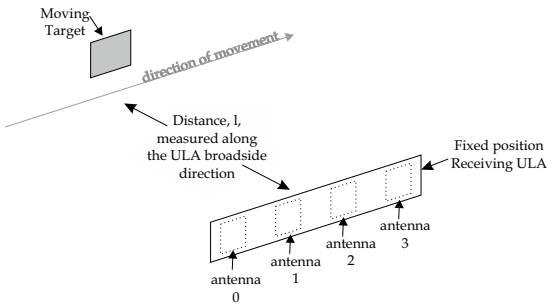

Figure 3.7: Experiment scenario in the case of a single source.

The samples were stored and fed to a MATLAB implementation of the proposed algorithm. For the comparison, the MATLAB implementations of the MUSIC algorithm in the single source case, and ESPRIT and RMUSIC algorithms for the multiple source scenario were used. All three algorithms are deployed through the Phased Arrays Toolbox^{TM}.

The experiment consisted in moving the transmitters in the direction perpendicular to the broadside axis of the receiving array with fixed steps, starting from the array center. The fixed steps were measured using the center as a reference. Figure 3.7 depicts the described scenario for the case of a single source for simplicity. In the case of multiple sources, all of them were moved together.

Each experiment was preceded by a calibration phase in which each one of the devices was placed in the center broadside array position and the following measurements were unbiased from the measured phase difference, arising from possible mismatches. In fact, in the array center position, in far-field condition, we can assume the received wave to be plane and the relative phase shift among the array elements to be null.

3.3.2 Single source

The experiment was performed at two different broadside distances, 1.6 m and 2.2 m. The output of the AoA estimation for the two distances are plotted in Figures 3.8a-b. The two estimations are compared with the theoretical values. In Table 3.2 the maximum error committed by the IQ LPM algorithm was computed as the maximum among the two datasets coming from the two distances. The same was done for MUSIC. The average error was computed for both algorithms mixing the AoA absolute estimation errors coming from the experiments performed at the two distances.

Distance	Max Error [deg]	Avg Error [deg]
IQ LPM	1.2961	0.3409
MUSIC	1.4484	0.4277

Table 3.2: Statistical metrics for the absolute error committed on the AoA estimation by the IQ LPM algorithm and the MUSIC algorithm.

To empirically compare the computational complexity, the time needed for performing the computations was measured through the MATLAB functions `tic` and

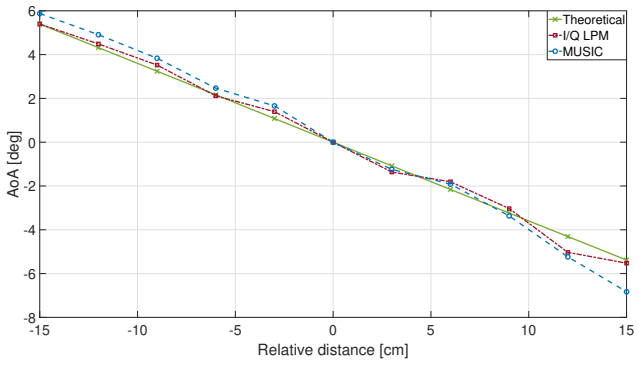

(a)

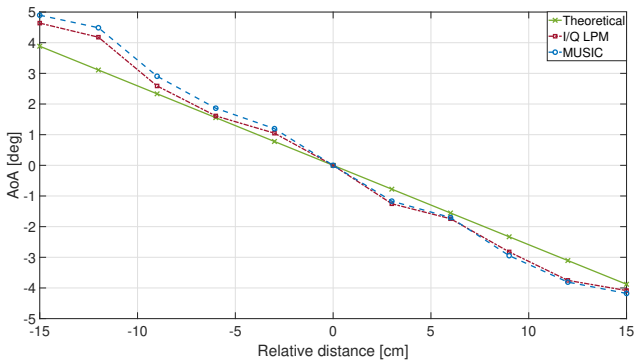

(b)

Figure 3.8: IQ LPM vs MUSIC algorithm AoA estimation compared to the theoretical ones at a distance of (a) 1.6 m and (b) 2.2 m. The positioning is relative to the array center position.

`toc`. To better unbias the execution time measurement from artifacts, the measurements were performed on the same machine only on the portions of the code involving computations, so don't take into account the data path delays (which are difficult to model). To obtain a significant benchmark of the execution time, each script was run 10 times on the same experiment samples, and the average execution time was taken to be the execution time for the specific algorithm on the given experiment samples. In Table 3.3 there are summarized the average and the maximum execution times for both algorithms. Specifically, since the execution time of both algorithms does not depend on the distance, the maximum execution time was computed as the maximum time over all the available time samples and the average execution time as the average over all the available time samples. As expected, the execution time associated with

Algorithm	Avg Exec time [s]	Max Exec time [s]
IQ LPM	0.1081	0.1572
MUSIC	0.9015	0.9969

Table 3.3: Statistical metrics for the execution times needed for the pure computation program portion of the IQ LPM algorithm and the MUSIC algorithm implemented on MATLAB.

the MUSIC algorithm is much higher ($+530\%$ in the best case) than the IQ LPM. Nevertheless, the estimation errors are very similar.

3.3.3 Multiple sources

In the first measurement campaign (Exp #1) two devices ($q = \{1, 2\}$) were placed at a broadside distance $l = 2.6$ m. First, the Ground Truth (GT) AoAs were computed for each measured position and each device. Then, the acquired samples were fed to the algorithms. The results of the estimation are shown in Figure 3.9a.

The second measurement campaign (Exp #2) was performed in the presence of three devices ($q = \{1, 2, 3\}$) at a broadside distance $l = 2.95$ m. Note that, since ESPRIT can estimate up to $M - 2$ incoherent sources, being M the number of array elements, the estimation made by this algorithm was not considered in the outcomes of the experiments. The results are reported in Figure 3.9b.

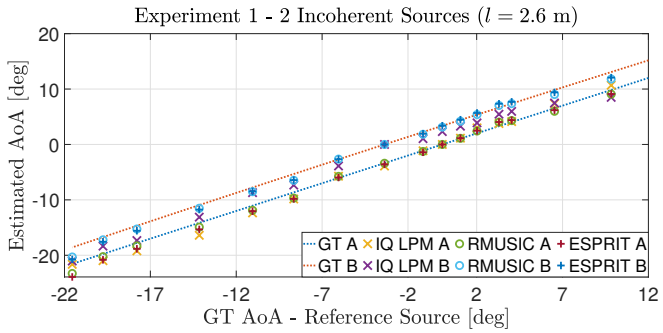

(a)

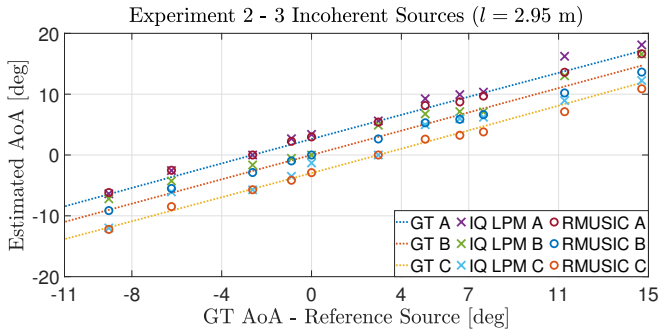

(b)

Figure 3.9: M-IQ LPM experimental results (a) 2 sources at a broadside distance of 2.6 m and (b) 3 sources at a broadside distance of 2.95 m. Note that, in the last experiment, ESPRIT data were not available.

The average absolute error was chosen as a metric for the comparison of the obtained results, using the following procedure. For the measurement campaign j, at broadside distance l, there were acquired p samples. So, the average absolute error $\epsilon_k(j, l)$ obtained with the algorithm k was computed as

$$\epsilon_k = \frac{1}{Q} \sum_q \left[\frac{1}{|B(l)|} \sum_i^{|B(j,l)|} \left| \tilde{\vartheta}_{i,k} - \vartheta_i \right| \right] \tag{3.17}$$

where $Q = \max_{(j,l)} q$, $|B(j, l)|$ is the number of spectrum slices, and $\vartheta_i(j, l)$ is such that

$$\vartheta_i(j, l) = \arctan\left(\frac{x_j(i)}{l}\right) \cdot \frac{180}{\pi} \tag{3.18}$$

Note that each $\tilde{\vartheta}_{i,k}$,$\vartheta_{i,k}$, Q and consequently ϵ_k is related to the trial (j, l) (the dependency was omitted in the (3.17) for the expression to be compact). The results obtained with the proposed metric are shown in Table 3.4. The considered metric shows that the

	I/Q LPM [deg]		**RMUSIC [deg]**		**ESPRIT [deg]**	
	avg	std	avg	std	avg	std
Exp #1	1.31	0.98	1.29	0.93	1.30	0.82
Exp #2	1.03	0.72	0.59	0.52	N.A.	

Table 3.4: Statistics on the absolute estimation errors achieved by the three algorithms.

errors are slightly higher when compared to those obtained using the other considered algorithms. However, the computational complexity impact is sensibly lower.

3.4 Conclusions

This chapter introduced a novel technique for estimating the AoA through phase interferometry, also in the presence of multiple incoherent sources. The proposed approach produced accurate results with low complexity, thus being eligible for the implementation of digital hardware.
A simulation campaign was designed to evaluate the impact of some sources of artifacts on received signals, such as noise, OSR, and quantization. The results showed that AWGN has the strongest impact on the distortion of the estimation. Also, a low number of quantization bits leads to a loss of accuracy. OSR was demonstrated to have a low impact. By considering an increasing number of sources, the AAE slightly increases, but at a lower rate with respect to the other considered algorithms.
The real-world experimental campaign demonstrated how the obtained error metrics are similar to those of the algorithms from the classical array signal processing literature but with sensibly lower computational complexity.

References

[1] W. K. Härdle, S. Klinke, and B. Röonz, *Introduction to Statistics*. Springer, 2015.

[2] H. Krim and M. Viberg, "Two decades of array signal processing research: the parametric approach," *IEEE Signal Processing Magazine*, vol. 13, no. 4, pp. 67–94, 1996.

[3] "ADF4355 Datasheet and Product Info, Analog Devices," (Last accessed on 05-Mar-2023). [Online]. Available: https://www.analog.com/en/products/adf4535.html

CHAPTER 4

Phase integrity issues and compensation for AoA estimation

This chapter is based on the publication: A. Florio, G. Avitabile, and G. Coviello, "A Linear Technique for Artifacts Correction and Compensation in Phase Interferometric Angle of Arrival Estimation", Sensors, vol. 22, no. 4, p. 1427, Feb. 2022, doi: 10.3390/s22041427.

In phase-critical approaches like AoA estimation through phase interferometry, even small errors in the phase estimation can hugely affect the overall system performance. Recall from (2.31) the AoA estimation $\tilde{\vartheta}_{ij}$ of the angle ϑ through phase interferometry on a pair ij of ULA elements is

$$\tilde{\vartheta}_{ij} = \arcsin\left(\frac{\lambda\,\Delta\varphi_{ij}(\vartheta)}{2\pi\,d\,(i-j)}\right) \tag{4.1}$$

Suppose a small additive phase estimation error δ_{ij}. The AoA ϑ estimation $\hat{\vartheta}_{ij}$ becomes

$$\hat{\vartheta}_{ij} = \arcsin\left(\frac{\lambda\,(\Delta\varphi_{ij}(\vartheta)+\delta_{ij})}{2\pi\,d\,(i-j)}\right) \tag{4.2}$$

Having $d = \psi\,\lambda$, and since $\psi < 1$ for minimizing side-lobe effects [1], we can rewrite the (4.2) as

$$\hat{\vartheta}_{ij} = \arcsin\left(\frac{\Delta\varphi_{ij}(\vartheta)}{2\pi\,\psi\,(i-j)} + \frac{\delta_{ij}}{2\pi\,\psi\,(i-j)}\right) = \tilde{\vartheta}_{ij} + err_{ij}(\vartheta) \tag{4.3}$$

In this chapter, a linear technique is proposed to minimize the error term $err_{ij}(\vartheta)$ to correct the estimation reaching the optimal value, represented by the theoretical AoA

values. There are many contributions to phase error generation. The proposed technique embeds in one single complex-valued matrix, called the α-matrix the amplitude and the phase of sinusoidal signals to be employed for the compensation of those effects. The frequency of those signals is the same as the system center frequency.

The main contributions offered by this study are the following:

- The effectiveness of an artifacts linear compensation technique for phase interferometric AoA estimation is mathematically introduced, and experimentally proved with a measurement campaign.
- The technique embeds in one single computation all the possible mismatches due to systematic errors and a first-order (linear) approximation of the mutual coupling effects acting on the antenna array that can damage the integrity of the phase information.
- Once the matrix has been computed, its values remain valid for the employed hardware and setup. Moreover, since the approach is linear, it is simple and fast to be implemented.
- Given the generality of the assumptions and the description, the technique can be implemented either in digital form by complex-number signal processing, or in the analog domain by means of Variable Gain Amplifiers (VGA) and phase shifters networks.

The rest of the chapter is organized as follows. In Section 4.1 the possible sources of error in an AoA estimation system based on phase interferometry are presented and discussed in detail. Section 4.2 discusses the theory behind the proposed error compensation technique. In Section 4.3 the experimental results of two AoA measurement campaigns are presented. The experimental campaign was conducted in an indoor environment. First, the AoA estimation results in the absence of the compensation technique are presented and compared with the ones obtained by applying the technique. Also, an experimental evaluation of the coherence time of the computed coefficients and the compensation repeatability is provided.

4.1 Problem description

To keep the forthcoming discussion as general as possible, in this chapter, it is assumed that each antenna of the array employed for the AoA estimation is connected to a separate RF front-end, which is in charge of amplifying, down-converting, and filtering the received signal. Figure 4.1 shows a block diagram of the reference system. It is further supposed each block in one RF chain (i.e. amplifiers, mixers, filters) is nominally identical to the other chains. This choice is made because depending on the component quality and technology, the experimental results, and thus the sources and entity of artifacts can be very different from the others.
However, attention should be put on two inevitable issues: the artifacts in building the interconnections of those discrete elements and the mutual coupling of the antenna array elements. The first problem is modeled as a systematic error generated by signal path length mismatches. The second issue is not a systematic error by its very definition, but in the proposed model it is approximated as a systematic one, capturing what happens in a given position and trying to extend it to the others.

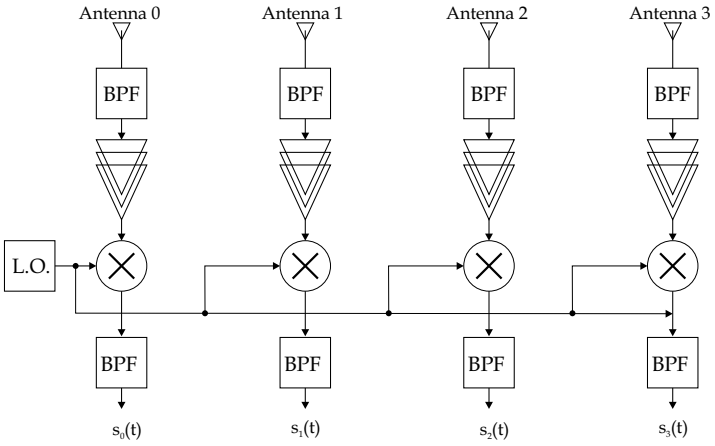

Figure 4.1: Block diagram depicting a 4-element ULA connected to four RF chains with basic blocks for the amplification, down-conversion and band-pass filtering of the received signal, prior to the AoA estimation.

4.1.1 Phase corruption due to different length of signal paths

The different cable lengths and/or signal paths on the PCB interconnections introduce a phase error. In fact, it is important to remark that at higher frequencies even small length mismatches impact the phase of the traveling signals. Those length mismatches can occur because of design errors or realization process tolerances. In the cabling case, it is caused by choosing different lengths. Let us imagine two identical lines of length l in which a signal travels, with signal frequency λ. By considering two realizations of the lines l_1 and l_2, where l_2 is affected by a mismatch, we see how $l_2 = l_1 + \Delta l$, hence the line l_2 introduces a delay on the propagation of the signal:

$$\tau \approx \sqrt{\epsilon} \cdot \frac{\Delta l}{c} \tag{4.4}$$

with ϵ being the effective dielectric constant of the propagating medium. Remembering that a time delay τ corresponds to a phase shift of $2\pi f \tau$, the phase error introduced by the lengths mismatch $err_{\Delta l}$ is

$$err_{\Delta l} \approx 2\pi f \sqrt{\epsilon} \cdot \frac{\Delta l}{c} \tag{4.5}$$

Therefore, a length mismatch introduces a systematic error in the phase estimation that linearly increases with the magnitude of the path length differences.

4.1.2 Phase corruption due to the mutual coupling of the antenna array elements

The setup of an AoA estimation system is based on an array of antennas. Microstrip patch antenna arrays are very popular in telecommunication systems, offering a good trade-off between fabrication costs and radiation efficiency. However, this implementation also brings some contributions to the estimation errors due to the mutual coupling between the array elements.
Let us consider an array of microstrip patch antennas with spacing d. For the sake of simplicity, we can consider the case of a ULA. According to what is described in [1],

even choosing different alignments for the array elements leads to different mutual coupling decay speeds. In fact, a horizontal arrangement leads to higher decays than the vertical one.
It is well known in the literature that mutual coupling is due to the near fields that exist along the air-dielectric interface [2]. If we call ρ the radial coordinate of the radiated field from the equivalent current element J, there are four possible field contributions [1]:

- Space waves, with ρ^{-1} asymptotic radial decay
- High order waves, with ρ^{-2} decay
- Surface waves, with $\rho^{-0.5}$ decay
- Leaky waves, with $e^{-\lambda\rho} \cdot \rho^{-0.5}$ decay

From the infinite and infinitesimals analysis, on small distances ($\rho \to 0$, i.e. $\rho \ll \lambda$), the surface and leaky waves are dominated by space and higher-order waves. Hence, the two former dominate on larger spacing, i.e. on large-size arrays their contribution cannot be supposed to be negligible.

Surface waves always exist and have cutoff frequency $f_c = 0$ [3]. However, their magnitude depends on the substrate thickness [2]. The surface wave couples with the feeding TEM mode as soon as the frequency increases. The lowest mode that can be coupled is the TM_0, then the TE_1, TM_2, ... surface modes [2]. The cutoff frequencies are [2]:

$$f_c(n) = \frac{nc}{4h\sqrt{\epsilon_r - 1}}, \quad n = 0, 1, 2, \cdots \tag{4.6}$$

for a substrate with thickness h and relative dielectric constant ϵ_r, being c the speed of light and n the coupled surface mode index. For thin substrate the contribution is negligible. However, since thicker and low-density substrates are usually chosen to increase the bandwidth and the gain of a microstrip antenna [1], the surface wave contribution may be significant.

Lui et al. in [4] propose a taxonomy on the mutual coupling compensation techniques for antenna arrays in transmitting and receiving modes. Although some techniques rely on the reuse of the impedance or scattering matrix computed with the array in transmitting mode also in receiving mode, this is not correct for several reasons. The main one is also stated by *Craye et al.* in [5], whose manuscript discusses the possibility of modeling an N-element array using its N-port scattering matrix. The elements of the scattering matrix $s_{ij} \in \mathbf{C}$ having $i, j \in \{0, \cdots, N-1\}, i \neq j$ can be seen as coupling coefficients only in the particular condition of single mode antennas, i.e. antennas in which the current distribution can be considered constant within a multiplying factor. Hence, this is not the case for patch antenna elements. Following the taxonomy proposed in [4], the main techniques for mutual coupling compensation are the Conventional Mutual Impedance Method (CMIM), the Receiving Mutual Impedance Method (RMIM), the Full-wave electromagnetic analysis, and the calibration techniques, sometimes supported by full-wave techniques. In the CMIM the impedance matrix is computed when the array is in transmitting mode with all the array elements in open circuit except the antenna element for which the coupling is evaluated. There are different problems with this approach. First, also the antennas

in open circuit radiate due to induced currents. Second, the antennas are normally connected to a load, and not open-circuited. Third, as already stated, the impedance matrix for an array in receiving mode is different from the transmitting one due to the different coupling paths and mechanisms. For instance, *Chen et al.* in [6] point out how another source of the mutual coupling between the antenna array elements is due to the reflected wave generated by a highly unmatched antenna element, which determines a performance degradation in MIMO applications. RMIM technique solves some of the CMIM issues [7]. First, the mutual impedance matrix is computed in the condition of receiving a plane wave from a known source, having all the array elements terminated on a given load. However, the main hypothesis is the uniform distribution of currents on the array elements (single-mode antennas). Nevertheless, results proved that RMIM significantly improves the AoA estimation performance on closely spaced arrays [8]. In full-wave methods, Method-of-Moments (MoM) or Finite-Element Method (FEM) simulation techniques are employed to characterize the coupling, at the cost of a high computational power required for the simulations themselves. Last, in calibration techniques, matrices are computed to capture the displacement between the expected quantities and the measured ones, and employed for the compensation. The proposed technique belongs to this latter category. The only cost is related to the storage of LUTs containing the compensation values.

Other ways to compensate for mutual coupling rely on the design of specific electromagnetic structures. For instance, *Vishvaksenan et al.* in [9] propose a compact parallel coupled line structure as an electromagnetic bandgap to limit mutual coupling also on closely spaced patch antenna array elements (Figure 4.2). The experimental results show how on a 0.07λ spacing the structure is capable of mitigating the mutual coupling of 26.2 dB. However, in this way, it is necessary to deploy a new array structure, so this technique cannot be employed for existing designs.

4.2 Mathematical description of the compensation technique

In order to simplify the proposed model, we consider a cluster of three antennas involved in the compensation procedure. This hypothesis does not impact the compensation effects on systematic errors, such as path length mismatches. As regards the

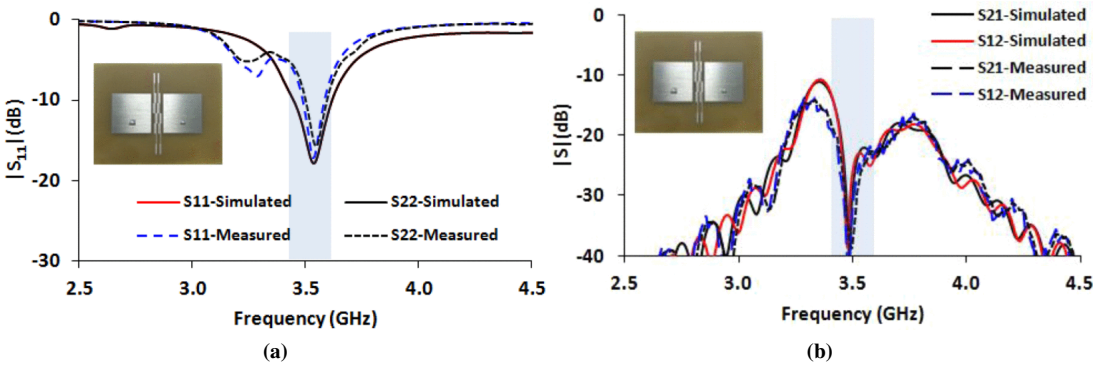

Figure 4.2: Analysis of the electromagnetic bandgap structure proposed by *Vishvaksenan et al.* in [9]: (a) matching and (b) mutual coupling in the band of interest. ©2017, IEEE.

antenna mutual coupling, the hypothesis is consistent with the rapid decay of mutual interactions, i.e. not adjacent elements interaction can be considered negligible.
From a general point of view, in the proposed model we consider two types of ports, the electrical and the radiative ones (Figure 4.3a). The electrical ports are the physically accessible ports of the system (i.e. the ones from which the signal can be connected to a signal processor or a measurement unit). The radiative ports are defined as the equivalent ports in the radiative plane, i.e. the ports on which the incident waves impinge the ULA in receiving mode. For a N-elements ULA, we can so identify N radiative ports and N electrical ports.
For the sake of simplicity it is considered a CW signal to impinge the array as a plane wave of frequency f. The equivalent voltage signal we measure at each electrical port of impedance Z_0 is represented by the phasor $\tilde{V}_i,\ i = 1, 2, 3$:

$$\tilde{V}_i = |\tilde{V}_i|\, e^{j2\pi ft}\, e^{j\angle\tilde{V}_i} \in \mathbb{C} \tag{4.7}$$

where $|\tilde{V}_i|$ is the amplitude and $\angle\tilde{V}_i$ is the phase of the measured signal at frequency f.
Analogously, the incident power wave to the radiative port i has an equivalent voltage represented by the phasor V_i.

We describe the mutual coupling phenomena by means of a function $c_{ij}(\cdot) \in \mathbb{C}$, i.e. the coupling function. This function associates the coupling source j and the coupled element i, modeling the coupling between radiative and electrical ports. The voltage signal at the i-th electrical port can be approximated as the composition of the contributions coming from the i-th antenna element and all the other contributions due to the coupling with the other two antennas, so that:

$$\tilde{V}_i = \sum_{j=1}^{3} c_{ij}(V_j), \quad j = 1, 2, 3 \tag{4.8}$$

In this model, the coupling function is a linear complex-valued map $c_{ij} : \mathbb{C} \to \mathbb{C}$ such that

$$c_{ij} : x \mapsto \alpha_{ij} x, \quad \alpha_{ij} \in \mathbb{C} \tag{4.9}$$

Hence, the (4.8) can be rewritten as

$$\tilde{V}_i = \sum_{j=1}^{3} \alpha_{ij} V_j, \quad j = 1, 2, 3 \tag{4.10}$$

or in matrix form,

$$\begin{bmatrix} \tilde{V}_1 \\ \tilde{V}_2 \\ \tilde{V}_3 \end{bmatrix} = \begin{bmatrix} \alpha_{11} & \alpha_{12} & \alpha_{13} \\ \alpha_{21} & \alpha_{22} & \alpha_{23} \\ \alpha_{31} & \alpha_{32} & \alpha_{33} \end{bmatrix} \begin{bmatrix} V_1 \\ V_2 \\ V_3 \end{bmatrix} \tag{4.11}$$

The interaction between the array elements by means of the $\alpha-$values is shown in Figure 4.3b. The directions of the arrows evidence the role of the antennas in the coupling, that is the pointer is the source of the coupling (j) and the pointee is the subject of the coupling (i). Ideally, in the absence of coupling

$$(\alpha_{ij} = 1 \iff i = j) \wedge (\alpha_{ij} = 0 \ \text{ elsewhere}) \tag{4.12}$$

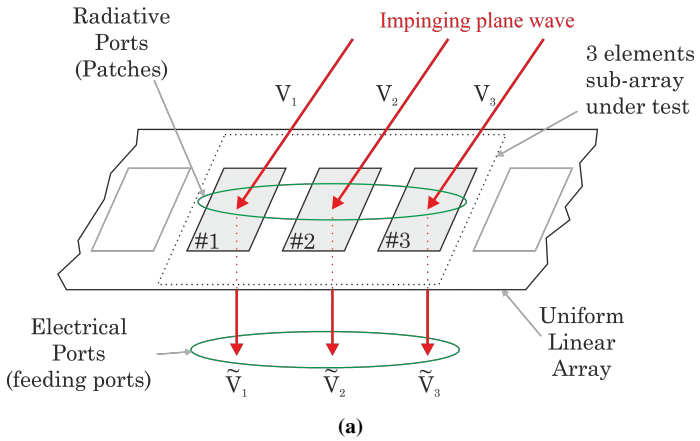

Figure 4.3: Microstrip patch antenna array mutual coupling support geometry for the proposed analysis: (a) The 3-element sub-array under test with radiative and electrical ports notation. (b) The considered interaction between the antenna array elements and coefficients notation considered in the proposed model.

so we can fix in our model $\alpha_{ii} = 1$. Note that this is true also when amplifiers or attenuators are present in the chain since we are supposing those to be equal for each channel.
For symmetry reasons which are evident in Figure 4.3b, the model can be further simplified. Under the hypothesis of symmetry with respect to the broadside axis, it is possible to state that

$$\alpha_{12} = \alpha_{32} \tag{4.13}$$

Therefore, by writing the relationships in matrix form, it is possible to obtain:

$$\begin{bmatrix} \tilde{V}_1 \\ \tilde{V}_2 \\ \tilde{V}_3 \end{bmatrix} = \begin{bmatrix} 1 & \alpha_{23} & \alpha_{13} \\ \alpha_{23} & 1 & \alpha_{23} \\ -\alpha_{13} & -\alpha_{23} & 1 \end{bmatrix} \begin{bmatrix} V_1 \\ V_2 \\ V_3 \end{bmatrix} \tag{4.14}$$

that is equivalent to write

$$\tilde{\mathbf{V}} = \boldsymbol{\alpha}\mathbf{V} \tag{4.15}$$

In this formulation, we also included all the possible systematic errors that are present and embedded in the $\tilde{V}_i$.
We aim to find the matrix α in order to recover the uncoupled voltages on the radiative ports $\mathbf{V}$. However, there are 3 equations and 4 unknowns, thus leading to ∞^1 possible

solutions. In order to find a new constraint, we remember that for an incoming signal from the broadside direction ϑ makes the receiving elements on the array experience different phase shifts according to their position. Let us take the central antenna $i = 2$ as the reference. Hence, by recalling the AoA-induced phase shift in a ULA

$$\Delta\varphi_{ij}(\vartheta) = \frac{2\pi}{\lambda}\,(i-j)\,d\,\sin\vartheta \tag{4.16}$$

it is possible to write

$$V_i = V_2\,\exp\{j\Delta\varphi_{i2}(\vartheta)\} \quad i = 1,2,3 \tag{4.17}$$

and the linear system (4.15) can be rewritten as

$$\tilde{\mathbf{V}} = V_2\,\boldsymbol{\alpha}\,\boldsymbol{\Phi}(\vartheta) \tag{4.18}$$

being

$$\boldsymbol{\Phi}(\vartheta) = \begin{bmatrix} \exp\{j\Delta\varphi_{12}(\vartheta)\} \\ 1 \\ \exp\{j\Delta\varphi_{32}(\vartheta)\} \end{bmatrix} \tag{4.19}$$

By performing a calibration phase, it is possible to determine the α-matrix. In fact, by considering the broadside direction $\vartheta = 0$,

$$\vartheta = 0 \implies \Delta\varphi_{i2}(\vartheta) = 0, \quad i = 1,2,3 \tag{4.20}$$

As a consequence, the α_{ij} values are determined by the ratio between the $\tilde{V}_i$.
Once the α-matrix has been computed, for each broadside position ϑ, the compensation is obtained by:

$$\mathbf{V} = \boldsymbol{\alpha}^{-1}\tilde{\mathbf{V}} \tag{4.21}$$

By its definition, the α-matrix is valid for narrow-band signals. Moreover, it is possible to prove that, supposing an ideal downconversion stage, the α-matrix computed at the IF is equal to the one that could have been computed at IF, with the great advantage of relaxing the complexity of the measurement hardware.

Theorem 1. *Let $\boldsymbol{\alpha}(f_{\mathrm{RF}})$ the α-matrix computed at frequency f_{RF}. Supposing an ideal downconversion stage, its values are proportional the ones computed at IF f_{IF}, that is*

$$\boldsymbol{\alpha}(f_{\mathrm{IF}}) = \dot{K}\,\boldsymbol{\alpha}(f_{\mathrm{RF}}), \quad \dot{K} \in \mathbb{C} \tag{4.22}$$

Proof. Starting from (4.15) we can write

$$\boldsymbol{\alpha}(f_{\mathrm{RF}}) = \tilde{\mathbf{V}}_{\mathrm{RF}}\mathbf{V}_{\mathrm{RF}}^{-1} \tag{4.23}$$

being $\tilde{\mathbf{V}}_{\mathrm{RF}}, \mathbf{V}_{\mathrm{RF}}$ the same matrices as before with the subscript denoting their relationship with RF frequency, so prior to the downconversion. Moreover, we can write also

$$\boldsymbol{\alpha}(f_{\mathrm{IF}}) = \tilde{\mathbf{V}}_{\mathrm{IF}}\mathbf{V}_{\mathrm{RF}}^{-1} \tag{4.24}$$

since the downconversion stage is operated only on the signals coming from the electrical ports.
In order to prove the statement, we should find the phasor $\dot{K} \in \mathbb{C}$ such that

$$\tilde{\mathbf{V}}_{\mathrm{RF}} = \dot{K}\,\tilde{\mathbf{V}}_{\mathrm{IF}} \tag{4.25}$$

However, denoting the downconversion to frequency f_{IF} as the linear operator $\otimes$ such that

$$\otimes(s(t), f_{\mathrm{IF}}) = \mathrm{LPF}\{s(t) \cdot \exp\left[j2\pi\left(f_{\mathrm{RF}} - f_{\mathrm{IF}}\right)t\right]\} \tag{4.26}$$

being $\mathrm{LPF}\{\cdot\}$ a low-pass filtering operation performed by a Linear Time Invariant (LTI) filter, we can see that

$$\tilde{\mathbf{V}}_{\mathrm{IF}} = \otimes(\tilde{\mathbf{V}}_{\mathrm{RF}}, f_{\mathrm{IF}}) \tag{4.27}$$

Hence,

$$\boldsymbol{\alpha}(f_{\mathrm{IF}}) = \otimes(\tilde{\mathbf{V}}_{\mathrm{RF}}, f_{\mathrm{IF}})\mathbf{V}_{\mathrm{RF}}^{-1} \tag{4.28}$$

and since $\otimes(\cdot)$ was defined as a linear operator over complex values, we can write

$$\boldsymbol{\alpha}(f_{\mathrm{IF}}) = \dot{K}\,\tilde{\mathbf{V}}_{\mathrm{RF}}\mathbf{V}_{\mathrm{RF}}^{-1} = \dot{K}\boldsymbol{\alpha}(f_{\mathrm{RF}}) \tag{4.29}$$

□

4.3 Experimental Results

In this section, the effectiveness of the proposed approach is proved through an experimental measurement campaign, by analyzing the results and applying the proposed technique to the output data. The section organization is as follows. First, the experimental setup is described. Then, the analysis of the estimated AoAs accuracy is carried out considering no compensation has been applied. After that, the α-matrix is computed and its values are analyzed in the time domain to evaluate their consistency. Then, the previously computed accuracy is compared to the one after the compensation technique is applied. The comparison has been done in terms of absolute error with respect to the GT AoA values.

4.3.1 Experiment setup

The experiment was set up in an indoor environment assuming a free LoS connection. The operating frequency was chosen to be $f_{\mathrm{RF}} = 3.30$ GHz to prevent interferences from other telecommunications systems in the ISM bands. The transmitter was operated with a f_{RF} single-tone frequency and a -3 dBm power, using the microstrip antenna described in Appendix A.1. Also, the used receiving array is described in the same Appendix. Each array element was connected to 4 nominally identical RF front-ends which are described in Appendix A.3. The output signals were then sampled with a 12-bit digital oscilloscope with 1 GHz bandwidth and 5 GS/s sample rate. The samples were then acquired on a 0.5 µs time window and processed with a custom MATLAB script.

The transmitter was placed at broadside distances $l_k = \{2.10, 3\}$ m, both of them greater than the Fraunhofer distance, allowing the wave to be considered plane. Then, each measurement was taken by moving the target in the direction parallel to the array, starting from the array center position, taken as a reference. The relative position for the distance l with respect to the array center position for experiment j is x_j. For each x_j we acquired 50 snapshots (one every 2 seconds). The GT angles were computed as

$$\mathrm{GT}(x_k) = \arctan\left(\frac{x_k}{l_k}\right)\frac{180}{\pi} \tag{4.30}$$

In Table 4.1 there are summarized the mean value of the Signal-to-Noise Ratio (SNR) on all the positions for each experiment.

Table 4.1: Average SNR values for channels and experiments.

Exp#	Average SNR [dB]				
	CH1	CH2	CH3	CH4	**AVG**
1	29.55	30.61	28.56	29.54	**29.56**
2	28.87	31.20	27.26	28.17	**28.88**

4.3.2 Analysis AoA estimation accuracy without the compensation

The AoA estimation through phase interefometry was performed on the phase difference values extracted through the algorithm described in [10] and Chapter 3. For a N-element array, in far-field, Q AoA estimations for the same GT angle were achieved, by taking the distinct Q antenna pairs and properly computing the phase difference, with Q being

$$Q = \sum_{j=1}^{N} (N - j) \tag{4.31}$$

Accordingly, we obtained the following AoA values by averaging on a pair-by-pair basis the estimated AoAs, to improve the precision. The results are summarized in Figure 4.4a and Figure 4.4b for Exp.#1 and Exp.#2, respectively.
The obtained values are compared to the GT values.
Table 4.2 summarizes the statistics regarding the computed absolute errors. The absolute error on the AoA estimated with the antenna array couple $\{ij\}$ during the experiment k for the broadside position x_k is computed as

$$err^k_{\{ij\}} = |\mathrm{GT}(x_k) - \mathrm{AoA}_{\{ij\}}(x_k)| \tag{4.32}$$

As expected, better results are obtained by averaging the values, in terms of both average and error dispersion. However, the results are still biased by the presence of non-negligible error components.

4.3.3 Computation and analysis of the α-matrix

As described in Section 4.2, the α-matrix was computed starting from the measured values when the transmitter is in the array broadside center position. Since the method

Table 4.2: Statistic indexes on the AoA estimation made without calibration.

	err^k_{21} [deg]		err^k_{32} [deg]		err^k_{43} [deg]		err^k_{avg} [deg]	
	avg	std	avg	std	avg	std	avg	std
Exp#1	2.06	1.67	3.68	1.76	3.64	1.75	1.81	0.72
Exp#2	2.25	1.69	3.32	1.74	4.36	3.07	1.93	0.89

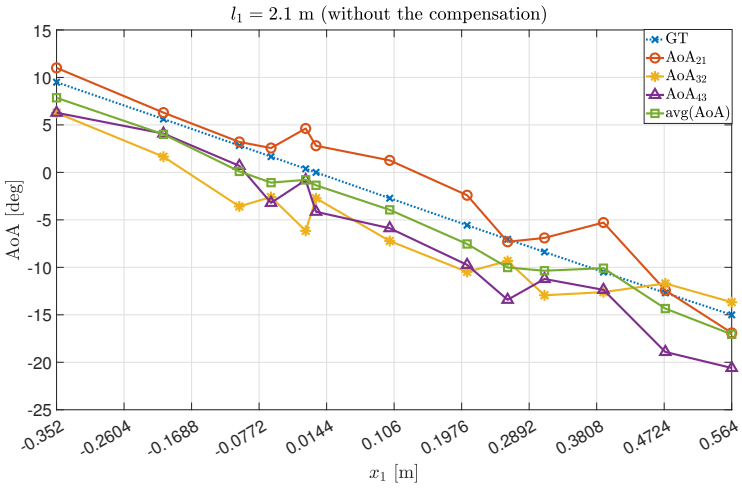

(a)

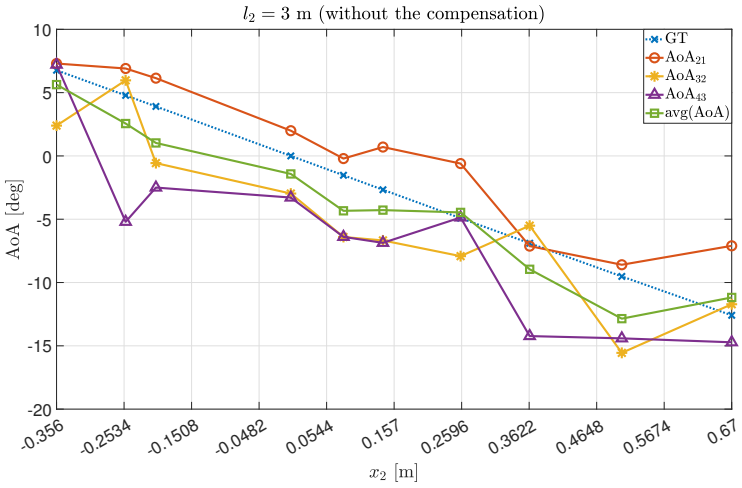

(b)

Figure 4.4: AoA estimation from the antenna pairs {21},{32},{43} and their average for (a) Exp. #1 and (b) Exp. #2.

is defined for 3 contiguous antennas, we chose to apply it to the subarray $\{2, 3, 4\}$. The α-matrix computation is demanded to a MATLAB script.

The α-matrix was computed once and it is valid for all the successive measurements, having a unique value. This statement was experimentally proved. To do that, first, the behavior of the α-values was studied in the time domain, for a time frame equal to the acquisition time of one experimental sample. As a reference it is considered the first acquisition window of Exp#1.
As shown in Figure 4.5, the amplitude is normally distributed around the mean value.

Table 4.3 shows how the standard deviation order of magnitude is lower than that of the mean value. Hence, it is possible to assume the mean value to be a good approximation of the dynamic behavior. Also, the phase values reported in the same table and in Figure 4.6 exhibit the same statistical properties. Hence it is possible to conclude

Table 4.3: Statistic indexes on the amplitude and phase of the α-matrix coefficients on the 50 snapshots of the single experimental calibration point.

	avg($\lvert\cdot\rvert$) [dB]	**std($\lvert\cdot\rvert$) [dB]**	**avg($\angle\cdot$) [rad]**	**std($\angle\cdot$) [rad]**
α_{23}	1.17	0.06	-3.13	0.007
α_{13}	2.13	0.07	-0.13	0.008

that the computed mean values for the α-matrix amplitude and phases are a good approximation of the overall dynamic behavior during the acquisition time window.

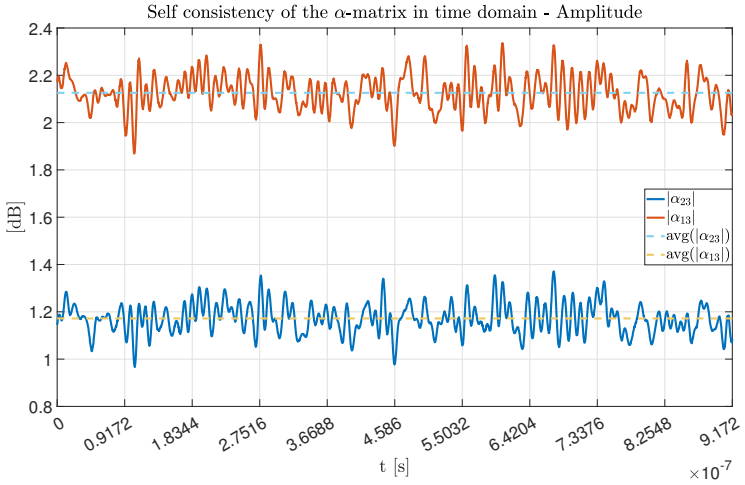

Figure 4.5: Amplitude values for the α-matrix coefficient during an experimental snapshot.

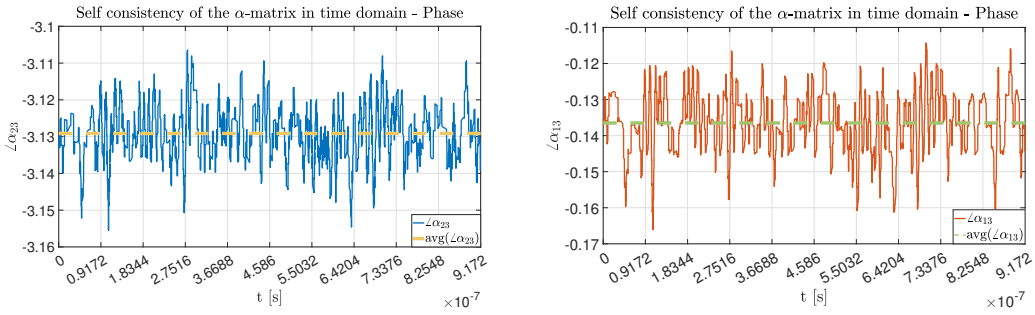

(a) **(b)**

Figure 4.6: Phase values for the α-matrix coefficient during an experimental snapshot. In particular, in (a) phase values for the α_{23} coefficient and in (b) phase values for the α_{13} coefficient.

In a similar way it is possible to prove the validity of the α-matrix computation for successive measurements. In other words, the compensation introduced by the matrix can be employed for the successive samples after the calibration phase. To prove so, the compensation errors were computed and evaluated for the center position for each experimental sample and for each antenna pair $\{23\}, \{43\}$. The results are shown in Figure 4.7, where it is possible to see how the phase errors for the uncompensated values are not stable, while the compensated values are stable for all the experiment

duration, except for a few outliers.

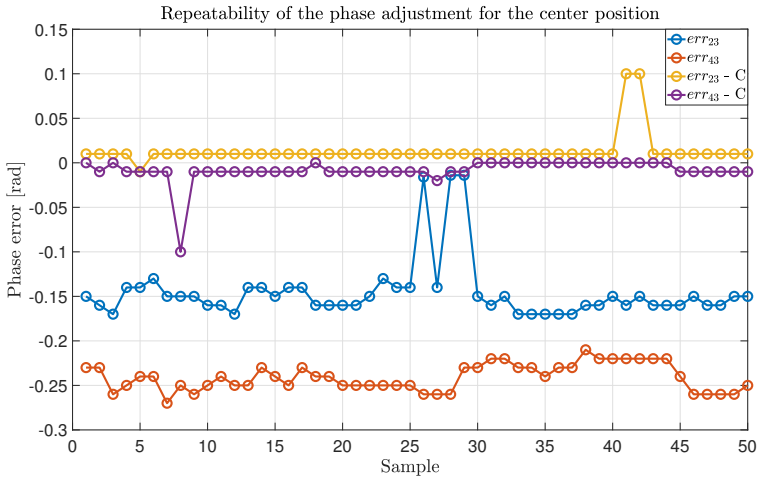

Figure 4.7: Analysis of the repeatability of the phase adjustment for the center position on 50 experimental samples, with err_{ij} represents the absolute error committed for the antenna elements $\{ij\}$ without the compensation and err_{ij} - C the absolute error committed with the compensation procedure.

4.3.4 Analysis AoA estimation accuracy with the compensation

Once the matrix has been computed for the center position, it was stored and recalled for the computation of the compensated waveforms for each of the positions. The compensated waveforms were then employed for the AoA estimation as previously described. The validation of this approach was performed with a custom MATLAB script.

For both experimental trials Exp#1 and Exp#2 the compensation method allowed the estimation points to be closer to the expected ones (Figures 4.8-4.9). The results from Exp#2 are less accurate than Exp#1 because of a greater impact of the multipath phenomenon on the estimation results. In fact, a greater distance between transmitter and receiver allows the power associated with the LoS component to drop and so the impact of the other paths on the estimation value increase, determining a loss of accuracy [11]. However, even in this case, the estimation quality improves with the adoption of the proposed technique.

As it was done in the uncompensated case, the impact of an averaging operation between the estimated AoA values was analyzed. The results are shown in Figure 4.10a for Exp#1 and in Figure 4.10b for Exp#2. As expected, the estimation quality improves even more: in Exp#1 the estimated values are very close to the GT ones, while for Exp#2 the introduction of the averaging better mitigates the estimation artifacts.

4.3.5 Comparison

In order to properly compare the compensated and uncompensated estimations, it was employed the absolute error metric (4.32) introduced in Section 4.3.2. The first comparison was done on the estimations made through the antenna pairs $\{23\}$ and $\{43\}$. The results and the percentage comparison with respect to the absolute errors committed without the compensation procedure (see Table 4.2) are shown in Table 4.4.

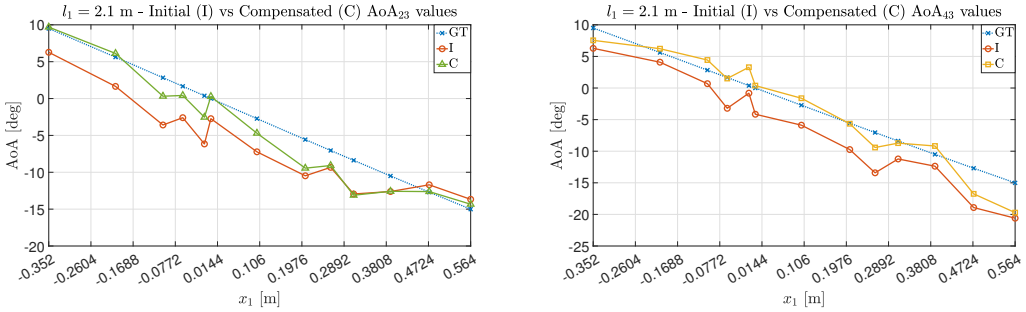

(a) **(b)**

Figure 4.8: AoA estimation values for the Exp#1 before and after the compensation obtained for (a) the antenna pair $\{23\}$ and (b) the antenna pair $\{43\}$.

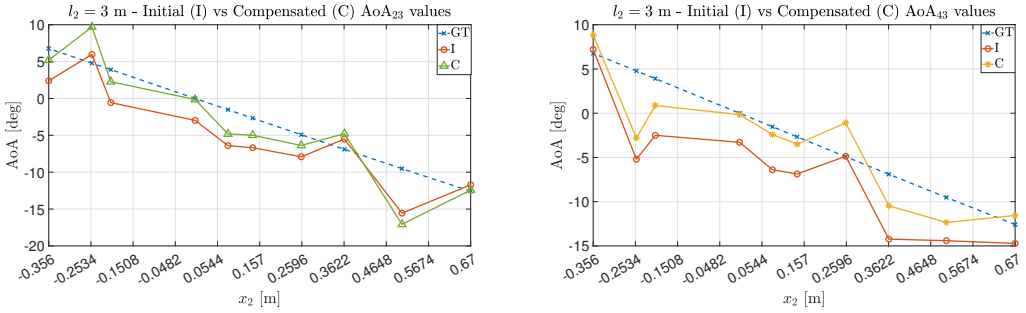

(a) **(b)**

Figure 4.9: AoA estimation values for the Exp#2 before and after the compensation obtained for (a) the antenna pair $\{23\}$ and (b) the antenna pair $\{43\}$.

Table 4.4: Statistic indexes on the absolute AoA estimation errors after the compensation for antenna pairs $\{23\}$ and $\{43\}$.

	err_{23}^k [deg]				err_{43}^k [deg]			
	avg		std		avg		std	
Exp#1	1.78	-51.6%	1.47	-16.4%	1.66	-54.4%	1.49	-14.9%
Exp#2	2.51	-24.4%	2.25	-22.7%	2.57	-41.0%	2.16	-29.6%

The average absolute errors decrease of more than 50% in the Exp#1 case and more than 25% in the Exp#2 case. Also, standard deviation values exhibit a reduction in their value. To better understand the compensation action, in Figure 4.11 it is evident how the initial artifacts in the calibration points are almost canceled by the compensation procedure.
Considering the estimation made by averaging the AoA values after the compensation, it is possible to see how, even in this case, a good reduction of the average absolute error is obtained (Table 4.5). However, in this case, the compensation introduces a distortion in the distribution of the errors around the mean value, even if not so strong in absolute terms.

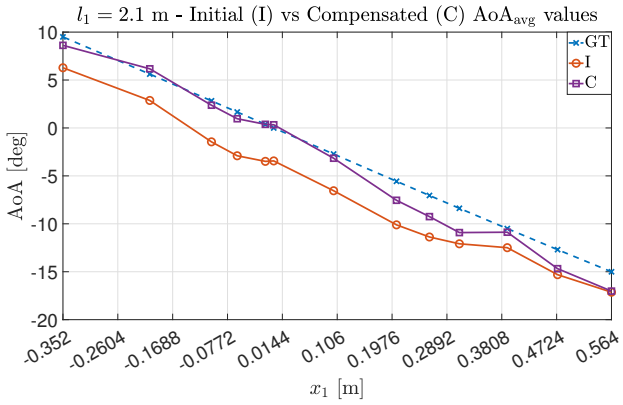

(a)

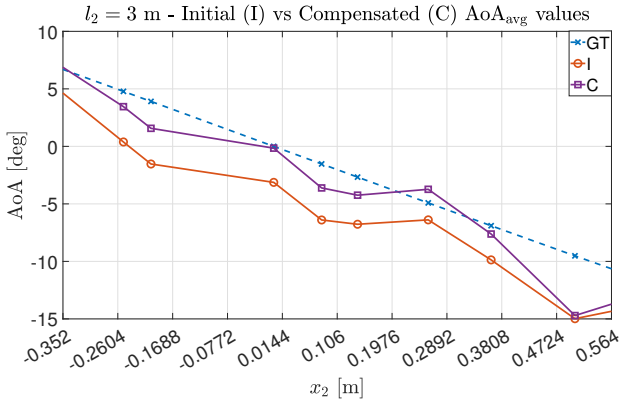

(b)

Figure 4.10: Average on the AoA estimation values before and after the compensation for (a) the Exp#1 and (b) the Exp#2.

4.4 Conclusions

This chapter introduced a linear technique for artifact correction and compensation AoA estimation through phase interferometry for narrowband radiolocation applications. The theoretical background and the mathematical formulation were discussed in detail.

The proposed technique embeds in one single computation the compensation for all the possible mismatches arising due to systematic errors. Also, the compensation takes into account also the mutual coupling effects acting on the antenna array through a first-order (linear) approximation. The α-matrix can be computed once in the calibration phase. Given the generality of the approach described, it can be implemented in either the analog or digital domain.

The experimental campaign validated the quality of the compensation introduced by halving the error trend even in the indoor environment, where multipath has a strong influence on the AoA estimation error.

References

[1] C. A. Balanis, *Antenna Theory: Analysis and Design*. New York, NY, USA: Wiley-Interscience, 2005.

Table 4.5: Statistic indexes on the absolute AoA estimation errors after averaging the estimated AoAs after compensation for antenna pairs {23} and {43}.

	$err^{k}_{\mathbf{avg}}$ [deg]			
	avg		std	
Exp#1	1.11	-38.7%	0.88	+18.1%
Exp#2	1.54	-54.0%	1.47	+39.4%

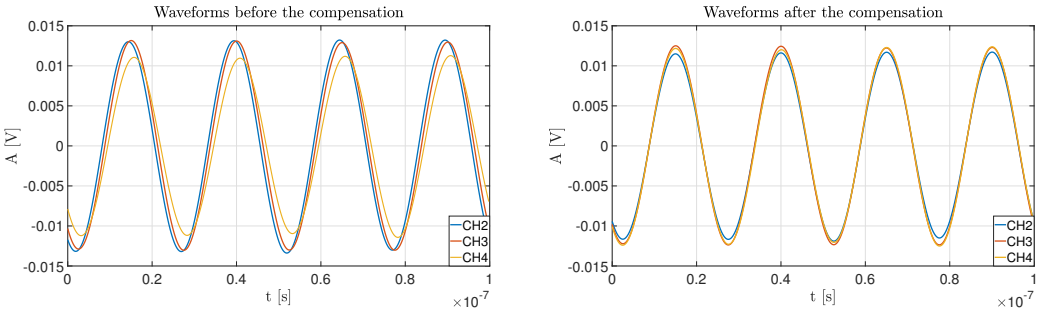

Figure 4.11: Time domain comparison of the compensated waveforms versus the acquired waveforms in the Exp #2 calibration point. The initial waveforms were pre-processed through a digital FIR filtering and downconversion stage to the IF of 40 MHz for better view the results.

[2] D. Pozar, "Considerations for millimeter wave printed antennas," *IEEE Transactions on antennas and propagation*, vol. 31, no. 5, pp. 740–747, 1983.

[3] R. J. Mailloux, *Phased array antenna handbook*. Artech house, 2017.

[4] H.-S. Lui, H. T. Hui, and M. S. Leong, "A Note on the Mutual-Coupling Problems in Transmitting and Receiving Antenna Arrays," *IEEE Antennas and Propagation Magazine*, vol. 51, no. 5, pp. 171–176, 2009.

[5] C. Craeye and D. González-Ovejero, "A Review on Array Mutual Coupling Analysis," *Radio Science*, vol. 46, no. 2, 2011.

[6] X. Chen, S. Zhang, and Q. Li, "A Review of Mutual Coupling in MIMO Systems," *IEEE Access*, vol. 6, pp. 24 706–24 719, 2018.

[7] H. S. Lui and H. T. Hui, "Mutual Coupling Compensation for Direction-of-Arrival Estimations Using the Receiving-Mutual-Impedance Method," *International Journal of Antennas and Propagation*, vol. 2010, p. 373061, Mar. 2010, publisher: Hindawi Publishing Corporation.

[8] H.-S. Lui and H. T. Hui, "Direction-of-Arrival Estimation: Measurement using compact antenna arrays under the influence of mutual coupling," *IEEE Antennas and Propagation Magazine*, vol. 57, no. 6, pp. 62–68, 2015.

[9] K. S. Vishvaksenan, K. Mithra, R. Kalaiarasan, and K. S. Raj, "Mutual Coupling Reduction in Microstrip Patch Antenna Arrays Using Parallel Coupled-Line Resonators," *IEEE Antennas and Wireless Propagation Letters*, vol. 16, pp. 2146–2149, 2017.

[10] A. Florio, G. Avitabile, and G. Coviello, "Digital Phase Estimation through an I/Q Approach for Angle of Arrival Full-Hardware Localization," in *2020 IEEE Asia Pacific Conference on Circuits and Systems (APCCAS)*, 2020, pp. 106–109.

[11] A. Florio, G. Avitabile, G. Coviello, J. Ma, and K. L. Man, "The Impact of Coherent Signal Reception on Interferometric Angle of Arrival Estimation," in *2020 International SoC Design Conference (ISOCC)*, 2020, pp. 167–168.

CHAPTER 5

A Digital Architecture for Hardware AoA estimation

This chapter is partially based on the following publication: A. Florio, C. Talarico, G. Avitabile, and G. Coviello, "A Synchronous Digital Phase Detector Architecture based on a Coarse Time-to-Digital Approach", in 2023 8th International Conference on Smart and Sustainable Technologies (SpliTech), 2023.

This chapter introduces a new technique for AoA estimation based on phase interferometry. The proposed solution is modular and reconfigurable according to the level of precision desired for a specific application. The architecture was implemented on the Terasic DE2-115 Development board for the Intel Cyclone IV E EP4CE115F29C7 FPGA. The approach was validated through a large set of experiments involving both custom-designed analog hardware boards and Hardware-in-the-Loop testing tools, aiming to evaluate the impact of the reconfiguration parameters on the accuracy of the approach. The achieved performance is compared with classical benchmark algorithms available in the literature.

5.1 Motivations and Mathematical Background

Consider a CW signal with central frequency f_{RF} impinges an array of two antennas i, j from direction ϑ in far-field. The received signals $s_i(t), s_j(t)$ can be expressed through:

$$s_q(t) = K_q \cos(2\pi f_{RF} t + \varphi_q),\ q \in \{i, j\} \tag{5.1}$$

Recalling the (2.6)

$$\varphi_j - \varphi_i = \Delta\varphi_{ij} = \frac{2\pi}{\lambda} d(i-j)\sin\vartheta \tag{5.2}$$

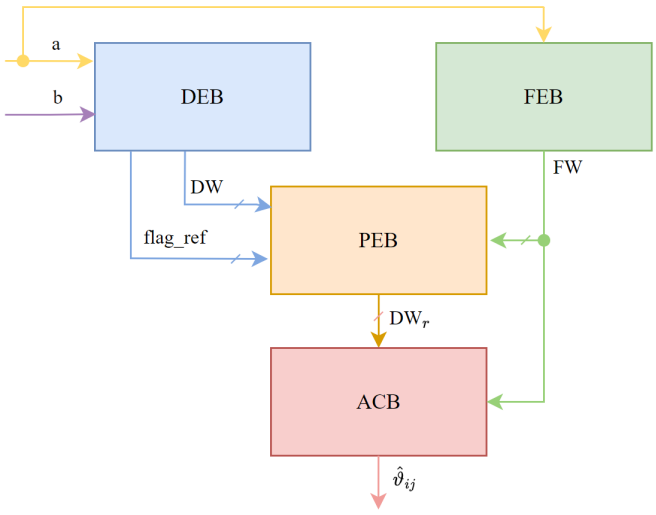

Figure 5.1: Macroblocks and main signals interaction diagram, with a and b being the sample input channels.

For a CW signal,

$$\Delta\varphi_{ij} = 2\pi f_{RF}\Delta\tau_{ij}(f_{RF}) \tag{5.3}$$

being $\Delta\tau_{ij}(f_{RF})$ the time difference of arrival at the two array elements at frequency f_{RF}. The time delay measurement can be also linked to the AoA (see Chapter 2). After the downconversion, the time delay in IF is:

$$\Delta\tau_{ij}(f_{IF}) = \frac{\Delta\varphi_{ij}}{2\pi f_{IF}} \tag{5.4}$$

By substituting the (5.3),

$$\Delta\tau_{ij}(f_{IF}) = \frac{2\pi f_{RF}\Delta\tau_{ij}(f_{RF})}{2\pi f_{IF}} \tag{5.5}$$

Inverting the (2.6) and substituting the found relationships,

$$\hat{\vartheta}_{ij} = \arcsin\left[\frac{\lambda}{d(i-j)} f_{IF}\Delta\tau_{ij}(f_{IF})\right] \tag{5.6}$$

Hence, by measuring the time delay $\Delta\tau_{ij}(f_{IF})$ and the frequency f_{IF} it is possible to estimate the AoA ϑ. Also, what is stated for CW signals holds for signals with sufficiently narrow bandwidth.

5.2 Description of the proposed architecture

The architecture is composed of four macroblocks: the Delay Estimation Block (DEB), the Frequency Estimation Block (FEB), the Phase Estimation Block (PEB), and the AoA Computation Block (ACB). In this section, the functionalities of each block are detailed. The macroblocks interaction diagram is shown in Figure 5.1. All blocks are driven by the same clock signal.

5.2.1 Delay Estimation Block (DEB)

The DEB is in charge of computing the time delay between two channels, by taking one of them as reference. The computed phase shifts are in the range $[0, 2\pi[$ and are represented by a binary word of length L, called the Delay Word (DW). The DW quantizes the time delay between the input signals and is equal to the number of system clock ticks corresponding to the measured delay. The DEB subblocks are depicted in Figure 5.2.

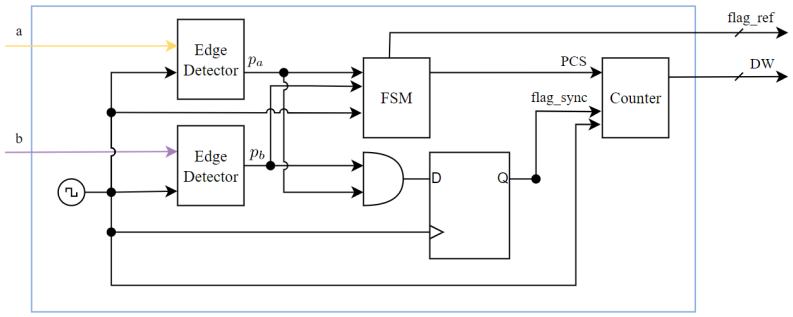

Figure 5.2: Delay Estimation Block (DEB) diagram.

Consider two channels labeled as a, b. A positive edge detection is performed on both channels (Figure 5.3), giving rise to the two pulses p_a, p_b with time duration $T_{clk} = 1/f_{clk}$, where f_{clk} is the system clock frequency. The frequency of p_a, p_b is nominally equal to the one of the input signals a and b, f_{IF}.

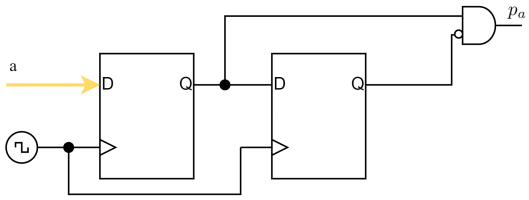

Figure 5.3: Structure of the positive-edge detector circuit for signal a.

The signals p_a, p_b are fed to a Moore-like Finite State Machine (FSM). The introduction of this subblock is to keep track of the reference channel with respect to the time delay is computed. As an example, let us assume a is the default reference channel. If at any point in time, b becomes the leading signal, without a reference tracking mechanism, the system would compute the phase shift considering the time difference between the pulses p_b and p_a. However, with a reference tracking mechanism, the value can be correctly referred to the channel a by computing the 2π-complement of the estimated phase. The choice of a Moore FSM improves the synchronicity to the clock. The FSM has two outputs: the Phase Control Signal (PCS), whose duty cycle is proportional to the phase shift between the signals, and flag_ref which labels the reference channel (Figure 5.4). The FSM is described by a state space $\mathcal{S}$ whose cardinality is $|\mathcal{S}| = 5$:

$$\mathcal{S} = \{zero, a\_lead, b\_lead, a\_zero, b\_zero\} \tag{5.7}$$

Each state is associated with a set of tasks:

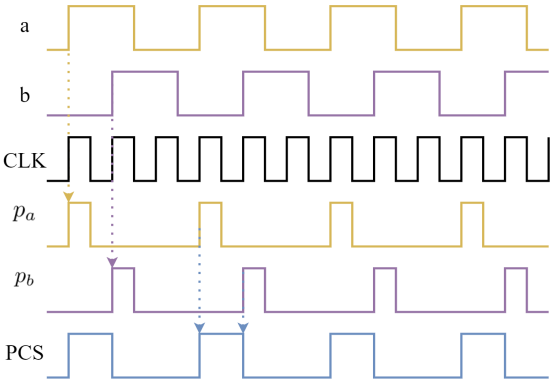

Figure 5.4: Timing diagram illustrating the PCS signal generation starting from the sample preconditioned input signals (neglecting the latency).

- $zero$: it is the initial state. In this state, the PCS is set to low, and the flag_ref is set to `"00"`
- a_lead: this state is triggered when the first detected pulse rising edge is on a. In this state, PCS is set to high, and flag_ref is set to `"01"`
- a_zero: this state is triggered after the state a_lead is reached and a pulse rising edge on b is detected. In that case, PCS is set to low and flag_ref is kept to `"01"`.
- b_lead: performs the same operations as a_lead, but when the first detected edge is on b. Hence, the flag_ref is set to be `"10"` and the PCS is set to high.
- b_zero: it is the dual of a_zero, with flag_ref set to be `"10"` and PCS set to low.

When the states a_zero and b_zero are reached, in case the inputs are synchronous (i.e. null phase difference), a transition towards $zero$ is triggered, thus resetting the choice on the reference channel. This feature is implemented to also keep track of moving objects. The FSM state transition graph is depicted in Figure 5.5. Note that in the picture we used the notation $(x, y) = (p_a, p_b) \in \{0, 1\} \times \{0, 1\}$ to illustrate the state transitions, where p_i, $i = \{a, b\}$ represent the outputs of the edge detectors. Figure 5.6 shows the PCS oscilloscope trace in the case of synchronous and non-synchronous inputs.

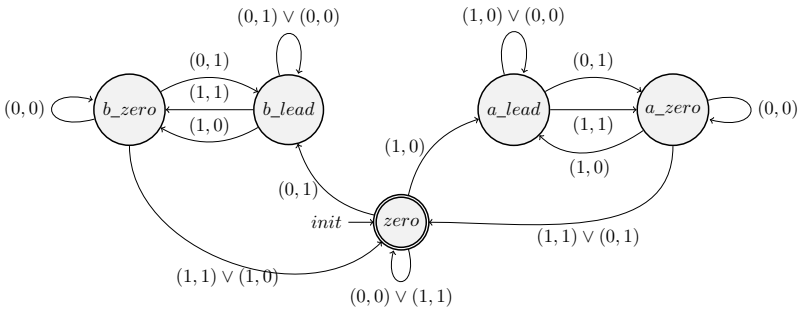

Figure 5.5: States transition diagram for the Moore-like FSM of the PEB with inputs $(p_a, p_b) \in \{0, 1\} \times \{0, 1\}$.

In parallel to the FSM there is another synchronization checking mechanism that takes

p_a, p_b as inputs and it performs a registered AND operation between them, generating as output the signal flag_sync (Figure 5.6).

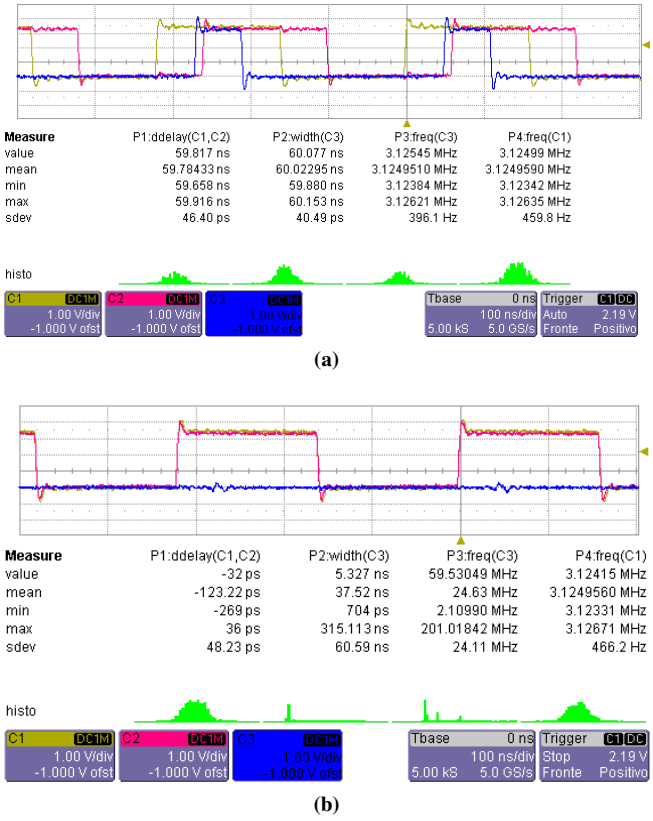

Figure 5.6: Oscilloscope screenshot with traces and statistics showing the case of (a) two phase shifted channels (on CH1 and CH2 respectively) and the PCS signal (on CH3). In (b) the same setup is showing the behavior for two nominally synchronous signals.

The PCS acts as the enable input of a *modulo* 2^L-counter driven by the system clock. The counter acts as a coarse Time-to-Digit (T2D) converter associating a DW to the measured delay. The counter output is stored and held until a change in the duty cycle of the PCS is detected. The count is updated only when the PCS goes to low (hence, the transition is masked). The signal flag_sync is in charge both of resetting the final counting value and disabling the counter with only one Clock Cycle (CC) of delay with respect to when synchronicity is detected.

The DEB latency depends on the phase shift estimated. The latency has a static component due to the edge detectors and the FSM, and a variable component due to the counter update mechanism. The static component takes 3 CCs, while the variable component takes in the worst case a number of CCs equal to the maximum value the DW can represent.

5.2.2 Frequency Estimation Block (FEB)

The FEB associates a binary word with the period of the input signals. The hypothesis each signal on each channel has the same frequency is made. The FEB needs to take the reference channel as its only input. The output of the FEB is a binary word of

length C, called Frequency Word (FW), and representing the number of clock ticks forming a period, that is:

$$\mathrm{FW} = \left\lceil \frac{f_{clk}}{f_{IF}} \right\rceil \tag{5.8}$$

where f_{IF} is the input signal frequency, f_{clk} is the system clock frequency, and $\lceil \cdot \rceil$ the ceiling operator. The structure of the FEB is very similar to the one of the PEB, with slight differences, and it is depicted in Figure 5.7.

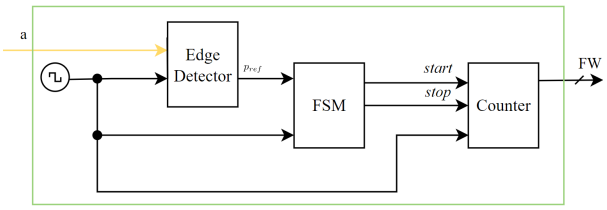

Figure 5.7: Frequency Estimation Block (FEB) diagram.

First, the edge detection is performed on the reference channel a. The edge detector has the same structure as the one used in the PEB, depicted in Figure 5.3. The pulse p_{ref} is fed to a Moore-like FSM with three states that generate a signal enabling and disabling a *modulo* 2^C-counter (Figure 5.8). The signal from the FSM is set to high when in the state *start* and is set to 0 in the other states. The FSM goes into the *start* state if the output of the edge detector is high, and it stays there until a new pulse is detected. The FEB latency is determined as the worst-case latency of the DEB.

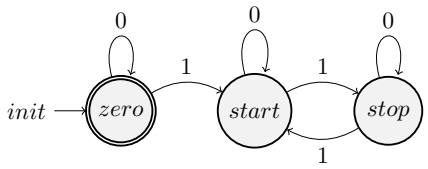

Figure 5.8: State diagram for the Moore-like FSM of the FEB, describing the state interaction depending on the input pulse $p_{ref} \in \{0, 1\}$.

5.2.3 Phase Estimation Block (PEB)

The PEB (Figure 5.9) takes as input the DW, FW, and flag_ref and returns DW_r, referring the measured delay to the reference channel. Its simplified behavior is described in Algorithm 2 in the time domain.

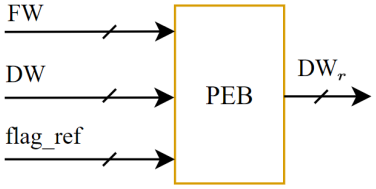

Figure 5.9: Phase Estimation Block (PEB) diagram.

DW_r is equal to DW only in case the word has been computed with respect to the reference channel (flag_ref = `01`). Otherwise, either the two channels are synchronous

Algorithm 2 Phase rotation with respect to the reference channel.

Require: DW, FW, flag_ref
  if flag_ref = `00` **then**
    $\mathrm{DW}_r = 0$
  else if flag_ref = `01` **then**
    $\mathrm{DW}_r = \mathrm{DW}$
  else if flag_ref = `10` **then**
    $\mathrm{DW}_r = \mathrm{FW} - \mathrm{DW}$
  else
    `- do nothing`
  end if
  return DW_r

(or the system is reset, flag_ref = `00`) or the word is computed having the other channel as the reference. In that case, the DW has to be "rotated" of the delay corresponding to the phase 2π, that is the signal period, represented by the FW.

5.2.4 AoA Computation Block (ACB)

The ACB determines the AoA estimation $\hat{\vartheta}_{ab}$. Its block diagram is depicted in Figure 5.10. Phase shift and AoA are linked through the inverse sine function. To perform the

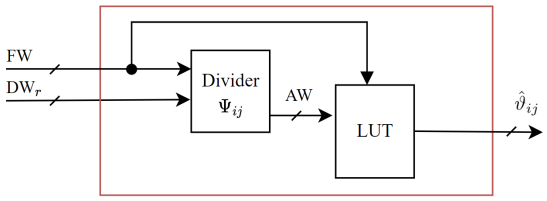

Figure 5.10: AoA Computation Block (ACB) diagram.

arcsine computation, there are several approaches, ranging from complex algorithms to Look-Up Tables (LUTs) [1]. This latter is the most straightforward technique. The LUT address length is referred to as A, expressed in bits. The LUT can be populated with 2^A different values. Note that the LUT depth choice imposes a trade-off between the precision of the AoA representation and the size of the LUT. First recall the (5.6), that can be rewritten as:

$$\vartheta_{ij} = \arcsin\left[\frac{\Delta\tau_{ij}(f_{IF})}{T_{IF}\cdot\Psi_{ij}}\right] \tag{5.9}$$

with $T_{IF} = f_{IF}^{-1}$ being the IF signal period, and Ψ_{ij} the effective array spacing, defined as

$$\Psi_{ij} = \frac{d(i-j)}{\lambda} \tag{5.10}$$

By substituting the measured values to the continuous time ones,

$$\hat{\vartheta}_{ij} = \arcsin\left[\frac{\mathrm{DW}_r}{\mathrm{FW}\cdot\Psi_{ij}}\right] \tag{5.11}$$

As an intuition, the argument of the (5.11) can be used as the indexing address for the LUT. To explain this step, first it is necessary to recall some basic concepts on the inverse sine function.

Definition 1. *Let* $I = [-1, +1] \subset \mathbb{R}$ *and* $S = \left[-\frac{\pi}{2}, +\frac{\pi}{2}\right] \subset \mathbb{R}$. *We define* $f : I \to S$ *as the function that* $x \rightarrowtail y$ *s.t.* $\sin(y) = x,\ x \in I, y \in S$. *The function* f *is called arcsine or inverse sine.*

The sine function is not invertible being periodic. The inverse is defined as a restriction on the interval S. The domain and codomain limits for the LUT are specified by a discretization of the intervals I, S. The argument of the (5.11) requires to perform a division. Since it is necessary to cover the I interval with an address of length A, the following holds:

$$\frac{\mathrm{DW}_r}{\mathrm{FW}} = \frac{\mathrm{AW}}{2^A} \implies \mathrm{AW} = \frac{\mathrm{DW}_r \cdot 2^A}{\mathrm{FW}} \tag{5.12}$$

being AW the LUT address (Angular Word) of length A, and so, the arcsine argument corresponds to the estimated phase difference. Applying the (5.12) leads to handling an integer division, from which only the quotient is considered as the result. It is known that the multiplication of a binary string with 2^A corresponds to a left shift of A positions. The result of this operation is the dividend input to the divider. On the other hand, the divisor input (i.e. the divisor of the (5.11) requires a further hypothesis. If $d = 0.5\lambda$ and $(i - j) = 1$ (case of adjacent antenna elements), then $\psi_{ij} = 0.5$ and the product has the effect of a right shift of FW of one position with 0 padding (since FW is an unsigned number).

The ACB has a latency of 6 CC: 5 CC are needed for the address generation and 1 CC for the LUT response. Figure 5.11 shows a ModelSim Register-Trasfer Level (RTL) simulation for the ACB structure.

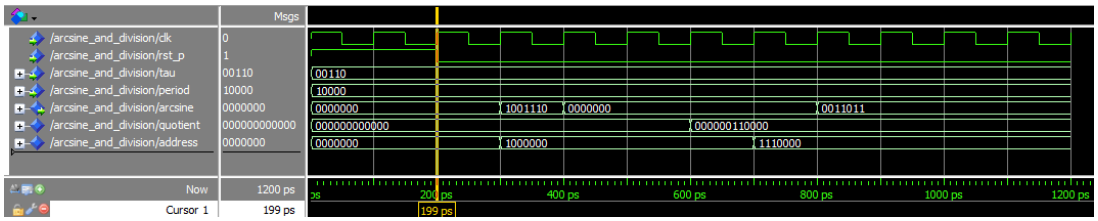

Figure 5.11: Arcsine component simulation performed on ModelSim.

5.2.5 System dimensioning

After having described each block functionality, we can now delve into the block parameters dimensioning.

Clock frequency The clock period of a digital synchronous system imposes a lower boundary on the minimum time delay it can resolve. If $\Delta\tau_{ij}(f_{IF})$ is the time delay to be resolved,

$$T_{clk} \leq \Delta\tau_{ij}(f_{IF}) \tag{5.13}$$

Therefore,

$$\Delta\tau_{min} = \frac{1}{f_{clk}} \tag{5.14}$$

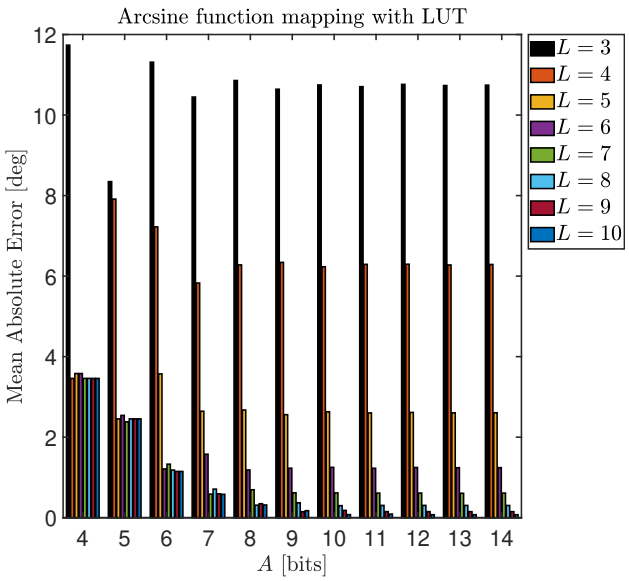

Figure 5.12: Mean absolute error varying the LUT address length A and the DW length L.

that leads to finding the minimum resolvable AoA through the (5.9) as follows:

$$\vartheta_{min,ij} = \arcsin\left(\frac{1}{\Psi_{ij}}\frac{f_{IF}}{f_{clk}}\right) \tag{5.15}$$

DW length The counter is enabled when the digital signal PCS is high. PCS has the same frequency as the input signals but with a variable duty cycle. If the DW is a L-bits word, the maximum time PCS may be high is $2^L - 1$ clock ticks, therefore:

$$T_{IF} \leq (2^L - 1) \cdot T_{clk} \tag{5.16}$$

with T_{IF} being the input signal period. Therefore, the minimum number of bits required to represent DW is:

$$L_{min} = \left\lceil \log_2\left(\frac{f_{clk}}{f_{IF}} + 1\right)\right\rceil \tag{5.17}$$

FW length and maximum input frequency Following the same considerations used for the DW length dimensioning, we can derive a similar expression for the FW length. The *start* signal produced by the FSM has the same frequency as the input signal, that is f_{IF}. Hence, similarly to (5.17):

$$C_{min} = \left\lceil \log_2\left(\frac{f_{clk}}{f_{IF}} + 1\right)\right\rceil \tag{5.18}$$

If we consider $C = L$, the maximum allowable input frequency is:

$$f_{IF,max} = \frac{f_{clk}}{(2^L - 1)} \tag{5.19}$$

ACB LUT dimensioning From the Definition 1, it is apparent that the values to store in the LUT always fall in the $[-\pi/2, +\pi/2]$ range, so the absolute value of the integer part can be only $\{0, 1\}$. To keep the complexity low, the values in the LUT are represented in fixed-point notation by words of length B. In those words, one bit is dedicated to the sign, one bit to the integer part, and $B - 2$ bits to the fractional part.

The cumulative AoA estimation error depends on the word length L (or, equivalently, the ratio between f_{IF} and f_{clk}), and the address length A of the LUT. To study their impact, the mean absolute error has been computed by considering a ULA spacing of $\lambda/2$ and two adjacent antenna elements (i.e., $|\Psi_{ij}| = 0.5$). The results are provided in Figure 5.12. The error exhibits a negative power dependency with the address length A. For $A \geq 7$ the effect of the LUT depth on the error becomes negligible and we can assume that the error depends only on L.

5.3 Experimental evaluation of the phase estimation accuracy

Before the full AoA estimation architecture assessment, the first characterization was made in terms of phase estimation accuracy. Hence, in this test, the ACB section of the Prototype-under-Test (PUT) was disconnected. The characterization was performed through an experimental setup whose purpose was to measure the phase shift imposed at RF at IF.

5.3.1 Digital PUT

The phase estimation architecture was tested on the Intel Cyclone IV EP4CE115F29C7 FPGA through the Terasic DE2-115 development board. The word lengths were set to $L = C = 7$ bits. Figure 5.13 and Table 5.1 summarize the FPGA fitting results in terms of resource allocation, and the resource distribution for the different blocks.

Figure 5.13: PUT post-fitting resources occupancy: (a) combinational function distribution, and (b) register resources distribution.

5.3.2 Experiment setup and description

The experimental setup is sketched in Figure 5.14. It involved two RF signals with a variable phase shift as the input of a downconversion stage. The output of this latter was then fed to the digital architecture which was in charge of measuring the phase

Table 5.1: PUT resources occupancy summary.

Parameter	Value
Combinational Functions	83
Logic Elements	94 (0.081%)
Total registers	70
Total pins	24 (4.53%)

shift. The digital values were read and collected through the FPGA Data Capture IP (FDC) of the MATLAB HDL Verifier Toolbox [2], which acted as a logic analyzer and collector tool.

The RF signals were provided by two ADF4355 PLLs by Analog Devices [3], a high-performance Fractional PLL with a programmable phase shift. The two devices were locked to the same external reference source. The internal registers were programmed employing a microcontroller setting the output frequency to $f_{RF} = 3.4$ GHz and shifting the phase of one of them, having the other as the reference. The phase jumps are set to be 10 degrees. The outputs of the two PLLs were fed to a pair of custom-designed RF front-ends described in Appendix A.3. The RF front-ends were in charge of the downconversion of the signal to the frequency $f = 20$ MHz through the feeding of a LO signal provided by a signal generator, whose frequency is set to $f_{LO} = 3.38$ GHz.

The downconverted signal was fed to the FPGA Development Board by means of an LTC6957-3 low phase noise driver by Analog Devices [4], deployed through the custom-designed board described in Appendix A.4. The device was in charge of translating the input signals to the correct logic level ready to be read by the FPGA, in our case the 3.3V CMOS logic family.

Two measurement campaigns were performed. The investigation involved mainly the impact of the clock frequency variation on the level of accuracy that can be reached. The tests were run for $f_{clk} = \{200, 300\}$ MHz. The phase range under test is $[0, 2\pi]$. Both the estimated time delays and the phase difference were evaluated by outputting the PCS signal to a digital oscilloscope and measuring its duty cycle, and by reading the DW and FW captured by the FDC. For this latter acquisition, we collected $N = 15$ chunks containing $M = 1024$ samples of each signal, for each experimental sample (i.e. each RF phase jump). Each sample has $L = 7$ bits of depth.

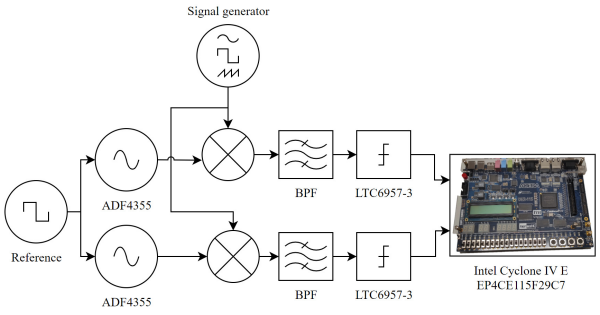

Figure 5.14: Setup block diagram for the phase estimation accuracy assessment.

To better analyze the results, the mean of the samples computed among the chunks was used as metric, according to

$$\begin{cases} \Delta\hat{\varphi}_j = \dfrac{2\pi}{N \cdot M} \displaystyle\sum_{k=1}^{N} \sum_{i=1}^{M} \mathrm{PW}^{(j)}(i,k) \\ \langle \Delta\hat{\tau}_j \rangle = \dfrac{1}{N \cdot M} \displaystyle\sum_{k=1}^{N} \sum_{i=1}^{M} \Delta\hat{\tau}_j(i,k) \end{cases} \tag{5.20}$$

where $\Delta\varphi_j$ is the estimation made for the j^{th} phase shift made by means of the phase word $\mathrm{PW}^{(j)} = \mathrm{DW}_r^{(j)}/\mathrm{FW}^{(j)}$, and $\Delta\hat{\tau}_j$ is the estimation made for the GT delay $\Delta\tau_j$ and $\langle\cdot\rangle$ the averaging operator.

5.3.3 Results

The results are presented in Figure 5.15a-5.15b for the time delays and in Figure 5.15c-5.15d for the phase difference estimation. A more compact view is in Table 5.2 where the Absolute Estimation Error (AAE) is employed as a metric to evaluate the achieved results.

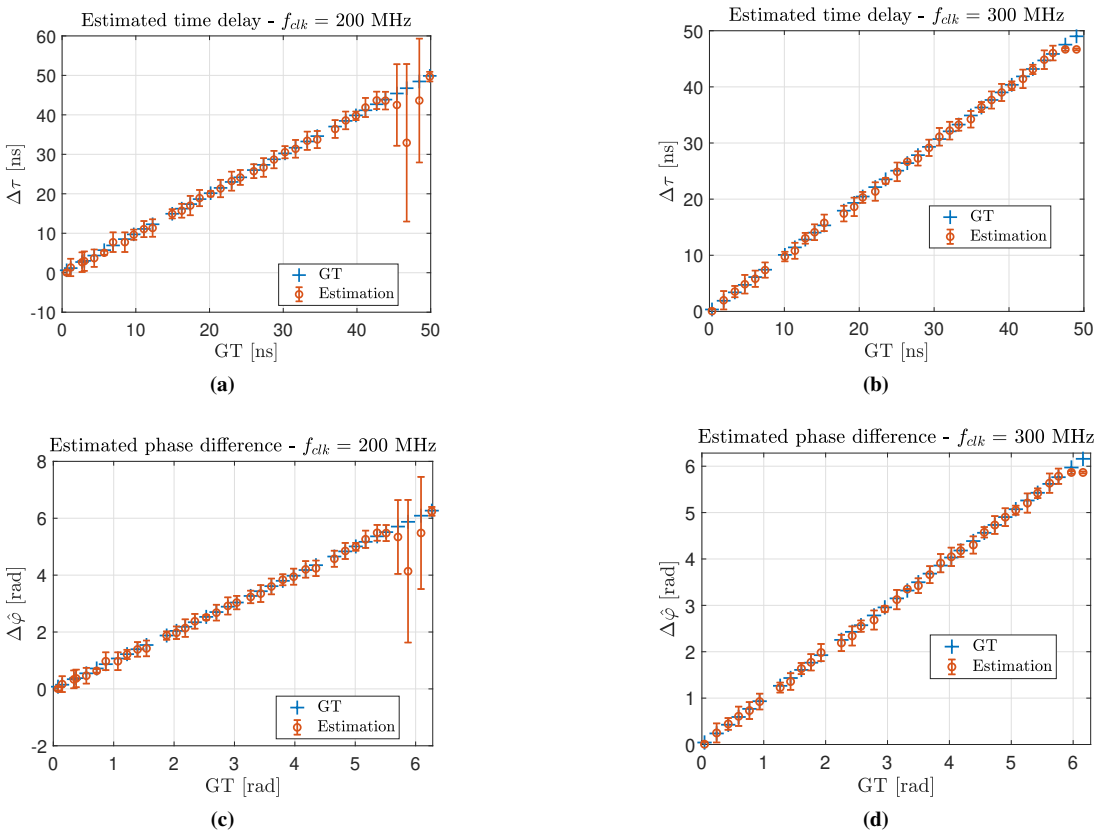

Figure 5.15: Results of the experimental campaign for estimating the time delays and the phase difference at clock frequencies $f_{clk} = \{200, 300\}$ MHz. In detail: (a) Time delay estimation at 200MHz and (b) 300MHz, (c) phase difference estimation at 200 MHz and (d) 300 MHz. The error bars indicate the uncertainty of the measure as the standard deviation from the mean for each measurement sample, and not from the GT.

Table 5.2: Statistical analysis of the AAE. In brackets, the increment with respect to the reference value.

	Max [rad]	**Mean [rad]**	**Std [rad]**
$f_{clk} = 200$ MHz	1.7371	0.1180 (+138%)	0.2994
$f_{clk} = 300$ MHz	0.4279	0.0614 (+24%)	0.0918

In particular, the AAE for the parameter Θ and experimental sample j is defined as

$$AAE(\Theta)_j = |\Theta_j - \hat{\Theta}_j| \tag{5.21}$$

where $\Theta = \{\Delta\varphi, \Delta\tau\}$ and $\hat{\Theta}$ denotes the estimation of the parameter Θ. For the results presented in Table 5.2 we considered the average and the standard deviation over the experimental samples for the AAE.
As it was expected, by incrementing the clock frequency, the AAE decreases. Moreover, it is evident how the standard deviation of the estimation error increases for low clock frequencies.

Another interesting detail involves the single estimation points. Both for the time delay and phase shift, it is visible an increase in the standard deviation of the single estimation, represented by the error bars, especially in those points that are between two periods, either picking the word representing 2π-x or x depending on the estimation made in that period and the signal's fluctuations. A finer clock frequency, instead, allows for a better resolution of the difference between the points and so, leads to a lower standard deviation and higher accuracy.
The percentage values in Table 5.2 are relative to the minimum achievable precision due to the word length:

$$\Delta\hat{\varphi}_{min}(L) = \frac{2\pi}{2^L - 1}\bigg|_{L=7} = 0.0495 \text{ rad} \tag{5.22}$$

5.4 Experimental evaluation of the AoA estimation accuracy

The AoA estimation accuracy was evaluated through another experimental setup that involved both hardware and software components. To assess the accuracy, the performance of the architecture was compared with reference array signal processing algorithms from literature: MUSIC, RMUSIC, and ESPRIT. To do so, their MATLAB implementations from the Phased Arrays System Toolbox were considered. Hence, it was necessary to store the waveforms of the received signals and process them through a MATLAB/Simulink model in charge of conditioning the experimental analog signals acquired by the receiving antennas, and feeding them to the digital hardware architecture and the reference algorithms. The interface between MATLAB and the hardware architecture was implemented inside the Intel Cyclone IV E EP4CE115F29C7 FPGA via the Simulink's FPGA-in-the-Loop® (FiL) feature [5]. The FiL feature was only employed as an interface between the stored waveforms and the FPGA.

To demonstrate the different performances achievable by simply scaling the clock frequency, the experiment was repeated at three different frequencies $f_{clk} = \{50, 100, 200\}$ MHz. Unfortunately, it was not possible to employ the same testbed for frequencies over 200 MHz, due to the limitations of the FiL feature [5].

5.4.1 Digital PUT

As the ACB-free architecture described in the previous section, also the complete architecture was prototyped on the Intel Cyclone IV-E EP4CE115F29C7 FPGA available on the Terasic DE2-115 development board, using the Intel Quartus Prime development environment.
The architecture has 4 input channels and delivers three estimations for each AoA. The DW length and the FW length have been set to $L = C = 8$ bits. The LUT address length is set to A = 7. The physical layout of the FPGA is shown in Figure 5.16.

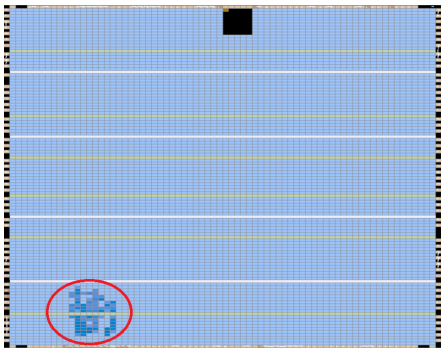

Figure 5.16: Layout of the proposed architecture mapped on the Intel Cyclone IV E EP4CE115F29C7 FPGA (4 channels, $L = C = 8$ bits, $A = 7$ bits).

Table 5.3 summarizes the FPGA fitting results in terms of resource allocation. The compilation reports outline a maximum clock frequency of 210 MHz and an estimated total power consumption of 136.73 mW.

Table 5.3: Intel Cyclone IV E EP4CE115F29C7 post-fitting resources occupancy summary.

Parameter	Value
Combinational Functions	1082
Logic Elements	1104 (0.98%)
Total registers	441
Total pins	27 (5%)

5.4.2 Experiment data acquisition

The experiment was conducted in an indoor environment (i.e., the laboratory) without any attempt to reduce or prevent the multipath phenomenon (Figure 5.17). Regarding the practical execution of the experiment, the transmitter was moved by an operator towards the different positions on the perpendicular to the array broadside axis, while the receiver was set to be fixed. The transmission frequency was chosen to be $f_{RF} = 3.36$ GHz, to be resilient to other telecommunication standard interference during the experiment. The distance was chosen to satisfy the condition of a plane wave. Given the considered frequency, the minimum distance is $l_{min} \approx 0.89$ m. Hence, the distance $l = 2.20$ m $> l_{min}$ was chosen. The transmitter radiated a CW signal at frequency f_{RF} with power $p_{tx} = +10$ dBm through the custom designed patch antenna

element described in Appendix A.1. The HP E4433B Series Signal Generator [6] was employed as the transmitter.

The receiving end of the system was composed of the custom-designed ULA and RF chains described in Appendix A.1 and A.3, respectively. The RF signal was down-converted to the IF $f_{IF} = 150$ MHz. The IF signal was then sampled and quantized through a digital oscilloscope with 12-bit ADC, 1 GHz bandwidth, and sampling frequency $f_s = 5$ GS/s. The local oscillator signal frequency was $f_{LO} = 3.21$ GHz generated through an Agilent N5182A Vector Signal Generator [7]. No hypothesis has been made on the synchronization between transmitter and receiver, i.e. each side of the communication pairs rely on its own frequency sources which are independent from one another.

The GT AoA to which compare the estimations is computed as

$$\vartheta(x) = \arctan\left(\frac{x}{l}\right) \cdot \frac{180}{\pi} \tag{5.23}$$

To study the repeatability of the estimations, for each experiment, 20 traces were acquired. Each of the acquisitions spanned the downconverted signal dynamic for a time window of 2 µs. To ensure statistical independence, each trace acquisition has been taken after an idle interval of time of 500 ms.

The calibration point is set in the geometrical center of the array at broadside distance l in the absolute reference system, to seek for the calibration condition:

$$\vartheta_{12} = \vartheta_{23} = \vartheta_{34} = 0 \tag{5.24}$$

5.4.3 Data processing and digital hardware interfacing

The receiver side of the architecture is depicted in Figure 5.18. The results of the oscilloscope acquisition were first undersampled to the clock frequency employed for performing the test, and then digitally downconverted, to the frequency $f_{IF} = 5$ MHz. Then, the waves are fed to a block whose operation models the behavior of a squaring

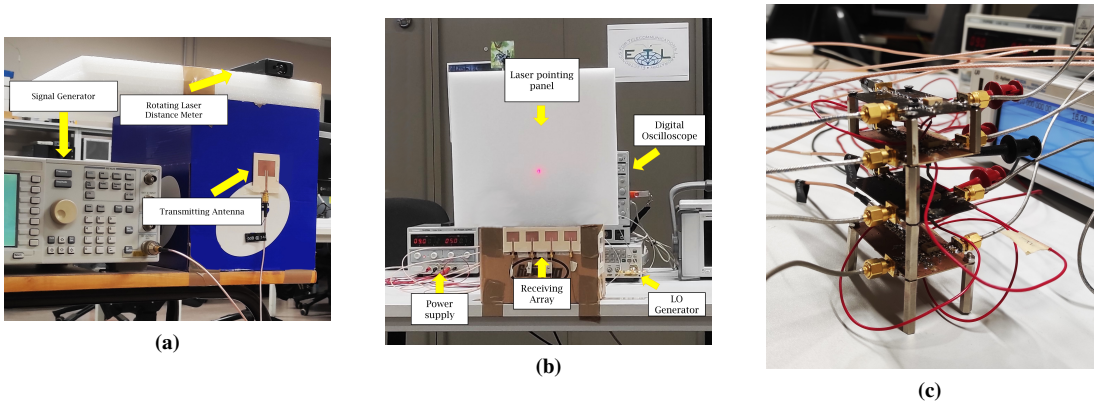

(a) (b) (c)

Figure 5.17: (a) Transmitter setup: transmitting antenna, signal generator, and laser distance meter to evaluate both l and x. (b) Receiving array setup. Behind the pointing panel, it is possible to glimpse the digital oscilloscope and the LO signal generator. (c) The connection of 4 different front-ends to the antenna array elements and to the oscilloscope.

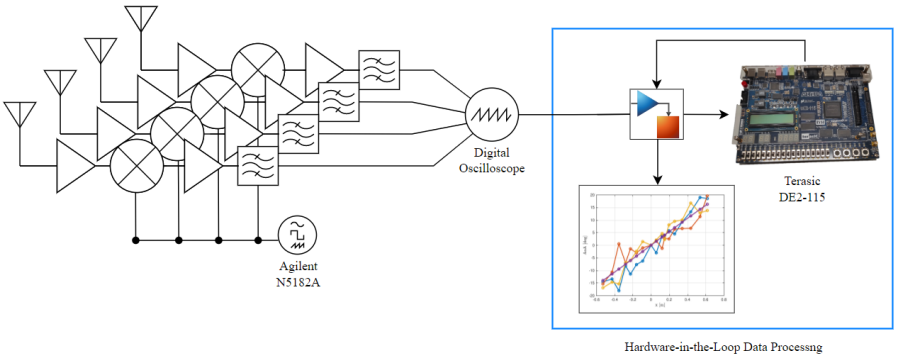

Figure 5.18: Block diagram depicting the receiver side of the experimental setup, along with the interfacing with Simulink.

circuit and is summarized in Algorithm 3. The output of this block is then processed through the FiL feature of MATLAB/Simulink (Figure 5.19) via Ethernet interfacing [5].

Algorithm 3 Squaring block model requiring high and low voltage thresholds V_H, V_L and discrete time input signal s.

Require: $V_H, V_L, s(k-1), s(k)$
  $\Delta = s(k) - s(k-1)$
  if $s(k) < V_L \wedge \Delta < 0$ **then**
    $y(k) = 0$
  else if $s(k) \geq V_H \wedge \Delta \geq 0$ **then**
    $y(k) = 1$
  else if $s(k) < V_H \vee s(k) \geq V_L$ **then**
    if $\Delta \geq 0$ **then**
      $y(k) = 0$
    else
      $y(k) = 1$
    end if
  end if
  return $y(k)$

This feature enables feeding the PUT with data from MATLAB/Simulink and captures the results of the computations. For each of the clock frequencies $f_{clk} = \{50, 100, 200\}$ MHz, a different programming binary file for the FPGA was generated.

The estimation of the AoA corresponding to the position x relative to the calibration point through the antenna pair composed by the elements i, j is denoted as $\hat{\vartheta}_{ij}(x)$. The considered antenna pairs are $\{12\}, \{23\}, \{34\}$.
Figures 5.20b-e, show some of the output test signals from the FiL block. Moreover, Figure 5.20a shows the input signal to the squarer block, and Figure 5.20f shows the AoA output plot.

Given the availability of three different estimations (one for each antenna pair), their average was considered. As already discussed, the estimation results of the architecture were compared to the MATLAB implementations of the MUSIC, RMUSIC, and ESPRIT algorithms through the built-in functions `musicdoa`, `rootmusicdoa`

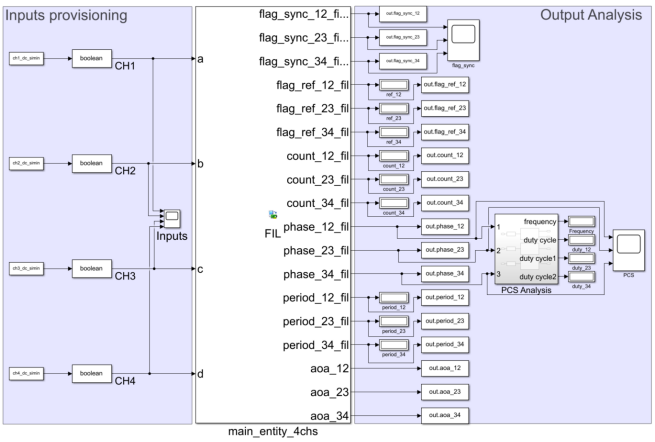

Figure 5.19: FiL block diagram for testing the digital architecture.

and `espritdoa` [8]. The sampling frequency for those signals was kept at $f_s = 5$ GS/s. For a more fair comparison of the results, the angle was quantized to be represented with the same precision as the ones in the digital hardware LUT.

5.4.4 Comparison metrics

Two error metrics were employed to evaluate the performances in terms of precision: the absolute error (also referred to as Absolute Estimation Error, AEE) and the Root Mean Square Error (RMSE) [9]. The precision of each experiment is computed with respect to the three considered algorithms.

Absolute Estimation Error The absolute error is computed for each position by considering the average estimation over the available acquisitions performed on the channels. Recalling there are $P = 20$ acquisitions available:

$$err_{mean}(x) = \frac{1}{P}\sum_{p=1}^{P} |\hat{\vartheta}_p(x) - \vartheta(x)| \tag{5.25}$$

with

$$\hat{\vartheta}_p(x) = \frac{1}{|\mathbf{C}|}\sum_{i\in\mathbf{C}} \hat{\vartheta}_i^p(x) \tag{5.26}$$

where $\mathbf{C}$ denotes the set of antenna pairs, $\mathbf{C} = \{12\}, \{23\}, \{34\}$, and $\hat{\vartheta}_i^p(x)$ denotes the estimation made through antenna pair $i \in \mathbf{C}$ when employing the sample p in position x.
The AEEs for the algorithms employed were computed as

$$err_{\alpha}(x) = \frac{1}{P}\sum_{p=1}^{P} |\hat{\vartheta}^{\alpha,p}(x) - \vartheta(x)| \tag{5.27}$$

where $\hat{\vartheta}_p^{\alpha}(x)$ denotes the estimation made by employing the sample p in position x using the algorithm $\alpha \in \mathcal{A}$, with $\mathcal{A}$ being the set of algorithms.

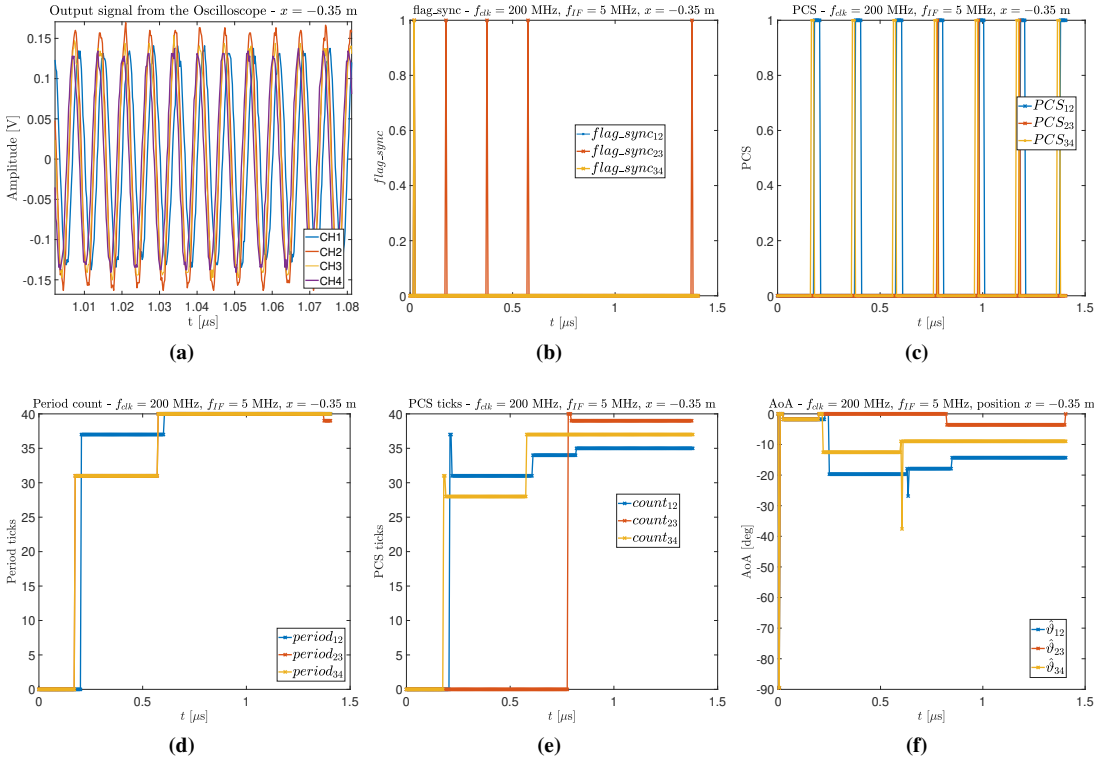

Figure 5.20: Example of the output signals from the digital architecture: (a) Zoom on the output signal from the digital oscilloscope (b) Synchronization flag (c) PCS (d) estimated period ticks count (e) estimated PCS ticks count (f) AoA output from the LUT.

Root Mean Square Error The adoption of the RMSE as a cumulative error evaluation metric is justified by the fact that it emphasizes the errors occurring in a much stronger way than the mean AEE. Two different kinds of RMSE were evaluated. The first one concerns the estimation made through each antenna pair by considering the increasing number of available experimental sample repetitions for each position. The cumulative average operator $\mathbb{A}(\gamma \,|\, q)$ for estimating γ is defined as:

$$\mathbb{A}(\gamma \,|\, q) = \frac{1}{q} \sum_{c=1}^{q} \gamma(c) \tag{5.28}$$

with γ being the parameter of interest varying on the repeated measure set. Therefore:

$$\mathrm{RMSE}_{ij}(q) = \sqrt{\frac{1}{|\mathbf{X}|} \sum_{x \in \mathbf{X}} \left[\mathbb{A}(\hat{\vartheta}_{ij}^{q}(x) \,|\, q) - \vartheta(x) \right]^2} \tag{5.29}$$

The second RMSE considered is the one regarding the cumulative average of the estimations made through the average AoA estimated by each antenna pair. The RMSE considering q samples is defined as:

$$\mathrm{RMSE}_{mean}(q) = \sqrt{\frac{1}{|\mathbf{X}|} \sum_{x \in \mathbf{X}} \left[\frac{1}{|\mathbf{C}|} \sum_{i \in \mathbf{C}} \mathbb{A}(\hat{\vartheta}_i(x) | q) - \vartheta(x) \right]^2} \tag{5.30}$$

with $\mathbf{X}$ denoting the set of positions relative to the array center position. Those two RMSE computations were compared to the ones achieved by using the three reference algorithms, taking into account the cumulative average made on the available experiment repetitions. Each experimental sample repetition contains 10 signal periods of the IF.

5.4.5 Results

The first analysis performed is the SNR evaluation of each experimental sample. Figure 5.21 depicts, for each position, the average SNR of all acquired samples.

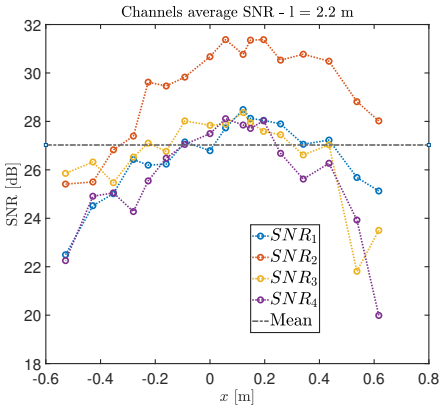

Figure 5.21: Average SNR for each position and channel.

As can be easily observed, the SNR for channel 2 is sensibly higher than the others. This is due to the fact nominally identical front-end prototypes can lead to different signal power levels due to realization mismatches. However, all the channels experience the same behavior, with the SNR lowering in the positions far from the array center. This is because the transmitting terminal approaches the walls, so there is an increase of the reflected paths that destructively compose at the receiver side, and hence the SNR lowering.

Figure 5.22 summarizes, for each clock frequency, the results of our hardware architecture and then compares them with the results obtained for the MATLAB reference algorithms. The single antenna pair estimations tend to be less accurate in estimating the GT, especially at $f_{clk} = 50$ MHz. As expected, when considering lower clock frequencies, the average curve tends to be less precise. However, as shown in Figure 5.22g, increasing clock frequency allows the proposed architecture to outperform the reference algorithms.

To quantify the achieved precision, first it was analyzed the AAE. The results are depicted in Figure 5.23a-b-c as empirical Cumulative Distribution Functions (CDFs) of the AEE, for each of the three clock frequencies and for each approach under analysis. When considering lower clock frequencies the AAE error increases, but when considering the maximum available clock, the result is 13 to 19% better than the one achieved with the reference algorithms.
In addition, the proposed architecture has the major advantage of requiring a significantly lower computational complexity. The time needed for the execution of the reference algorithms is sensibly lower because of the simpler operations to perform.

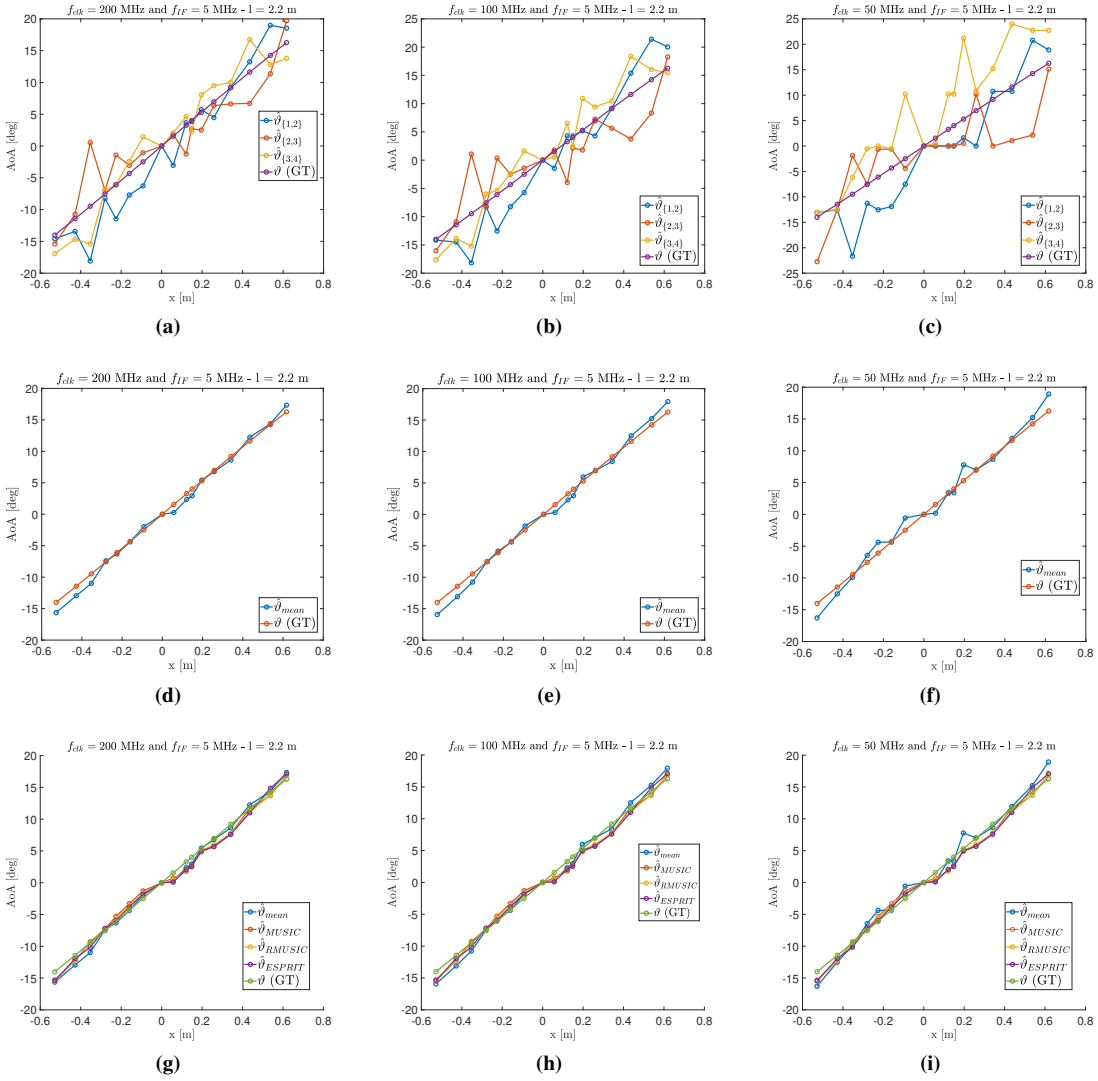

Figure 5.22: Experiment results: antenna pairs estimations with (a) $f_{clk} = 200$ MHz (b) $f_{clk} = 100$ MHz and (c) $f_{clk} = 50$ MHz. Figures (d)-(e)-(f) show the average estimations for the available antenna pairs at $f_{clk} = 200$ MHz, $f_{clk} = 100$ MHz and $f_{clk} = 50$ MHz respectively. Figures (g)-(h)-(i) show the comparison of the mean value with the considered reference algorithms at the usual frequencies.

Moreover, as expected, for all the considered algorithms the errors are higher in those positions where the SNR was said to be lower due to higher multipath components. Therefore, the results considering the cumulative RMSE of the mean estimation were analyzed. Figure 5.23d-e-f summarize the results. For high clock values the RMSE again decreases, and is either very close or in the case of MUSIC about 10 to 40% lower than the references. Furthermore, the independence between the number of samples considered for the estimation and the RMSE suggests that the proposed AoA approach is actually eligible for real-time and memory-less implementations. Finally, by looking at the RMSE of each individual channel with respect to the number of samples, it is apparent that the fluctuations observed have the same magnitude as the ones in the global RMSE.

Table 5.4 summarizes the results of the comparison between the AEE and the RMSE for the three clock frequency realizations of the proposed approach and the three other classical algorithms. In detail, with respect to the RMSE, the table summarizes the average values, the standard deviation values, and the maximum values over all the available periods.

5.5 Conclusions

In this chapter, a novel architecture for real-time AoA estimation based on phase interferometry was introduced. The architecture is fully digital and synchronous.

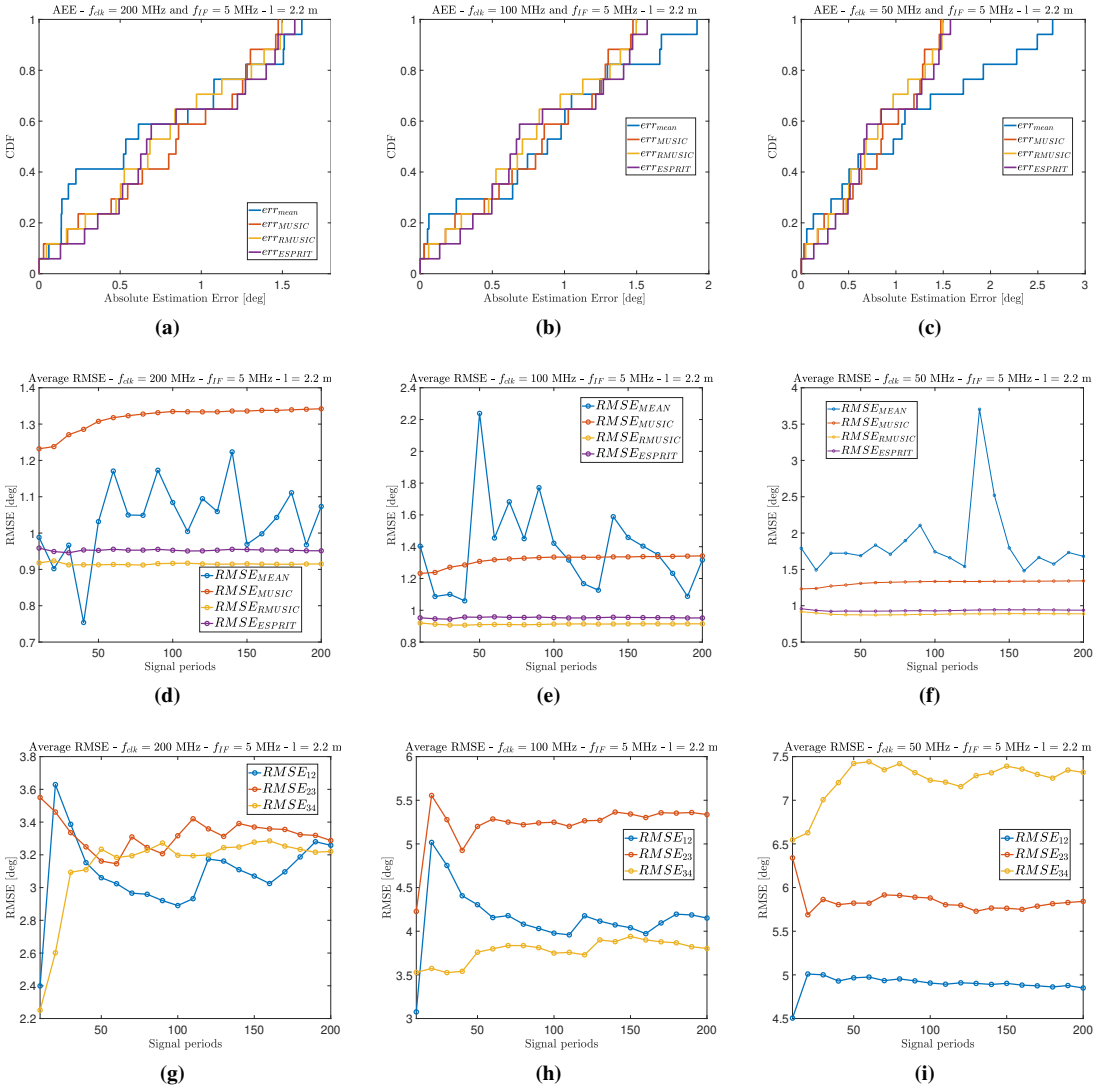

Figure 5.23: Comparison of the empirical CDF for the AEE of the proposed approach and the three reference algorithms when considering (a) $f_{clk} = 200$ MHz (b) $f_{clk} = 100$ MHz and (c) $f_{clk} = 50$ MHz. Figures (d)-(e)-(f) show the RMSE comparison of the proposed approach with the three algorithms for $f_{clk} = 200$ MHz, $f_{clk} = 100$ MHz and $f_{clk} = 50$ MHz respectively. Figures (g)-(h)-(i) show the comparison of the RMSE for each of the three antenna pairs for $f_{clk} = 200$ MHz, $f_{clk} = 100$ MHz, and $f_{clk} = 50$ MHz respectively.

Table 5.4: Statistics on the AEE and on the RMSE for the analyzed approaches and clock frequencies. All the values are expressed in degrees. (and $\pm\%$ error vs reference)

	f_{clk} 200 MHz [reference]	f_{clk} 100 MHz	f_{clk} 50 MHz	MUSIC	RMUSIC	ESPRIT
			AEE			
Mean	0.67	0.83 (+24%)	1.04 (+55%)	0.79 (+18%)	0.76 (+13%)	0.80 (+19%)
Std	0.57	0.62 (+ 8%)	0.90 (+58%)	0.49 (-14%)	0.48 (-16%)	0.50 (-12%)
Max	1.61	1.92 (+19%)	2.65 (+64%)	1.47 (- 8%)	1.50 (- 7%)	1.58 (- 2%)
			RMSE			
Mean	1.02	1.38 (+35%)	1.85 (+81%)	1.28 (+25%)	0.89 (-12%)	0.93 (- 9%)
Std	0.10	0.28 (+180%)	0.49 (+390%)	0.07 (-30%)	0.01 (-90%)	0.01 (-90%)
Max	1.22	2.23 (+83%)	3.70 (+203%)	1.23 (-0.8%)	0.92 (-24%)	0.96 (-21%)

The proposed solution is modular, and varying the clock frequency allows us to achieve different levels of granularity for the AoA estimation. The experimental analysis proved the capability of the approach to operate in real-time. The obtained performance confirms the possibility of employing the proposed technique for implementing real-world applications where other classical algorithms for AoA estimation are adopted.
Moreover, the proposed architecture can be integrated into an ASIC to deploy a low-cost RTLS solution, given the limited prototype area occupation.

References

[1] X. Liu, Y. Xie, H. Chen, and B. Li, "Implementation on FPGA for CORDIC-based computation of arcsine and arccosine," in *IET International Radar Conference 2015*, 2015, pp. 1–4.

[2] "FPGA Data Capture - MATLAB & Simulink," (Last accessed on 05-Mar-2023). [Online]. Available: https://www.mathworks.com/help/hdlverifier/fpga-data-capture.html

[3] "ADF4355 Datasheet and Product Info, Analog Devices," (Last accessed on 05-Mar-2023). [Online]. Available: https://www.analog.com/en/products/adf4535.html

[4] "LTC6957 Datasheet and Product Info | Analog Devices," (Last accessed on 05-Mar-2023). [Online]. Available: https://www.analog.com/en/products/ltc6957-1.html#product-overview

[5] "FPGA-in-the-Loop - MATLAB & Simulink," (Last accessed on 07-Nov-2022). [Online]. Available: https://www.mathworks.com/help/hdlverifier/fpga-in-the-loop.html

[6] "E4433B ESG-D Series Digital RF Signal Generator, 4 GHz, Keysight," (Last accessed on 07-Nov-2022). [Online]. Available: https://www.keysight.com/us/en/product/E4433B/esgd-series-digital-rf-signal-generator-4-ghz.html

[7] "5182A MXG Vector Signal Generator, 100 kHz to 6 GHz, Keysight," (Last accessed on 07-Nov-2022). [Online]. Available: https://www.keysight.com/us/en/product/N5182A/mxg-vector-signal-generator-100khz-6ghz.html

[8] "Direction of Arrival Estimation - MATLAB & Simulink - MathWorks," (Last accessed on 07-Nov-2022). [Online]. Available: https://www.mathworks.com/help/phased/direction-of-arrival-doa-estimation-1.html

[9] S. M. Ross, "Chapter 7 - parameter estimation," in *Introduction to Probability and Statistics for Engineers and Scientists (Fifth Edition)*, 5th ed., S. M. Ross, Ed. Boston: Academic Press, 2014, pp. 235–296.

CHAPTER 6

LEO-based Coarse Positioning through AoA Estimation

This chapter is based on the visit final report edited during the permanence as Visiting Expert at the European Space Research and Technology Centre (ESTEC) of the European Space Agency (ESA), Commercial User Segment and Navigation System Validation Section, Radio Frequency Systems Division, Electrical Department, Directorate of Technology, Engineering and Quality (TEC-ESG).

This chapter introduces a novel coarse positioning technique based on AoA estimation through phase interferometry from multiple receiver nodes. The technique works with SoOp from LEO spacecraft. The AoA estimations are used in a simplified flat-earth geometric model to determine the 2D target position given the position of a reference node. The phase estimation is performed through the hardware architecture presented in Chapter 5. The architecture was prototyped on a Digilent Nexys A7 Development Board for the AMD Xilinx Artix-7 100T FPGA. A robust measurement campaign was designed and performed to assess the viability of this approach, determining the overall positioning accuracy of the developed system and meticulously analyzing the possible contributions to its accuracy degradation.

6.1 Context

When employing geometrical localization techniques the loss of LoS can lead to a huge precision degradation [1]. The existence of a non-negligible signal power ratio between secondary and direct paths demands complex techniques for achieving better performance. Those techniques can be both time-consuming and computationally complex. In a Space-to-Earth (S2E) link, the direct path is usually the strongest component.

Hence, it began to be exploited as a way to perform localization. Well-known examples which constitute the *de facto* standard for positioning are the GNSSs, enabling positioning services that can reach a meter-level accuracy under the best conditions [2], along with navigation and timing services. Those services are deployed through launching specific constellations of satellites in the MEO (2000 km $\leq h < 35786$ km in altitude) and Geostationary Earth Orbit, GEO ($h = 35786$ km) [3]. Due to the high distance from the Earth's surface, the signal experiences a high path loss that impacts the positioning accuracy or even prevents its use in indoor or dense urban environments [4].

During the last decades, the space industry started to invest in the LEO, i.e. at altitudes from a few hundred to a thousand kilometers. LEO allows to achieve lower transmission delays and path-loss than the MEO and GEO constellations, at the cost of a higher Doppler shift because of the higher speeds [2]. The first LEO constellations were mostly employed for telecommunications purposes, in particular voice services and low-speed data transfer, like Iridium, Globalstar, and Orbcomm [5]. Lately, other services were provided from other constellations, like Starlink (from SpaceX), Project Kuiper (from Amazon), and OneWeb for broadband internet access or Argos for earth observation [4].

Several approaches are proposed in the literature for the development of LEO positioning systems [6]. The first one is to employ LEO for rebroadcasting GNSS signals from MEO constellations with higher power on other frequency bands [3]. The performance can sensibly increase when compared to classical GNSS, but still, it is required to increase the mission costs since it is necessary to equip the LEO spacecraft with expensive and dedicated hardware for the PNT purposes. A second possible approach is to use LEO positioning systems as support to GNSS in GNSS-denied areas [7]. One example is the Iridium Satellite Time and Location (STL) signal. Another approach is to deploy a specific LEO-PNT solution with optimized design parameters. However, still in the last two examples, specific equipment for the LEO satellites must be deployed. Some constellations are already providing navigation messages to their subscribers containing information on the range and the orbit [8]. However, the service is not publicly available.

A possible solution that does not impact the space segment is represented by the positioning through SoOp. SoOp are defined as signals which do not carry any specific positioning information since they are designed for other purposes. The position retrieval is in charge of the receiver by means of the measurement of the RSS, ToA/TDoA, AoA, FDoA or Doppler shift [3]. A distinction is made between terrestrial (e.g. radio, cellular, television) and non-terrestrial SoOp, i.e. LEO communication satellites signals [9]. As previously mentioned, non-terrestrial SoOps have the great advantage of a better LoS. Also, SoOps enable the reuse of the existing signals for a novel purpose, rather than implementing new standards.

The aim of the proposed solution is to provide the first estimation with the lowest latency and with low complexity. Hence, the coarse positioning system introduced in this chapter is based on the real-time AoA estimation of SoOp from multiple receivers through phase interferometry of a pilot tone signal. Pilot tone signals are present in the Iridium downlink signals (Figure 6.1). The main reason behind the choice of this reference constellation is because of its great coverage: thanks to its polar orbit, the

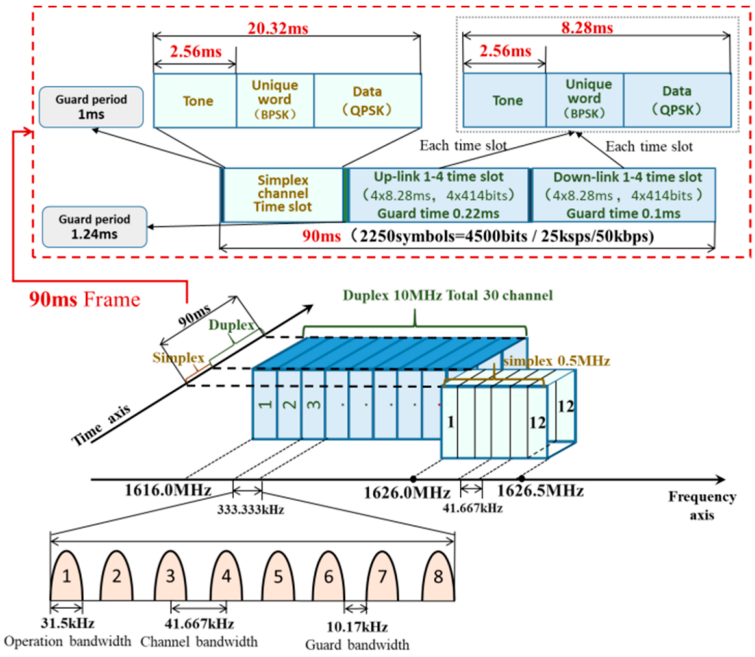

Figure 6.1: The Iridium frame structure. Image by *Tan et al.* from [10]. *Image licensed under CC BY 4.0.*

constellation allows it to cover the entire Earth's surface in an efficient way [11]. Previous works in literature make use of Iridium SoOp to perform localization. Most of them are based on the estimation of the Doppler shift, which is employed for spacecraft trajectory tracking. Thanks to Bayesian filtering and Kalman filtering, those time-varying measurements can lead to position determination [2, 12]. In [13], *Lang et al.* propose an anchor-aided localization scheme based on one Iridium downlink signal. The scheme requires a minimum knowledge of the Iridium spacecraft's position and velocity that is obtained by means of the SGP84 model [14]. *Tan et al.* [5] propose a Doppler-based positioning scheme based on a single satellite. The assessment is made through the TDS-1 by Surrey Satellites. *Huang et al.* in [8] propose an approach based on the Doppler shift estimation in time domain by measuring the change rate of the phase and by performing curve fitting on the obtained data. The entire Iridium burst is employed, both pilot and modulated signal. Even if more accurate, Doppler positioning relies on highly nonlinear equations, thus making the positioning system complex and not capable of operating in real-time [15].

6.2 Geometrical Model

The simplified geometrical model for 2D distance and position estimation based on AoA estimation from multiple receivers is introduced in this section. The reference situation is depicted in Figure 6.2a. The setting involves an anchor node, A, with known coordinates (x_A, y_A, z_A), a target node $T = (x_T, y_T, z_T)$ and the spacecraft $S = (x_S, y_S, z_S)$. The target and the anchor node are static and the spacecraft is moving. The position of each element in the setting can be described in terms of azimuth and elevation angles with respect to the observation point i, denoted as α_i and ε_i respectively.

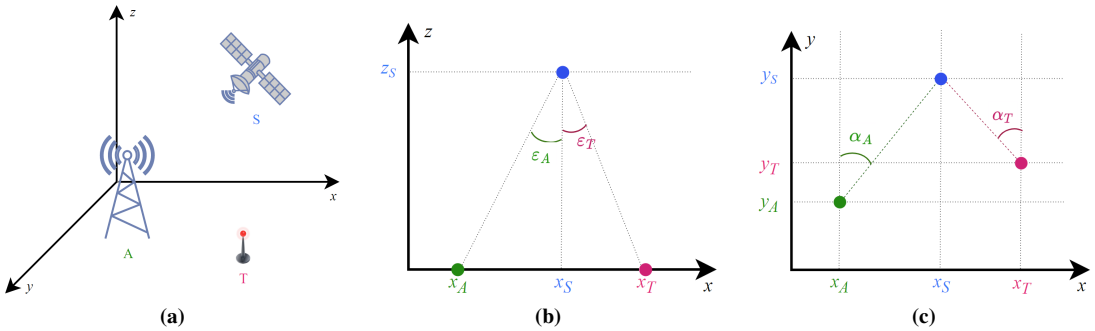

Figure 6.2: Reference sketches for the geometrical model: (a) 3D view of the scenario, (b) elevation plane view (xz-plane), and (c) azimuth plane view (xy-plane).

The plane extension has to be sufficiently limited to consider the flat-earth approximation valid.
From the hardware equipment point of view, the anchor and the target nodes must be equipped with a planar array of antennas. Also, the anchor and the target have to rely on a clock synchronization technique.

6.2.1 Derivation of the relative position from AoA estimation

For the derivation of the equations, the 3D model is split into two planes: the azimuth plane (xy-plane) and the elevation plane (xz-plane).
Consider the elevation plane, as represented in Figure 6.2b. Since $z_S \gg z_A, z_T$ we can assume those last two to be negligible. Hence, taking into account the different orientations of the angles, we can write:

$$\begin{cases} x_S - x_A = z_S \tan \varepsilon_A \\ x_T - x_S = -z_S \tan \varepsilon_T \end{cases} \tag{6.1}$$

Therefore, by summing member-to-member the two equations,

$$x_T - x_A = z_S(\tan \varepsilon_A - \tan \varepsilon_T) \tag{6.2}$$

By looking at the azimuth plane (as in Figure 6.2c), it is possible to write the trigonometric relationships as did before:

$$\begin{cases} x_S - x_A = (y_S - y_A) \tan \alpha_A \\ x_T - x_S = (y_S - y_T) \tan \alpha_T \end{cases} \tag{6.3}$$

Therefore,

$$\begin{cases} y_S - y_A = \dfrac{(x_S - x_A)}{\tan \alpha_A} \\ y_S - y_T = \dfrac{(x_T - x_S)}{\tan(-\alpha_T)} \end{cases} \tag{6.4}$$

By substituting what was found in (6.3),

$$\begin{cases} y_S - y_A = z_S \dfrac{\tan \varepsilon_A}{\tan \alpha_A} \\ y_T - y_S = z_S \dfrac{\tan \varepsilon_T}{\tan \alpha_T} \end{cases} \tag{6.5}$$

By summing the two linear system members,

$$+y_T - y_A = z_S\left(\frac{\tan\varepsilon_A}{\tan\alpha_A} + \frac{\tan\varepsilon_T}{\tan\alpha_T}\right) \tag{6.6}$$

Hence, the position (x_T, y_T) is determined as:

$$\begin{cases} x_T = z_S(\tan\varepsilon_A - \tan\varepsilon_T) + x_A \\ y_T = z_S\left(\dfrac{\tan\varepsilon_A}{\tan\alpha_A} + \dfrac{\tan\varepsilon_T}{\tan\alpha_T}\right) + y_A \end{cases} \tag{6.7}$$

It is worth mentioning that if we consider the time series of the estimated AoAs for both anchor and target nodes, that estimation can be employed for generating a sequence of estimations for the position of the target with respect to the anchor. Those values can be averaged over a proper time window to refine the final result or establish a closed-loop estimation aiming to minimize the error. In this work, a memoryless open-loop estimation is employed. Furthermore, it is clear how the AoA estimation accuracy directly impacts the position estimation.

6.2.2 The needed AoA estimation precision

It is interesting to investigate the needed AoA resolution (i.e. the minimum resolvable AoA) to distinguish two points in the space. To do so, it was performed a simulation. Considering the Netherlands as the reference zone, the following approximations hold:

$$\begin{cases} 1^\circ_{latitude} \approx 111 \text{ km} \\ 1^\circ_{longitude} \approx 66 \text{ km} \end{cases} \tag{6.8}$$

A 20 x 20 grid point map was created with 250 m of spacing and the AoAs both for azimuth and elevation were computed for each one of those positions, and compared to the fixed one.
Considering the height associated to LEO, the results are in Figure 6.3. Figure 6.3a depicts the azimuth angle deviation while Figure 6.3b the elevation one.

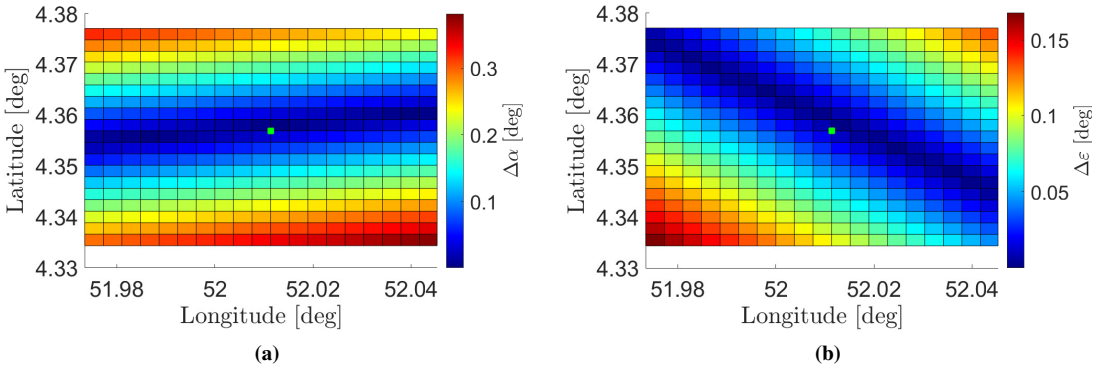

Figure 6.3: Needed AoA accuracy for discriminating points on Earth for signals coming from LEO. Each of the squares has a side lenght 250 m.

To distinguish distances up to 250 meters, a high level of precision (on the order of hundredths of degrees) is required. As anticipated, pure AoA estimation alone is insufficient for achieving precise positioning without additional post-processing. Consequently, this approach is more suitable for coarse positioning. Increasing the accuracy would necessitate an AoA precision that would result in significant computational effort and require a powerful receiving front end. This would contradict the objective of maintaining low complexity.

6.3 Experiments description

This section describes the experimental setup and the motivations behind the choices in the experiment arrangement. The aim was to track the azimuth and the elevation AoAs of a signal transmitted by a moving spacecraft in the LEO and to exploit those angular estimations to determine the position of the target node according to the anchor's one. In detail, the objectives of the experimental campaign were:

- Testing the angular estimation accuracy.
- Comparing it with other approaches to assess its performance.
- Verifying the reliability of the simplified geometrical model.
- Assessing the accuracy of the estimated position.

The hardware signal acquisition chain is sketched in Figure 6.4a. The data processing stages are represented as a block diagram in Figure 6.4b.

6.3.1 Setup description

The signal data were generated through the Spirent TS1140 Multi Output GNSS Signal Generator, configured to operate in Dual-box mode, i.e. the outputs can be provided by the two GNSS generators in Figure 6.5a.
The signal generators were governed by the Spirent SimGEN software, with a customized scenario. For the space segment, the scenario involved the simulation of a LEO spacecraft transmitting a CW signal at frequency $f_{RF} = 1575.42$ MHz in the L1 band, because of licensing limitations.

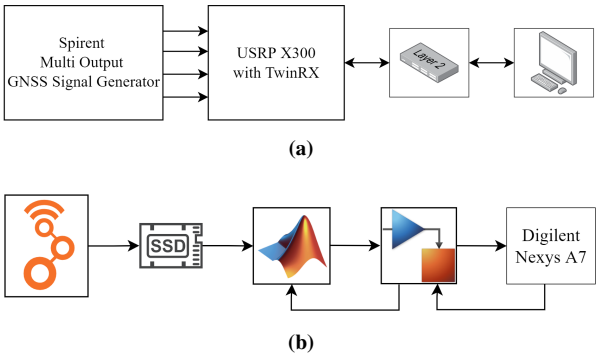

Figure 6.4: Block diagram of (a) the hardware chain involved in the sample acquisition and (b) the software data acquisition and processing chain.

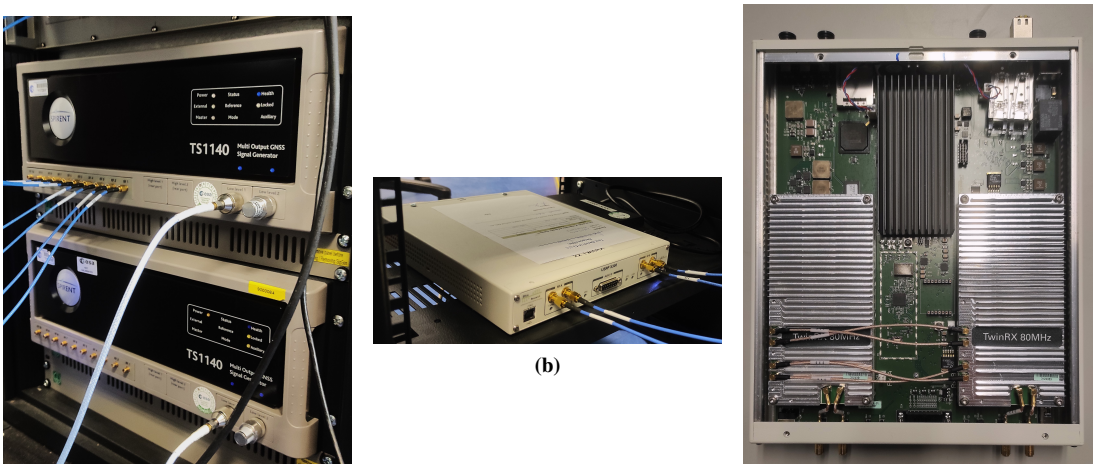

(a) (b) (c)

Figure 6.5: (a) The Spirent TS1140 Multi Output GNSS Signal generator boxes: the upper principal box and the lower box in auxiliary mode. (b) The USRP X300 by Ettus Research equipped with the pair of TwinRx daughterboards connected to the Spirent Signal generator through four shielded coaxial cables. (c) Internal of the USRP X300 showing the TwinRx daughterboards and the connections to the 4 rx channels and for the LO sharing.

The base signal power was set to -120 dBm, with the simulator modulating it according to the spacecraft movements and the geometric path loss model. As regards the radiowaves propagation setting, the scenario involved a pure LoS between the satellite and the target, with a specific model for the propagation artifacts. In particular, for the tropospheric model, the SimGEN was set to simulate a tropospheric delay according to the NATO Standard Agreement STANAG 4294 with a surface refractivity index 324.8. As regards the ionospheric model, the delay model is the default method employed for the GPS (Klobuchar ionospheric model). The ionospheric model switch altitude from terrestrial to spacecraft is set to 80 km. For the ground segment, the simulation involved two static vehicles, one for the reference node and one for the target. Each of the vehicles was equipped with a 2x2 URA in which each antenna element had an omnidirectional pattern. The array spacing was set to 9.5 cm which grossly approaches $\lambda/2$ in the L1 band. Each of the antenna elements' output was mapped to a proper signal generator output.
During each simulation, various parameters were logged to serve as GT for the final estimation. The log entries were generated with a time step of 50 ms. The SimGEN logs represent both azimuth and elevation angles with a precision up to the fourth decimal digit. Moreover, the satellite positions were logged as Earth-Centered Earth-Fixed (ECEF) and Azimuth Elevation Range (AER) coordinates systems. The position of the vehicles was logged also in Latitude Longitude Height (LLH) geodetic coordinate system. An example of the logs is in Figure 6.6.

The outputs of the signal generator were connected to a USRP X300 [16] equipped with a pair of TwinRX daughter boards [17]. The USRP X300 by Ettus Research [16] (Figure 6.5b) is a high-performance and scalable Software Defined Radio (SDR) platform. It can be equipped with up to two wideband daughterboards covering a frequency range from 0 to 6 GHz with up to 160 MHz of bandwidth for each daughterboard. It provides multiple high-speed interfaces such as the PCIe, the Dual 10Gb

Ethernet, and the Dual 1 Gb Ethernet. The core of the device is a Xilinx Kintex-7 XC7K325T FPGA. It also provides an ADS62P48 14 bit 200MS/s ADC and an AD9146 16 bit 800MS/s DAC both from Analog Devices. Two master clock rates are supported: 200 MHz and 184.32 MHz. Both can be decimated through a 10 bits word. The clock is cleaned thanks to an LMK04816BISQ Jitter Cleaner with dual loop PLLs.
The TwinRX is a daughterboard for the USRP X300 designed for spectrum monitoring and direction-finding applications. It deploys a two-channel superheterodyne receiver. The RF frequency range spans 10 to 6000 MHz with 80 MHz bandwidth for each channel. It is delivered with RF shielded to avoid coupling providing nominally independent RF signal channels with optional LO sharing between them. For each channel, the tuning is independent. Receiver gains range from 0 to 93 dB. A block diagram provided by Ettus Research is shown in Figure 6.7. In the L1 band, the noise figure can range up to 5 dB. All RF ports are matched to 50 ohms with a return loss that can range up to -10dB. In this work, it was used a pair of TwinRx daughterboards which were cabled to share the same LO available in channel 1 (as shown in Figure6.5c). The USRP was connected to a Gigabit Ethernet switch which allowed it to connect also a host computer to a Layer 2 network. The SDR hardware will be managed through GNU Radio [18]. GNU Radio is a C++ written framework distributed under the terms of the GNU General Public Licence (GPL). It provides the possibility to simulate various digital signal processing features or with external hardware such as the USRP, it is capable of managing digital signal stream in near real-time. GNU Radio comes with GRC, a graphical interface that makes it easier to define functions and operations thanks to a modular approach. The whole SDR application looks like a chain of sub-elements, each one of them fully customizable in the spirit of the SDR paradigm. The set of chains that are implemented for a single application is called a flowgraph. The flowgraph used in the experiments is shown in Figure 6.8.
To enable LO sharing between the two daughter boards it is necessary to introduce specific attribute values in the object interfacing the USRP with GRC software. Three possible values can be set for the LO-sharing option. The internal setting allows to employ the internal LO for each channel on the same TwinRX unit. The companion setting allows to use the same LO as the companion channel on the same TwinRX

sat_data_V1A1.csv

	A	B	C	D	E	F	G	H	I	J	K	L	M	N	O	P	Q
							satdataV1A1										
	Time_ms	Channel	Sat_type	Sat_ID	Sat_PRN	Echo_Num	Sat_Pos_X	Sat_Pos_Y	Sat_Pos_Z	Sat_Vel_X	Sat_Vel_Y	Sat_Vel_Z	Azimuth	Elevation	Range	PRangeGro...	PRangeG
	Number	Number	Categorical	Number	Number	Number	Number	Number	Number	Number	Number	Number	Number	Number	Number	Number	Number
4	L1/E1/S/B1I	L2/E6/B2I	L5/E5/B2A/...	L6/B1C/C2	B3I/C3	B2b											
5	Time_ms	Channel	Sat_type	Sat_ID	Sat_PRN	Echo_Num	Sat_Pos_X	Sat_Pos_Y	Sat_Pos_Z	Sat_Vel_X	Sat_Vel_Y	Sat_Vel_Z	Azimuth	Elevation	Range	P-Range Gr...	P-Range
6	50	1	GPS	9	9	0	5487028.51...	1258992.39...	41111240.32...	4438.488	597.221	-6106.674	2.7225	0.1456	2053076.24...	2053096.70...	0.0000
7	50	2	GPS	12	12	0	3417492.65...	2430730.17...	5568405.11...	5099.461	3251.769	-4549.156	1.3014	0.1066	2249925.44...	2249951.28...	0.0000
8	50	3	GPS	20	20	0	4593128.86...	-1433126.8...	5044219.98...	-2073.741	6017.723	3598.004	-1.7981	0.1933	1869417.27...	1869433.75...	0.0000
9	50	4	GPS	25	25	0	17735323.7...	1281618.14...	23656363.8...	-1336.291	3327.854	790.014	-0.2164	1.5493	23230731.8...	23230730.8...	0.0000
10	50	5	GPS	3	3	0	3916583.69...	-660839.70...	5728743.64...	6079.404	-1319.502	-4308.532	-1.0995	0.4500	1202396.08...	1202404.63...	0.0000
11	50	6	GPS	4	4	0	5470483.72...	-923027.08...	4220979.68...	4447.547	-1160.699	-6017.937	-2.4540	0.1265	2140073.90...	2140096.66...	0.0000
12	50	7	GPS	21	21	0	3548766.77...	917118.8208	5929585.83...	-3659.134	6205.218	1230.186	0.6683	0.4777	1157891.89...	1157900.04...	0.0000
13	50	8	GPS	18	18	0	3574544.45...	485725.6330	5965026.67...	704.291	7203.594	-1008.627	0.2409	0.5735	1023682.94...	1023689.99...	0.0000
14	50	9	GPS	24	24	0	3989897.05...	2371971.62...	5200895.39...	-5931.216	2685.938	3325.191	1.6083	0.1432	2075865.07...	2075885.80...	0.0000
15	50	10	GPS	15	15	0	4489307.23...	-564135.34...	5303085.19...	4324.482	4994.974	-3129.515	-1.8139	0.5225	1085477.27...	1085484.87...	0.0000
16	50	11	GPS	8	8	0	3980231.69...	913259.5955	5649650.72...	6039.788	1080.299	-4429.716	1.1125	0.7101	881836.7826	881842.7478	0.0000
17	100	1	GPS	9	9	0	5487250.42...	1259022.25...	4110934.99...	4438.171	597.114	-6106.916	2.7225	0.1455	2053395.01...	2053415.48...	0.0000
18	100	2	GPS	12	12	0	3417747.62...	2430892.76...	5568177.64...	5099.284	3251.590	-4549.483	1.3015	0.1066	2249967.33...	2249993.17...	0.0000
19	100	3	GPS	20	20	0	4593025.17...	-1432825.9...	5044399.88...	-2073.966	6017.822	3597.707	-1.7980	0.1934	1869102.25...	1869118.72...	0.0000
20	100	4	GPS	25	25	0	17735256.9...	1281784.53...	23656403.3...	-1336.276	3327.863	789.996	-0.2160	1.5493	23230730.8...	23230729.8...	0.0000
21	100	5	GPS	3	3	0	3916887.66...	-660905.67...	5728528.21...	6079.165	-1319.508	-4308.869	-1.0999	0.4501	1202323.21...	1202331.76...	0.0000

Figure 6.6: Example of a SimGEN log for the antenna element 1 in the position "LUMC".

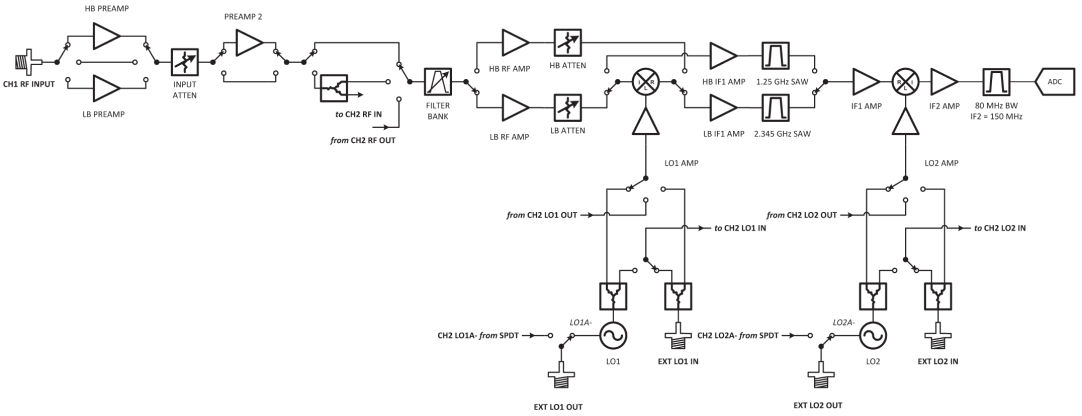

Figure 6.7: Main blocks of the TwinRx daughterboard [17].

unit. Finally, the external option allows to share the LO with another TwinRX unit.
The acquired data were processed through custom-designed MATLAB routines and the results were fed to the FPGA unit which hosted the hardware architecture described in Chapter 5. The interface was built through the FPGA-in-the-Loop (FiL) feature of Simulink [19].
The results of the processing were compared with the estimations made through two other approaches: the 2-Dimensions MUSIC algorithm (2D MUSIC) and the phase interferometry by means of the IQ samples (IQ Interf). This latter is described in the Appendix B. For the first approach, we employed its implementation in MATLAB `phased.MUSICEstimator2D` object from the Phased Array System Toolbox. As for the IQ interf, it was chosen to extract the phases of the IQ samples through the MATLAB implementation of the 2-dimensional arctangent function, `arctan2`.

6.3.2 Frequency planning and hardware prototype

The received signals at frequency f_{RF} were downconverted to the IF $f_{IF} = 50$ kHz. This choice allowed to operate always with signals having positive frequencies, even in the presence of Doppler shift, thus avoiding dealing with the related $\pm\pi$ ambiguity for the results. The USRP also sampled the downconverted signal. A discussion on the USRP sampling rate impact is postponed to Section 6.4.3. The receiver gain was set to 50 dB.

The FiL interface cannot be driven by clock signals with frequencies below 25 MHz. Hence, we set $f_{clk} = 25$ MHz. Under these hypotheses, following the (5.17), and remembering for LEO satellites the Doppler shift can lead to ± 45 kHz shifts, the lowest possible frequency would be around 5 kHz and so $L = 13$ bits. To keep the architecture flexible, it was chosen a word length of 14 bits, so the lowest frequency that can be estimated is 1.526 kHz.

The acquired waveforms were fed to an algorithm developed for emulating the behavior of a zero-crossing detector (Algorithm 3).

The digital architecture described in Chapter 5 was prototyped on the Digilent Nexys A7 Evaluation and Development board for the AMD Xilinx Artix-7 100T FPGA (Figure 6.9). Recall from Chapter 2 that for a 2x2 URA, namely three phase shifts are sufficient to estimate the azimuth and elevation angles, while to tackle all the

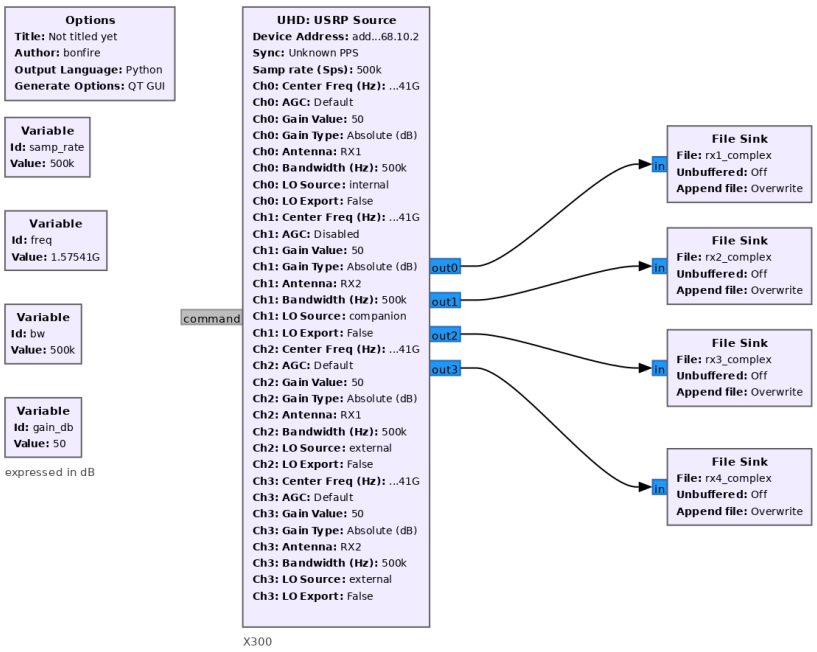

Figure 6.8: GRC flowgraph with UHD settings for the signals samples acquisition.

so-called "L"-shapes antenna arrangement it is necessary to handle two more phase shifts.
All these phase estimation blocks operate concurrently and independently one from the others. The implementation stage of the FPGA bitstream synthesis was run for both three and five phase shift estimations, in order to study the different impacts in terms of resource occupancy on the FPGA. The results are shown in Table 6.1.
In absolute terms, the resource occupation on the FPGA is very low ($< 1\%$) for both implementations, testifying the low-complexity of the proposed architecture. In relative terms, adding two other concurrent phase estimations determines an increment in terms of resource occupations around the 65% for both LUTs and Register Slices. To improve the accuracy, all the available "L"-shapes were used and averaged. The post-implementation layout is shown in Figure 6.10.

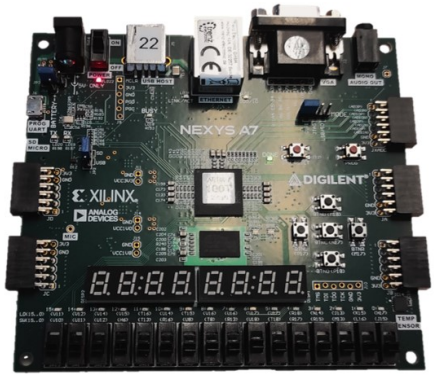

Figure 6.9: Digilent Nexys A7 Evaluation and Development board for the Xilinx Artix-7 100T.

Table 6.1: Resources utilization comparison between three or five instances of the phase detector, tackling one or all the possible "L"-shapes for the phase difference estimation.

Slice	Single "L"-shape		Full "L"-shapes	
	Used	Utilization	Used	Utilization
LUTs	250	0.39%	413	0.65% (+65.2%)
Registers	360	0.28%	592	0.47% (+64.4%)

6.3.3 Initial phase calibration

Due to possible mismatches in the reference oscillator locking, the initial phase for the Local Oscillator (LO) of each channel has a static random additive component that has to be calibrated. Many techniques have been deployed to perform calibration [20]. One of them employs a target with known position in the far-field region. Thanks to the geometric relationships, it is possible to retrieve the expected direction vector of the array corresponding to that given position. The error between the actually measured phase shifts and the expected ones corresponds to the value that is necessary to introduce to perform the calibration. In our case, the known target was a space craft in the MEO orbit in an almost-zenith position. This choice was driven by the fact the object in the MEO orbit is much slower than the LEO.

6.3.4 Reference and target positions

Five places were taken as positions for the target (marked as: "Oegstgeest", "Amstedam", "Delft", "Noordwijkerhout", "North Sea") and one place for the reference node, marked as "LUMC". First, the AoA estimation accuracy was evaluated for each of these sites. For the positioning accuracy evaluation, the estimation is made by taking data from the reference and the targets. The places map is in Figure 6.11.

6.3.5 Comparison metrics

The core metric for the evaluation of the performance is the Absolute Estimation Error (AEE) with respect to the GT value. In the following paragraphs, the two definitions of the AEE are introduced.

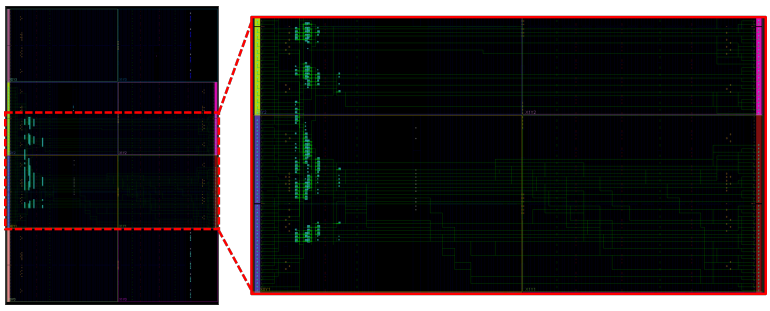

Figure 6.10: Vivado post-implementation layout view with zoom on the occupied area.

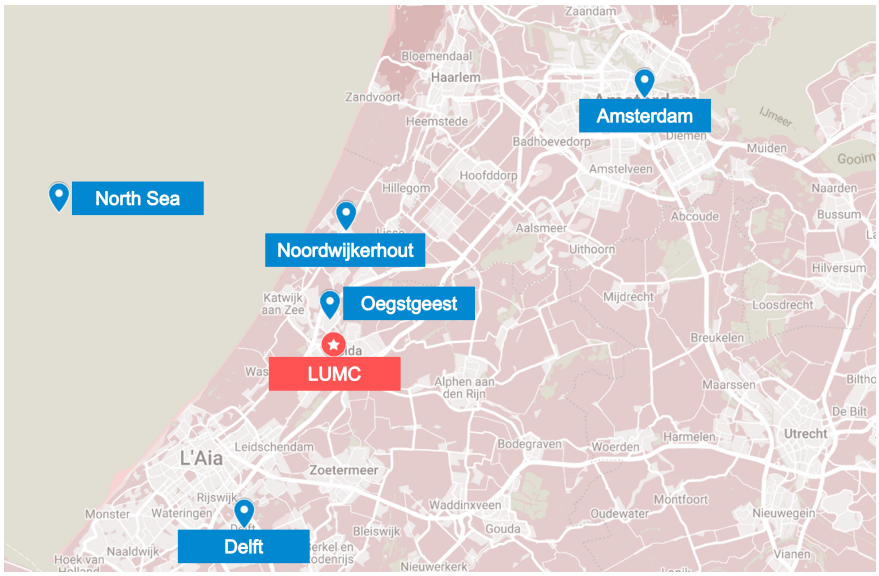

Figure 6.11: Locations for targets (in blue) and the reference node (in red) on the map.

Evaluation of the AoA estimation accuracy The GT angular pair (α, ε) and its estimation $(\hat{\alpha}_k, \hat{\varepsilon}_k)$ made through the sample $k \in \mathbb{N}$ were compared. The AEE is defined on both azimuth and elevation as follows:

$$\begin{cases} \text{AEE}(\alpha_k) = |\alpha - \hat{\alpha}_k| \\ \text{AEE}(\varepsilon_k) = |\varepsilon - \hat{\varepsilon}_k| \end{cases} \tag{6.9}$$

Evaluation of the position and distance estimation accuracy First of all, recall the definition of the Euclidean norm to introduce the notation for the AEE definition in the case of position accuracy evaluation. Supposing to compute the Euclidean distance δ between two points $A = (x_A, y_A)$ and $T = (x_T, y_T)$, the expression is

$$\delta(A, T) = \sqrt{[x_A - x_T]^2 + [y_A - x_T]^2} \tag{6.10}$$

The target location T_i is represented by its estimated coordinates $\hat{T}_i(k) = (\hat{x}_{T_i,k}, \hat{y}_{T_i,k})$, being i the location index, and k the sample index. Hence, the estimated norm is

$$\hat{\delta}(A, T_{i,k}) = \sqrt{[x_A - \hat{x}_{T_i,k}]^2 + [y_A - \hat{y}_{T_i,k}]^2} \tag{6.11}$$

The AEE for the distance is computed as

$$\text{AEE}(\delta_{T_i,k}) = |\delta(A, T) - \hat{\delta}(T_i, k)| \tag{6.12}$$

while the AEE computed for the single coordinates is

$$\begin{cases} \text{AEE}(\hat{x}_{T_i,k}) = |x_{T_i} - \hat{x}_{T_i,k}| \\ \text{AEE}(\hat{y}_{T_i,k}) = |y_{T_i} - \hat{y}_{T_i,k}| \end{cases} \tag{6.13}$$

6.4 Results

This section presents the results obtained from the validation campaign. First, the validation of the geometrical model is discussed to test its compliance and its level of approximation. Therefore, the calibration effects are studied in terms of temporal consistency, which is the key requirement for the phase interferometric system to operate correctly. Then, it was evaluated the performance in terms of AoA estimation accuracy, and the possible improvements obtained by increasing the sampling rate. Finally, the position estimation accuracy reached by the system is discussed.

6.4.1 Geometric model validation

To validate the geometrical model, the angles in the SimGEN logs and the ones computed using the model in Section 6.2.1 for the same position were compared. The error corresponds to the fitting mismatch of the model with respect to real data. As an example, the discussion is done on the target position "Oegstgeest" and the reference node in the "LUMC" position.
The ECEF and the AER coordinates of the reference, the targets, and the satellites from the SimGEN logs were converted into the East-North-Up (ENU) coordinates system centered in the reference node position. Then, the azimuth and elevation angles were computed as:

$$\begin{cases} \hat{\varepsilon}_A = \arctan\left(\dfrac{x_S^{\mathrm{ENU}}}{z_S^{\mathrm{ENU}}}\right) \\ \hat{\varepsilon}_T = \arctan\left(\dfrac{x_S^{\mathrm{ENU}} - x_T^{\mathrm{ENU}}}{z_S^{\mathrm{ENU}}}\right) \\ \hat{\alpha}_A = \arctan\left(\dfrac{x_S^{\mathrm{ENU}}}{y_S^{\mathrm{ENU}}}\right) \\ \hat{\alpha}_T = \arctan\left(\dfrac{x_S^{\mathrm{ENU}} - x_T^{\mathrm{ENU}}}{y_S^{\mathrm{ENU}} - y_T^{\mathrm{ENU}}}\right) \end{cases} \tag{6.14}$$

being $(\hat{\alpha}_A, \hat{\varepsilon}_A)$ the retrieved azimuth and elevation angles pair for the reference node and $(\hat{\alpha}_T, \hat{\varepsilon}_T)$ the retrieved angles pair for the target node. Therefore, it was computed the absolute error between the retrieved angles and the GT angles. The average results along with the standard deviation of the error are presented in Figure 6.12. A very small error in the order of 10^{-2} rad is present in the AoA estimation. This error has to be related not only to the model itself but also to the number of digits used for the representation of the GT angular values in (four digits), the approximation introduced by the arctangent function implemented in MATLAB, and the overall model precision when performing the change of coordinate system. However, given the result, the model can be considered to be a good approximation of reality.

6.4.2 Study of the calibration vector consistency

It is important to ensure the calibration vector containing the phase offset remains constant throughout the duration of all experiments. Otherwise, it means a sort of intermodulation or other sources of non-systematic offset is introduced, determining the degradation of the accuracy.

Consecutive blocks of signals were taken. Their temporal duration corresponds to one record in the SimGEN logs. For each of these records, the phase calibration vector was computed, resulting in one point of the plot in Figure 6.13a.
Figure 6.13b shows the difference between the phase offset vector sample $k+1$ and the sample k, i.e. the variation of the calibration vector values from the previous to the next phase calibration step. The behavior for all three values oscillates with values in the order of 10^{-3} rad.
The graph in Figure 6.13c describes the Probability Distribution Function (PDF) of the error, which clearly exhibits the behavior of a normal distribution. Hence, the effect that is dominating the phase drift is the zero-mean Gaussian noise.

6.4.3 AoA estimation validation

In this section, the AoA estimation accuracy is characterized. This latter is compared to the MATLAB implementation of the 2D MUSIC algorithm and to the performance reached by IQ Interf. The proposed approach is referred to as Digital AoA. In the analysis, the impact of the sampling rate was taken into account. Also, it was analyzed the overall AoA estimation accuracy with $f_s = 2.5$ MS/s and the capability of the system to track the fast-moving LEO spacecraft.

Study of the impact of the sampling rates The sampling rate of the signal also has an impact on the overall estimation accuracy. Normally, the sampling rate is identified with the clock frequency f_{clk}. However, in the specific situation employed as an experiment setup, there is a difference between the sampling frequency f_s employed by the USRP to sample the analog signals and the clock frequency of the FPGA, f_{clk}. The USRP sets an upper bound for the sampling rate that is lower than the FiL lower bound on the clock frequency. Thanks to a feature already implemented in FiL it was possible to upsample the signal to f_{clk}: in this way, the bottleneck is not anymore the clock frequency but the sampling rate.

The AoA estimation accuracy is related to the phase shift estimation accuracy, which is linked to the clock frequency (see Chapter 5). The test was performed for the sampling frequencies $f_s = \{0.5, 2.5, 5\}$ MS/s.
The Nyquist sampling theorem states the lowest allowable sampling frequency for a CW signal is $f_{\text{Nyq}} = 2 \cdot f$ being f the tone frequency.

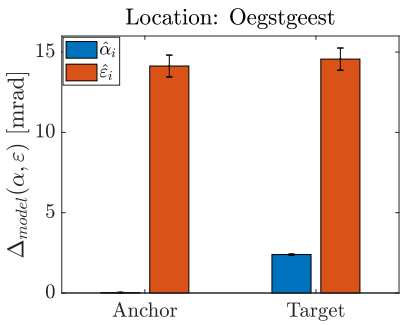

Figure 6.12: Study of the error between the GT AoAs from SimGEN logs and the ones obtained from the geometrical model.

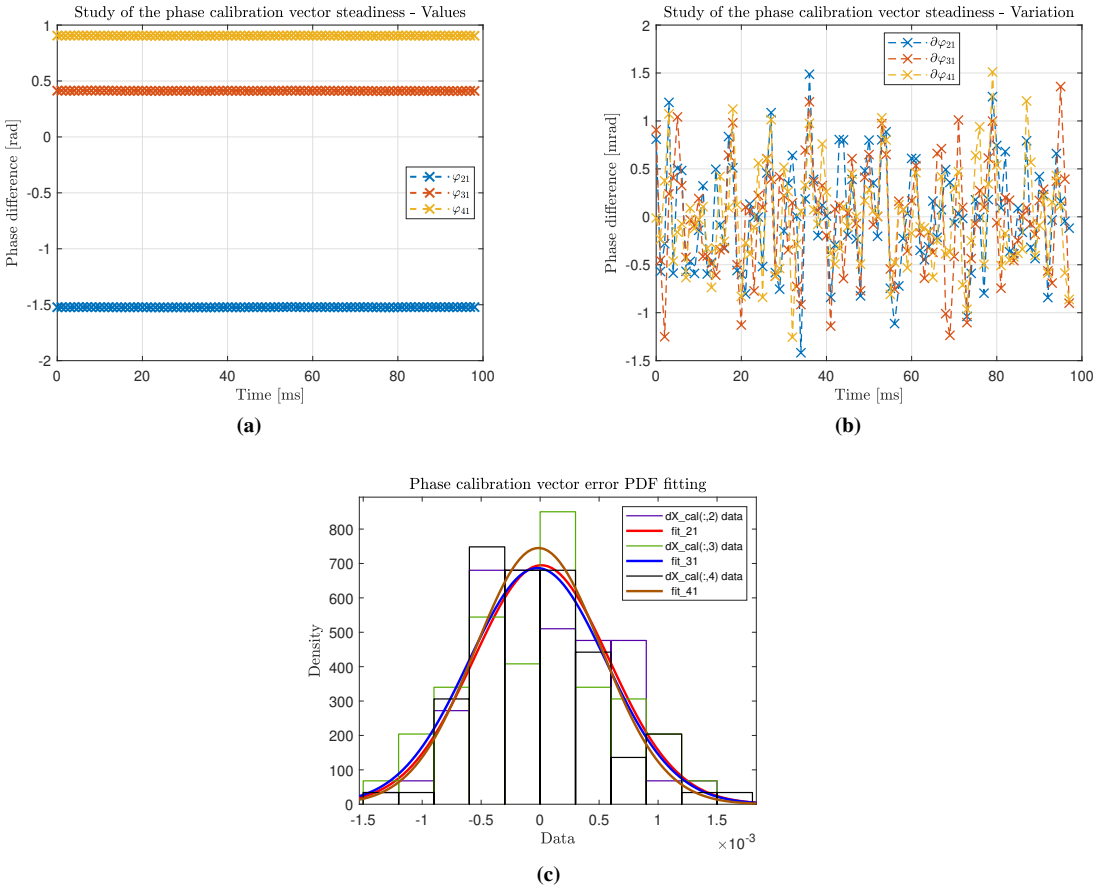

(a) (b) (c)

Figure 6.13: Study of the calibration vector steadiness through the time. (a) Calibration vector values (b) Sample-by-sample variation of the calibration vector (c) PDF fitting of the variation.

Recalling the OSR definition:

$$\mathrm{OSR} = \frac{f_s}{f_{\mathrm{Nyq}}} \tag{6.15}$$

In our case, $\mathrm{OSR} = \{5, 25, 50\}$. In uniform sampling, the OSR represents the number of available signal samples for each semiperiod. On average,

$$\Delta\varphi_{min,OSR} = \frac{\pi}{\mathrm{OSR}} \tag{6.16}$$

By increasing the OSR it is expected an increase in the phase shift estimation accuracy. This statement is proved by the results shown in Figure 6.14, which represent the Cumulative Distribution Function (CDF) of the absolute error on the phase estimation with the different considered sampling rates. The results for AoA estimation with different sampling rates are shown in Figure 6.15 and Table 6.2.
The improvement of the sampling rate leads to an increase in the estimation accuracy (and thus, as it was proved in Section 6.2.2, to the final positioning system accuracy). This comes at the cost of a higher number of samples to be processed for the 2D MUSIC and IQ Interf approaches, leading to a higher load due to higher storage capacity and the increased number of computations for the same time frame. As an example, let us consider the MUSIC algorithm which has to deal with the computation of

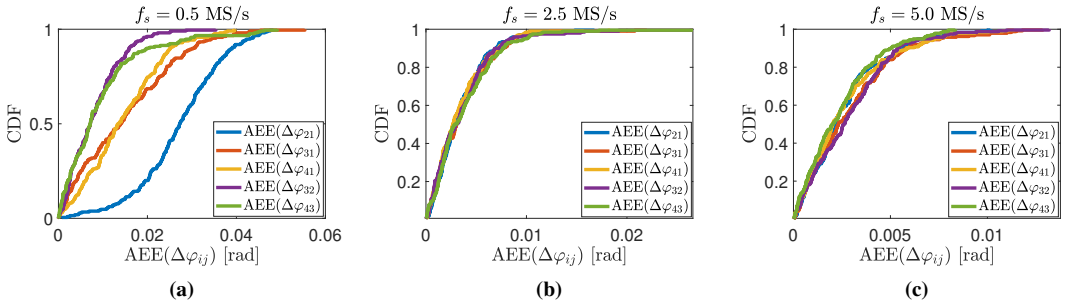

Figure 6.14: CDF analysis of the phase AEE for the three different sampling rates, on all the estimation pairs. In detail (a) Results for OSR = 5, $f_s = 500$ KS/s, (b) Results for OSR = 25, $f_s = 2500$ KS/s, and (c) Results for OSR = 50, $f_s = 5000$ KS/s.

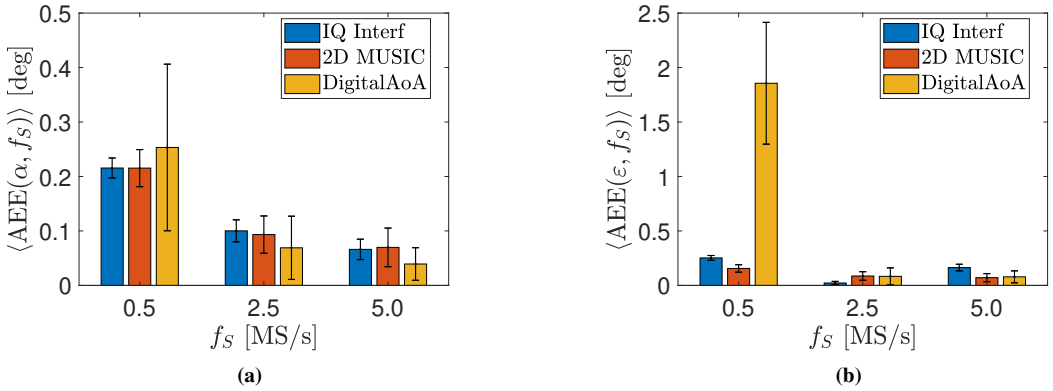

Figure 6.15: Comparison in terms of mean AEE for the azimuth and elevation angles based on the three different approaches under comparison and the three analyzed sampling frequencies. In detail: (a) azimuth and (b) elevation mean AEE. The error bars represent the sample standard deviation.

Table 6.2: Mean AAE vs sampling rates for the three different approaches under test. The results are presented in the (α, ε) angle pair form, specifying the standard deviation.

f_s [MS/s]	**IQ Interf [deg]**	**2D MUSIC [deg]**	**Digital AoA [deg]**
0.5	$(0.21 \pm 0.02, 0.25 \pm 0.03)$	$(0.21 \pm 0.03, 0.16 \pm 0.03)$	$(0.25 \pm 0.15, 1.86 \pm 0.56)$
2.5	$(0.10 \pm 0.02, 0.02 \pm 0.01)$	$(0.09 \pm 0.03, 0.08 \pm 0.04)$	$(0.07 \pm 0.06, 0.08 \pm 0.08)$
5	$(0.07 \pm 0.02, 0.16 \pm 0.03)$	$(0.07 \pm 0.03, 0.07 \pm 0.04)$	$(0.03 \pm 0.02, 0.07 \pm 0.05)$

the autocorrelation matrix for its first phase. The computational complexity of this operation is roughly $\mathcal{O}(NM^2)$, where N is the number of acquired samples and M is the number of antenna array elements. Being the proposed approach an open-loop single-snapshot estimation algorithm, the increase in sampling rate does not determine a complexity increase as soon as the employed prototyping platform supports it.

AoA estimation accuracy For each of the positions mentioned in Section 6.3.4, it was performed the estimation of both azimuth and elevation angles.
The architecture described in Chapter 5 is also capable of keeping track of the Doppler

Shift. Recalling the (5.11), this is done by means of the FW whose variation is depicted in Figure 6.16a. Also, the system operates in real-time giving the first estimates with a transient of a few periods, directly depending on the clock frequency for the digital system and the input signal frequency. A sample result is shown in Figure 6.16b, where all five estimations are performed concurrently and independently one from the others.

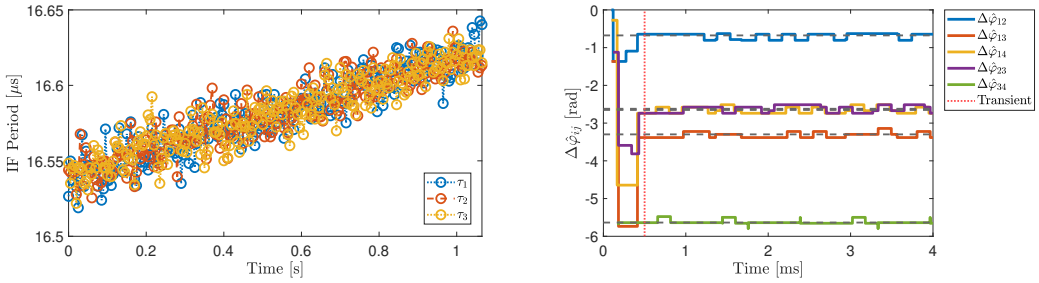

(a) **(b)**

Figure 6.16: Example graphs from the "LUMC" location representing (a) the capability of tracking the Doppler shift induced by the high-speed motion of the spacecraft and (b) the possibility of having the first result after a few IF signals period, neglecting an initial transient for the digital architecture

Table 6.3 summarizes the number of available samples for the AoA estimation. Each of these experiment samples (the ones that were indexed as $k \in \mathbb{N}$ in Section 6.3.5) captures 5 ms of signal data and generates one estimation for the azimuth and one estimation for the elevation.

Table 6.3: Size of the experimental sample (i.e., the estimated AoAs) on which it was performed the position estimation. Each experimental sample captures 5 ms of data.

Location	# Samples
LUMC	401
Oegstgeest	316
Amsterdam	239
Delft	459
Noordwijkerhout	395
North Sea	397

The results for the AoA estimation in each location are summarized in Table 6.4, in which the average AEE and its standard deviation are reported. As an example, for the locations "LUMC" and "Oegstgeest" there are also reported the time series of azimuth and elevation angles estimations (Figures 6.17a-6.17b for "LUMC" and Figures 6.18a-6.18b for "Oegstgeest") and the time series of the AEE (Figures 6.17c-6.17d for "LUMC" and Figures 6.18c-6.17d for "Oegstgeest") thus proving the capability of tracking moving objects thanks to the described approach.
To better analyze the AEE trend, it was also computed an empirical CDF for the three approaches under analysis. The results are shown in Figures 6.17e-6.17f for the "LUMC" location and in Figures 6.18e-6.18f again for both azimuth and elevation

Table 6.4: Mean AEE for the AoA estimation for each location, comparing the three approaches under analysis. The results are presented in the (α, ε) angle pair form, with the specification of the standard deviation.

Location	2D MUSIC [deg]	IQ Interf [deg]	Digital AoA [deg]
LUMC	$(0.03 \pm 0.02, 0.12 \pm 0.04)$	$(0.01 \pm 0.01, 0.22 \pm 0.02)$	$(0.08 \pm 0.06, 0.11 \pm 0.09)$
Oegstgeest	$(0.03 \pm 0.02, 0.06 \pm 0.04)$	$(0.02 \pm 0.01, 0.16 \pm 0.02)$	$(0.07 \pm 0.06, 0.08 \pm 0.06)$
Amsterdam	$(0.03 \pm 0.02, 0.19 \pm 0.03)$	$(0.02 \pm 0.01, 0.28 \pm 0.02)$	$(0.08 \pm 0.06, 0.16 \pm 0.09)$
Delft	$(0.14 \pm 0.04, 0.03 \pm 0.02)$	$(0.14 \pm 0.02, 0.12 \pm 0.02)$	$(0.06 \pm 0.06, 0.15 \pm 0.09)$
Noordwijkerhout	$(0.18 \pm 0.03, 0.08 \pm 0.03)$	$(0.19 \pm 0.02, 0.18 \pm 0.02)$	$(0.06 \pm 0.05, 0.19 \pm 0.09)$
North Sea	$(0.04 \pm 0.03, 0.06 \pm 0.04)$	$(0.04 \pm 0.02, 0.16 \pm 0.02)$	$(0.18 \pm 0.08, 0.17 \pm 0.11)$

angles. The order of magnitude of the mean AEE for each of the three techniques is the same. The proposed approach exhibits lower accuracy that the other algorithms under evaluation as a mean value, at the advantage of sensibly lower computational complexity and time needed for the estimation. By looking at the time evolution of the AEE we observe how the 2D MUSIC experiences a stair-like behavior, probably due to sampling frequency. The random profile of the errors for Digital AoA suggests a strong impact of zero mean effects on the estimation accuracy.

6.4.4 Position estimation accuracy validation

For each of the target locations described in Section 6.3.4, it was estimated the position of the target given the reference node position, "LUMC". The final estimation accuracy is compared to the ones obtained by the other approaches under analysis by means of the metrics introduced in Section 6.3.5.
In Table 6.5, it is summarized the outcome of the position estimation through mean AEE on the distance for each location and each approach under analysis. The uncertainty is expressed in terms of the standard deviation.
As it was done for the AoA estimation, and also for the positioning the example case of the location "Oegstgeest" is detailed. In Figure 6.19a it is shown a bar graph comparing the average AEE on the distance for each of the three approaches under analysis. The error bars indicate the standard deviation of the AEE. In Figure 6.19b it is represented the CDF for the distance AEE. In Figure 6.19c and Figure 6.19d it is shown the AEE on the estimation of the x and y coordinate of the target, respectively. The

Table 6.5: Mean AEE for the distance for each location, comparing the three approaches under analysis, along with its standard deviation. All the values are expressed in kilometers.

Location	GT [km]	2D MUSIC [km]	IQ Interf [km]	Digital AoA [km]
Oegstgeest	3.38	0.67 ± 0.38	0.71 ± 0.36	1.70 ± 1.72
Amsterdam	56.26	1.85 ± 1.01	1.16 ± 0.71	3.39 ± 2.94
Delft	32.02	1.24 ± 0.60	0.63 ± 0.55	3.12 ± 2.43
Noordwijkerhout	16.64	1.72 ± 1.07	1.56 ± 0.63	3.16 ± 2.43
North Sea	26.14	0.92 ± 0.59	0.52 ± 0.36	3.21 ± 2.09

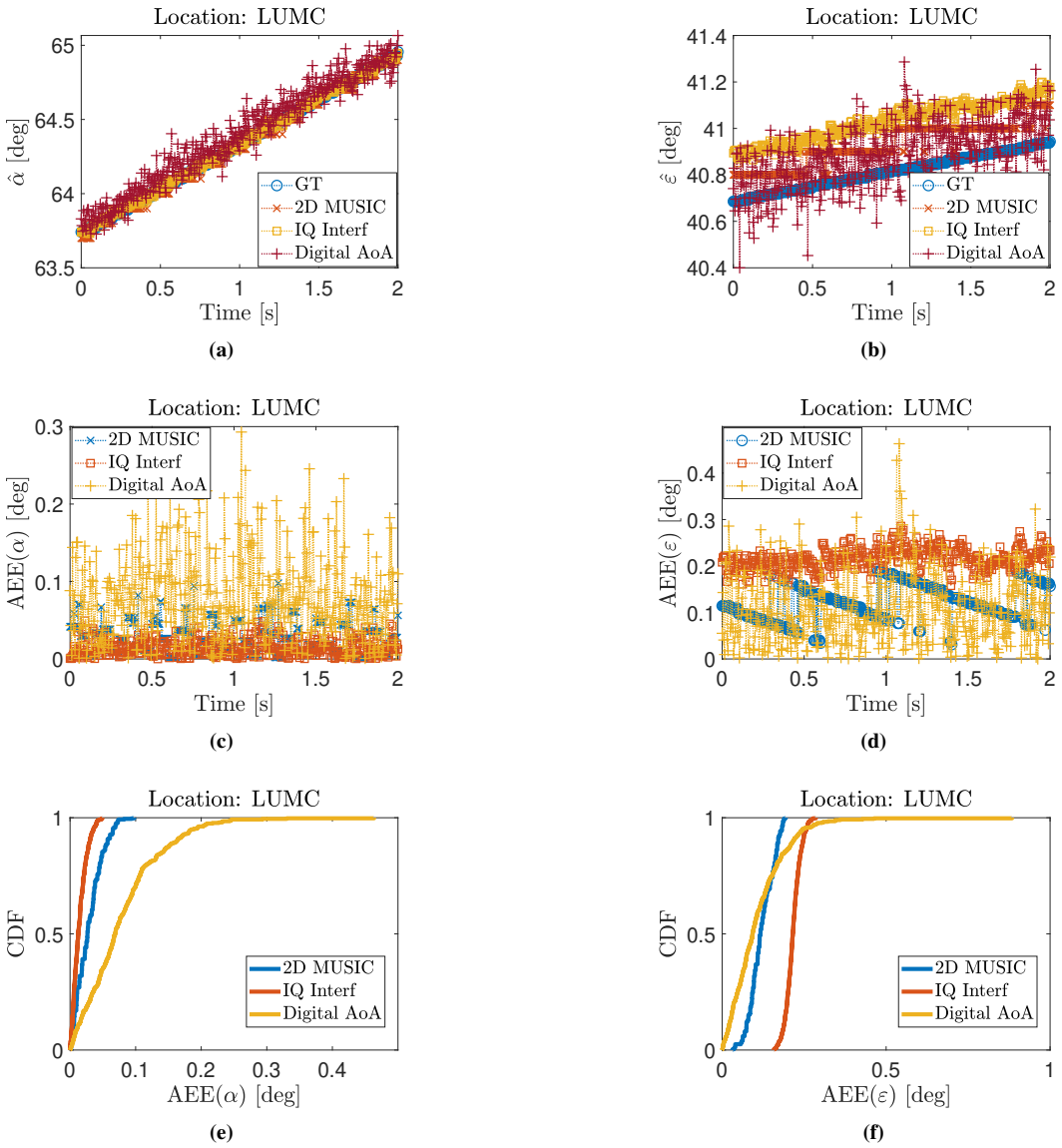

Figure 6.17: Results of the AoA estimation and Location "LUMC" using the three approaches under comparison: (a) Azimuth angle tracking over time, (b) Elevation angle tracking over time, (c) AEE for the azimuth angle over time, (d) AEE for the elevation angle over time, (e) CDF of the AEE for the azimuth angle, and (f) CDF of the AEE for the elevation angle.

proposed approach leads to higher errors with slightly higher dispersion around the mean value than the other two approaches under analysis. Nevertheless, the order of magnitude is practically the same. This is due to the different accuracy reached by the AoA estimations by the different approaches. The order of magnitude for this distance estimation error is compatible with what was expected after the analysis in Section 6.2.2.

From that analysis, it was proven that even errors in the order of tenths of a degree for the final AoA estimation can lead to a precision up to units of kilometers for the distance estimation.

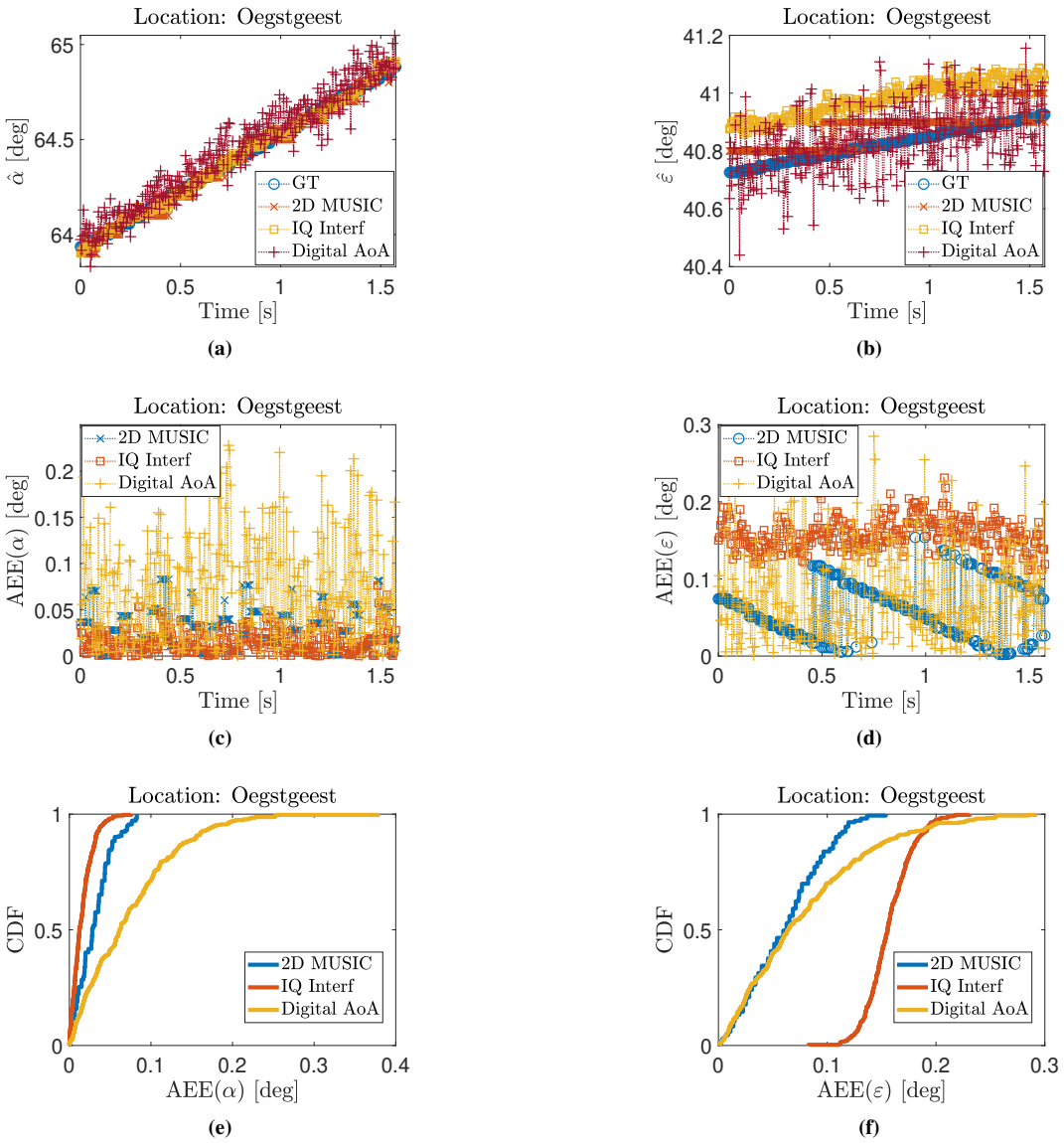

Figure 6.18: Results of the AoA estimation and Location "Oegstgeest" using the three approaches under comparison: (a) Azimuth angle tracking over time, (b) Elevation angle tracking over time, (c) AEE for the azimuth angle over time, (d) AEE for the elevation angle over time, (e) CDF of the AEE for the azimuth angle, and (f) CDF of the AEE for the elevation angle.

6.5 Conclusions

This chapter introduced a novel local positioning system relying on the AoA estimation of LEO SoOp from multiple receivers. The AoA estimation is provided in real-time through the digital hardware architecture described in Chapter 5.
The position estimation is achieved through a simplified Euclidean model that links the differential AoA estimation to the planar cartesian coordinates. After introducing and describing the experimental setup, the results achieved in terms of positioning and AoA estimation error were presented. With an OSR of 25, thus having 50 signal samples for each signal period, the system reached a sub-degree AoA estimation accuracy

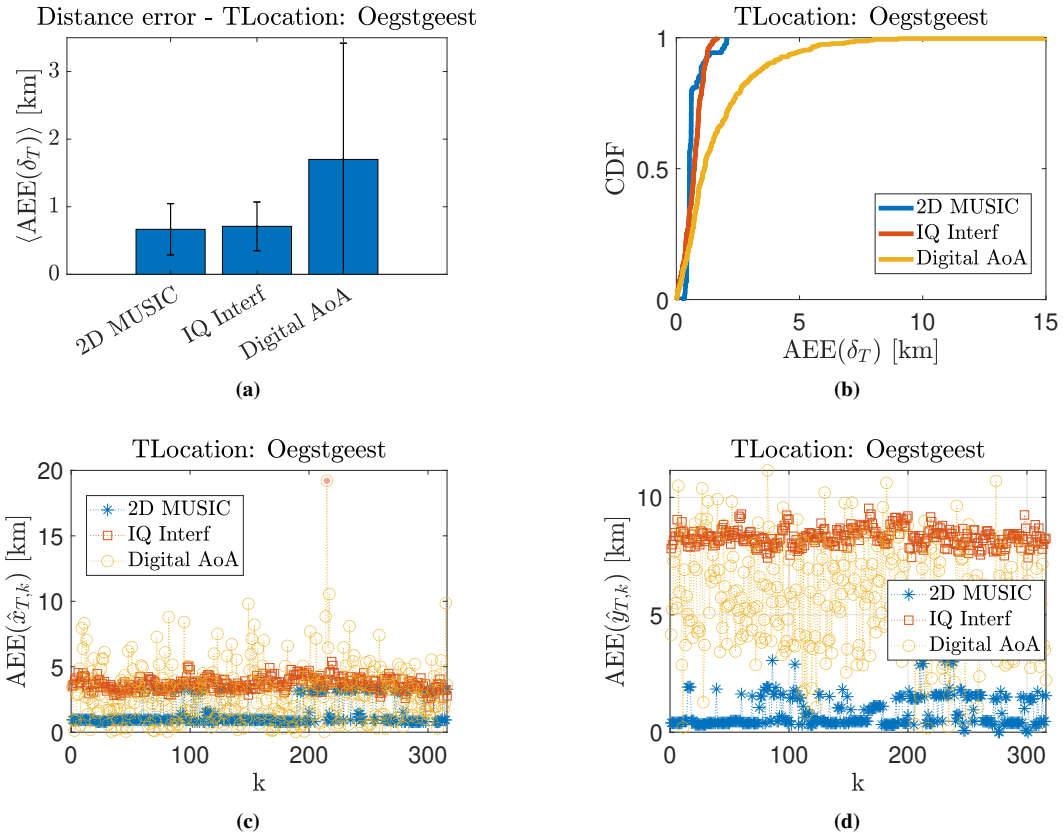

Figure 6.19: Results of the position estimation for target location "Oegstgeest" on both reference and target. (a) Comparison of the mean AAE and standard deviation for the three approaches under comparison (b) AAE for the x_T estimation (c) CDF of the error computed on the norm for the three approaches and (d) AAE for the y_T estimation.

($\approx 0.1°$) that is comparable to the other two approaches under analysis, which came at the same result with higher computational complexity and hardware complexity. The proposed approach, in fact, can operate just with real values, while the other two approaches require the presence of a quadrature demodulator and downconverter. In terms of distance resolution, generally, the system achieves performance in the order of units of kilometers, which was expected due to the AoA estimation accuracy.

References

[1] F. Zafari, A. Gkelias, and K. K. Leung, "A Survey of Indoor Localization Systems and Technologies," *IEEE Communications Surveys Tutorials*, vol. 21, no. 3, pp. 2568–2599, 2019.

[2] R. M. Ferre and E. S. Lohan, "Comparison of MEO, LEO, and Terrestrial IoT Configurations in Terms of GDOP and Achievable Positioning Accuracies," *IEEE Journal of Radio Frequency Identification*, vol. 5, no. 3, pp. 287–299, Sep. 2021.

[3] F. S. Prol, R. M. Ferre, Z. Saleem, P. Valisuo, C. Pinell, E. S. Lohan, M. Elsanhoury, M. Elmusrati, S. Islam, K. Celikbilek, K. Selvan, J. Yliaho, K. Rutledge, A. Ojala, L. Ferranti, J. Praks, M. Z. H. Bhuiyan, S. Kaasalainen, and H. Kuusniemi, "Position, Navigation, and Timing (PNT) Through Low Earth Orbit (LEO) Satellites: A Survey on Current Status, Challenges, and Opportunities," *IEEE Access*, vol. 10, pp. 83 971–84 002, 2022.

[4] T. Janssen, A. Koppert, R. Berkvens, and M. Weyn, "A Survey on IoT Positioning leveraging LPWAN, GNSS and LEO-PNT," *IEEE Internet of Things Journal*, pp. 1–1, 2023.

[5] Z. Tan, H. Qin, L. Cong, and C. Zhao, "New Method for Positioning Using IRIDIUM Satellite Signals of Opportunity," *IEEE Access*, vol. 7, pp. 83 412–83 423, 2019.

[6] U. K. Singh, M. R. B. Shankar, and B. Ottersten, "Opportunistic localization using LEO signals," in *2022 56th Asilomar Conference on Signals, Systems, and Computers*. Pacific Grove, CA, USA: IEEE, Oct. 2022, pp. 894–899.

[7] W.-H. Hsu and S.-S. Jan, "Assessment of using Doppler shift of LEO satellites to aid GPS positioning," in *2014 IEEE/ION Position, Location and Navigation Symposium - PLANS 2014*. Monterey, CA, USA: IEEE, May 2014, pp. 1155–1161.

[8] C. Huang, H. Qin, C. Zhao, and H. Liang, "Phase-Time Method: Accurate Doppler Measurement for Iridium NEXT Signals," *IEEE Transactions on Aerospace and Electronic Systems*, vol. 58, no. 6, pp. 5954–5962, Dec. 2022.

[9] M. Orabi, J. Khalife, and Z. M. Kassas, "Opportunistic Navigation with Doppler Measurements from Iridium Next and Orbcomm LEO Satellites," in *2021 IEEE Aerospace Conference (50100)*. Big Sky, MT, USA: IEEE, Mar. 2021, pp. 1–9.

[10] Z. Tan, H. Qin, L. Cong, and C. Zhao, "Positioning using iridium satellite signals of opportunity in weak signal environment," *Electronics*, vol. 9, no. 1, 2020.

[11] *Manual on the Aeronautical Mobile Service Satellite (Route) Service. Chapter 2 - Iridium Satellite Network*, 1st ed. International Civil Aviation Organization (ICAO), 2010, pp. 1–19.

[12] H. Benzerrouk, Q. Nguyen, F. Xiaoxing, a. amrhar, H. Rasaee, and R. J. Landry, "LEO satellites Based Doppler Positioning Using Distributed nonlinear Estimation," *IFAC-PapersOnLine*, vol. 52, no. 12, pp. 496–501, 2019.

[13] M. Leng, F. Quitin, W. P. Tay, C. Cheng, S. Gulam Razul, and C. M. Samson See, "Anchor-Aided Joint Localization and Synchronization Using SOOP: Theory and Experiments," *IEEE Transactions on Wireless Communications*, vol. 15, no. 11, pp. 7670–7685, Nov. 2016.

[14] D. Vallado, P. Crawford, R. Hujsak, and T. Kelso, *Revisiting Spacetrack Report #3*, (Last accessed on 29-May-2023). [Online]. Available: https://arc.aiaa.org/doi/pdf/10.2514/6.2006-6753

[15] P. Ellis, D. V. Rheeden, and F. Dowla, "Use of Doppler and Doppler Rate for RF Geolocation Using a Single LEO Satellite," *IEEE Access*, vol. 8, pp. 12 907–12 920, 2020.

[16] "USRP X300 High Performance Software Defined Radio Ettus Research | Ettus Research, a National Instruments Brand | The leader in Software Defined Radio (SDR)," (Last accessed on 21-Mar-2023). [Online]. Available: https://www.ettus.com/all-products/x300-kit/

[17] "TwinRX USRP Daughterboard (10 MHz - 6 GHz, 80 MHz BW, 2 RX) | Ettus Research, a National Instruments Brand | The leader in Software Defined Radio (SDR)," (Last accessed on 21-Mar-2023). [Online]. Available: https://www.ettus.com/all-products/twinrx/

[18] "GNU Radio - The Free & Open Source Radio Ecosystem." (Last accessed on 15-Jun-2023). [Online]. Available: https://www.gnuradio.org/

[19] "FPGA-in-the-Loop Simulation - MATLAB & Simulink," (Last accessed on 30-Mar-2023). [Online]. Available: https://www.mathworks.com/help/hdlverifier/ug/fpga-in-the-loop-fil-simulation.html

[20] R. A. Monzingo, R. L. Haupt, and T. W. Miller, *Introduction to Adaptive Arrays*, ser. Electromagnetic Waves. Institution of Engineering and Technology, 2011.

APPENDIX $\mathcal{A}$

Hardware design and discussion

In this appendix the (mostly analog) hardware boards and components designed to support the presented experiments is discussed, along with the motivations of some design choices.

A.1 Design of a ULA of Inset Fed Microstrip Patch Antennas

A.1.1 Design and optimization of the single element

In order to determine the rectangular patch dimensions that are the starting point of the optimization process, classical formulas from the antenna theory were employed [1]. The objective is to design an inset-fed rectangular patch, with a center frequency of 3.30 GHz, without any particular constraint on the bandwidth, using a Rogers RO4003C substrate [2] having $\epsilon_r = 3.38$ and thickness $h_{sub} = 1.524$ mm. The copper sheet thickness is 35 µm. The parameters to determine are in Figure A.1.
First, the width W of the patch was determined as

$$W = \frac{\lambda}{2}\sqrt{\frac{2}{\epsilon_r + 1}} \tag{A.1}$$

resulting in the theoretical value $W_{th} = 30.24$ mm. Then it was computed the effective dielectric constant of the substrate, ϵ_{eff} according to

$$\epsilon_{eff} = \frac{\epsilon_r + 1}{2} + \frac{\epsilon_r - 1}{2}\left[1 + 12\frac{h_{sub}}{W}\right] = 3.13 \tag{A.2}$$

Hence, the effective length L of the patch was determined as

$$L = \frac{\lambda}{2\sqrt{\epsilon_{eff}}} - 2\Delta L = 23.95 \text{ mm} \tag{A.3}$$

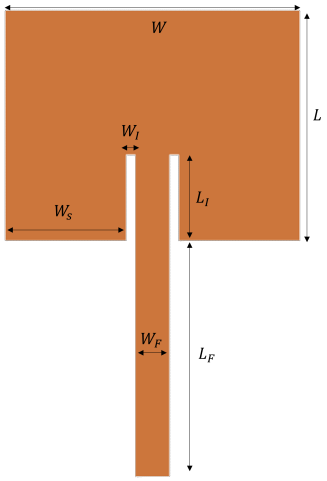

Figure A.1: Inset feed rectangular patch dimensions to be determined.

having

$$\Delta L = 0.412 \cdot h \cdot \frac{\left(\epsilon_{eff} + 0.3\right)\left(\frac{W}{h_{sub}} + 0.264\right)}{\left(\epsilon_{eff} - 0.258\right)\left(\frac{W}{h_{sub}} + 0.8\right)} \approx 0.67 \text{ mm} \tag{A.4}$$

since it is necessary to take into account the virtual "stretching" of the patch length due to the fringing of the electromagnetic field on the patch borders.
Once all those values are known, it is necessary to determine the point at which the patch antenna should be fed in order to maximize the power transfer (i.e. the antenna is matched to the characteristic impedance of the feed). Usually, the matching is done towards 50 Ω. The real part of the input impedance of the patch along its length can be approximated with a cosine function. In fact, by assigning the variable y to the displacement along the y axis, $y \in [0, L]$,

$$R_{in}(y) = R_{in}(0)\, \cos^2\left(\frac{\pi}{L} y\right) \tag{A.5}$$

having the input resistance of the patch at $y = 0$ to be

$$R_{in}(0) = 90\, \frac{\epsilon_r^2}{\epsilon_r - 1}\left(\frac{L}{W}\right) \tag{A.6}$$

By plotting the function (A.5) in the case of the computed dimensions, the resulting curve is in Figure A.2. The indicated point is $\hat{y} = 8.98$ mm.
The feed length has to be $\lambda/2$ long, i.e. ≈ 25.3 mm.
Some simulations were performed and through a trial-and-error procedure, the final values for the best results were reached. The ground plane was set to be $\approx W/4$ wider and longer than W and L respectively. Those values are summarized in Table A.1, and they are not so different from the theoretical ones.
The single element was realized using an LPKF Protomat C60 circuit board plotter. After soldering an SMA connector to the realized antenna, the reflection coefficient was measured and compared to the simulated one. The result is in A.3a. It is possible

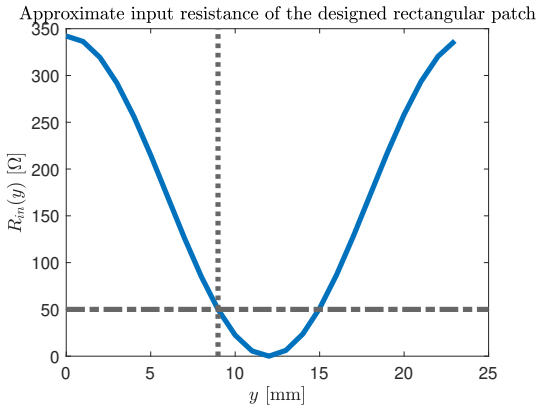

Figure A.2: Approximate input resistance variation along the patch length with respect to the bottom.

Parameter	Value [mm]
W	30
L	23.4
W_I	1
L_I	8.8
W_S	12.3
W_F	3.4
L_F	24

Table A.1: Final dimensions of the designed patch

to observe the center frequency is shifted 80 MHz above the simulated one but still in target for the initial specifications. The bandwidth is approximately unchanged (simulated 45 MHz vs realized 60 MHz).
As regards the far-field characteristic of the antenna element, the simulated gain and directivity plots in the azimuth plane are in Figure A.3b. The maximum gain $G_{max} = 6.38$ dBi at $\vartheta = 0$ deg. The Half Power Beam Width (HPBW) is around 90 degs. The radiation efficiency is 56.46%.

A.1.2 Design of the ULA and characterization

For realizing the Uniform Linear Array (ULA), the single patch element was replicated at distance $\lambda/2$ one from the other, taking as reference the center of the patch. Each element of the array shares a common ground plane. A picture of both the realized patch antenna element and the array is in Figure A.4.
The simulation results for the insertion loss are in Figure A.5a, showing how the presence of multiple elements determines an impact on the shift of both magnitude and frequency position of the minimum return loss. Therefore, those results can be compared with the measured ones in Figure A.5b, which show again almost the same frequency shift as for the single patch element.
The array bandwidth was designed as the range of frequencies in which the return loss is under the reference value -10 dB (i.e. at least $2/3$ of the energy is not reflected

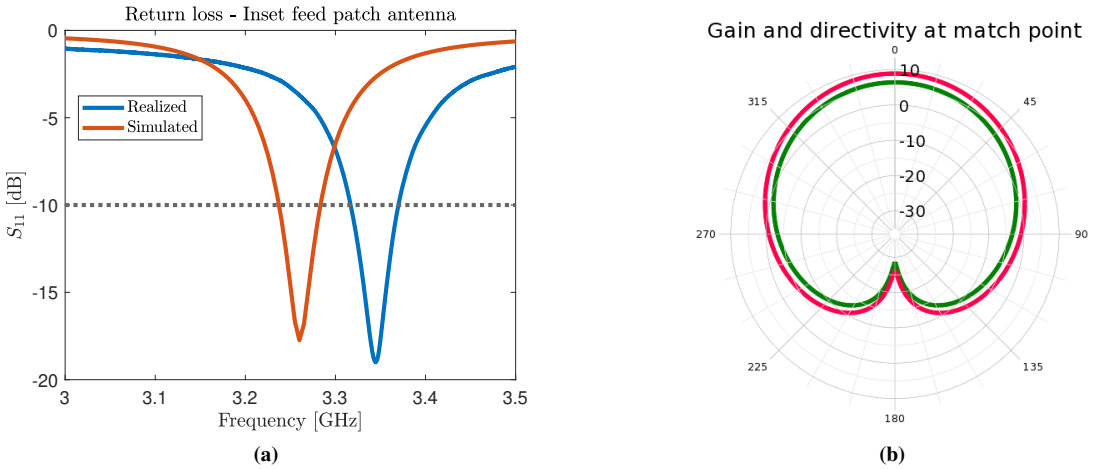

Figure A.3: (a) Simulated and measured return loss (S_{11}) of the designed patch antenna and (b) Simulated gain (in green) and directivity (in red) of the designed patch antenna.

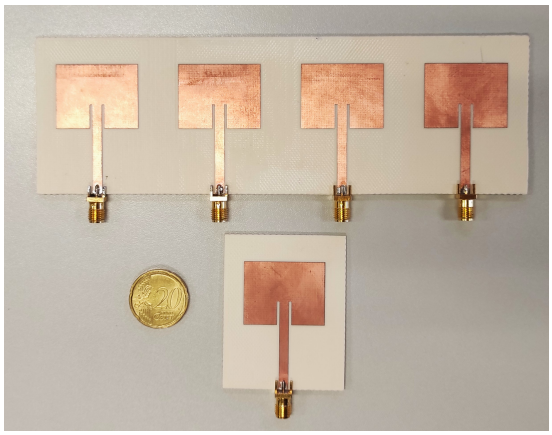

Figure A.4: Realized patch antenna element and ULA.

back to the generator) for each of the array elements. Indeed, the array bandwidth is 30 MHz with a center frequency of 3.24 GHz. As regards the realized bandwidth and center frequency, they are 43 MHz and 3.4 GHz respectively.
Even if the patch antennas do not have a constant current distribution, and so the transmission S-parameters (i.e. $s_{ij},\ i \neq j\,\forall i, j \in \mathrm{ULA}_{index}$) do not model properly the mutual coupling, still they provide a qualitative measure of this phenomenon. The transmission S-parameters of adjacent array elements were first simulated and then measured on the realized antenna elements. Results are in Figure A.6. At the frequency of interest, the transmission S-parameters follow what was simulated in terms of magnitude and reach an acceptable level of isolation.
With each of the array elements being powered in phase, the simulated gain and directivity are represented in Figure A.7. In detail, the maximum gain is 11.2 dBi at 0 deg. The HPBW reduces to 16 degs. The simulated radiation efficiency is 67.29%.

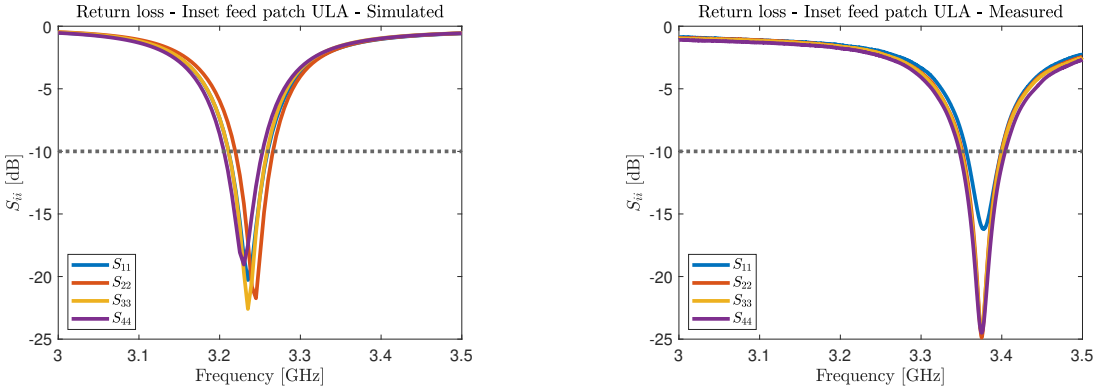

(a) **(b)**

Figure A.5: (a) Simulated and (b) measured return loss for the antenna elements of the ULA.

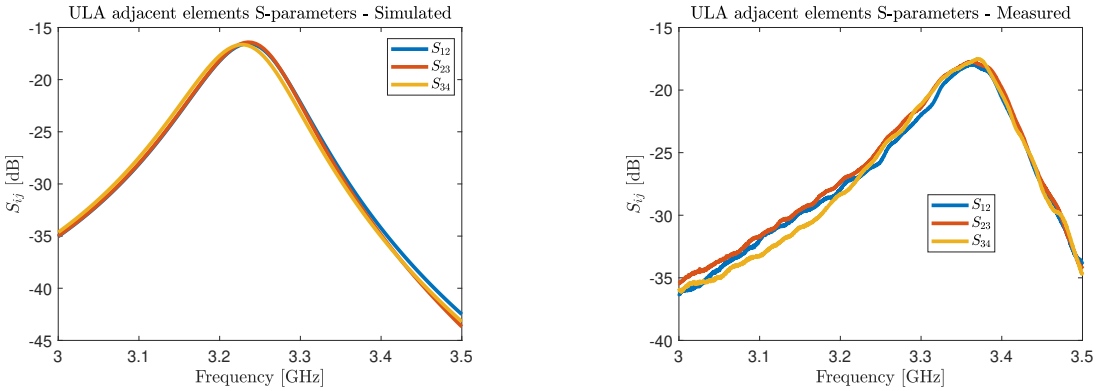

(a) **(b)**

Figure A.6: (a) Simulated and (b) measured transmission S-Parameters for the adjacent elements of the ULA.

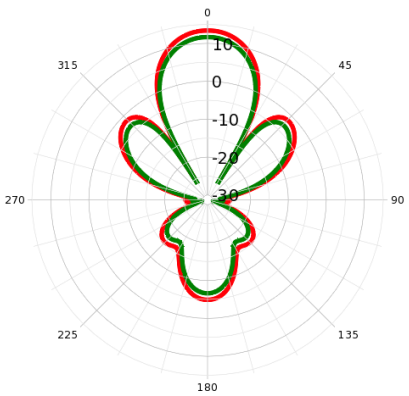

Figure A.7: Simulated gain (in green) and directivity (in red) of the designed patch antenna.

A.2 RxFE5900 RF front-end for complex demodulation

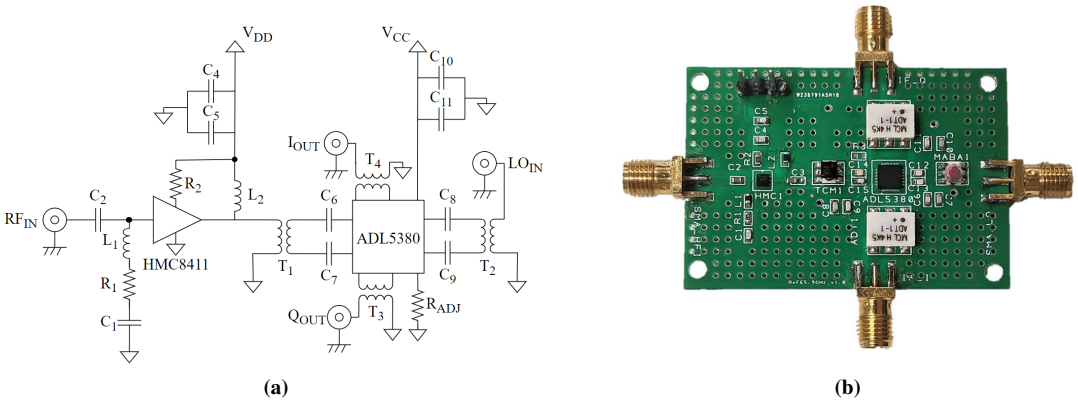

Figure A.8: (a) Schematic and (b) realized PCB of the RxFE5900.

RxFE5900 is a custom-designed board for the preconditioning and complex downconversion of RF signals. Its schematic is shown in Figure A.8a and a photo of the prototype is in Figure A.8b.
The board deploys a Low-Noise Amplifier stage and an active complex demodulator. The whole structure was designed for unbalanced (single-ended) signals. The inputs and the outputs of the board are matched to 50 Ω. The filtering stage after the complex downconversion is deployed through external components, to allow the downconversion to different frequencies and with different bandwidths. The RF input frequency range spans from 400 MHz to 6 GHz. The IF frequency range is from 200 kHz up to 200 MHz. The LO maximum frequency is 5.8 GHz.

For the amplification stage it was chosen an HMC8411 LNA by Analog Devices [3]. The LNA has a typical noise figure of 1.7 dB, providing a gain of 15.5 dB and an output IP3 of 34 dBm. The device can nominally operate from 10 MHz up to 10 GHz, but the best performance for the noise figure is guaranteed in the 100 MHz to 6 GHz frequency range.

The ADL5380 by Analog Devices [4] is in charge of the complex downconversion of the input signal. The device operates from 400 MHz to 6 GHz, providing a conversion gain that depends on the operating frequency. Approximately, the voltage conversion gain is around 7 dB. The phase accuracy is around 0.2 degs and the amplitude balance is 0.07 dB. For the three inputs (RF, LO, and IF), the device works with balanced (differential) signals. Hence, it is necessary to introduce baluns to match the single-ended output of the HMC8411 to the differential input of the ADL5380. The same has to be done for the LO input and the in-phase and quadrature outputs of the demodulator. To do so, it was inserted a TCM1-83X by Mini-Circuits [5] as the balun between the HMC output and the ADL RF input. The TCM is a 1:1 impedance transformer from differential to single-ended 50 Ω. It has a wide operating frequency, from 10 MHz to 8 GHz, thus being suitable for the interfacing of the HMC to the ADL. In the frequency of interest (0.4 to 6 GHz), the insertion loss is 1.28 dB on average, introducing a peak amplitude unbalance of 0.76 dB at 6 GHz and a peak phase unbalance of 13 degs at 3 GHz.

For the LO, it was used a MABA-011082 by Macom [6]. The MABA is another 1:1 impedance transformer operating from 5 MHz to 8 GHz. The insertion loss is typically 1.5 dB on all the operating bandwidth. The peak amplitude unbalance is 0.8 dB in the 5 MHz - 3 GHz frequency range and 3.1 dB in the 3-8 GHz range. The peak phase unbalance is 8 degs in the 5 MHz - 3 GHz frequency range and 20 degs in the 3-8 GHz range. The MABA was chosen for its capability of managing an RF power up to 1 W.
The in-phase and quadrature differential outputs of the quadrature demodulator were interfaced to the single-ended output of the board through a pair of ADT-1-1+ by Mini Circuits [7]. Their operating frequency range is from 150 kHz to 400 MHz and they provide a 1:1 impedance transformation as the previous two baluns. The peak insertion loss is 3 dB. The amplitude unbalance is lower than 0.5 dB up to 150 MHz, reaching a peak of 4 dB at 400 MHz. For the phase unbalance, it is lower than 6 degs up to 150 MHz, and it reaches 25 degs at 400 MHz. Hence, practically the balun ensures appreciable performance for IFs up to 200 MHz.
Both the ADL5380 and the HMC8411 have 5 V power supply. Thus, a single DC supply source is necessary.

The PCB was designed on RO4350B [8] with dielectric constant $\epsilon_r = 3.66$ and thickness 0.762 mm. The copper foil has 35 µm thickness. The substrate provides low dissipation factor $\tan\delta = 3 \cdot 10^{-3}$ up to 10 GHz. The power traces width was dimensioned taking into account the copper thickness and the amount of carried current. The IPC-2221 [9] establishes a standard for the power traces width (expressed in mils) in PCB according to the conductor thickness h_C expressed in Oz, the allowed temperature increase in Celsius degrees ΔT and the maximum current flow I in Amperes:

$$W = \frac{\sqrt[0.725]{\dfrac{I}{(0.048\Delta T)^{0.44}}}}{h_C \cdot 1.378} \tag{A.7}$$

The signal traces were dimensioned using the LineCalc tool of Keysight PathWave ADS. Considering the whole circuit drains as peak current less than 1 A, the widths in Table A.2 were chosen for both signal and power traces.

	Min [mm]	Nom [mm]	Avg [mm]
Signal	0.25	1.6	0.6
Power	0.15	0.2	0.3

Table A.2: Signal and power traces minimum (Min), nominal (Nom) and average (Avg) values.

A.3 RF Downcoverter

This section describes the RF downconverter with an integrated IF bandpass filter. The schematic is in Figure A.9a. Figure A.9b depicts the realized PCB and the mounted components. The board is in charge of amplifying, downconverting, and filtering an

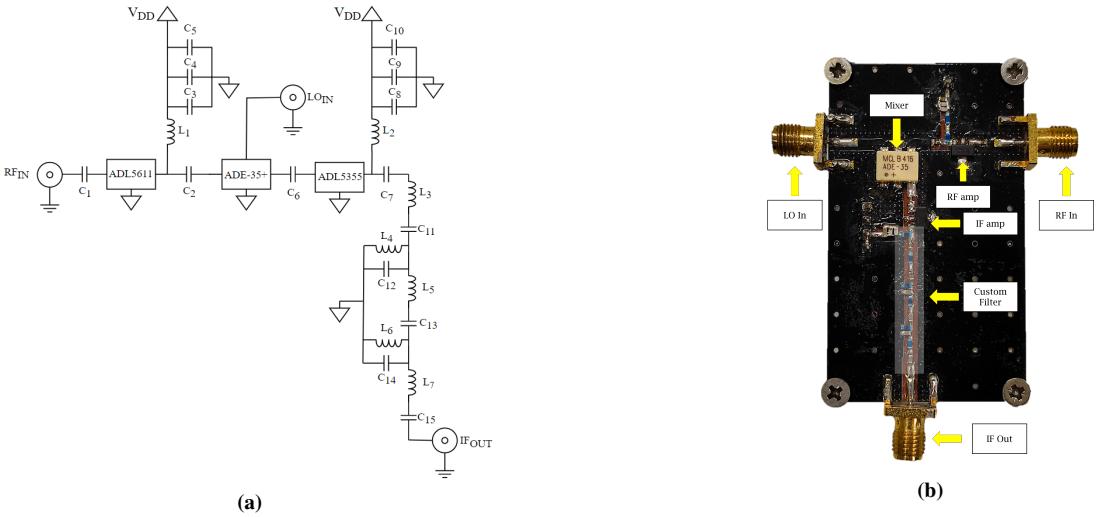

Figure A.9: (a) Schematic and (b) realized PCB of the described RF downconverter.

RF signal with center frequency $f_{RF} = 3.35$ GHz. The first stage is an amplifier, the ADL5611 by Analog Devices [10]. The block operates from 30 MHz to 6 GHz, with a gain of 23 dBm up to 2 GHz, 20 dBm up to 4 GHz, and sensibly decreases to 15 dBm when reaching 6 GHz. Hence, at the frequency of interest, the gain is 20 dBm, with a noise figure NF ≈ 3 dB. The 1dB compression point and the Third Order Intercept (IP3) are respectively ≈ 17.4 dB and ≈ 28.6 dB. The bias is on the RFout port of the device and requires an RF choke $L_1 = 43$ nH. The output is connected to the ADE-35+ passive mixer by Mini-circuits [11]. The ADE-35+ is a surface-mount frequency mixer operating from 1.6 GHz up to 3.5 GHz. Being a passive mixer, it introduces a conversion loss that in the frequency of interest is approximately 8 dB. It provides a good LO to RF isolation (16 dB minimum, 25 dB typical) and also a good LO to IF isolation (12 dB minimum, 22 dB typical). The minimum power for the LO branch signal is +7 dBm. Because of the fact the mixer introduces a strong attenuation, another gain block is on the IF path. The ADL5535 [12]. Its structure is very similar to the ADL5611, but it operates from 20 MHz up to 1 GHz. Hence, a different RF choke is required ($L_2 = 470$ nH).
As regards the performance in terms of gain, the board was employed for different experiments (see Chapter 4 and Chapter 5), in which the IF frequency was different. In one case, the interest was in having a $f_{IF} \approx 200$ MHz, while in the other the interest was in $f_{IF} \approx 20$ MHz. The gain associated with the first frequency is ≈ 16 dB while for the second one, the gain is ≈ 16.7 dB.

A.3.1 Design of the IF band-pass filters

Having two IF also means the two IF filters to reject the high-frequency components should be different. In order to employ the same PCB layout, the first filter developed by *Piccinni* in [13] (which reflection and transmission coefficients in the frequency domain is in Figure A.10a-A.10b respectively) was substituted by only changing the lumped components because both IF allows the use of them.

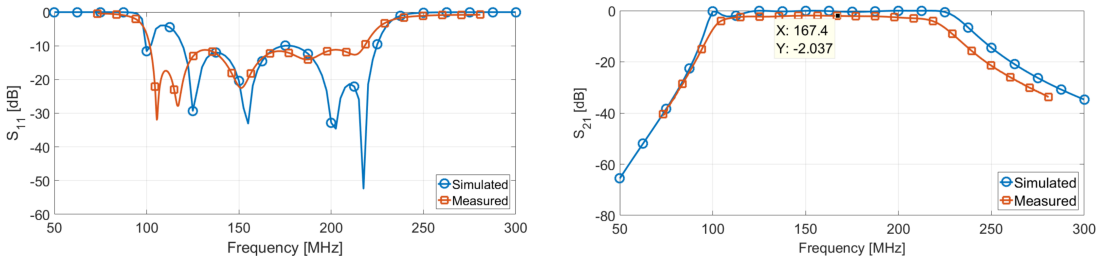

Figure A.10: 5th order Chebyshev band-pass filter designed by *Piccinni G.* in [13]: (a) simulated and measured return loss and (b) simulated and measured transmission loss (S_{21}) coefficient.

The second (low-IF) designed filter was designed through Keysight ADS and the resulting simulation is in Figure A.11.

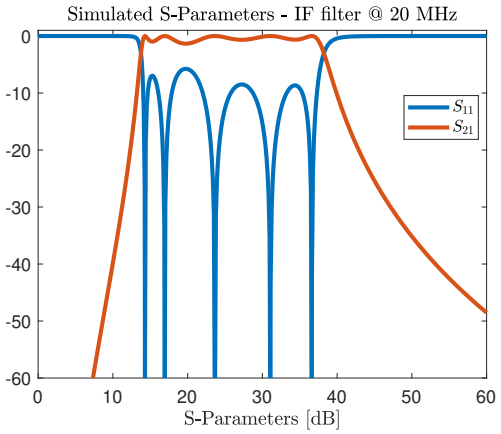

Figure A.11: Designed pin-to-pin compatible 5th order Chebyshev band-pass filter return loss and transmission loss coefficient.

A.4 LTC6957 logic interface board

The LTC6957 by Analog Devices [14] is a low-phase noise, dual output logic converter. The device is available in several versions, providing different output logic levels corresponding to different logic families. The LTC6957-3 provides a pair of in-phase CMOS logic outputs. The device operates in the frequency range of 0 to 300 MHz. The differential input signal level peak-to-peak range spans from 0.2 to 2 V. The bias voltage is $V_{DD} = 3.3$ V which is almost equal to the output high-level voltage. The low-level voltage is in the order of tenths of a Volt. The device provides an internal filter bank. The wanted filter can be chosen by setting high or low logic values on the `FILTA` and `FILTB` inputs.

The aim of the designed board was to provide the possibility of converting CW signals to CMOS square waves that can be logically interfaced with the digital architecture described in Chapter 5. The board schematic is in Figure A.12a while the realized board is in Figure A.12b.

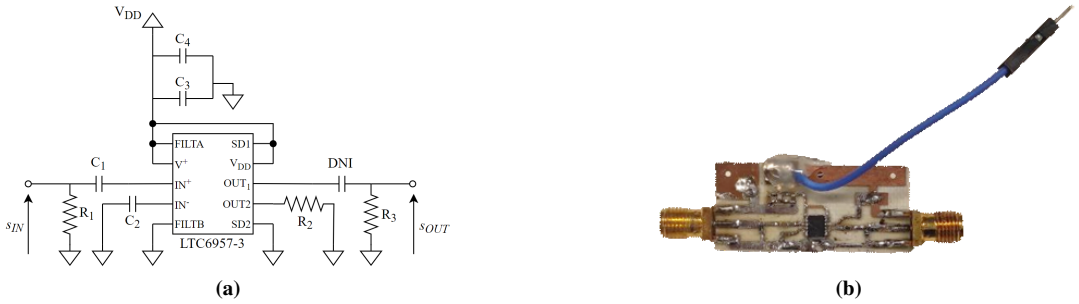

Figure A.12: (a) Schematic and (b) realized PCB of the described squaring circuit.

The board layout was prototyped using an FR4 substrate. The biasing and interfacing networks include lumped components because of the low frequency of operation. The board was realized in the laboratory using an LPKF Protomat C60, without the possibility of plating via holes. Therefore, the designed architecture, `FILTA` is on logic HIGH while `FILTB` is on logic low to simplify the PCB layout. With this configuration, the input filter edge is at 500 MHz. The inputs and outputs of the device are matched to 50 Ω. The AC-coupling capacitor marked as "DNI" on the schematic was substituted with a zero-ohm resistor, while the second output of the device was connected to the ground because it was not needed.

A.4.1 Validation of the phase coherency

Some tests were performed to assess the introduced jitter and the phase/frequency coherency test after the squaring stage. The CWs were generated as the result of a downconversion procedure by means of the RF downconverter described in Section A.3. It employed the version with the bandpass filter centered at 27 MHz. The setup was composed as follows. A pair of ADF4355 PLL evaluation boards by Analog Devices [15] were connected to a pair of RF downconverters to the RF-in port to generate single-tone signals. To ensure phase consistency of the generated waveforms, both

PLL were connected to the same reference signal source, i.e. the Keysight E4433B ESG-D Series Digital RF Signal Generator [16]. The reference signal frequency was 100 MHz, while the PLL output frequency was set to $f_{RF} = 3.4$ GHz. The LO input of the RF downconverter was generated by an Agilent N5182A Vector Signal Generator [17], with frequency $f_{LO} = 3.38$ GHz. Both signal generators have a single output, hence a power divider was employed to split the single output into a pair of in-phase outputs for both instruments. To measure the waveform parameters, it was used a LeCroy Wave Pro 7300A digital oscilloscope (DSO). The DSO has a 3 GHz analog bandwidth and a 20 GB/s maximum sampling rate. The RF downconverter setup results in an IF $f_{IF} = 20$ MHz.
The test consisted of four phases:

- Measurement of the imposed phase shift at RF
- Measurement of the imposed phase shift at IF at the output of the downconverter
- Measurement of the imposed phase shift at IF at the output of the LTC6957 board
- Characterization of the jitter of the LTC6957 board

The RF phase shift was imposed by keeping one of the two PLLs as a reference and setting the phase shift on the second one. For a waveform at a frequency of 3.40 GHz, the maximum sampling rate guarantees ≈ 6 points per period, thus introducing a ≈ 1.07 rad phase ambiguity that is too high for phase critical application. Since the measured signal is periodic and the trigger event is identical for every sweep (the rising edge of the waveform generated by the reference PLL is taken as the trigger event), it is possible to exploit the Random Interleaved Sampling (RIS) function of the DSO [18]. The RIS generates a very high effective sampling rate by moving the trigger *between* samples. In this way, successive asynchronous acquisitions of the same signal are stored and properly reordered to generate a virtually higher sampling rate that can reach 200 GS/s. A visual representation of the operations performed by RIS is in Figure A.13. With the new sampling frequency, the phase resolution nominally drops

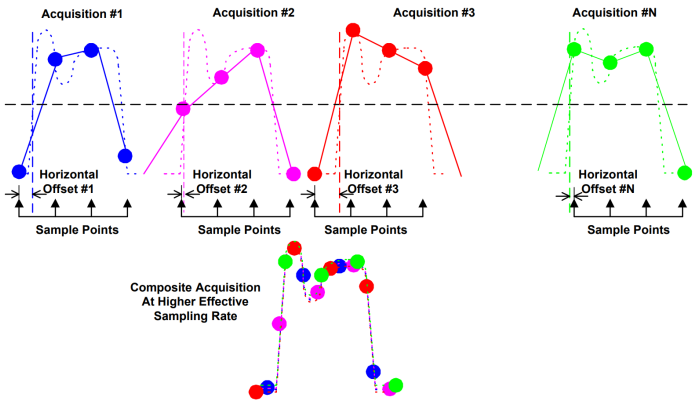

Figure A.13: Visual representation of the RIS procedures from the LeCroy whitepaper [18].

to 0.1 rad for the RF signal. However, since the sampling is not anymore uniform, this value is not reliable. After having imposed the phase shift, the result of the phase shift measurement is in Figure A.14. By zooming the timebase, it is possible to measure a

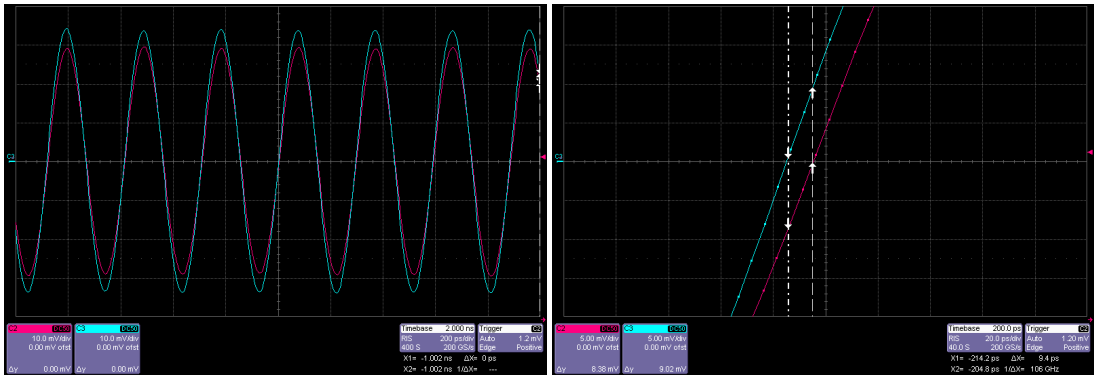

(a) (b)

Figure A.14: RF phase shift analysis: (a) large and (b) small time base for acquired waveforms.

time delay $\Delta\tau_{RF} = 9.4$ ps. Hence, the relative phase shift is

$$\Delta\varphi(\Delta\tau_{RF}) = 2\pi f_{RF}\Delta\tau_{RF} \approx 0.20 \text{ rad}$$

Then it was measured the IF output of the downconversion stage. The result is in Figure A.15. Note that the sampling frequency is 20 GS/s in single-shot mode, hence

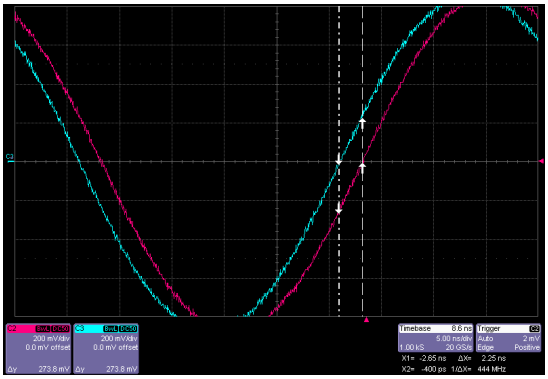

Figure A.15: IF phase shift analysis of the downconverter output: zoom on a small time base capture.

the phase resolution for IF is $2\pi \cdot 10^{-3}$ rad. In this case, $\Delta\tau_{IF} = 2.25$ ns. Hence,

$$\Delta\varphi(\Delta\tau_{IF}) = 2\pi f_{IF}\Delta\tau_{IF} \approx 0.28 \text{ rad}$$

Given the error in the RF phase estimation, it is possible to consider this value an indicator of an acceptable level of phase difference conservation in the downconversion stage.
Therefore, by connecting the LTC6957 board, the result is as in Figure A.16. The two squared signal have a time delay $\Delta\tau_{IF}^{S} = 2.6$ ns that lead to

$$\Delta\varphi(\Delta\tau_{IF}^{S}) = 2\pi f_{IF}\Delta\tau_{IF}^{S} \approx 0.32 \text{ rad}$$

The squaring stage introduces a relative error of 0.04 rad.

The jitter of the generated square waves was characterized by time domain measurements and statistical analysis. The results are in Figure A.17. The period analysis resulted in an equal mean value of approximately 50 ns with a standard deviation of

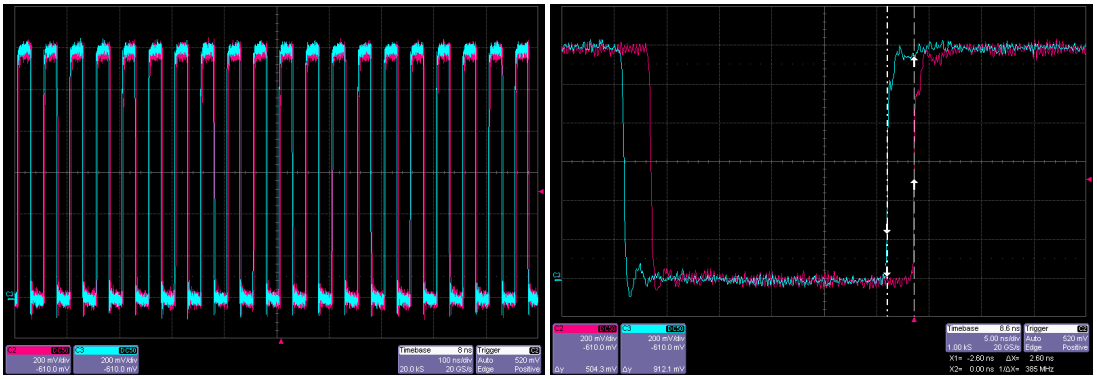

(a) **(b)**

Figure A.16: IF phase shift analysis of the squaring board output: (a) large and (b) small time base for acquired waveforms.

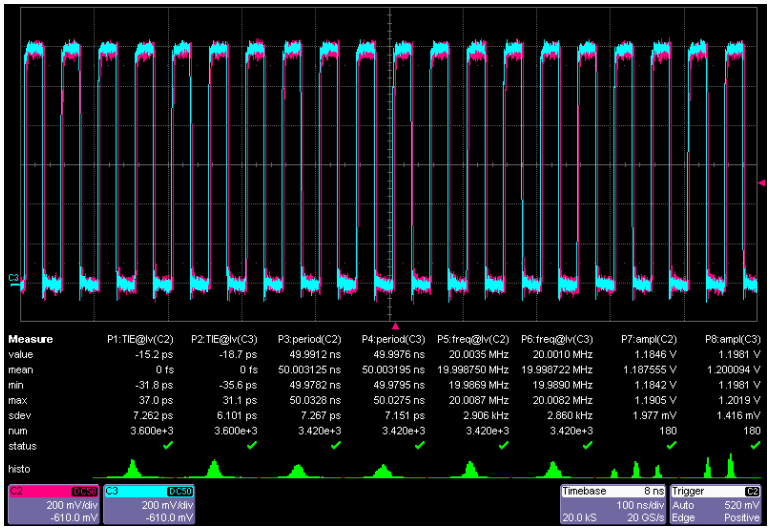

Figure A.17: Statistics on the output of the squaring board for the jitter analysis in the time domain.

units of picoseconds ($\approx 1.4 \cdot 10^{-3}$ %). The histogram plot shows a Gaussian-like distribution of the measurements. To further study the signal jitter, it was taken into account the Time Interval Error (TIE). The TIE measures the position of the rising and falling edges of a square wave and it compares with the expected position of an ideal square wave with the same frequency and duty cycle. By setting 20 MHz as the target (expected) frequency, the results show a 0 mean effect on both devices under test with minimum and maximum values in the order of $\approx \pm 30$ ps. The TIE captures both cycle-to-cycle and period jitter. Hence, it is possible to state the jitter effects are limited to the output of the squaring circuit.

References

[1] C. A. Balanis, *Antenna Theory: Analysis and Design*. New York, NY, USA: Wiley-Interscience, 2005.

[2] "Rogers Corporation RO4003C™ Laminates," (Last accessed on 21-Jun-2023). [Online]. Available: https://www.rogerscorp.com/advanced-electronics-solutions/ro4000-series-laminates/ro4003c-laminates

[3] "HMC8411 Datasheet and Product Info, Analog Devices," (Last accessed on 10-Jul-2023). [Online]. Available: https://analog.com/en/products/hmc8411.html

[4] "ADL5380 Datasheet and Product Info, Analog Devices," (Last accessed on 10-Jul-2023). [Online]. Available: https://analog.com/en/products/adl5380.html

[5] "1:1 CORE & WIRE Transformer, 10 - 8000 MHz, 50 Ω, TCM1-83X+, Mini-Circuits," (Last accessed on 10-Jul-2023). [Online]. Available: https://www.minicircuits.com/WebStore/dashboard.html?model=TCM1-83X%2B

[6] "MABA-011082, Macom," (Last accessed on 10-Jul-2023). [Online]. Available: https://www.macom.com/products/product-detail/MABA-011082

[7] "1:1 CORE & WIRE Transformer, 0.15 - 400 MHz, 50 Ω, ADT1-1+, Mini-Circuits," (Last accessed on 10-Jul-2023). [Online]. Available: https://www.minicircuits.com/WebStore/dashboard.html?model=ADT1-1%2B

[8] "Rogers Corporation RO4350B™ Laminates," (Last accessed on 11-Jul-2023). [Online]. Available: https://www.rogerscorp.com/advanced-electronics-solutions/ro4000-series-laminates/ro4350b-laminates

[9] "IPC-2221A Generic Standard on Printed Board Design," (Last accessed on 11-Jul-2023). [Online]. Available: https://www.ipc.org/TOC/IPC-2221A.pdf

[10] "ADL5611 Datasheet and Product Info, Analog Devices," (Last accessed on 07-Nov-2022). [Online]. Available: https://www.analog.com/en/products/adl5611.html

[11] "ADE-35+, Level 7, SMT Double Balanced Mixer, RF/LO Freq 1600 - 3500 MHz, Mini-Circuits," (Last accessed on 07-Nov-2022). [Online]. Available: https://www.minicircuits.com/WebStore/dashboard.html?model=ADE-35%2B

[12] "ADL5535 Datasheet and Product Info, Analog Devices," (Last accessed on 07-Nov-2022). [Online]. Available: https://www.analog.com/en/products/adl5535.html

[13] G. Piccinni, "Analysis, Modelling and Design of an Indoor Positioning System for Biomedical Applications," Ph.D. dissertation, Politecnico di Bari - Department of Electrical and Information Engineering, 2018.

[14] "LTC6957 Datasheet and Product Info, Analog Devices," (Last accessed on 05-Mar-2023). [Online]. Available: https://www.analog.com/en/products/ltc6957-1.html#product-overview

[15] "ADF4355 Datasheet and Product Info, Analog Devices," (Last accessed on 05-Mar-2023). [Online]. Available: https://www.analog.com/en/products/adf4535.html

[16] "E4433B ESG-D Series Digital RF Signal Generator, 4 GHz, Keysight," (Last accessed on 07-Nov-2022). [Online]. Available: https://www.keysight.com/us/en/product/E4433B/esgd-series-digital-rf-signal-generator-4-ghz.html

[17] "5182A MXG Vector Signal Generator, 100 kHz to 6 GHz, Keysight," (Last accessed on 07-Nov-2022). [Online]. Available: https://www.keysight.com/us/en/product/N5182A/mxg-vector-signal-generator-100khz-6ghz.html

[18] "Peter J. Pupalaikis - LeCroy Random Interleaved Sampling (RIS) - Whitepaper," (Last accessed on 30-Jun-2023). [Online]. Available: https://cdn.teledynelecroy.com/files/whitepapers/wp_ris_102203.pdf

APPENDIX $\mathcal{B}$

IQ Samples Phase Extraction

Suppose an N-element array of antennas receives a signal $s_i(t)$ at each element:

$$s_i(t) \approx K\cos(2\pi f_{RF}t + \varphi_i),\ i = 0, \cdots N-1 \tag{B.1}$$

Suppose this downconversion stage of the RF chain is a complex demodulator. The low-pass equivalent of each signal is:

$$\begin{cases} I(t) = \dfrac{K}{2}\cos(2\pi f_{IF}t + \varphi_i) \\ Q(t) = \dfrac{K}{2}\sin(2\pi f_{IF}t + \varphi_i) \end{cases} \tag{B.2}$$

under the hypothesis no amplitude or phase imbalance affects the two branches. After passing through an ADC stage, the equivalent passband in complex notation is:

$$s_i^{IF}[k] = \frac{K}{2}\Big(I[k] - jQ[k]\Big) \tag{B.3}$$

The phase difference can be computed through the argument of the complex number $s_{IF}[k]$ if the sampling frequency is high enough:

$$\angle s_i^{IF}[k] = \arctan2(s_{IF}[k]) = \arctan2\left(\frac{Q[k]}{I[k]}\right) = \varphi_i \tag{B.4}$$

where $\arctan2(\cdot)$ is the 2-argument arctangent function. The arctan2 for a complex number $x + jy \in \mathbb{C}$, where $y, x \neq 0$ is defined as

$$\arctan2(y,x) = \begin{cases} \arctan(y/x) \ \text{ if } x > 0 \\ \arctan(y/x) + \pi \ \text{ if } x < 0 \text{ and } y \geq 0 \\ \arctan(y/x) - \pi \ \text{ if } x < 0 \text{ and } y < 0 \\ \pi/2 \ \text{ if } x = 0 \text{ and } y > 0 \\ -\pi/2 \ \text{ if } x = 0 \text{ and } y < 0 \end{cases} \tag{B.5}$$

In this case, the phase difference between array elements i and j can be computed as

$$\Delta\varphi_{ij} = \varphi_j - \varphi_i = \angle s_j^{IF}[k] - \angle s_i^{IF}[k] \tag{B.6}$$

The IQ downconversion has the drawback of being strongly dependent on the actual quadrature of the I and Q local oscillators. If a small imbalance is present, and so the I and Q oscillators are not phase-shifted of a quantity $\pi/2$, determining a cross-talk between the I and Q components. For the phase integrity point of view, from the (B.2) by denoting with φ_e the error, we get for instance

$$\begin{cases} \hat{I}(t) = \dfrac{K}{2}\cos(2\pi f_{IF} t + \varphi_i) \\ \hat{Q}(t) = \dfrac{K}{2}\sin(2\pi f_{IF} t + \varphi_i + \varphi_e^i) \end{cases} \tag{B.7}$$

By substituting in the (B.6), the estimated phase difference is:

$$\Delta\hat{\varphi}_{ij} = \varphi_j - \varphi_i + (\varphi_e^j - \varphi_e^i) \tag{B.8}$$

that may lead to AoA estimation errors in phase interferometry. This problem may be partially solved by implementing the IQ downconversion stage directly in digital, so the IQ beating is done after the sampling. However, in this case, a key role is played by the word length for the sample representation and the sampling frequency itself.

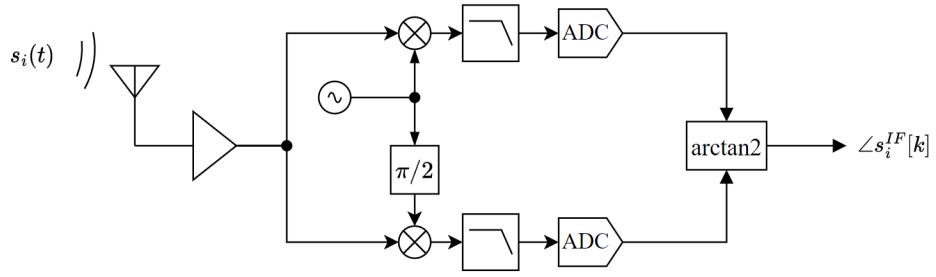

Figure B.1: Phase extraction from IQ samples using complex demodulation.

List of Publications by the author

International journals

1. **A. Florio**, G. Avitabile, and G. Coviello, “Multiple Source Angle of Arrival Estimation through Phase Interferometry,” IEEE Transactions on Circuits and Systems II: Express Briefs, vol. 69, no. 3, pp. 674–678, 2022.
2. **A. Florio**, G. Avitabile, and G. Coviello, “A Linear Technique for Artifacts Correction and Compensation in Phase Interferometric Angle of Arrival Estimation,” Sensors, vol. 22, no. 4, p. 1427, 2022.
3. G. Coviello, **A. Florio**, G. Avitabile, C. Talarico, and J. M. Roveda, “Distributed Full Synchronized System for Global Health Monitoring based on FLSA,” IEEE Transactions on Biomedical Circuits and Systems, 2022.
4. G. Avitabile, **A. Florio**, V. L. Gallo, A. Pali, and L. Forni, “An Optimization Framework for the Design of High-Speed PCB VIAs,” Electronics, vol. 11, no. 3, p. 475, 2022.
5. G. Coviello, G. Avitabile, **A. Florio**, C. Talarico, and J. M. Wang-Roveda, “A Novel Low-Power Time Synchronization Algorithm Based on a Fractional Approach for Wireless Body Area Networks,” IEEE Access, vol. 9, pp. 134916–134928, 2021.
6. G. Coviello, G. Avitabile, and **A. Florio**, “A Synchronized Multi-Unit Wireless Platform for Long-Term Activity Monitoring,” Electronics, vol. 9, no. 7, p. 1118, 2020.
7. G. Avitabile, **A. Florio**, and G. Coviello, “Angle of Arrival Estimation through a Full-Hardware Approach for Adaptive Beamforming,” IEEE Transactions on Circuits and Systems II: Express Briefs, vol. 67, no. 12, pp. 3033–3037, 2020.

International conferences and workshops

1. **A. Florio**, C. Talarico, G. Avitabile, and G. Coviello, "A Synchronous Digital Phase Detector Architecture based on a Coarse Time-to-Digital Approach," in 2023 8th International Conference on Smart and Sustainable Technologies (SpliTech), 2023.
2. **A. Florio**, C. Talarico, and G. Avitabile, "A Simple Synchronous Architecture for Angle of Arrival Estimation Based on Phase Interferometry," in 2022 IEEE Asia Pacific Conference on Postgraduate Research in Microelectronics and Electronics (PrimeAsia), IEEE, 2022, pp. 18–21.
3. **A. Florio**, G. Avitabile, and K. L. Man, "Estimating the Angle of Arrival from Multiple RF Sources using Phase Interferometry," in 2022 19th International SoC Design Conference (ISOCC), IEEE, 2022, pp. 193–194.
4. **A. Florio** and G. Avitabile, "Characterization of a Multisource Angle of Arrival Estimation Technique based on Phase Interferometry," in 2022 18th International Conference on Synthesis, Modeling, Analysis and Simulation Methods and Applications to Circuit Design (SMACD), IEEE, 2022, pp. 1–4.

5. G. Coviello, G. Avitabile, C. Talarico, J. M. Wang-Roveda, and **A. Florio**, "Master-Slave Mutual Time Synchronization in a Wireless Body Area Network," in 2022 IEEE 65th International Midwest Symposium on Circuits and Systems (MWSCAS), IEEE, 2022, pp. 1–4.

6. G. Coviello, G. Avitabile, C. Talarico, J. M. Wang-Roveda, and **A. Florio**, "A Wireless Synchronized System for Long-Term Global Health Monitoring," in 2022 7th International Conference on Smart and Sustainable Technologies (SpliTech), IEEE, 2022, pp. 1–4.

7. G. Avitabile, **A. Florio**, K. L. Man, and C. Zhao, "A Long-Term Synchronized System for Healthcare," in 2022 19th International SoC Design Conference (ISOCC), IEEE, 2022, pp. 191–192.

8. **A. Florio** and G. Avitabile, "The Correlation between Phase Interferometric Angle of Arrival Estimation Quality Degradation and Uniform Linear Array Spacing," in 2021 29th Mediterranean Conference on Control and Automation (MED), IEEE, 2021, pp. 244–248.

9. **A. Florio** and G. Avitabile, "A Linear Array Mutual Coupling Compensation Technique for Angle of Arrival Estimation," in 2021 18th International SoC Design Conference (ISOCC), IEEE, 2021, pp. 193–194.

10. G. Coviello, G. Avitabile, C. Talarico, J. Roveda, and **A. Florio**, "A Fractional Approach to Time Synchronization in Wireless Body Area Networks," in 2021 IEEE International Midwest Symposium on Circuits and Systems (MWSCAS), IEEE, 2021, pp. 933–936.

11. G. Coviello, G. Avitabile, and **A. Florio**, "Wireless Sensor Networks Time Synchronization Algorithms and Protocols Message Complexity Comparison: The Small-Size Star-Topology Case," in International Conference on Innovations in Bio-Inspired Computing and Applications, Springer International Publishing Cham, 2021, pp. 665–674.

12. G. Coviello, G. Avitabile, **A. Florio**, C. Talarico, and J. Roveda, "Relationship between Timer Resolution and Synchronization Message Repetition Frequency in a Synchronized Wireless Sensor Network," in 2021 International Conference on Computer Engineering and Artificial Intelligence (ICCEAI), IEEE, 2021, pp. 535–538.

13. G. Avitabile, K. L. Man, and **A. Florio**, "Power Consumption Analysis of a Fractional Approach to BANs Time Synchronization," in 2021 18th International SoC Design Conference (ISOCC), IEEE, 2021, pp. 189–190.

14. **A. Florio**, G. Avitabile, G. Coviello, J. Ma, and K. L. Man, "The Impact of Coherent Signal Reception on Interferometric Angle of Arrival Estimation," in 2020 International SoC Design Conference (ISOCC), IEEE, 2020, pp. 167–168.

15. **A. Florio**, G. Avitabile, and G. Coviello, "Digital Phase Estimation through an I/Q Approach for Angle of Arrival Full-Hardware Localization," in 2020 IEEE Asia Pacific Conference on Circuits and Systems (APCCAS), IEEE, 2020, pp. 106–109.

16. **A. Florio**, G. Avitabile, and G. Coviello, "An Experimental Validation of the Naïve Approach to Angle of Arrival Estimation for Green WSNs," in 2020 IEEE 20th Mediterranean Electrotechnical Conference (MELECON), IEEE, 2020, pp. 165–168.

17. **A. Florio** and G. Avitabile, "A study on the Impact of the Array Pitch on the Angle of Arrival Estimation through an Interferometric Approach," in 2020 7th International Conference on Information Science and Control Engineering (ICISCE), IEEE, 2020, pp. 155–158.

18. G. Coviello, G. Avitabile, and **A. Florio**, "The Importance of Data Synchronization in Multiboard Acquisition Systems," in 2020 IEEE 20th Mediterranean Electrotechnical Conference (MELECON), IEEE, 2020, pp. 293–297.

19. G. Coviello, G. Avitabile, and **A. Florio**, "The Effects of Timing Error Sources in Wireless Multi-Unit Off-Line Acquisition Systems," in 2020 International SoC Design Conference (ISOCC), IEEE, 2020, pp. 159–160.

20. G. Coviello, G. Avitabile, **A. Florio**, and C. Talarico, "A Study on IMU Sampling Rate Mismatch for a Wireless Synchronized Platform," in 2020 IEEE 63rd International Midwest Symposium on Circuits and Systems (MWSCAS), IEEE, 2020, pp. 229–232.

21. G. Avitabile, **A. Florio**, and G. Piccinni, "A Hybrid Hardware Estimation of the Angle of Arrival for Industrial IoT purposes," in 2019 International SoC Design Conference (ISOCC), IEEE, 2019, pp. 89–90.

Book chapters

1. **A. Florio**, G. Avitabile, and G. Coviello, "Geometric Indoor Radiolocation: History, Trends and Open Issues", in Machine Learning for Indoor Localization and Navigation, S. Tiku and S. Pasricha, Eds. Cham: Springer International Publishing, 2023, pp. 49–69.

Biography

Antonello Florio was born in Bari (Italy) in 1995. He received the BSc in Computer and Automation Engineering and the MSc in Telecommunications Engineering both with honors from Polytechnic University of Bari. He took part to a Double Degree program with University of Nice-Sophia Antipolis (France) where he achieved the *Master de Recherche* in Ubiquitous networking and computing. He collaborated with the DIANA team at INRIA Sophia-Antipolis for his *projet de fin d'étude*. In 2023, he served as Visiting Expert in the Radio Frequency Division at the European Space Research and Technology Centre (ESTEC, The Netherlands) of the European Space Agency (ESA). Since 2019, he is with the Department of Electrical and Information Engineering of Politecnico di Bari as member of the Electronics for Telecommunications Laboratory. His research interests involve phased arrays, theories and techniques for localization and green WSN.

Prizes and Achievements

- Cadence Best Paper Award at the 2021 IEEE 18th International Conference on SoC (ISOCC 2021) with "A Linear Array Mutual Coupling Compensation Technique for Angle of Arrival Estimation" by A. Florio and G. Avitabile.
- Finalist of the Huawei Italy University Challenge 2021 with the project "A Full-Hardware Approach to AoA Estimation for the Green WSNs of the future".
- Donation of two Intel FPGA boards, licenses, and several daughterboards from the Intel FPGA Academic Program for research on Full-Hardware Angle-of-Arrival Estimation.

Editorial roles

- Reviewer for IEEE Access, MDPI Remote Sensing, and MDPI Electronics journals.
- Guest editor of the Special Issue "Theory and Techniques for the Deployment of Future Wireless Sensor Networks in 5G and beyond" for MDPI Sensors.
- Guest editor of the Special Issue "Biomedical Applications of Information Technology: History, Trends and Future Challenges" for MDPI Bioengineering.

Teaching

- Teaching assistant and exam jury member for the Electronics for Telecommunication course.
- Teaching assistant and exam jury member for the Digital Programmable System course.
- Exam jury member for the High Frequency Electronic Systems design.
- Co-supervisor of MSc theses in the field of Electronics for Telecommunications.